

**University of Strathclyde Department of  
Pure and Applied Chemistry**

**Developments in Raman spectrometry and intracavity laser  
absorption spectrometry for quantitative analysis**

**Nichola Townshend**

A thesis submitted to the Department of Pure and Applied Chemistry, University of Strathclyde, Glasgow, in fulfilment of the regulations for degree of Doctor of Philosophy.

March 2010

This thesis is the result of the author's original research. It has been composed by the author and has not been previously submitted for examination which has led to the award of a degree.

The copyright of this thesis belongs to the author under the terms of the United Kingdom Copyright Acts as qualified by the University of Strathclyde Regulation 3.50. Due acknowledgement must always be made of the use of any material contained or derived from, this thesis.

This is for the many inspirational people I have met along the way.

## **Abstract**

A primary focus of this work was the investigation of reflectance mode and transmission Raman spectrometry for direct non-invasive quantitative analysis of a pharmaceutical tablet with < 3% w/w active ingredient (API). In the initial part of the study, an HPLC method was devised to quantify chlorpheniramine maleate (the API) in a sample set of more than 280 Chlortrimeton allergy tablets containing a stated API mass of 4 mg. Despite utilising a multi-stage, destructive sample preparation sequence, the average calculated API mass was found to be in good agreement with the stated mass. Nevertheless, sample anomalies were identified which suggested inconsistencies in the manufacturing process.

Reflectance and transmission mode Raman spectrometry (herein referred to as solely reflectance and transmission Raman spectrometry) at a laser wavelength of 785 nm were then used to non-destructively analyse 380 Chlortrimeton tablets. With external calibration tablets, predictions of the API mass based on reflectance Raman spectra were in good agreement with the stated mass. However, predictions from transmission Raman spectra were less successful, with acceptable accuracy only achieved when there was a good match in the photon transmission properties of the calibration and sample tablets. An investigation of the effect of powder properties on the propagation of photons through diffusely scattering media was carried out; the magnitude of the transmission Raman signal obtained for any position of a Raman active layer of flowers of sulphur within or on the surface of the loose powder was found to be dependent upon the size and shape of the particles of the powder. The findings helped explain the results of the tablet analysis.

In addition to investigating Raman spectroscopy as an alternative technique to HPLC for the determination of the API mass in tablets, the feasibility of developing an intracavity laser absorption spectrometry (ICLAS) system for liquid analysis, with the intention of using it as alternative detector to those commonly used in HPLC, was also investigated. It was demonstrated that ICLAS is capable of enhancing the absorption of analytes in liquid samples by utilising a multipass effect of radiation through the sample. ICLAS measurements acquired using a cavity operating at 860 nm constructed

on an optical bench, and operated at an input current of 1.25 times the threshold current, provided an enhancement factor of x14. The magnitude of the enhancement observed depended on the input current utilised and how suited this was to the concentration range being analysed. A compact ICLAS system was constructed, but could not replicate the analysis carried using the optical bench set-up – highlighting the difficulties associated with ICLAS analysis of liquids.

## **Acknowledgements**

I would like to thank Professor David Littlejohn for his advice and continued support throughout this research. I will always be grateful for the opportunities he has given me and wherever I am, he will always be ‘the boss’. I would also like to thank Dr Alison Nordon for her invaluable input as a supervisor and a friend and for the many hours spent discussing over tea, writing Matlab programmes and putting the world to rights.

For three fantastic months the University of South Carolina was home and I am very appreciative of the friendly welcome from my American friends. Special thanks is given to Dr Michael Myrick who kindly let me loose in his lab and who introduced me to the ‘coffee culture’ and let me share an unforgettable Thanksgiving dinner with him and his family. I would also like to thank Heather, Luisa and Lori for the many girls’ days out and for the shopping trips I made you endure.

Clair Scientific, and in particular Dr Paul Dallin and Dr John Andrews have supported a significant proportion of this research through equipment loans, many visits to Northampton and useful advice. I would also like to thank Sue, Amit, Colin and the remaining Pauls for making the experience one to remember.

This research has been possible due to the Centre for Process Analytics and Control Technology (CPACT) and the network of industrial members and vendor companies. Funding for this research was gratefully received from EPSRC, CPACT and the University of Strathclyde.

This experience would not have been the same without the many friends I have made along the way; the many chats and outings with Pamela, Nats and Alison, mischievous activities with my partner in crime, ‘Nicci tea’ with Sergey, and boys..... what can I say? I have enjoyed being your Leader!

## **Contents**

|   |           |
|---|-----------|
| <b>Abstract</b>   | <b>iv</b> |
| <b>Acknowledgments</b>  | <b>v</b>  |
| <b>Contents</b>   | <b>vi</b> |
| <b>1. Introduction</b>  |           |
| 1.1 Process Analytical Technology   | 1         |
| 1.2 Integration of PAT in the pharmaceutical industry   | 3         |
| 1.3 Manufacture and testing of solid dosage forms   | 4         |
| 1.4 Research aims   | 14        |
| <b>2. Raman Spectroscopy</b>  |           |
| 2.1 Raman theory  | 16        |
| 2.2 Raman and Infrared spectroscopy   | 25        |
| 2.3 Raman signal  | 28        |
| 2.4 Raman instrumentation   | 29        |
| 2.5 Raman instruments used in this study  | 38        |
| <b>3. Study of tablet-to-tablet variation with respect to the mass of a low concentration API</b>                 |           |
| 3.1 Introduction  | 50        |
| 3.2 Experimental  | 52        |
| 3.3 Preparation of mobile phase, standards and samples  | 53        |
| 3.4 Results and discussion  | 55        |
| 3.5 Conclusions   | 64        |
| <b>4. Investigation of the effect of powders on the propagation of photons through diffusely scattering media</b> |           |
| 4.1 Literature Review   | 66        |
| 4.2 Experimental for fundamental studies  | 73        |
| 4.3 Results and discussion  | 78        |

|  |     |
|--|-----|
| 4.4 Conclusions  | 113 |
| <b>5. Non-invasive analysis of Chlortrimeton tablets by Raman Spectrometry</b>                   |     |
| 5.1 Review of literature on the direct analysis of tablets                                       | 115 |
| 5.2 Experimental   | 128 |
| 5.3 Results and discussion   | 132 |
| 5.4 Conclusions  | 175 |
| <b>6. The development of intracavity laser absorption spectrometry For trace liquid analysis</b> |     |
| 6.1 Introduction   | 176 |
| 6.2 ICLAS theory   | 181 |
| 6.3 Experimental set-up  | 185 |
| 6.4 Results and discussion   | 187 |
| 6.5 Conclusions  | 200 |
| <b>7. Conclusions and suggestions for future work</b>  |     |
| 7.1 Conclusions  | 202 |
| 7.2 Future work  | 207 |
| <b>8. References</b>   | 209 |



## **1. Introduction**

### **1.1 Process Analytical Technology**

Within the chemical industry, the large scale manufacture of products is a competitive business which is increasingly reliant on the development of analytical techniques capable of providing a route to cost-effective, consistent manufacture, resulting in assured product quality. Traditional methods of controlling chemical manufacturing processes have relied on the measurement of physical variables of the process including temperature and pressure. Recently, however, process analytical applications of at-, on- and in-line spectroscopic techniques such as near and mid infrared and Raman spectrometries<sup>1</sup> have been employed to allow the careful monitoring of a process from the first stages of method development through to “end-of-process testing” in order to rapidly detect potential problems, thus preventing loss of time, money and feedstock, and in turn ensuring that the tightest possible product quality can be achieved and maintained at the lowest possible cost<sup>2-6</sup>.

There is now growing enthusiasm in the pharmaceutical industry for the potential benefits offered by Process Analytical Technology (PAT), an initiative introduced by the Food and Drug Administration (FDA) that aims to promote improvements in manufacturing efficiency and product quality whilst still complying with regulatory constraints. PAT is being actively promoted by the FDA as ‘a system for designing, analyzing, and controlling manufacturing through timely measurements (i.e., during processing) of critical quality and performance attributes of raw and in-process materials and processes with the goal of ensuring final product quality’<sup>7</sup>.

The goal of the PAT approach is to encourage the industry to adopt innovative technologies that will improve quality without raising concerns that the new approach will lead to validation problems and in turn delays in production. In order to achieve this, the key components of the process analytical approach have to be identified: a sound understanding of the product manufacturing process, appropriate data analysis and process analytical tools available, and the introduction of the

continuous feedback of information during the manufacturing process. From intuition, the best performing organisations will pay meticulous attention to their processes – relating better understanding of the process operations and the need to control them to provide improvements in quality. The PAT initiative emphasises the importance of process understanding and is designed to determine the critical variables of a system and where controls should be inserted into the systems to provide good monitoring and control of these factors. The foundation that the PAT approach is based on is that quality cannot be tested into products; rather it should be built in or should be by design.

## **1.2 Integration of PAT in the pharmaceutical industry**

Conventional pharmaceutical manufacturing is generally achieved using batch processing followed by off-line laboratory testing on collected samples to determine the quality of the product with respect to the relevant specifications. This approach has been used for many years and has been sufficient in providing pharmaceuticals to the public, however, in this instance the focus is entirely on the end stage product. Consequently, any deviations in the manufacturing processes are not identified until the quality of the final product is assessed and hence are not rectified. Adoption of this approach by the pharmaceutical industry is a consequence of traditions, cost considerations and a general reluctance to change, and as a result several disadvantages exist: a need for reactive re-optimisation of processes, high levels of out of specification products, and the limited integration of innovative technologies. Whilst the application of PAT in the petroleum and petrochemical industry<sup>8-10</sup> is not a novel concept, the pharmaceutical industry has generally been hesitant to introduce innovative systems into their manufacturing processes owing to the primary problem of regulatory uncertainty.

The conventional method of demonstrating to a regulatory body that a pharmaceutical manufacturing process is fit for purpose, delivering a safe, pure and effective product, is to validate the process. Once a process is validated, it is then assumed that it is understood and consequently can be maintained by tuning a small number of critical controls during commercial manufacturing; furthermore, in order

to ensure variability can be controlled and minimised, the process is trialed using a large number of test batches. As the stages in a validation process can be extensive they are described in detail in a validation protocol and the results are presented in a validation report. The validation of a product is not only time consuming but also has significant resource requirements for the planning and execution stages and furthermore, failure to achieve first time validation of the product results in the delay of approval and market launch. Once a successful validation has been completed, only limited and very minor changes can be made to the process without requiring revalidation of the product.

This detailed and complicated validation process has historically been cited as the barrier between the pharmaceutical industry and continuous improvement and, therefore, instead of using the economic advantage of increased efficiency, the benefits of the PAT approach have been mainly disregarded owing to the large cost and risk of newly validating and regulating processes in line with the PAT framework. Furthermore, the validation of a process requires the expertise of personnel from multiple sectors including manufacturing, technology transfer and research and development, and the use of these personnel to modify processes for existing products is not favourable in an industry that is striving to achieve rapid development and high speed to market approach. Consequently, the changes that follow a shift to the continuous improvement approach have been seen as an unfavourable move by the pharmaceutical industry until recently.

Despite having legitimate reservations, the hesitancy of the industry to introduce an innovative approach in pharmaceutical manufacturing is undesirable from a public health perspective. Efficient pharmaceutical manufacturing is a vital part of an effective healthcare system and as pharmaceuticals are at the centre of health care, utilising cutting edge technology in the pharmaceutical industry together with the principles of quality control to respond to the challenges of their business is an obvious choice.

Recognising the need to change the mindset of the pharmaceutical industry, the FDA launched an initiative, 'Pharmaceutical cGMPS for the 21<sup>st</sup> Century: A Risk-Based Approach.' This proposal stated that the most up to date concepts of risk management and quality systems would be incorporated into the manufacturing process whilst still maintaining good quality products. Furthermore, manufacturers would be encouraged to innovate and hence use the latest scientific advances in pharmaceutical manufacturing and technology. The FDA initiative is designed to facilitate the removal of both real and perceived barriers by improving the efficiencies of the manufacturing and regulatory processes, and hence assessing and mitigating risks associated with poor product and process quality. Consequently, the approach suggested by the FDA initiative will ensure:

- Good product quality and performance through the design of effective and efficient manufacturing processes, product and process specifications.
- Product and process specifications are based on a sound understanding of how formulation and process factors affect the product performance.
- Continuous, real-time quality assurance.
- Relevant regulatory policies are adapted to account for the most current level of scientific knowledge.

### **1.3 Manufacture and testing of solid dosage forms**

Pharmaceutical companies worldwide make over-the-counter (OTC) and prescription medicines to treat a range of medical problems. The physical form of these medicines vary from liquids to solids encompassing suspensions, gel filled capsules and coated and uncoated tablets. Whilst there are associated difficulties with the manufacturing process of each dosage form, solid dosage forms can be especially difficult to manufacture owing to the complexity of achieving a homogeneous blend of ingredients and maintaining this through to the final compaction stage.

The pharmaceutical tablet is the most common dosage form of prescription drugs and accounts for 43.7% of all approved drug products that are listed in the orange book<sup>11</sup> – an FDA publication that provides information regarding approved drug products with therapeutic equivalence evaluations. Tablet dosage forms provide patients with a convenient means of handling and administering medicine and the success and popularity of this method has resulted in the more sophisticated development and manufacturing of conventional and advanced controlled release tablets. The processes of granulating, drying, milling, blending and compacting powders into a tablet are multivariate problems. Therefore, to ensure repeatable, good quality tablets are produced first time, every time, the optimisation and monitoring of each step of the process is necessary to ensure that on entering the subsequent step, the product is of as high a quality as possible.

Consequently, spectroscopic techniques capable of such analysis have been identified for monitoring the different stages of tablet manufacture. Near infrared spectrometry (NIRS) has in recent years, shown good potential for the monitoring of powder blending. In 1994 a patent was filed regarding the mixing of powders with on-line NIR measurements to assess the homogeneity and potency of the mixture<sup>12</sup>; this patent was shortly followed by a publication<sup>13</sup>. The work described in both documents featured a static measurement system that allowed the acquisition of real-time measurements without having to disturb the cycle of the mixer – a problem associated with invasive probes used for in-situ measurements in earlier years<sup>14, 15</sup>. In 1999, Miller reported on the use of NIRS to monitor the compaction steps of a powder (blend concentration, compactor roll pressure, granule size etc). It was shown that NIR facilitated an understanding of the influence of the compactor parameters on the characteristics of the resulting products<sup>16</sup>. NIRS has also been evaluated by Han and Faulkner as a method for the analytical control of the steps of tablet production<sup>17</sup> - it was utilised during fluid-bed drying to monitor moisture content and also as to determine end of granulation and end of blending process assays. Furthermore, the thickness of the tablet coating and the identification of tablets in blister packs were carried out by NIRS. A similar study was carried out by Blanco and it was found that tablets could be analysed using a simple single

calibration set built using tablets with a broad concentration range of active pharmaceutical ingredients (API) that were generated in the laboratory from production samples<sup>18</sup>.

Acoustic Emission (AE) analysis is a technique which utilises the transmission and reception of energy in the form of vibrational waves in matter. This technique has also demonstrated its applicability to the manufacturing stages of solid dosage forms: the monitoring of a crystallisation reaction allowed particle size information of the reactor contents to be determined<sup>19</sup> and Whitaker<sup>20</sup> also used acoustic measurements to monitor and determine the end point of a high shear granulation process, which illustrated a high correlation between the AE signals and the particle size and flowability of the granules. Furthermore, Townshend demonstrated that model particles of varying size, shape and density (parameters which require to be controlled in tablet manufacturing) could be distinguished from their different AE signals<sup>21</sup>.

### **1.3.1 *Raman spectroscopy in pharmaceutical operations***

There is an increasing number of publications regarding the use of Raman spectroscopy in the chemical industry<sup>22-24</sup> however, until recently pharmaceutical applications of this technique were not widely investigated. Nevertheless, in recent years Raman spectroscopy has emerged as a potentially useful technique for pharmaceutical applications (see Table 1 ). In 2007, Strachan et al. reviewed the use of Raman spectroscopy for the determination of pharmaceutical solids<sup>25</sup> and in 2004 Finni also described the potential of this technique for pharmaceutical analysis<sup>26</sup>. The published studies are mainly concerned with the analysis of small, solid state organic compounds, but Raman spectroscopy is by no means limited to solid samples as it can also be used successfully with liquids, suspensions and gels<sup>27,28</sup>.

**Table 1 – Description of the stages of manufacture of solid dosage forms and the associated potential applications of Raman spectroscopy<sup>29</sup>**

| <b>Stage of production</b> | <b>Information that could be obtained by Raman spectroscopy</b>                            |
|----------------------------|--|
| Synthesis                  | Process monitoring – progress of chemical reaction   |
| Crystallisation            | Process monitoring – monitoring of solid state properties                                  |
| Milling                    | Monitoring and detection of polymorphic transitions – detection of particle size changes   |
| Blending                   | Process monitoring – determination of powder blend homogeneity                             |
| Granulation                | Monitoring of polymorphic transitions  |
| Drying                     | Monitoring of polymorphic transitions  |
| Tableting                  | Quantification of API<br>Detection of compression effects on physical properties of tablet |
| Coating of tablets         | Determination of coating thickness   |
| Packing                    | Identification of substances and their authenticity  |
| Shelf life                 | Stability monitoring   |

Table 1 highlights that Raman spectroscopy can be applied throughout the multiple stages of solid dosage form manufacture, starting with the initial synthesis and ending with shelf life monitoring.

#### Synthesis

In 1999, Svensson et al. used Raman spectroscopy for monitoring the synthesis and hydrolysis of ethyl acetate<sup>30</sup>. This study demonstrated the suitability of Raman as a monitoring technique when using clear solutions which was attributed to its rapid

speed of analysis and ability to monitor processes non-invasively, through the wall of glass reaction vessels. Furthermore, Svensson concluded that when simple univariate calibrations could not be used, multivariate options such as principle components analysis (PCA) and partial least squares (PLS) could be used in a similar manner as for reaction monitoring with NIRS<sup>30</sup>. The success of Raman spectroscopy as a reaction monitoring technique, using laser wavelengths from 496 to 1064 nm, has been demonstrated in a number of other publications<sup>31-33</sup>.

### Crystallisation

Crystallisation is the subsequent step to the synthesis stage and is a key point in the entire process as its function is to produce material with the desired purity, surface properties, particle size and size distributions. It is important, therefore, to have an in-depth knowledge and understanding of this stage as an unsuccessful crystallisation can cause problems in the forthcoming manufacturing steps. Despite being such a vital stage in the process, crystallisation is not well understood and hence is a poorly controlled variable which costs pharmaceutical companies worldwide, in terms of time, effort and consequently, money. As a result there is a strong interest in the monitoring of crystallisation processes and as the crystallisation of pharmaceuticals is often carried out in aqueous media, the use of Raman spectroscopy for this purpose has been investigated. In 1999, Schwartz monitored *in-situ* lysozyme concentration changes in a hanging drop crystallisation process<sup>34</sup> and changes in polymorphic composition have also been monitored and quantified using in-line Raman spectroscopy<sup>35, 36</sup>. In 2005, Hu et al. reported the simultaneous monitoring of solution concentration and the polymorphic outcome of a crystallisation process by Raman spectroscopy<sup>37, 38</sup> and recently Schöll reported the simultaneous *in-situ* Raman measurement of particle size distribution together with solid and liquid phase analysis<sup>38</sup>.

### Blending

Another complex process in the manufacturing of solid dosage forms is the blending of powders, where a mixing process is used to mix the individual powder



components to a homogeneous state. Whilst the mixing of gases and liquids is a somewhat simple operation, powder mixing is complex as powders demonstrate characteristics of all three states – solids, liquids and gases. Although powders can flow, they are not liquids, although they can endure a degree of deformation, they are not solids and despite their ability to be compressed they are not gaseous<sup>39</sup>. Even when care is taken to ensure that good mixing is achieved, the resultant mixture may not be homogeneously blended owing to the act of segregation.

Segregation is the movement of particles to favoured regions within a container, be it a mixer or storage keg, owing to differences in their physical properties (shape, density, size and size distribution). As the individual component powders of the final blend will exhibit different ranges of physical properties most of the time, this introduces the possibility of segregation during and after the mixing process. Mixing and segregation, therefore, oppose each other – the purpose of mixing is to achieve a state of randomness, however, particles resist this by segregating<sup>39, 40</sup>. This means that a system containing components of varying physical properties will never be truly homogeneously mixed; rather the final blend will be an equilibrium of the two processes. As a result of the complexity of mixing and segregation in powder systems, dose uniformity in solids is difficult to attain. In 2004, Vergote et al. reported the use of Raman for the in-line monitoring of powder blending<sup>41</sup> and Clarke also demonstrated the application of Raman mapping together with NIR mapping to describe powder mixtures in detail<sup>42</sup>. Furthermore, an investigation into the role of different sampling optics for the analysis of solids was carried out and a multivariate model for the monitoring of powder mixing was constructed<sup>43</sup>.

### Tableting

Raman spectroscopy possibly has the greatest potential as a process analytical technique in the tableting stage, where it can be used for the real-time quantification of the API in the tablets. The FDA insist that a verified standard method for the determination of active ingredient concentration in solid dosage forms is in place and currently tablets are analysed destructively by high performance liquid

chromatography (HPLC) – a well understood analytical technique. A sample set of 30 tablets from each production batch are selected and analysed using HPLC to determine their active ingredient content<sup>44</sup>. If the active ingredient mass is within the set specification limits then the distribution of active ingredient and excipients is assumed to be homogeneous within the selected tablets and this assumption is also extended to cover the entire batch in question. Despite off-line HPLC being the accepted method of analysis, it is destructive, expensive and incurs relatively long analysis times. Analysis often requires dedicated instruments and quality control laboratories to be in place and owing to the high volume of samples for analysis, it is common practice for samples to be stored for several weeks prior to analysis. This, therefore, introduces a delay in the determination of the success or failure of a batch, which is costly in both labour intensive analysis as well as in production costs. Additionally, HPLC often requires extensive sample preparation which introduces the potential for multiple sources of error; furthermore, only a small sample of the entire batch is analysed and hence a truly representative analysis may not be achieved, introducing the possibility for the false negative rejection or false positive acceptance of batches.

The increasing demand for efficient quality control in the production of pharmaceutical tablets has sparked a growing interest in the implementation of faster, more robust analytical techniques, such as Raman spectroscopy, that can provide non-invasive, non-destructive analysis<sup>45-47</sup> and most importantly, real-time quality control. The integration of such techniques, allowing real-time control into the compaction stage of a tableting process, for example, allows rapid feedback regarding the success or failure of the unit operation and hence immediate intervention can be taken to correct for any deviation that may have occurred in the process. Moreover, the analysis time associated with Raman spectroscopy is short and hence the potential to move towards a situation where every twentieth tablet during production can be analysed, will not only allow for a better statistical description of the batch, but will also provide a means of facilitating a move towards real-time release and continuous manufacturing (albeit an adventurous target).

The success of Raman spectroscopy for the quantitative determination of active components in tablets has been demonstrated. The quantification of matrix components in antacid tablets was achieved by Kontoyannis<sup>48</sup> and Wang et al. reported the use of Raman for the direct assay of acetylsalicylic acid and furthermore, the identification of the major degradation product, salicylic acid<sup>49</sup>. The analysis of intact gel capsules through unopened blister packs by Raman spectroscopy was also reported<sup>50</sup> and the use of Raman as a monitoring technique during the tableting process has been discussed<sup>51</sup>.

Despite the availability of literature describing the use of Raman spectroscopy for the analysis of pharmaceutical tablets, a perceived disadvantage of this approach arises from the problem of sub-sampling, a consequence of two factors. Traditional Raman instruments adopt a confocal approach, where the laser beam is focused to a sharp point at shallow depths beneath the sample surface and hence the volume of the sample analysed is small. Additionally, owing to the perceived limited penetration depth of NIR light, only a small volume of the tablet will be sampled and in the case of an inhomogeneous tablet, the precision of the method is often limited<sup>52</sup>. Furthermore, it has recently been suggested that the Raman spectrum acquired from measurements made in the reflectance mode is dominated by the Raman signal from the surface layers of the sample – Matousek stated that for a 4 mm thick tablet, 88% of the signal originated from the first millimetre and only 12 % of the signal originated from the remaining 3 mm of sample. The initial method adopted to address this problem was the use of spinning devices to increase the sampled proportion of the tablet<sup>53, 54</sup> however, two more attractive solutions to this problem have been explored.

Multiple fibre probes have been developed to provide larger sample spot sizes and hence achieve global illumination of the sample<sup>55, 56</sup> and examples of the use of such probes for the analysis of pharmaceutical tablets exist in the literature<sup>57-59</sup>. Kim et al. reported that the determination of ambroxyl content in intact capsules using a wide area illumination probe provided results that were more representative of the overall concentration compared to those obtained with a conventional confocal small spot

system<sup>58</sup>. Another solution to the problem of sub sampling has been the use of transmission Raman spectroscopy. Transmission measurements are made by illuminating the sample from the opposite side to the collection optics and hence by doing this the entire thickness of the tablet is sampled providing a more representative measurement. Adoption of transmission Raman measurements for the determination of the API content in tablets has been shown in a number of studies<sup>57, 59, 60</sup>. Johansson et al. compared reflectance and transmission Raman spectroscopy for the quantitative determination of propranolol hydrochloride in pharmaceutical tablets and found that the prediction errors for the transmission Raman approach were 25-30% lower than for the equivalent reflectance mode measurements. Furthermore, it was reported that the construction and interpretation of calibration models for the transmission mode measurements were simpler than for the reflectance mode equivalents<sup>60</sup>. Johansson credited this improvement to the highly representative sampling achieved by the transmission approach compared to the limited sampling of the reflectance Raman measurements. This was also suggested in 2006 when Matousek identified a strong bias of reflectance Raman measurements towards the surface layers of the probed sample whereas with the transmission geometry this was largely absent<sup>59</sup>.

Despite the demonstrated success of wide area illumination probes and transmission Raman measurements for the representative sampling of solid dosage forms, the literature describes only examples of the determination of active ingredients in relatively high concentrations, of which the average minimum is approximately 16% w/w<sup>57, 60</sup>. Studies investigating the use of these approaches for the determination of low content active ingredients in pharmaceutical tablets are therefore lacking and could provide further information as to the value and capability limits of Raman spectroscopy for this application.

It has been shown by the wide range of literature reviewed that Raman spectroscopy is a useful analytical tool with a diverse range of abilities, encompassing many aspects of chemistry. An area of great promise for Raman spectroscopy however, is that of pharmaceuticals and it has been demonstrated that this technique could be of

great benefit in monitoring the manufacturing processes of solid dosage forms, from the initial synthetic stage through to the final stages of compaction. Future research focusing on the successful development of Raman approaches for the non-invasive quantitative determination of active ingredients in solid dosage forms (gels, capsules, coated and uncoated tablets) over a wide range of concentrations, together with the achievement of simple lean prediction models will potentially facilitate the move away from traditional destructive wet chemistry based techniques currently accepted by the FDA. This in turn will benefit pharmaceutical companies worldwide in terms of saving time, money and precious feed stocks as well as allowing for a rapid detailed analysis of batches which will more effectively assess product quality and by implication, consumer safety.

## 1.4 Research aims

The initiative introduced by the FDA has motivated the pharmaceutical industry to employ process analysis, be receptive to innovative technologies and take an interest in the different types of measurements that can be obtained. The manufacture of solid dosage forms and in particular end of process testing, has been highlighted as an area which can benefit greatly from PAT owing to the intrinsically complex nature of solid systems. Furthermore, the development of novel probes and sampling methods for Raman spectroscopy have facilitated the movement of this technique in to the process domain and moreover, has highlighted the suitability of Raman for the analysis of solid pharmaceutical products.

Trace liquid analysis is also an area of interest in a variety of industries and currently, the most widely used technique for this application is high performance liquid chromatography (HPLC). This often requires a complex, time consuming chemical derivatisation step to increase the absorptivity of the target analyte and in turn, improves the sensitivity of the measured absorbance. Alternatively, a physical increase in the pathlength can improve the measurement sensitivity however, in most applications a significant increase in the flow cell pathlength is not possible. Intracavity laser absorption spectrometry is an absorption technique that increases the effective absorption pathlength by multiple passes of radiation through the cavity of a laser and has shown potential for trace liquid analysis.

The specific aims of this research are:

- To characterise the propagation of light through solid pharmaceutical samples in both reflectance and transmission Raman modes and assess the effect of particle size and shape on Raman measurements. A rigorous experimental study will provide complementary data to the theoretically modeled studies reported in the literature.
- To assess the effect of the attenuation of the laser beam and the propagation of the scattered photons on the resulting Raman spectra.

- To investigate the variation in the API mass in a large sample set of low concentration OTC pharmaceutical tablets using HPLC.
- Assess the feasibility of transmission and reflectance Raman spectroscopy for the determination of the API in low concentration pharmaceutical tablets.
- To investigate the use of large spot size Raman mapping for assessing the content uniformity of pharmaceutical tablets.
- Assess an ICLAS system for the analysis of liquid samples.
- Identify the sensitivity enhancements, if any, achieved when using ICLAS compared to conventional single pass absorption techniques.

## 2. Raman spectroscopy<sup>10, 61, 62</sup>

### 2.1 Raman theory

The elastic scattering of light by particles of a smaller wavelength is known as Rayleigh scattering and is the phenomenon that is primarily responsible for the blue colour of the sky. Rayleigh scattering denotes the elastic process where the incident photons interact with and distort the electron cloud surrounding the nucleus of the molecule before scattering. As little or no energy is transferred to or from the photons in this process, the frequency of the scattered light is identical to that of the incident light. In 1928 however, C. V. Raman and K. S. Krishnan demonstrated that when monochromatic light encountered gaseous, liquid or solid matter, a small proportion of the incident light was in-elastically scattered owing to an energy exchange with the vibrational – rotational states of the scattering molecule<sup>63</sup>. This discovery led to the introduction of Raman spectroscopy as a novel technique for the determination of the structure and properties of analyte molecules and in 1930, Raman was awarded the Nobel Prize for his contribution. It was not until the 1980s, however, that advances in near infrared lasers, computer technology and detector sensitivity by and large overcame the problems associated with this technique: inefficient collection and detection of an already weak signal and interferences from fluorescence.

When a sample is irradiated by monochromatic light, the light scattered from the molecule is primarily made up of elastically scattered photons which have the same energy and wavelength as the incident photons, known as Rayleigh scattering. Nevertheless, approximately 1 in  $10^7$  photons are scattered at frequencies either higher or lower than that of the incident photons (inelastic scattering) and this is known as Stokes and anti-Stokes Raman, respectively. Collectively, these two energy altered events are known as Raman scattering.

The intensity of Raman scattered light is proportional to the number of molecules that are used to produce the scattered light and hence for this reason, Raman spectroscopy can be used for quantitative analysis. Furthermore the pattern of a



Raman spectrum is unique for each substance (although will only exhibit minor differences for substances with similar structures) and hence can provide information regarding the molecular vibrations present in the sample which in turn can be used for qualitative analysis. As molecular vibrations are receptive to their local surroundings, changes in temperature and crystal structure can also be detected by Raman spectroscopy.

Classical Raman theory states that a change in the polarisability,  $\alpha$ , of a molecule occurs with a change in the vibrational motion of that molecule. That is, there is an interaction between the incident light and a polarisable analyte molecule to induce in it an oscillating dipole,  $P$ . The induced dipole then releases radiation in all directions and hence light is scattered. The magnitude of the induced dipole moment is proportional to the applied electric field,  $E$ , and the polarisability of the electron cloud of the molecule,  $\alpha$ .

$$P = \alpha E \quad (1)$$

The polarisability is a property of the molecule which describes the mobility of the electrons in that molecule and furthermore, is a function of the size and shape of the molecule. During a vibration, the bonds of a molecule will stretch and contract therefore resulting in a change in the polarisability of the molecule. The polarisability will vary with the natural vibrational frequency of the molecule. If the electric field used to induce the dipole moment is supplied by electromagnetic radiation,  $\nu_0$ , then an intermittent fluctuation of the electric field will occur.

$$E = E_0 \cos(2\pi\nu_0 t) \quad (2)$$

Hence,

$$P = \alpha E_0 \cos(2\pi\nu_0 t) \quad (3)$$

Where,  $E_0$  is the amplitude of the electric field,  $\nu_0$  is laser frequency and  $t$  is time.

Only molecules which exhibit a change in polarisability will be Raman active and if the molecule is vibrating at frequency  $\nu_i$ , then distortion of the molecule from its equilibrium position,  $q$ , will be given by,

$$q = q_0 \cos(2\pi\nu_i t) \quad (4)$$

Where,  $q_0$  is the maximum distortion of the electron cloud.

If it is highly probable that distortion of the electron cloud will result in a change in the polarisability of the molecule and an assumption is made that the amplitude of displacement is small and any variation will be linear, then the polarisability of the intermittently distorting molecule will be described as,

$$\alpha = \alpha_0 + \left(\frac{\delta\alpha}{\delta q}\right)_0 q \quad (5)$$

Where,  $\alpha_0$  is the polarisability of the molecule at equilibrium and  $\left(\frac{\delta\alpha}{\delta q}\right)_0$  is the rate of change of the polarisability with the distortion around the equilibrium molecule.

The change in the polarisability as the molecule vibrates will therefore be:

$$\alpha = \alpha_0 + \left(\frac{\delta\alpha}{\delta q}\right)_0 q_0 \cos(2\pi\nu_i t) \quad (6)$$

As the polarisability varies with time, substituting (6) into (3) gives,

$$P = \alpha_0 E_0 \cos(2\pi\nu_0 t) + \left(\frac{\delta\alpha}{\delta q}\right)_0 q_0(E_0) (\cos(2\pi\nu_i t) \cos(2\pi\nu_0 t)) \quad (7)$$

However, as  $\cos A \cos B = \frac{1}{2} [\cos(A+B) + \cos(A-B)]$ , (7) can be written as,

$$\begin{aligned} P = & \alpha_0 E_0 \cos(2\pi\nu_0 t) & (8) \\ & + \frac{E_0}{2} \left(\frac{\delta\alpha}{\delta q}\right)_0 q_0 \cos(2\pi(\nu_0 - \nu_i)t) \\ & + \frac{E_0}{2} \left(\frac{\delta\alpha}{\delta q}\right)_0 q_0 \cos(2\pi(\nu_0 + \nu_i)t) \end{aligned}$$

From (8), it can be seen that the scattered radiation is comprised of three different components,  $\nu_0$ ,  $(\nu_0 + \nu_i)$  and  $(\nu_0 - \nu_i)$  of which the strongest scattering intensity arises from  $\nu_0$  and hence is the Rayleigh scatter. Scattering which arises from  $(\nu_0 + \nu_i)$  and  $(\nu_0 - \nu_i)$  is much weaker and is known as anti-Stokes and Stokes Raman scattering, respectively, and of the two, Stokes scattering is more intense than its anti-Stokes counterpart. This can be explained by considering the excitation and relaxation processes that occur between the different energy levels in the molecule. Figure 1 illustrates the three combinations of excitation and relaxation processes that can occur to produce Rayleigh, Stokes and anti-Stokes scattering.

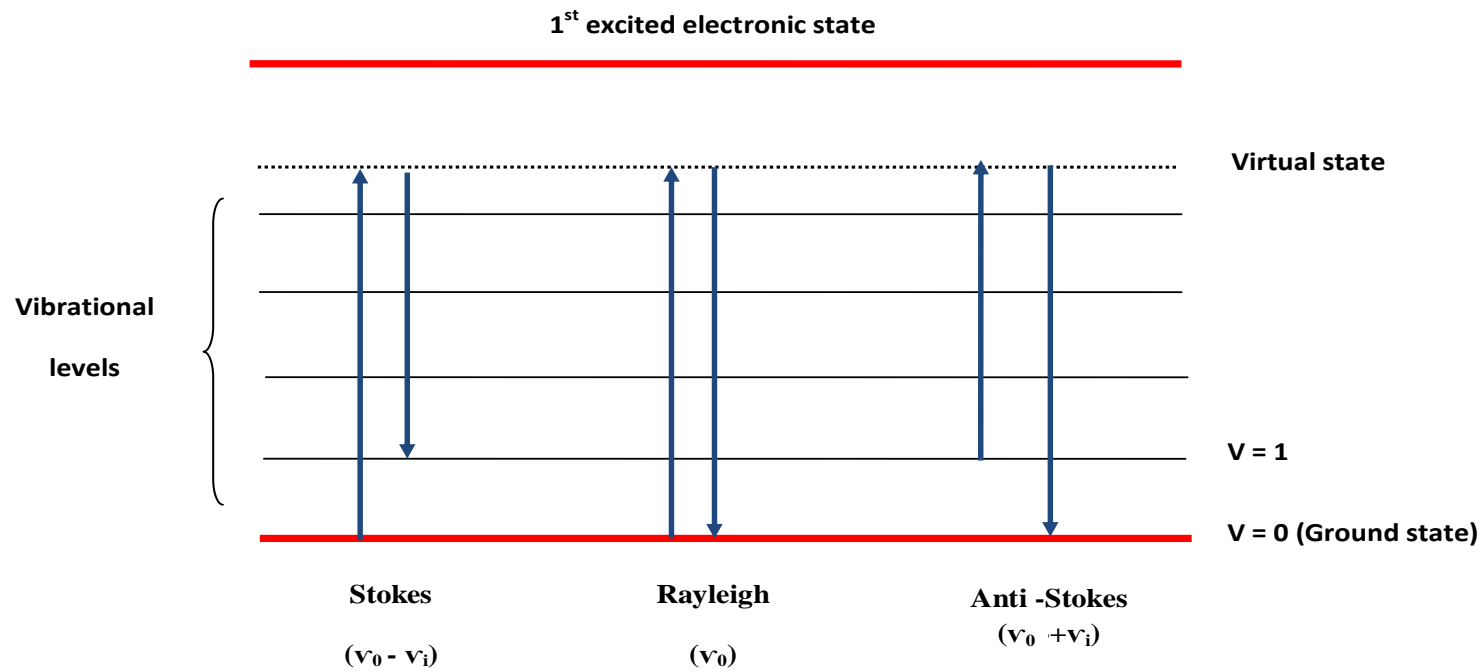


Figure 1 – Illustration of Rayleigh, Stokes and anti – Stokes scattering using an energy level diagram

When photons of energy,  $h\nu_0$  interact with a molecule, the energy of the vibrational system is raised and in turn the molecule becomes polarized, that is the shape of the polarisability ellipsoid changes owing to the vibrational action of the stretching or compression of a bond which alters the bond length. This polarised state however, is not a true energy level and hence is known as a virtual state which represents the distortion of the molecule by the incident radiation and is present at a level equivalent to the energy of the exciting laser beam. Excitation to and relaxation from this virtual state can occur in three ways as is shown in Figure 1. The most probable case is that of Rayleigh scattering where excitation occurs from the ground state and the scattered photon relaxes from the virtual state back to this ground state with no overall difference in vibrational quantum number,  $\Delta V = 0$ .

Stokes scattering however, results in a change in the vibrational quantum number, where  $\Delta V = +1$ . This is the case as excitation occurs from the lowest vibrational energy (ground state) to a short lived virtual state of equal energy to the exciting wavelength. The scattered photon, however, does not return to the ground state on relaxation, rather it relaxes to the first vibrational energy level and light is emitted. The resulting scattered photon will have a lower energy and hence longer wavelength than the incident photon. Conversely, anti-Stokes scattering results in a change in the vibrational quantum number of  $\Delta V = -1$ . In this case, excitation is from a higher vibrational level above the ground state, followed by relaxation to a lower level. The resulting anti-Stokes scattered photon has a greater energy and hence shorter wavelength than the incident photon.

### **2.1.1 Boltzmann distribution**

According to the Boltzmann distribution (9), it is more common for molecules at room temperature to be in their ground state and hence Stokes Raman is what is usually observed and is always more intense than the anti-Stokes Raman counterpart. Nevertheless, a small proportion of molecules are in vibrationally excited states hence anti-Stokes Raman can still be observed at room temperature and is strong enough to be used for vibrational frequencies less than approximately  $1500\text{ cm}^{-1}$ .

$$\frac{N_m}{N_n} = \frac{g_m}{g_n} \exp \left[ \frac{-(E_n - E_m)}{kT} \right] \quad (9)$$

Where,

$N_m$  is the number of molecules in energy level  $m$

$N_n$  is the number of molecules in energy level  $n$

$g$  is the degeneracy of the energy levels

$E_n - E_m$  is the difference in energy between energy states  $E_n$  and  $E_m$

$k$  is Boltzmann's constant ( $1.3807 \times 10^{-23} \text{ JK}^{-1}$ )

$T$  is the temperature (K)

### 2.1.2 The states of a system

All molecules consist of a series of electronic states, each of which are comprised of a number of vibrational and rotational states. Figure 2 illustrates a typical ground electronic state of a molecule.

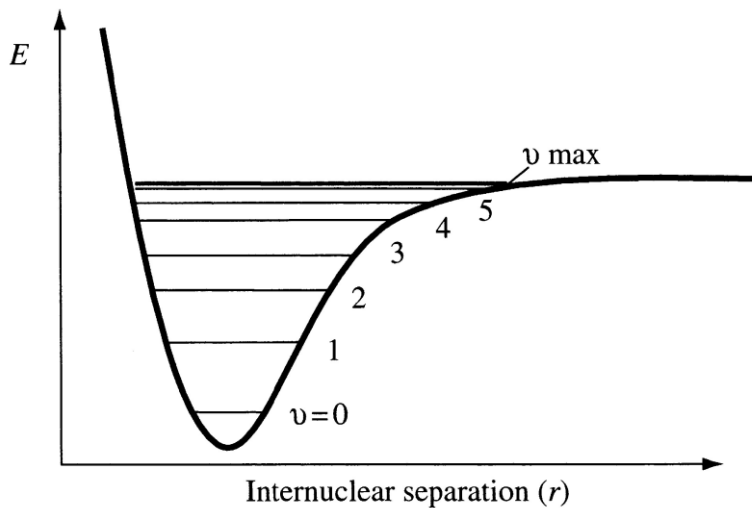


Figure 2 – A typical Morse curve for an electronic state showing the vibrational levels<sup>64</sup>

The curved line in Figure 2 represents the electronic state of the molecule, the x-axis represents the internuclear separation and the y-axis, the energy of the system. When atoms are separated by large internuclear distances, they are not bonded together and are essentially free, however, as the separation distance decreases, the atoms are attracted to each other and form a bond. In the case that the internuclear separation is too small and the atoms are too close to each other, the nuclear forces cause repulsion of the atoms and the energy of the molecule rises significantly, as is shown in Figure 2. The lowest energy possible is at the molecular bond length. In the electronic state not every energy is possible, as there will be vibronic motion, and the quantized vibrational energies must be taken into account.

The illustration in Figure 2 depicts one vibration; the first level ( $V = 0$ ) is the ground state where there is no vibronic motion, however, the second level ( $V = 1$ ) is the level where one quantum of the correct energy is absorbed and the molecule vibrates. Furthermore, the vibrational levels above this require energies approximately two, three, four, five times etc of the quanta required to move the molecule from the ground state to the first excited state. If a change of  $\Delta v > 1$  occurs, the resulting peak is known as an overtone and in the majority of Raman spectra most overtones are weak or nonexistent.

In Figure 1, the energy changes which occur when the exciting radiation interacts with the molecule to generate a virtual state and the scattering that is produced when the molecule relaxes, is illustrated. The scattered radiation is what we refer to as Raman scattering and the difference in energy between the excitation and scattering processes corresponds to the energy of vibrations of the molecule and for fundamental vibrations, the two levels for Stokes Raman must be  $v = 0$  and  $v = 1$ . Although the shape of the Morse curve makes calculating the energy of the vibronic levels difficult, a simplified approach is to replace the curve with a parabola calculated for a diatomic molecule by considering it as two masses connected by a vibrating spring. This approach is known as Hooke's law (10) and gives the relationship between the frequency, the mass of the atoms involved in the vibration and the bond strength for a diatomic molecule.

$$\nu = \frac{1}{2\pi c} \sqrt{\frac{K}{\mu}} \quad (10)$$

$$\mu = \frac{M_A M_B}{M_A + M_B} \quad (11)$$

Where,  $c$  is the speed of light,  $K$  is the force constant of the bond between A and B,  $\mu$  is the reduced mass of atoms A and B of masses  $M_A$  and  $M_B$ .

Hooke's law allows for approximate orders of the energies of specific vibrations to be understood – the lighter the atom, the higher the frequency will be. For example, C-H vibrations will occur at significantly higher frequencies than C-Br. Furthermore, the force constant indicates the strength of the bond between the two atoms, the stronger the bond the higher the frequency.

### 2.1.3 *The basic selection rule*

As has been shown, the oscillation of an induced dipole moment,  $P$ , causes the emission of scattered light, however Stokes and Anti-Stokes frequencies are only possible if molecular vibrations result in a change in the polarisability of the molecule, i.e.  $\left(\frac{\partial\alpha}{\partial q}\right) \neq 0$ . Furthermore, the magnitude of  $\left(\frac{\partial\alpha}{\partial q}\right)$  describes a fundamental characteristic of the molecule known as the Raman cross section,  $\sigma$  which varies with vibrational types.

In addition to the polarisability of a molecule, it is important to consider the mutual exclusion rule when using Raman spectroscopy which states that any vibration in a molecule with a centre of symmetry can be either Raman or infrared active but not both. For molecules with no centre of symmetry, this rule does not apply; in general,



symmetrical vibrations are more intense in Raman scattering and asymmetric vibrations more intense in infrared absorption spectrometry.

For centrosymmetric molecules there are two types of vibration – even vibrations (gerade) which have g character and odd vibrations (ungerade) which are u in character. Consequently only vibrations which are g in character can be Raman active and u character vibrations are infrared active. This is owing to the fact that the two vibrational types can be multiplied out and the final product must contain only the symmetric representation (g vibration).

**Table 2 – Rules for the multiplication of g and u character vibrations**

| <b>Vibration character</b> |          | <b>Vibration character</b> | <b>Product</b> |
|----------------------------|----------|----------------------------|----------------|
| G                          | multiply | g                          | g              |
| U                          | multiply | u                          | g              |
| G                          | multiply | u                          | u              |

As the Raman vibrations are g in character and the ground state is g, if the vibration is to be allowed, the excited state must also be g. Conversely if the infrared vibration is u in character then the excited state must also be u for an allowed vibration. Therefore, when considering a centrosymmetric molecule, vibrations which are Raman active will not be infrared active and vice versa. Further illustration of IR and Raman active vibrations are shown in section 2.2.

## **2.2 Raman and Infrared spectroscopy**

Both Raman and mid-infrared spectroscopy (MIRS) are concerned with the fundamental vibrations of a molecule, however, MIRS is an absorption technique whereas Raman spectroscopy is concerned with the scattering of light. Consequently these techniques, despite both being concerned with fundamental vibrations, are complementary to each other and different selection rules exist for the excitation of molecular vibrations by scattering and absorption.

The intensity of Raman scattering is proportional to the square of the polarisability derivative and hence if a vibration results in only a small change in the polarisability, then the corresponding derivative will be close to zero and the intensity of the Raman band will be low. The strength of a resulting Raman band is also proportional to the concentration of the species and the intensity of the excitation laser. In contrast to Raman spectroscopy, MIRS is most favourable with polar molecules. Whereas a change in polarisability is required for a Raman active response, a net change in the dipole moment of the molecule is required for IR activity. Consequently, for a molecule which has a centre of symmetry, Raman active vibrations will be dormant in the infrared and vice versa. For these reasons IR and Raman spectroscopy provide complementary information. For example, carbon dioxide has four modes of vibration as can be seen from Figure 3.

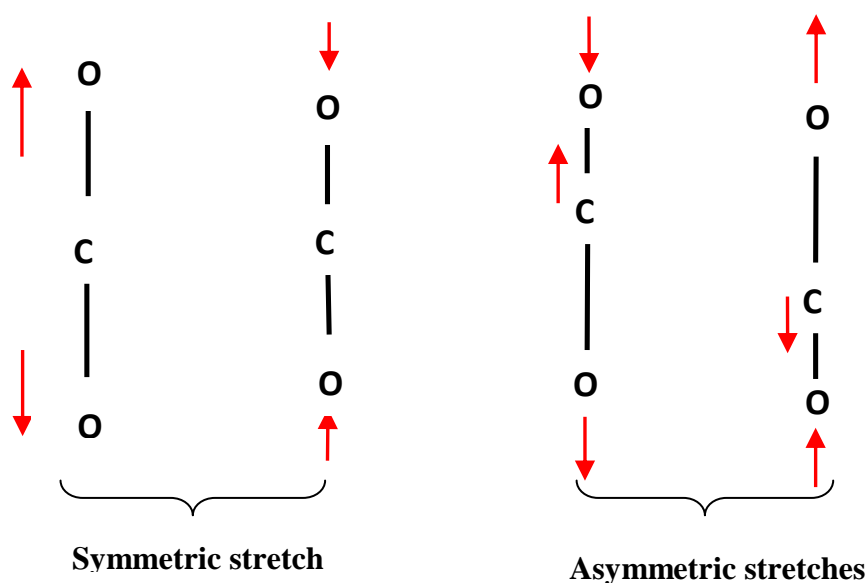


**Figure 3 – Symmetric and asymmetric stretches of carbon dioxide**

Changes in the dipole moment occur during the asymmetric bending and stretching vibrations, however there is very little change in the shape of the polarisability ellipsoid as there is no overall change in the molecule bond length during asymmetric vibrations compared to the bond length at equilibrium. Consequently, the polarisability derivative will be close to zero and hence the asymmetric stretches do

not meet the criteria for Raman activity, rather they are IR active. Conversely, the symmetric stretch of carbon dioxide is Raman active as the electron cloud of the molecule is significantly distorted during vibrational motion, resulting in a change in the polarisability derivative and hence the shape of the polarisability ellipsoid.

## 2.3 Raman signal

### 2.3.1 Intensity

According to scattering theory, the intensity of the scattered wave is proportional to the intensity and the fourth power of the frequency of the incident radiation<sup>65</sup>. As Rayleigh, Stokes and Anti-Stokes frequencies are linearly related to the amplitude of the electric field, the intensity of Raman scattering,  $I_R$ , also depends on the intensity of the excitation beam,  $I_{ex}$  and the frequency of the laser (Raman photons),  $\nu$ , (12)

$$I_R = kI_{ex}\alpha^2\nu^4 \quad (12)$$

Despite Raman being an effective analytical technique, even pure compounds with high Raman cross section values require in excess of  $10^7$  incident photons to produce just one Raman scattered photon, owing to the low probability of Raman scattering. Furthermore, background signals and strong Rayleigh light can hinder the detection of Raman bands and hence the Raman signal must be optimised to overcome this problem. Four main parameters influence the intensity of the Raman signal: the intensity of the laser, the frequency of the excitation beam, the Raman cross section of the molecule and the collection efficiency. Increasing the laser intensity, improving the collection efficiency and using shorter wavelength excitation sources easily increases the Raman signal, according to (12) (see Table 3). This, however, is not a straightforward solution and care has to be taken to optimise each parameter as high power radiation can cause sample damage and highly powered lasers can exhibit poor spectral quality and stability. As the Raman signal intensity is proportional to the fourth power of radiation frequency, using shorter excitation wavelengths to enhance the Raman signal is an obvious approach, however, a consequence of this is fluorescence, as shorter excitation wavelengths found in the

ultraviolet and visible regions are greater in energy than longer wavelengths and hence can result in electronic excitation of the molecule. Fluorescence emerges as an intense broad background signal on the Raman spectrum and can entirely obscure the Raman signal; even fluorescent impurities in an otherwise non fluorescing material can severely degrade the quality of the resultant spectra.

**Table 3 - Decrease in Raman intensity as a function of laser wavelength**

| <b>Laser wavelength (nm)</b> | <b>Intensity <math>(1/\lambda)^4</math><br/>(% relative to wavelength)</b> |
|------------------------------|--|
| 480                          | 100  |
| 532                          | 62.27  |
| 633                          | 33.06  |
| 785                          | 13.98  |
| 840                          | 10.66  |
| 1064                         | 4.14   |

Furthermore, CCD detectors are noisy and have a limited response at longer NIR wavelengths and hence it is important to select lasers and detectors together to maximise their compatibility. Finally, the Raman signal can be increased by improving the signal throughput and the efficiency of its collection. The collection of the scattered photons in Raman spectroscopy is difficult owing to the random nature and multi-directional path that the photons take. Nevertheless, signal throughput and collection efficiency have been aided by developments in FT-Raman and high-throughput multichannel dispersive spectrometers. Additionally, the development of fibre optic probes and more efficient detectors have also enhanced the sensitivity of Raman analyses. These developments will be discussed further in forthcoming sections.

### **2.3.2 Noise**

As with all instrumental analysis methods, the acquired signals are affected by noise which in turn limits the reproducibility of the measurements and the detection limit of the method. A signal to noise ratio (SNR) is generally used to compare and

describe the magnitude of the signal to that of the noise level and is simply calculated by dividing the intensity of the analyte signal by the standard deviation of that signal. For a signal to be considered analytically detectable, the signal level must be three times greater than the standard deviation of the noise. There are three main types of noise in Raman spectroscopy: shot noise, dark noise and readout noise.

Shot noise is a result of the statistical nature of light – the greater the number of photons in a beam, the higher the uncertainty of accurately detecting them. Shot noise is the counting of random events and is given as the square root of the total signal,  $\sqrt{I_R}$ . Shot noise can originate from the sample, background sources or even from fluorescence of trace constituents of a sample.

Dark noise is the signal acquired from the spontaneous generation of electrons in the detector and is referred to as the dark signal. Dark current is predominantly due to thermally produced charge and therefore most detectors are cooled to reduce this effect. For example, in most array detectors the dark current is reduced by a factor of two for every seven to eight degrees Celsius the detector is cooled. If the temperature is dropped too far however, it can result in detrimental effects on other detector parameters.

Readout noise is intrinsically present in the electronics that amplify and process the signal from the detector and is independent of the integration time and signal intensity. For easily reproducible experiments, multiple acquisitions can be averaged to reduce the readout noise by the square root of the number of averaged signals.

## **2.4 Raman instrumentation**

### **2.4.1 *Experimental configurations***

Since Raman spectroscopy is a process concerned with two photons (incident and scattered), there are two main optical geometries used for signal acquisition – reflectance (also known as backscatter) and transmission Raman which differ according to the relative position of the excitation and collection optics.

The reflectance mode configuration illuminates the sample and collects the resultant scattered photons from the same side of the sample. This mode is a popular sampling method in Raman spectroscopy owing to its instrumental simplicity and ease of use. Nevertheless, an inadequacy of this approach is its inability to probe sub-surface layers of turbid media, for example only a small penetration depth of several hundred micrometers is achieved when using traditional confocal reflectance Raman spectroscopy in living tissue<sup>66</sup>.

Transmission Raman spectroscopy utilises a different optical configuration to that of reflectance Raman. In this case, the laser beam illuminates one side of the sample and the resultant signal is collected from the opposite side. This approach is useful for the effective suppression of surface generated Raman signals and is also a method adopted to bypass the problem of sub-sampling<sup>67</sup>. Sub-sampling is when only a small portion of a sample is analysed and hence representative measurements can only be achieved if the ingredients in the sample are homogeneously distributed. A detailed discussion of the applications and advantages of both Raman modes will be given in later chapters.

#### **2.4.2 Scattering**

The interaction of radiation with matter results in absorption, transmission and reflection of that radiation and the law of conservation requires that the incident radiation is entirely accounted for. Consequently, the total intensity of the incident radiation is equal to the sum of the intensities of the absorbed, transmitted and reflected radiation. A matt surface, for example a powder, can be thought of as a series of interfaces orientated randomly at many different angles. The multiple interfaces of such a surface cause reflectance to be diffused over all angles<sup>68</sup>. Some radiation may pass through the initial interface and result in absorption, however the diffusely reflected light is a consequence of random reflections, refractions and scattering inside the sample. Diffuse reflectance arises when a portion of the incident radiation penetrates the sample, part of which will be returned to the surface,

some will be absorbed and there will also be multiple scattering events at the boundaries of the individual particles of the sample.

Scattering is incomplete destructive interference when the incident radiation encounters particles within a sample that are much larger than the radiation wavelength. The term scattering was introduced in 1869 when Tyndall discovered that after collision with a particle, multiple propagation paths of radiation were seen<sup>69</sup>. The physical properties of the sample – particle size, shape and surface characteristics – will all affect the extent of scattering<sup>70</sup>.

There is no one theory that is entirely valid for reflections from matt surfaces and the exact path of the propagation of radiation through particulate matter is difficult to describe mathematically. The most widely used theory however was proposed in 1931 by Kubelka and Munk<sup>71, 72</sup>. The Kubelka–Munk theory is based on the general radiation transfer equation which describes the change in intensity of a beam of radiation,  $\partial I$ , in a sample of density  $\rho$  and pathlength  $\partial s$ . The attenuation coefficient,  $\kappa$ , describes the loss in radiation as a result of scattering or absorption and  $I$  is the radiation intensity.

$$-\partial I = \kappa \rho I \partial s \quad (13)$$

Kubelka and Munk proposed two fundamental equations to describe the passage of radiation through a model solid sample; this is illustrated by Figure 4. The model assumes the following: the particles of the sample are much larger than the wavelength of the incident radiation, much smaller than the sample thickness and are evenly distributed<sup>72</sup>.

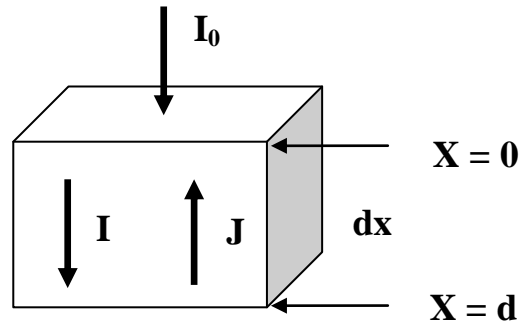


**Figure 4 – Schematic of the passage of radiation through a model sample from which Kubelka-Munk theory was developed**

Based on the model system shown in Figure 4, Kubelka and Munk developed two equations (14) and (15) to describe the change in intensity of radiation travelling in the forward direction (I) and the scattered light travelling in the reverse direction (J).

$$\partial I = -(\kappa + s)I\partial x + sJ\partial x \quad (14)$$

$$\partial J = +(\kappa + s)J\partial x + sI\partial x \quad (15)$$

Where,  $\kappa$  and  $s$  are the absorption and scattering coefficients, respectively.

The radiation which passes through the sample will be attenuated due to absorption (proportional to the absorption coefficient,  $\kappa$ ) and scattering (proportional to the scattering coefficient,  $s$ ). As  $\partial x$  increases, the intensity of radiation travelling in the forward direction will decrease and the scattered light will increase. The Kubelka-Munk function,  $F(R)$  shown by (16) is the result of the solution to (14) and (15).



$$F(R_{\infty}) = \frac{(1 - R_{\infty})^2}{2R_{\infty}} = \frac{\kappa}{s} = \frac{\epsilon c \ln 10}{s} = \frac{c}{a} \quad (16)$$

Where,  $R$  is the absolute reflectance,  $\kappa$  and  $s$  are the absorption and scattering coefficients, respectively,  $\epsilon$  is the molar absorptivity,  $c$  is the sample concentration and  $a = s/2.303\epsilon$ . The measurable reflectance of an infinitely thick sample,  $R_{\infty}$ , is a function of only the ratio of the scattering and absorption coefficients and not their absolute values. This advantage is why the Kubelka-Munk function is the most widely accepted and used solution<sup>71</sup>.

The Kubelka-Munk approach gives optimal results when applied to dilute dispersions of absorbing materials in a non-absorbing matrix. Even for low concentrations of absorbing species, it has been shown that the K-M function can deviate from linearity in the mid infrared and ultraviolet-visible regions<sup>71</sup>. As near infrared spectra have lower band absorptivities than mid infrared spectra, the linear region of absorbing materials in the near infrared region is greater. Furthermore, the absorbing properties of the sample matrix can affect the success of the K-M function as even weakly absorbing matrix components can cause the theory to fail. Consequently, the K-M function is a limiting equation and should only be used with weakly absorbing bands.

### 2.4.3 *Fibre optic probes*

It is now common practice in the majority of Raman instruments to use fibre optics for the excitation and collection steps of the Raman measurement. The use of such optics provides a means for the sample to be spatially remote from the spectrometer, a feature which has simplified the use of Raman spectroscopy in process environments, but furthermore, increases instrument flexibility and throughput. An optical fibre is a cylindrical dielectric waveguide that transmits light along its axis by the process of total internal reflection. The fibre consist of a glass cylinder core of refractive index  $n_1$ , surrounded by cladding of refractive index  $n_2$ , where  $n_1 > n_2$  in order to confine the optical signal in the core. The law of refraction (17), states that light will enter the fibre at an angle of incidence,  $\alpha$ , be refracted, and continue

travelling along the length of the fibre core at an angle  $\beta$ , through total internal reflection provided  $\cos \beta \geq n_2/n_1$ .

$$\sin \beta = \frac{\alpha}{n_1} \quad (17)$$

There are two different types of probes in common use in Raman spectroscopy: the unfiltered fibre bundle or "n-around-1" probe and the filtered probe. The fibre bundle is less expensive, while the filtered probe offers better signal-to-background in certain applications. Figure 5 illustrates the design of a fibre bundle probe.

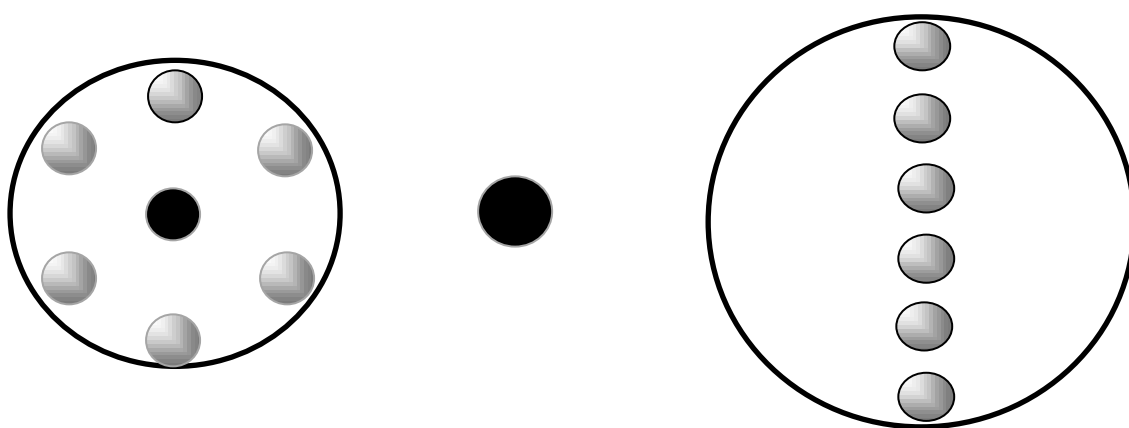


**Figure 5 – Schematic of a 6-around-1 probe showing from left to right, the probe tip end, excitation fibre and collection fibres aligned along the spectrometer entrance slit height<sup>73</sup>**

**Figure 5** illustrates a “6-around-1 probe” consisting of seven optical fibres cemented into a cylindrical holder. The central excitation fibre delivers laser light to the sample, whilst the surrounding fibres collect Raman scatter. The laser beam is focused into the delivery fibre with a microscope objective or other short focal length lens. For coupling to the spectrograph entrance slit, the output ends of the collection fibres are arranged in a line, as shown in

Figure 5 and the linear bundle is placed directly against the entrance slit of the spectrograph. Probes containing multiple numbers of fibres are used as a single fibre collects only 10-15% of the light as a multi-fibre bundle. The fibre bundle can be directly inserted into liquid samples or held a short distance from solid samples to acquire spectra.

The optical fibres themselves contribute significantly to the background signal, as when laser light travels down a length of fibre an intense silica Raman spectrum is generated. Furthermore, fluorescence from the fibre cladding and cement holder can also be generated and these interferences are delivered from the fibre along with the laser light and are reflected from the surface of the sample and are collected along with the analyte Raman spectrum. Generally, background signals can be subtracted from the spectrum, however weak Raman signals of interest may still be obscured.

One approach used to overcome this problem has been the development of filtered probes where the light is doubly filtered, once before the sample is excited and once again before the light is passed into the collection fibre<sup>10, 61</sup>. Modern commercial Raman probes generally utilise the double filtration method, however the filtering method used varies from type to type: dielectric filters<sup>74</sup>, dielectric beamsplitters<sup>75</sup> and more recently a combined holographic transmission grating and spatial filter<sup>76</sup> have been used. Filtered fibre optic probes offer flexibility with respect to optical attachments, such as microscope objectives for sub-scale analysis and immersion sleeves for process applications, which make them a useful tool for Raman spectroscopy. In 2005, Kaiser Optical Systems patented a filtered probe known as the PhAT probe<sup>77, 78</sup> which offers wide area illumination and multiplexed collection using a fibre bundle, primarily for the analysis of solid samples. The design, benefits and use of the Kaiser PhAT probe will be discussed in detail in forthcoming sections.

#### **2.4.4 Spectrometers and detectors**<sup>10, 64, 79, 80</sup>

In Raman spectroscopy, the ideal spectrometer will have a highly sensitive detector, a spectral coverage allowing shifts of up to 3500 cm<sup>-1</sup> to be detected and a spectral

resolution of  $2\text{ cm}^{-1}$ . Generally there are two types of spectrometer: dispersive and non-dispersive. A dispersive spectrometer separates the light spatially in order of wavelength by a diffraction grating (or prism in older instrumentation) and analyses the individual wavelengths via a single detector or over the entire wavelength range by means of an array detector.

Dispersive techniques have been used in Raman spectroscopy since its introduction as a viable method of chemical analysis in the early twentieth century. The introduction of lasers to Raman spectroscopy in the 1960's vastly improved its sensitivity; however, the short-wavelength lasers that have been used in these systems can excite fluorescence emission from organic and biological samples. Because fluorescence emission is usually several orders of magnitude more efficient than Raman scattering, the fluorescence signal from a relatively small concentration of contaminant species can easily overwhelm the Raman signal, rendering the spectrum useless. The simplest solution to this problem is to use a longer excitation wavelength. As discussed previously, the lower energy associated with longer-wavelength lasers is not enough to excite fluorescence, so only a Raman signal (and Rayleigh scattering) is obtained. For example, a near infrared Nd:YAG laser operating at 1064 nm can be used for Raman spectroscopy, successfully avoiding the problem of fluorescence, however the NIR radiation is not compatible with the normal detectors used in dispersive systems and consequently the signal is collected by an InGaAs detector. The radiation in this case is not dispersed; rather it is modulated using an interferometer which results in different modulation frequencies for each wavelength. This is processed and converted into a spectrum.

FT-Raman exhibits several advantages over dispersive Raman spectroscopy: using long wavelength excitation lasers avoids sample fluorescence and additionally, the entire Raman spectrum can be collected simultaneously rather than over separate regions sequentially ( Fellgett's multiplex advantage). Furthermore, non-dispersive systems provide better throughput than that of dispersive systems as they do not rely on the use of narrow slits to achieve high resolution (Jacquinot advantage). Also, the

use of a HeNe laser of a precisely known wavelength to reference the interferometer means that the consequent FT-Raman spectra are very accurate and precise (Connes advantage). Table 4 summarises the advantages and disadvantages of FT and dispersive instruments.

**Table 4 – Comparison of dispersive and FT spectrometers**

|               | Dispersive spectrometers  | FT Spectrometers  |
|---------------|---|---|
| Advantages    | <ul style="list-style-type: none"> <li>• High SNR</li> <li>• No moving parts (if fixed grating or prism)</li> <li>• Can be used with NIR, UV and Visible excitation</li> <li>• Multiplex advantage</li> </ul> | <ul style="list-style-type: none"> <li>• Good frequency precision</li> <li>• Good NIR and MIR excitation</li> <li>• Compact design</li> </ul>   |
| Disadvantages | <ul style="list-style-type: none"> <li>• Throughput and resolution trade off depending on slit size</li> </ul>  | <ul style="list-style-type: none"> <li>• Not cost effective for UV or visible regions</li> <li>• Analysis time is limited by the instrument scanning speed</li> <li>• Shot noise is distributed across all wavelengths</li> </ul> |

Whilst both dispersive and non-dispersive Raman instruments have advantages and disadvantages it is dispersive Raman spectroscopy that is the preferred Raman technique for the majority of applications especially in process environments where extreme conditions generally prevent the use of less robust FT-Raman instruments.

The improvement of detector technology has also been a significant advancement for Raman spectroscopy as owing to the low probability of Raman scattering, high quality detectors are required to see the realise the real potential of the technique.

**Table 5 – Comparison of detectors for Raman spectroscopy**

| <b>Photomultiplier tube</b>   | <b>Photodiode</b>   | <b>Charged Coupled Device</b>  |
|---|---|--|
| <ul style="list-style-type: none"> <li>• Vacuum tube using photoelectric effect to produce current</li> <li>• High sensitivity for wavelengths less than 1.1 <math>\mu\text{m}</math></li> <li>• High voltage supply needed</li> <li>• Cooling needed to achieve optimum SNR</li> </ul> | <ul style="list-style-type: none"> <li>• Solid state device of Si, Ge or InGaAs</li> <li>• Photons hitting the material create electron – hole pairs which recombine to produce current</li> <li>• Low voltage</li> <li>• InGaAs devices sensitive to wavelengths up to 4 <math>\mu\text{m}</math></li> <li>• Can be used as single detectors or arranged in linear arrays</li> <li>• Cooling improves sensitivity</li> </ul> | <ul style="list-style-type: none"> <li>• Usually Si solid state device</li> <li>• Electrons generated by photons striking material</li> <li>• Electrons held in potential well before being released and measured to determine the total energy of incident light on CCD for that time period</li> <li>• Wavelength range of up to 1.1 <math>\mu\text{m}</math></li> <li>• Manufactured in 2D arrays so collection of multiple spectra simultaneously is possible</li> <li>• Cooling to reduce dark current noise</li> </ul> |

## **2.5 Raman instruments used in this study** <sup>73</sup>

Kaiser Optical Systems, Inc. is a world leader in spectrographic instrumentation and applied holographic technology. The company’s principal products include Raman sensors and instrumentation, advanced holographic components for spectroscopy, telecommunications, astronomy and ultra-fast sciences, and display systems for aircraft. As a leader in Raman spectroscopy, Kaiser Optical Systems, Inc., develops

and manufactures a variety of components for Raman spectroscopy, Raman systems for research and development and Raman process analysers. Furthermore, Kaiser pioneered the holographic technology that has had a profound positive impact on Raman spectroscopy – holographic notch filters allow the collection of Raman scatter close to the Rayleigh line (with smoother filter edges than conventional dielectric notch filters) and holographic transmission gratings allow rapid, simultaneous collection of the Raman spectrum in one acquisition.

### **2.5.1 *Non-invasive Raman PhAT system***

Whilst traditional Raman systems are confocal in nature, providing a tightly focused beam and hence a small spot size of approximately 80  $\mu\text{m}$ , the Kaiser Raman PhAT probe is a wide area illumination Raman probe providing large diffuse sampling spots of 1, 3 and 6 mm in diameter. As PhAT technology utilises an essentially collimated beam, the PhAT probe not only allows for larger sampling areas, it also results in greater sampling volumes and in turn provides a means of achieving a representative analysis of samples.

The PhAT system addresses the sensitivity needs of Raman spectroscopy by efficiently processing and detecting Raman photons. As the PhAT system is based on the HoloSpec *f/1.8i* spectrograph, it utilises holographic optical elements based on Volume Phase Technology in an axial transmissive spectrograph configuration and hence the PhAT system provides complete spectral coverage, good spectral resolution and high throughput. Furthermore, a cooled CCD detector is used to simultaneously measure all of the Raman wavelengths, an advantage over other Raman instruments which can measure only a limited spectral region at an one time, meaning that all Raman photons out with this region are lost. The combined use of a CCD detector and a holographic transmission grating in the PhAT system allows instantaneous collection of the composite Raman spectrum.

### 2.5.1.1 Holographic Notch Filters

Holographic notch filters have benefited Raman spectroscopy significantly by providing high attenuation of the Rayleigh line whilst still allowing bands as close as  $50\text{ cm}^{-1}$  to the laser wavelength to pass. Initially the filters used in Raman spectroscopy were edge filters however these only provided good transmission on one side of the Rayleigh line. Such filters have been replaced by notch filters which exhibit good transmission either side of the Rayleigh line. Additional advantages of holographic notch filters include sharp spectral edges, good transmission outside the rejection band, a high damage threshold and good stability. The position of the rejection band in a notch filter can be adjusted by tilt-tuning the notch filter, that is changing the angle of the filter relative to the laser. Figure 6 illustrates the narrow rejected band width of a holographic notch filter compared to that of a dielectric notch filter.

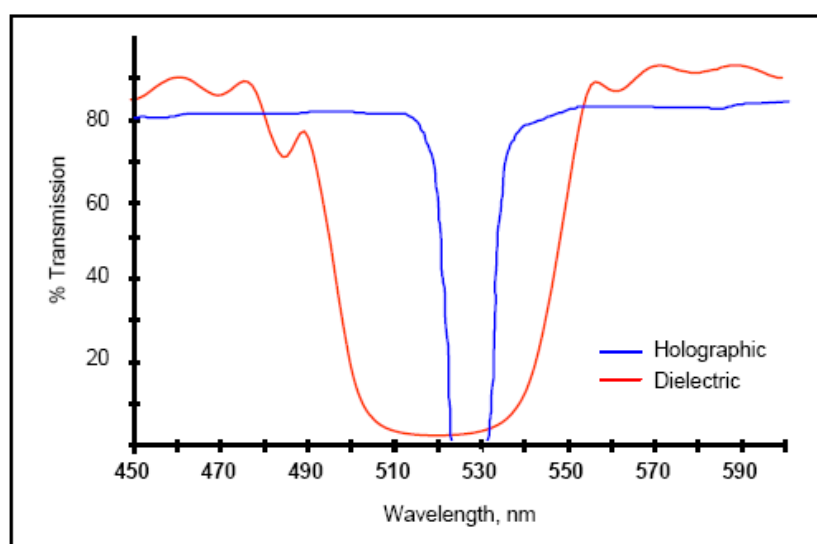


Figure 6 – Comparison of the rejection band of a holographic and dielectric notch filter<sup>81</sup>

The manufacture of dielectric and holographic edge filters differ; the former is produced by illuminating a dichromated gelatin film with two laser beams to create interference patterns and the latter by depositing two components in alternating layers. The different manufacturing methods together with the film thickness result in the two filter types exhibiting different refractive indices. As the film thickness



varies so does the refractive index of the filter, however, the variation is sinusoidal in the holographic filter and square wave in the dielectric and consequently holographic filters have significantly greater laser damage thresholds.

### 2.5.1.2 *HoloPlex™ Holographic Transmission Grating*

The patented HoloPlex™ transmission grating facilitates the instantaneous collection of the entire Raman spectrum provides robust, reliable operation and stable wavelength calibration, together with wide spectral coverage at high spectral resolution without the need for moving parts. This unique performance is achieved by the simultaneous dispersion of two separate spectral tracks onto the detector.

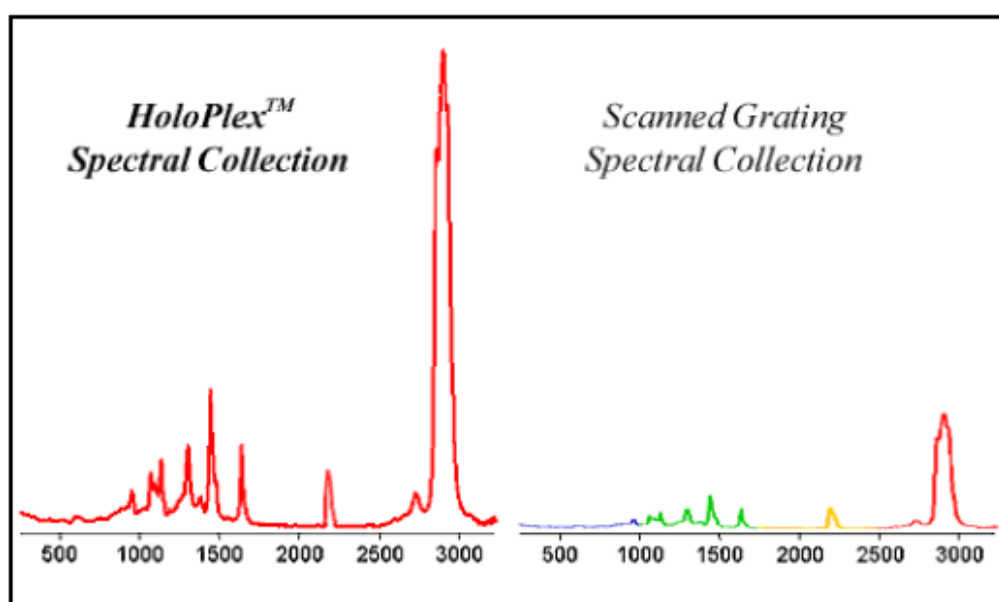


Figure 7 – Comparison of spectral data acquired with a HoloPlex™ transmission grating and a scanned grating<sup>81</sup>

Figure 7 illustrates the advantages of the HoloPlex™ technology with respect to the signal collected – by looking at all wavelengths simultaneously, the signal collected by the HoloPlex™ grating is significantly greater than that collected with the scanned grating. The simultaneous nature of this data collection is known as the HoloPlex™ advantage.

A primary advantage of this approach is that no moving parts are required. This is because the HoloPlex™ holographic transmission grating disperses the scattered light as two separate spectral tracks onto the CCD detector using optics and additionally this method adds to the stability of the system. Sections of the resulting image are then binned to produce the spectrum. Furthermore, HoloPlex™ technology is beneficial when looking at dynamic systems as the effects of sample turbulence and laser power fluctuations are eliminated as all the light from both spectral tracks is collected simultaneously and hence all observed features correspond to the same moment in time. This is not the case for scanning systems which observe different spectral features from different points in time making it difficult, if not invalid, to compare different parts of the spectrum when dealing with a rapidly changing dynamic system. Another advantage of simultaneous data acquisition is speed and this is owing to the ability to capture the entire spectral range in just one measurement time frame. Consequently, higher sampling rates can be used and in turn, higher throughputs are seen; furthermore, the contact time of the laser and the sample is reduced, reducing the possibility of sample damage by the laser.

### 2.5.1.3 Axial transmissive spectrograph

An axial transmissive spectrograph forms the basis of the entire range of Raman instruments produced by Kaiser Optical Systems Inc. It uses a volume holographic transmission grating together with high quality lenses to achieve almost aberration free imaging in a compact package. Figure 8 illustrates the basic design of the axial transmissive spectrograph.

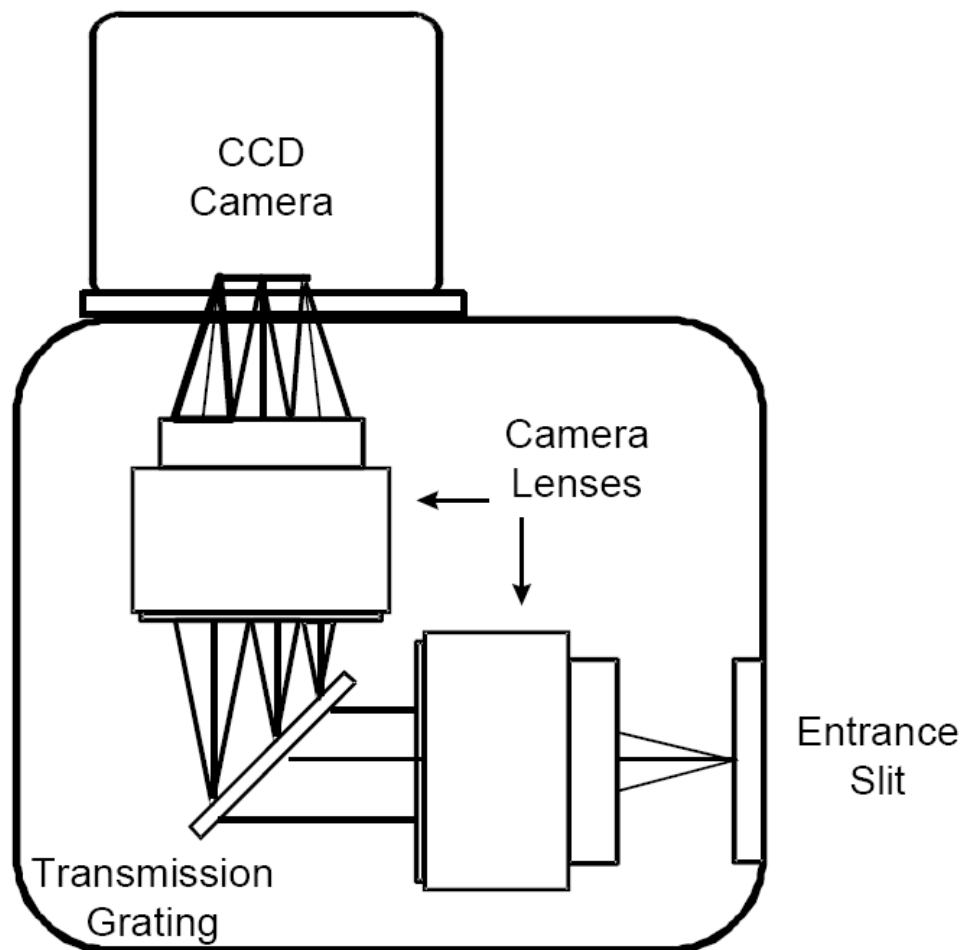
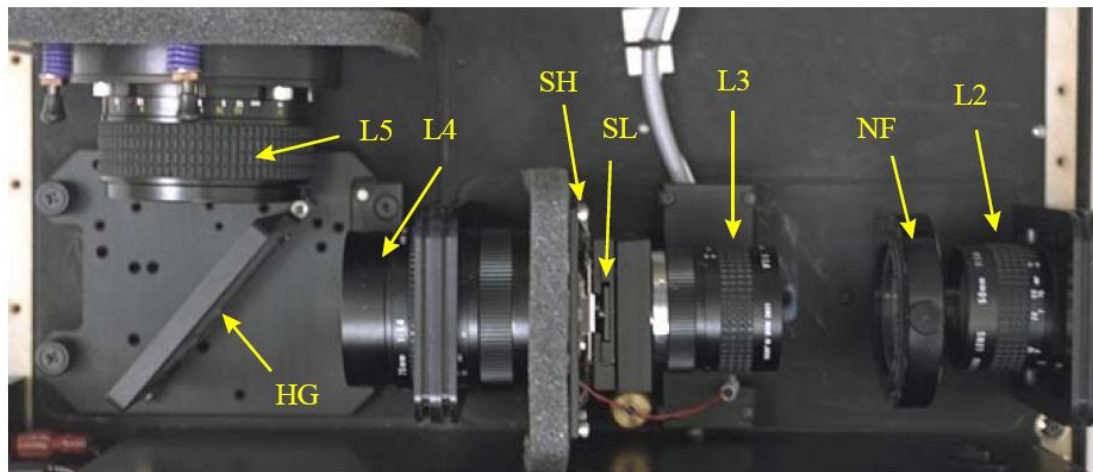


Figure 8 – Schematic of the dispersion stage of the axial transmissive spectrograph showing the location of the slit, lenses, grating and camera<sup>82</sup>

Figure 8 shows that high quality lenses are used as collimating and focusing elements and a holographic transmission grating is placed in the collimated region between the lenses. The diffracted light from the spectrograph is then focused onto the surface of a CCD detector which records the spectrum. As the light path is axially symmetric through the input and output lenses aberrations in the system are minimized.

The axial transmissive design allows the system to operate at a very low  $f$ /number also known as the focal ratio and is the focal length divided by the entrance aperture diameter. The spectrographs used in the PhAT system operate at  $f/1.8$  and hence gathers light very efficiently resulting in a greater intensity being delivered to the detector compared to other designs. Figure 9 shows the complete spectrograph design.



**Figure 9 – Spectrograph stage of PhAT system: (L2) pre-filter collimating lens, (NF) holographic notch filter, (SH) shutter, (L3) pre-filter focusing lens, (SL) spectrograph entrance slit, (L4) spectrograph collimating lens, (HG) holographic transmission grating, (L5) spectrograph focusing lens, (FP) spectrograph focal plane for CCD detector<sup>78</sup>.**

The PhAT system Raman analyser includes a pre-filter stage which contains a notch filter for laser line rejection as is shown in Figure 9. The pre-filter stage consists of a 50 mm  $f/1.4$  camera lens (L2) which collimates the laser light, this then passes through the notch filter (NF) and the laser light is attenuated. The filtered signal is then focused on a 50  $\mu\text{m}$  wide spectrograph entrance slit (SL) by a 50 mm  $f/1.4$

camera lens (L3). Light from the slit is collimated by an  $f/1.8$  camera lens (L4) and is passed to the holographic transmission grating (HG). Diffracted light from the grating is imaged onto the detector by an 85 mm  $f/1.4$  camera lens (L5).

#### 2.5.1.4 CCD camera

The PhAT system uses a CCD detector to measure the intensity of the Raman scattered light. The CCD detector is a rectangular two dimensional array of pixels; along the spectrograph dispersion axis there are 1024 pixels and along the slit height axis there are 256 pixels: each pixel is  $26 \times 26 \mu\text{m}$ . As there is no dead space between pixels, the CCD photoactive area is  $26.6 \times 3.6 \text{ mm}$ .

#### 2.5.1.5 Probe

The PhAT probe head shown in Figure 10 focuses and delivers the 785 nm excitation light to the sample and collects the Raman scattered radiation. The probe is designed to focus the excitation light on a spot of approximately 1, 3 or 6 mm in diameter for large area sampling. The PhAT probe is designed for simplistic “point and shoot” sampling with no adjustment or alignment of its internal optical components.

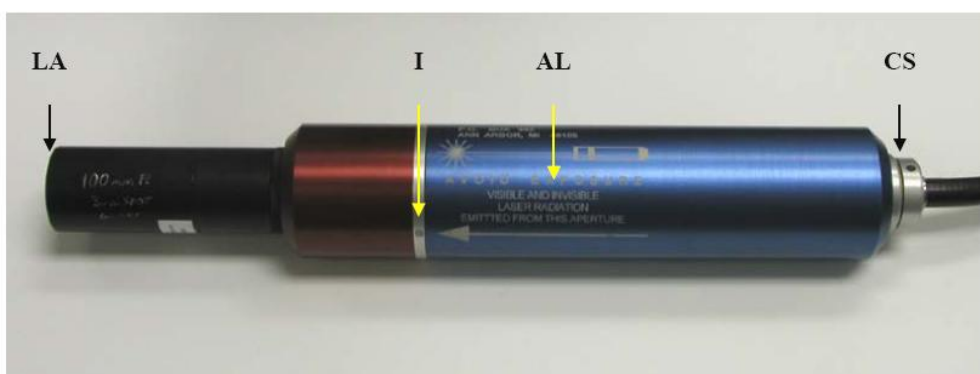


**Figure 10 – The PhAT probe head: fibre optic strain relief connector (CS), probe head aperture label (AL), laser emission indicator (I), interchangeable optic (LA)<sup>82</sup>**

The probe images the laser excitation light from a single excitation fibre onto the sample and a fifty fibre bundle in an ‘n-around-1’ formation (refer to

Figure 5) collects the scattered radiation. Laser light travelling through a silica optical fibre generates silica Raman emission which could obscure the Raman spectrum if it reached the spectrometer; the longer the optical fibre length, the more severe this problem becomes. The PhAT probe however, removes the silica Raman light from the laser light after the light exits the excitation fibre, before it reaches the sample and furthermore removes laser light from the sample emission before it reaches the collection fibre bundle. Consequently, silica Raman does not pose a problem for the PhAT system even when long lengths of optical fibres are used.

### **2.5.2 Raman workstation**

The PhAT probe head can be used in conjunction with the PhAT enabled Raman Workstation (Kaiser Optical Systems, Inc.) which provides unique sampling and measurement versatility. The Raman Workstation is a fully integrated Raman system consisting of the PhAT system base unit (discussed previously in section 2.5.1) that connects the fibre optic PhAT probe and a computer system. Furthermore, it includes a Class 1 enclosure with motorized sampling stage for unattended laboratory use. Automated data collection and processing is also provided for continuous monitoring applications.

Figure 11 and Figure 12 show the side and front view of the Raman Workstation, respectively.

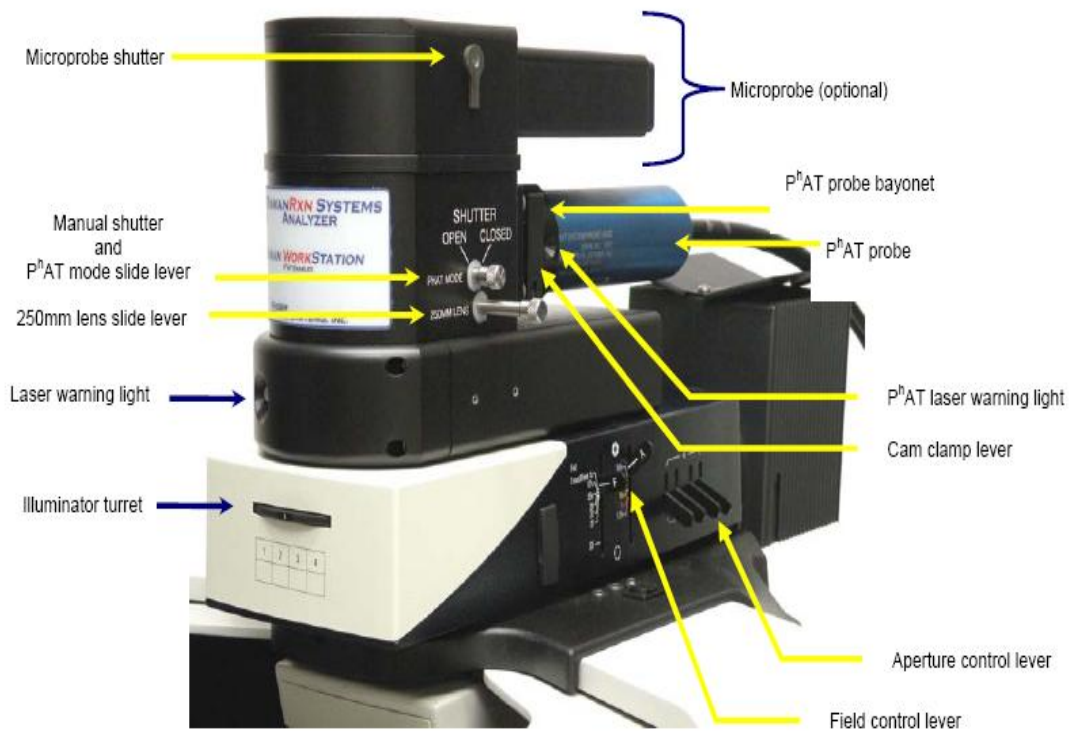


Figure 11 – Side view of Raman Workstation <sup>83</sup>

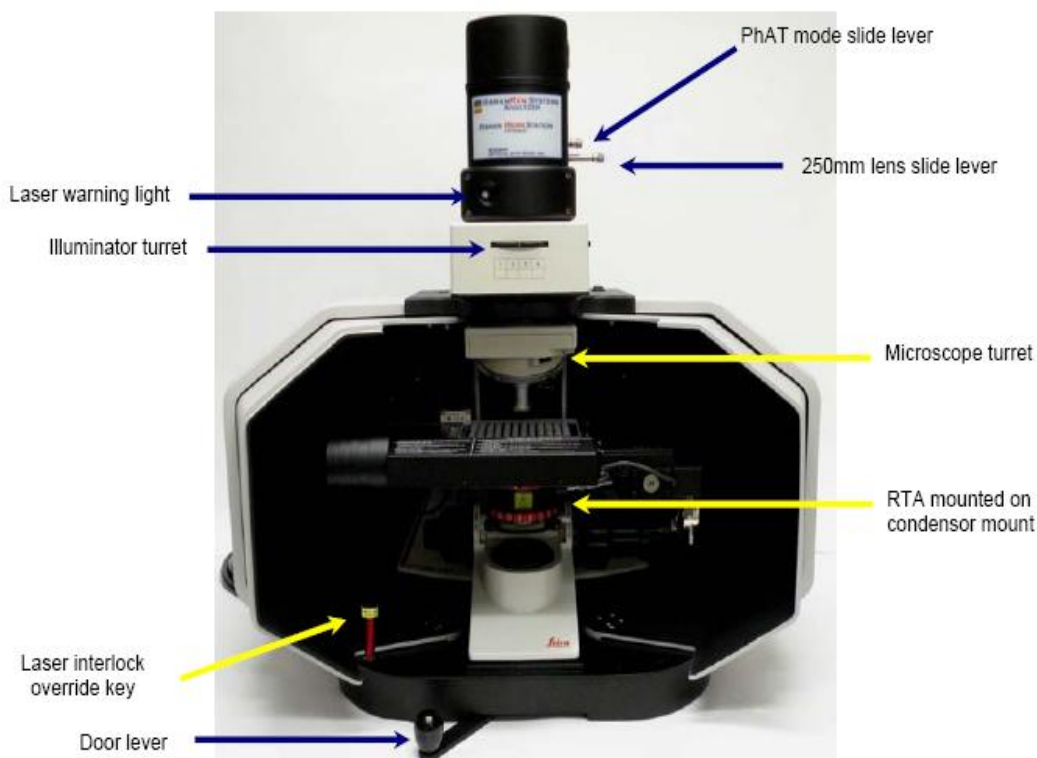
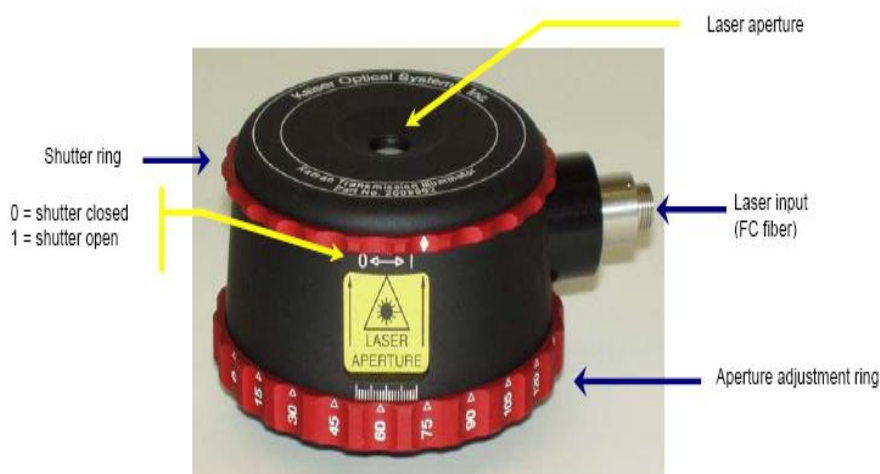


Figure 12 - Front view of the Raman Workstation with open doors

Figure 11 shows the side view of the Raman Workstation which incorporates the PhAT probe head and the lens turrets to choose the required analysis spot sizes. With the PhAT enabled configuration, the Raman Workstation provides three laser spot sizes. The different illumination spots are achieved by selecting the appropriate lens lever: selecting the 250, 150 or 35 mm lens will result in a 6, 3 or 1 mm laser illumination spot, respectively. Figure 12 shows the front view of the Raman workstation which encompasses the motorized sampling stage, the microscope turret and the Raman transmission accessory (RTA). The sampling stage consists of 72 sample wells which can hold both solid and contained liquid samples; the stage can be automated to allow unattended sample analysis.

An additional feature of the PhAT enabled Raman workstation is the ability to achieve both reflectance and transmission Raman analysis. Reflectance Raman analysis with the Raman Workstation is achieved in the same manner as with the independent PhAT analysis system; the PhAT probe head is used to illuminate the sample and collect the scattered radiation. The Raman Transmission Accessory (RTA) enables the projection of laser light onto one side of the sample and the collection of the scattered radiation from the opposite side. In this configuration, the RTA provides the excitation beam (with the same wide area illumination options as the PhAT probe head) and the PhAT probe head serves to collect the resultant scattered light. Figure 13 shows the Raman Transmission Accessory.



**Figure 13 – Raman Transmission Accessory<sup>83</sup>**



The RTA fits into the condenser mount in the workstation (shown in Figure 12) and has two adjustable dials as is shown in Figure 13. The shutter ring simply opens and closes the shutter; the aperture adjustment ring however changes the size of the beam to provide the same range of illumination spot sizes as with traditional PhAT probe head illumination.

### **3. Study of tablet- to- tablet variation with respect to the mass of a low concentration API**

One of the aims of this project was to compare reflectance and transmission Raman spectrometry for tablet analysis. An associated aim was the investigation of tablet-to-tablet variations when determining the concentration of an active pharmaceutical ingredient (API) at levels of a few % w/w.

This part of the study was conducted using the widely applied technique of high performance liquid chromatography (HPLC) to determine the concentration of chlorpheniramine maleate in a large number of tablets. This involved development of the HPLC method and then its application to establish the range of masses of the API in the tablets. In a subsequent part of the investigation (chapter 5) the data collected was used for comparison with results obtained by Raman spectrometry.

#### **3.1 Introduction**

To ensure the quality, clinical performance, efficacy and safety of a pharmaceutical product, specifications are fixed and approved by the regulatory authorities of each country in which the drug is marketed. To guarantee that these specifications are met, the identity, purity and potency of the product and the components that it is comprised of are confirmed by analytical testing methods prior to releasing them for commercial use.

HPLC is the most utilised separation technique for drug substance and drug product testing and its growing importance is a result of the increasingly complex structures of medicinal drug substances and the need for the detection and quantification of chiral products and impurities has become more significant<sup>84-86</sup>. For drug substances, HPLC is mainly focused on assay determination and impurity testing, however, it can also be used for dissolution testing (which is an indicator for the consistency of the bioavailability of the drug) and also to ensure a good content uniformity of the API in a batch of blended powders.

Separation by HPLC is most commonly achieved by the reversed phase method and although various detectors can be employed, UV-visible detection is most typical. HPLC functions by separating a sample into its constituent parts based on the interaction and partitioning of the sample components between the liquid mobile phase and stationary phase. For reversed phase HPLC, a non polar stationary phase such as chemically modified silica and an aqueous, moderately polar mobile phase are used. Consequently, the retention time will be longer for molecules exhibiting non polar characteristics, whereas polar molecules will elute faster.

Whilst HPLC is the technique of choice for the assay determination of pharmaceutical tablets, the extensive literature available is focused on the development and validation of HPLC methods suitable for quantifying a specific analyte<sup>87, 88</sup> or the simultaneous detection and quantification of multiple analytes<sup>89-91</sup>. Although an array of literature exists, there is a lack of information regarding the variation in API assay values for large sample sets of commercial tablets. Publications that do involve commercial tablets<sup>87, 92, 93</sup> are not focused on the variation in the API over a batch of the product; rather they are concerned with the development and validation of an HPLC method capable of determining the product assay. Furthermore, these studies often use fewer than 13 commercial tablets when validating the methods and moreover, the total number of tablets used are crushed and mixed together before being separated into the appropriate mass of powdered sample (equivalent to the mass of an intact tablet) and then analysed<sup>87, 92, 93</sup>. Not only does this limit the information regarding the product batch owing to the small sample sizes used, it also eliminates the possibility of analysing individual samples and determining its quality with respect to API content, whether it be higher, lower or in line with the target value. Published studies utilising HPLC with larger numbers of commercial tablets for the purpose of demonstrating variations in API mass are clearly lacking. This gap, however, could possibly be ascribed to the nature of the analysis method which is labour intensive and prone to error, which could in turn potentially exaggerate the true variation between samples. Owing to the drive to implement innovative process analytical techniques, this topic has been investigated using optical spectroscopic techniques such as NIRS<sup>94-96</sup> and Raman spectroscopy<sup>57</sup>.

<sup>58, 60</sup> which provide rapid non-invasive, non-destructive analysis in real-time. A full review of the literature detailing the use of spectroscopic techniques for the API content in pharmaceutical tablets will be given in subsequent chapters.

The aim of the research described in this chapter was to analyse a large number of pharmaceutical tablets by HPLC to assess the variability of the amount of active compound. 254 OTC Chlortrimeton allergy tablets from the same batch were analysed. Chlortrimeton allergy tablets were chosen owing to their low API mass to excipients ratio, equating to an API concentration of approximately 2% w/w (based on the average whole tablet mass calculated from the sample set); the expected dose per tablet was 4 mg chlorpheniramine maleate

## **3.2 Experimental**

### **3.2.1 Materials**

Chlortrimeton antihistamine OTC tablets (Schering-Plough HealthCare Products, Inc., Memphis, TN, USA) were purchased from CVS pharmacy (South Carolina, USA); 11 boxes of the same manufactured batch, each containing 24 tablets were purchased. Each tablet contained chlorpheniramine maleate (active pharmaceutical ingredient), corn starch, D&C yellow No 6 & 10, lactose monohydrate and magnesium stearate.

Chlorpheniramine maleate (99.8% purity), reagent grade ammonium acetate, HPLC grade acetonitrile and reagent grade glacial acetic acid were purchased from Sigma Aldrich, USA. Figure 14 shows the structure of chlorpheniramine maleate.

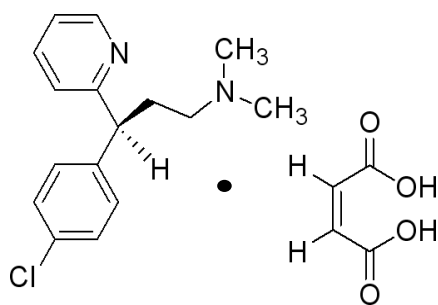


Figure 14–Structure of the active pharmaceutical ingredient, chlorpheniramine maleate

### 3.3 Preparation of mobile phase, standards and samples

#### 3.3.1 *Mobile Phase*

The mobile phase used was an 80:20 mix of 25 mM ammonium acetate and acetonitrile, adjusted to pH 5.5 using glacial acetic acid. The mobile phase was sonicated and degassed after preparation.

#### 3.3.2 *Standard solutions*

Seven standard solutions were prepared covering the range of 0-240 mg L<sup>-1</sup> of chlorpheniramine maleate. Calculated masses of active ingredient were accurately weighed, dissolved in the mobile phase and diluted quantitatively. Serial dilutions were carried out using the mobile phase to obtain standard solutions of the desired concentration.

#### *Preparation of sample solution from Chlortrimeton tablet*

Before preparation, each tablet was weighed and then crushed. The crushed tablet was transferred into a 25 mL volumetric flask, dissolved in mobile phase and diluted to volume. If the tablet contained the target mass of 4 mg of the API, the concentration of chlorpheniramine maleate in the solution would be 160 mg L<sup>-1</sup> API. Samples were sonicated for five minutes and then filtered using 0.2 µm disposable Acrodisc filters (Sigma Aldrich, USA) before injecting into the HPLC.

### 3.3.3 *Chromatographic conditions*

The HPLC system consisted of a Waters 660 pump with a 626S controller, in-line degasser, 717 autosampler and diode array detector. Data were acquired and processed using Waters Empower software. Separation was achieved using an Agilent column (C<sub>18</sub>, 4.6 mm x 150 mm, 5 μm particle size) at an ambient temperature (normally 20-23 °C). A flow rate of 1 mL min<sup>-1</sup>, sample volume of 20 μL, separation time of 16 minutes and detection wavelength of 254 nm were used.

### 3.3.4 *Validation of Chromatographic method*

The chromatographic method described in section 3.3.3 was validated for precision, linearity, specificity, limit of detection (LOD) and limit of quantitation (LOQ). Example sample and standard chromatograms are shown in Figure 15 and 16 respectively; the analyte peak appeared at 1.71 min and the excipient peaks at 10 and 12.5 min.

#### **Precision**

Precision was assessed by analysing six replicate injections of a 160 mg L<sup>-1</sup> chlorpheniramine maleate standard. The % coefficient of variation (CV) of the six analyte peak areas was calculated (18) and found to be 0.93%. Following the ICH guidelines of less than 2%, the calculated CV was deemed acceptable.

$$\% CV = \left( \frac{\text{standard deviation}}{\text{mean}} \right) \times 100 \quad (18)$$

#### **Linearity**

The linear range of the chromatographic method was assessed by analysing seven standards containing chlorpheniramine maleate over the range of 0-240 mg L<sup>-1</sup>. A calibration plot was constructed using the analyte peak areas from the standards and the correlation (r<sup>2</sup>) between the concentration and response was found to be 0.9986.

## Stability

A standard solution containing 160 mg L<sup>-1</sup> chlorpheniramine maleate was prepared and analysed at four time points over 72 hours; no change in the signal was observed.

## Specificity

No peaks interfering with the analyte peak were recorded.

## LOQ and LOD

Five replicate injections of a 40 mg L<sup>-1</sup> standard were analysed and the mean and standard deviations of the analyte peak areas were calculated. The slope of the calibration plot referred to in section 3.3.4 (Linearity) was also calculated. The LOD and LOQ were calculated using equation (19) and (20), respectively, where SD is the standard deviation.

$$LOD = \frac{3 \times SD \text{ of } 5 \text{ standard injections}}{\text{slope of calibration plot}} \quad (19)$$

$$LOQ = \frac{10 \times SD \text{ of } 5 \text{ standard injection}}{\text{slope of calibration plot}} \quad (20)$$

## 3.4 Results and discussion

### 3.4.1 Sample tablet analysis

256 Chlortrimeton tablets were analysed and the resulting peak areas were used together with linear regression analysis to calculate the mass of the active ingredient in each tablet. Before the samples were prepared for analysis, each tablet was weighed to assess the degree of variation in the whole tablet mass. The average whole tablet mass was found to be 201.4 mg, with a maximum and minimum whole tablet mass of 118.5 and 250.7 mg, respectively; the resulting CV for the tablet mass

was 6.1 %. Due to the large spread in whole tablet mass, it was evident this was a source of variation. Figure 17 shows the variation in the active ingredient mass over the 256 sample tablets.



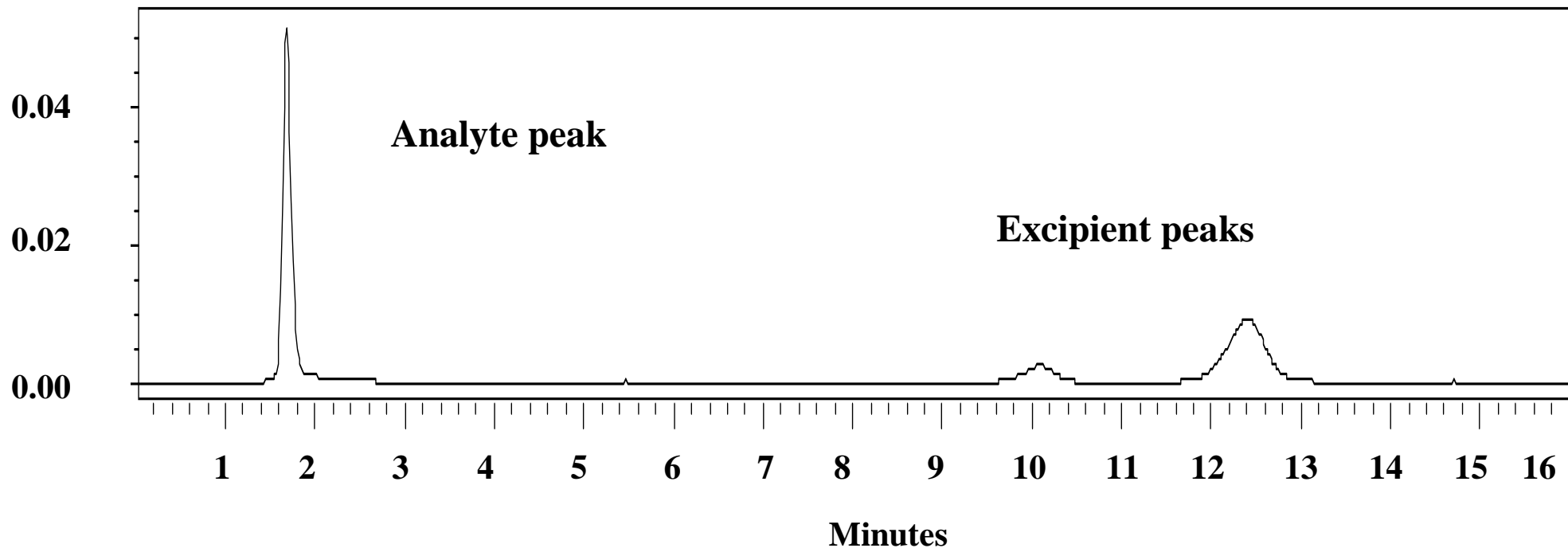


Figure 15 – Chromatogram of a solution of a single Chlortrimeton tablet, containing approximately  $160 \text{ mgL}^{-1}$  of chlorpheniramine maleate

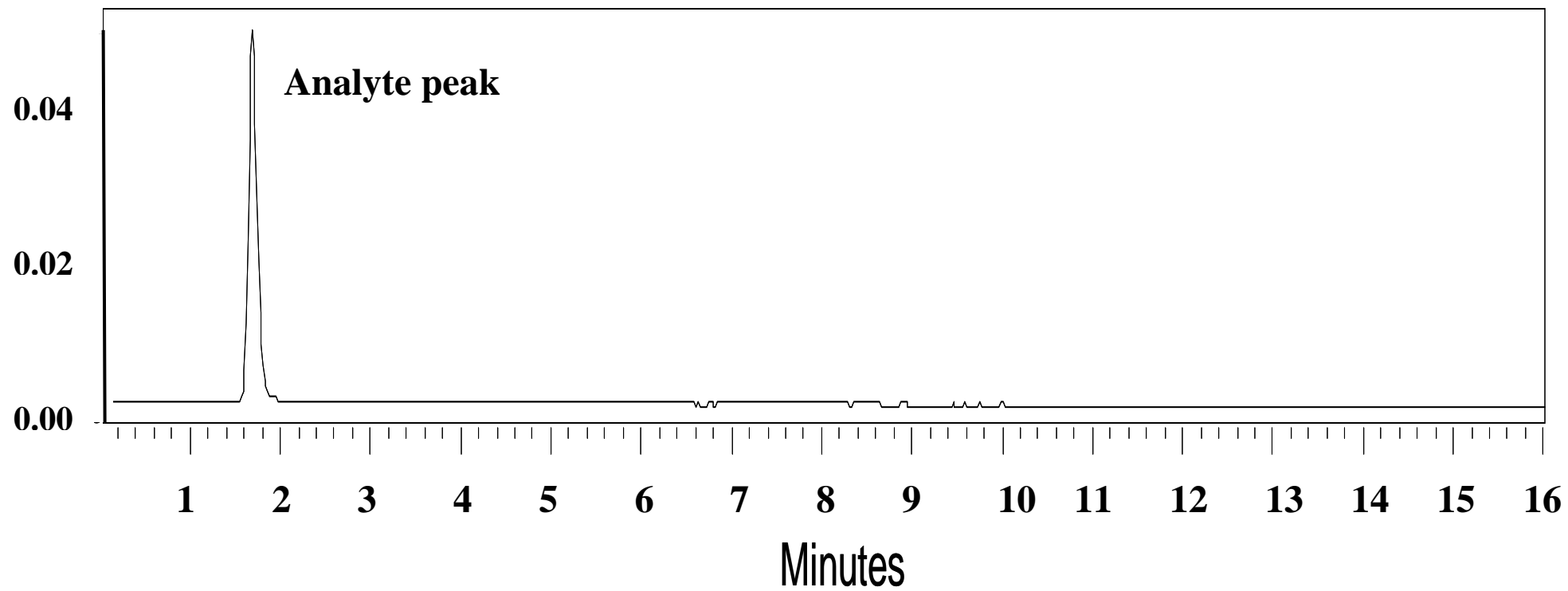


Figure 16 – Chromatogram of a standard solution containing 160 mg L<sup>-1</sup> of chlorpheniramine maleate

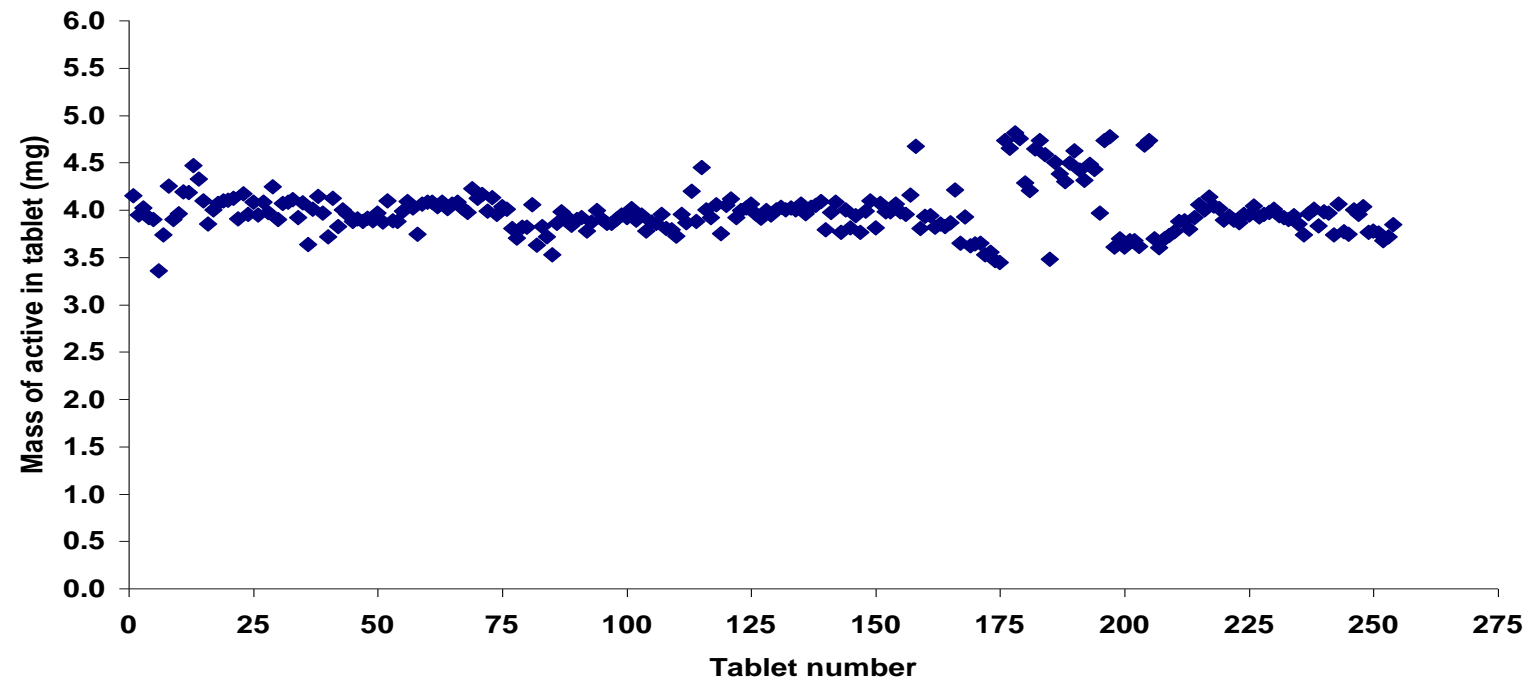


Figure 17 – Plot of the variation in mass of chlorpheniramine maleate in the sample set of Chlortrimeton tablets

From the derived chlorpheniramine maleate mass values represented in Figure 17, the mean was found to be 3.98 mg, with minimum and maximum values of 3.36 and 4.81 mg, respectively. The CV of the API mass was 6.3 %, the mean concentration of chlorpheniramine maleate in the tablets was 1.98 % w/w. Table 6 gives a summary of the data obtained for the API mass and whole tablet mass.

Figure 17 shows higher calculated active ingredient mass values for the group of samples between tablet number 175 and 200 than for the majority of the other tablets in the sample set; these samples were from the same packet and were analysed over a two day period. In order to confirm the calculated active ingredient mass values, the sample solutions were re-analysed and calculation of the chlorpheniramine maleate content from the re-injected solutions was consistent with the values shown in Figure 17. Furthermore, precision checks based on the area of the analyte peak were carried out each day, before and after sample analysis and the variation in the analyte peak areas was calculated to be less than 0.5%. As other samples were analysed in the same time period and were found to have active mass values that were in good agreement with the mean value, the higher values calculated for tablets 175-200 were believed to be truly representative of the actual chlorpheniramine maleate content.

**Table 6 – Summary of maximum, minimum, mean and % CV values for the whole tablet mass and chlorpheniramine maleate mass of 256 Chlortrimeton tablets**

|               | Whole tablet mass (mg) | Chlorpheniramine maleate mass (mg) |
|---------------|------------------------|------------------------------------|
| Mean value    | 201.4                  | 3.98                               |
| Minimum value | 118.5                  | 3.36                               |
| Maximum value | 250.7                  | 4.81                               |
| % CV          | 6.1                    | 6.3                                |

Despite a good agreement between the calculated mean API mass of 3.98 mg and the stated mass of 4 mg, the range of calculated API and whole tablet masses over the 254 samples was found to be larger than expected. This suggests that regardless of good theoretical and experimental agreement with respect to the active ingredient mass on average, stages within the process used to manufacture the samples may not be repeatable as a number of samples were outliers with respect to API and whole tablet mass.

In order to ensure good quality tablets, the constituent powders used in the manufacturing process are expected to be in the form of homogeneous blends; however, the use of blending cycles that have not been optimized with respect to the blending time may lead to inhomogeneity and in turn problems with the production of tablets that meet the required specifications<sup>97</sup>. The use of a homogeneous blend of powders would eliminate any potential problems affecting the API content of the tablets arising from the large range in whole tablet mass that is apparent in this case. Assuming a homogeneous blend of powders is used, a correlation between low whole tablet mass and low active mass would be expected, this however is not the case as can be seen from Figure 18 and Table 7.

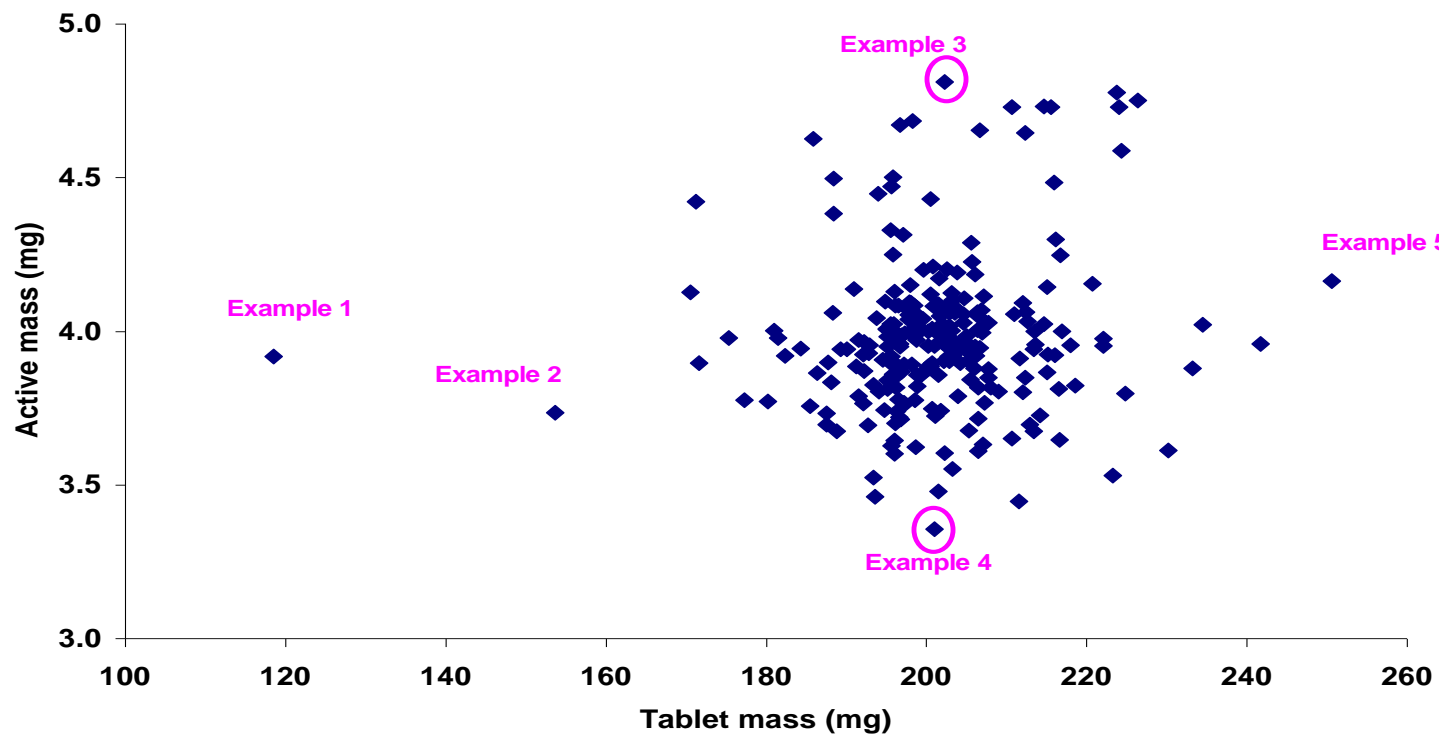


Figure 18 – Plot showing the correlation between chlorpheniramine maleate mass (active) and whole tablet mass for 254 Chlortrimeton tablets

**Table 7 – Active mass, whole tablet mass and concentration values for example samples 1-5 highlighted in Figure 18**

|                               | Tablet example number (Figure 18) |        |        |        |        | Average of 256 tablets |
|-------------------------------|-----------------------------------|--------|--------|--------|--------|------------------------|
|                               | 1                                 | 2      | 3      | 4      | 5      |                        |
| Chlorpheniramine maleate (mg) | 3.92                              | 3.73   | 4.81   | 3.37   | 4.17   | 3.98                   |
| Whole tablet mass (mg)        | 118.5                             | 153.73 | 202.35 | 201.01 | 250.66 | 201.40                 |
| Concentration of API (%w/w)   | 3.31                              | 2.43   | 2.38   | 1.67   | 1.66   | 1.98                   |

Figure 18 highlights that for a number of samples the expected correlation between whole tablet mass and active ingredient mass is not apparent, resulting in outlier samples. Examples 1 and 2 from Figure 18 are significantly lighter than the average tablet however, the active ingredient mass calculated for this tablet is only 0.063 mg less than for the average tablet and hence does not exhibit a proportional decrease; this is also the case for example 2. Consequently, despite being 24-40% lighter than the average tablet, close to the target API mass of 4 mg is provided by the tablet because the concentration of chlorpheniramine maleate is greater than the average value that would be expected.

Examples 3 and 4 from Figure 18 are similar to each other with respect to whole tablet mass (202.35 and 201.01 mg, respectively) and are close to the average whole tablet mass of 201.4 mg. Nevertheless, despite having a similar mass, they differ significantly in their active mass content (4.81 and 3.37 mg, respectively) and furthermore, these values differ significantly from the average mass of chlorpheniramine maleate. As examples 3 and 4 have a whole tablet mass that is

similar to the average whole tablet mass, it would also be expected that the active ingredient mass would match that of calculated average active ingredient mass; however, the differences described result in chlorpheniramine maleate concentrations in the tablet that are higher and lower, respectively, than the average value.

Example 5 is significantly heavier than the average tablet and hence it would be expected that this tablet would also have a greater mass of chlorpheniramine maleate than the average tablet, assuming that the blend of powders used in the manufacturing process was homogeneous. However, close to the target API mass of 4 mg is provided by this tablet as the concentration is less than the average value of 1.66% w/w, compared to an average value of 1.98% w/w. Furthermore, from Figure 18 examples 4 and 5 look to be different with respect to the correlation between the API and whole tablet mass values; example 5 is 50 mg heavier than example 4 and contains 0.8 mg more active ingredient, nevertheless when comparing their API concentration values, the tablets are essentially the same (1.67 and 1.66% w/w).

### **3.5 Conclusions**

An HPLC method has been developed and validated for the determination of chlorpheniramine maleate in Chlortrimeton allergy tablets. It has been demonstrated that whilst the average calculated active ingredient mass is in good agreement with the stated mass of 4 mg API per tablet, outlier samples displaying active mass values significantly removed from the mean value are apparent. Two sources of variation within this study have been identified, whole tablet mass and active ingredient mass and a large range of values have been calculated for both sources.

A solid dosage form is often comprised of a number of constituents, all of which must be homogeneously blended to ensure good quality products as well as control over the process. Assuming a homogeneous blend is used, any fluctuation in the whole tablet mass should result in a proportional increase or decrease of the API mass. From the data discussed in section 3.4, it is clear that the outliers identified do



not conform to this paradigm; in each of the five examples there is no correlation between the fluctuating tablet mass and the API mass. Consequently, the outlier samples discussed suggest that the process used to make these tablets is not robust and repeatable – a target set by the FDA<sup>98</sup> – as samples of inconsistent quality have been identified. Furthermore, when considering assay limits of  $\pm 10\%$ <sup>99</sup>, compliance would require chlorpheniramine values in the range of 3.6 – 4.4 mg based on a target active ingredient mass of 4 mg. The range calculated from the HPLC study however, was greater (3.36 – 4.81 mg), so despite achieving an accurate average API mass, the range of results do not meet the specified limits. Fortunately, as these tablets are ‘4 hour tablets’ and hence are designed to be taken up to four times in one day for a prolonged period of time, the potential problem of variations in the amount of active ingredient delivered to the patient is mitigated.

The outlier samples discussed in this chapter illustrate the potential problems associated with the preparation of powder mixtures; real-time monitoring using spectroscopic techniques such as Raman spectrometry could help address such issues. Furthermore, as tablet analysis by HPLC is time consuming and destructive, direct analysis using spectroscopic techniques can provide quality control benefits via non-destructive analysis and faster analysis times allowing for a better statistical description of the batch; techniques such as Raman spectrometry has shown potential for the direct analysis of tablets<sup>100-102</sup>. Prior to the development of a non-invasive method for the determination of chlorpheniramine maleate by Raman spectrometry (chapter 5), an in depth study of the factors affecting the propagation of photons in powders (chapter 4) was undertaken in order to attain a fundamental understanding of the technique that could be applied to direct tablet analysis.

## **4. Investigation of the effect of powders on the propagation of photons through diffusely scattering media**

### **4.1 Literature Review**

Non-invasive analysis by a highly chemically specific technique is required in a range of pharmaceutical<sup>57</sup>, defence science<sup>103</sup> and medical applications<sup>66</sup> to investigate the deep layers of a turbid sample. As Raman spectroscopy has a high chemical specificity and can also probe samples in the presence of water, it shows particular promise in this area in comparison to near infrared spectrometry (NIRS), which has a limited chemical specificity, and mid infrared spectrometry (MIRS), which is incompatible with aqueous samples, as water strongly absorbs MIR radiation<sup>61</sup>. Until recent years, Raman spectroscopy has been used primarily in the reflectance (or backscattering) mode owing to the simplistic nature of the sampling configuration and ease of use, however it has been demonstrated that this configuration is limited to only shallow depth analysis<sup>59</sup>. For example, the penetration depth of Raman photons in living tissue, in the reflectance mode is only several hundred micrometers and although there is a greater penetration depth when analysing pharmaceutical tablets, the accessible depth can be approximately 1 mm with conventional probes, which is not sufficient for investigating the sample as a whole<sup>59, 66</sup>.

As demands increase for more sophisticated methods of analysis, capable of providing information regarding the entire character of a sample (whether it is a pharmaceutical tablet, counterfeit drug or living tissue) the key to achieving this is not only understanding the attributes of the sampling geometries available, but just as importantly, a sound fundamental understanding of the propagation of light in diffusely scattering media is required. The main obstacle that discounts the use of conventional optical methods from analysing sub-surface layers of turbid samples is the highly scattering nature of such media; the propagation of photons (for example in Raman spectroscopy) in such samples is a consequence of diffuse scattering<sup>66</sup>. To understand the propagation of light through a diffusely scattering sample, for example a pharmaceutical tablet, it is important to understand the three types of propagation of radiation through such samples (see Figure 19).

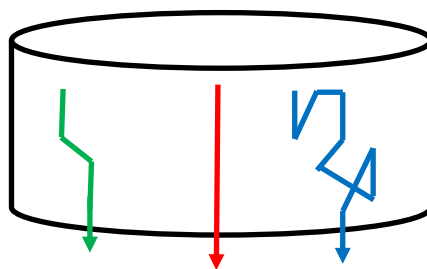


**Figure 19 – Schematic showing the three main components of light within turbid media: ballistic (red), snake (green) and diffuse (blue)<sup>66</sup>**

Figure 19 illustrates the three propagation processes that arise in the analysis of turbid samples<sup>66</sup>. The ballistic light is not scattered by the medium through which it is travelling and its intensity decreases exponentially with the penetration depth of the photons. As the ballistic light travels through the sample, it gradually converts to the snake component which is only mildly affected by scattering events and in turn the light only deviates marginally from its original pathway and continues to move in a forward direction. In the same manner as the ballistic component, the intensity of the snake photons decay exponentially with depth, but they demonstrate a greater penetration depth than that of the ballistic photons. The component with the greatest penetration depth is the diffuse light, which is formed from both the ballistic and snake photons through a large number of scattering events. The high number of scattering events randomise the direction of the diffuse photons to the extent that the path they follow does not resemble the original direction<sup>66, 104</sup>. As the diffuse component travels further than the other components, it is the most useful for the investigation of sub-surface layers in turbid media.

Increased research in to the fundamental behavior of light in samples has led to a number of studies which have shown that the penetration depth of reflectance mode Raman photons can be increased significantly by utilising the diffuse rather than the ballistic component of light<sup>105-107</sup> together with selecting the optimum sampling geometry for the analysis, which could involve measurement of reflectance,

transmission or spatially offset Raman spectroscopy (see Figure 20). The intense reflectance Raman signals that originate from the surface layers of the sample overwhelm the considerably weaker sub-surface signals and consequently the conventional reflectance Raman method is unable to probe deep layers of samples. The sub-surface signals are in essence diluted owing to the wide spread diffusion of photons from these layers, resulting in a wider spatial spread of these signals escaping from the sample surface. Conversely, the surface Raman photons are much more efficiently collected in the reflectance geometry owing to their close proximity to the collection optics of the instrument.

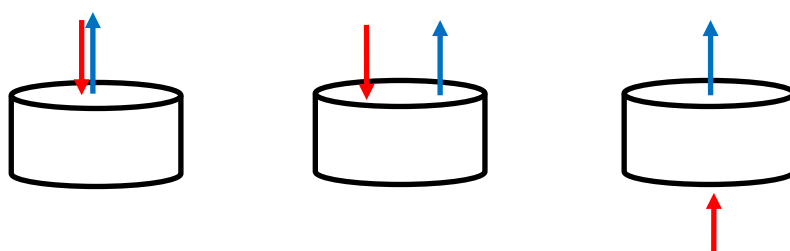


**Figure 20 – Schematic of basic Raman spectroscopy geometries: (from left to right) reflectance Raman, SORS and transmission Raman, where the laser beam is depicted by the red arrow and the Raman scattered photons by the blue arrow.**

A method which effectively suppresses the impact of the surface generated signals in the Raman spectrum and hence allows the sub-surface information to emanate is temporal gating of the Raman signal<sup>66, 108</sup>. Raman gating experiments are generally performed using the conventional reflectance geometry where the laser illumination and Raman collection areas overlap on the surface of the sample. The concept is based on the larger travelling distances of the photons emerging from deeper depths within the sample compared to the smaller distances travelled by the surface generated photons; these different signals can be separated in time by up to hundreds of picoseconds owing to the random nature of diffuse scattering<sup>108</sup>.

The first application of this technique was demonstrated by Wu in 1995, who imaged an object in a turbid medium using temporally resolved Raman light. Wu showed that the time resolved approach could detect a  $\beta$ -carotene signal at depths of several centimeters in a semi-turbid medium<sup>109</sup>. Matousek et al. were the first to demonstrate the full recovery of a Raman spectrum of a deeply buried layer in a turbid sample<sup>110</sup>; they successfully demonstrated how pulsed laser Raman excitation followed by fast optical Kerr gating could be used to separate deep layer Raman signals from those of the sample matrix; furthermore, the study showed that this approach vastly improved the ratio of surface to bulk Raman signals. Everall et al. used picosecond time-resolved Raman spectroscopy to investigate the temporal response of scattering in powders and demonstrated that for powdered samples, the Raman signal decayed much more slowly than the corresponding Rayleigh signal<sup>106</sup>. It was found that when using a 5 mm deep, 3 mm in diameter powdered trans-stilbene sample and a 1 ps laser pulse, the Rayleigh and Raman signals decayed over a period of tens to hundreds of picoseconds after the incident 1 ps laser pulse. It was concluded that the Rayleigh and Raman signals conformed to different decay kinetics – the Rayleigh signal was spread over 100 ps in time whereas the Raman signal was still present after 300 ps; approximate kinetics were calculated for both Rayleigh and Raman signals and were found to be  $t^{-3/2}$  and  $t^{-1/2}$ , respectively.

Despite proving to be an effective method, the temporal gating approach is limited by a number of intrinsic weaknesses. Primarily, the technique suffers from instrumental complexity and consequently high costs. Also, owing to the use of high intensity laser pulses, there are potential safety concerns associated with this approach. An alternative approach which utilises safer, lower power continuous beam lasers and hence has a much simpler set-up has been used successfully to separate surface and deep layer Raman signals. In 2005, Matousek demonstrated the use of spatially offset Raman spectroscopy (SORS) to analyse the sub-surface layers of diffusely scattering media<sup>105</sup>. This study collected Raman photons from points that were laterally offset from the laser impact region. The use of SORS allows Raman photons to be collected at a range of distances from the laser impact position (each of which will have different spatial distributions on the sample owing

to the different depths they originated from). This study used the same sample as with the temporal Kerr gated approach<sup>110</sup> (a 1 mm thick poly(methyl methacrylate) powder layer in front of a trans-stilbene powder layer), which allowed a direct comparison of the two techniques to be made. Matousek et al. showed that despite using a simpler instrumental set up, the signal quality obtained using the SORS approach was much improved and this was attributed to the significant reduction in the detected signal in the gated approach owing to the ultrafast gating and hence chopping of relatively long Raman signals. Furthermore, the study showed that when using a two layer system, the detected Raman spectra can be separated further using a scaled subtraction of two spectra obtained at different spatial offsets, to produce pure Raman spectra of the individual layers<sup>105</sup>. Although SORS is primarily known for its ability to suppress surface layer Raman signals, it is also capable of suppressing the fluorescence signals originating from the surface layer of a sample as they have the same spatial but not temporal character as the Raman signal originating from the same layer of the sample<sup>66</sup> – this is a beneficial feature in the analysis of pharmaceutical tablets and capsules which often fluoresce.

Another Raman sampling geometry that has become popular owing to the recent interest in Raman photon migration in turbid samples is transmission Raman spectroscopy. In some analytical applications, the primary aim may in some cases be the analysis of the bulk content of a sample rather than the interrogation of individual layers; an example of this is the determination of the bulk content of pharmaceutical tablets, where the interest lies in the sample as a whole. The concept of transmission Raman spectroscopy is thought of by some as an extreme version of SORS, where the laser beam is incident on one side of the sample and the resultant Raman signal is collected from the opposite side (see Figure 20). This approach was identified as early as 1967<sup>111</sup>, however, its ability to probe non-invasively the bulk content of a sample has not been extensively utilised. Transmission Raman spectroscopy has demonstrated the ability to detect deep layers in turbid samples<sup>102</sup> thus removing the sub-sampling limitation of reflectance mode measurements and furthermore has shown to suppress effectively surface layer Raman and fluorescence signals<sup>67</sup>.

In 2006, Matousek and Parker compared reflectance and transmission mode Raman geometries to identify their potential for monitoring the bulk composition of turbid media<sup>59</sup>. It was reported that the strong bias of the reflectance Raman collection geometry towards the surface layers of the probed sample was by and large absent with the transmission geometry, and consequently the technique was reported to be insensitive to the depth of impurities in the sample<sup>59</sup>. The study showed that when using a two layer sample comprising of a 3.9 mm paracetamol tablet on top of a 2 mm thick layer of powdered trans-stilbene (and also the inverted sample configuration), not only could both the bulk and impurity materials (paracetamol and trans-stilbene, respectively) be detected in the transmission spectra, but also this geometry demonstrated an insensitivity to the position of the impurity layer. Regardless of the sample orientation, the trans-stilbene layer was clearly and equally identified, with respect to the Raman intensity. This, however, was not shown to be the case with the equivalent reflectance mode experiments, where only the material present on the top surface of the sample was present in the recorded Raman spectra<sup>59</sup>.

Matousek and Parker also reported Monte-Carlo simulations which were used to model the response in both Raman geometries when an impurity layer was moved through a bulk medium. The model used followed the Rayleigh and Raman photons as they randomly propagated through the medium. A number of assumptions were made - in each step, initially the photon would propagate in a straight line until the next scattering event where its direction would be fully randomised. Additionally, the model assumes that the sample is an infinite turbid medium with one air-medium interface located at the top surface. The sample used in the model was composed of a uniform turbid medium with an intermediate layer of a different substance to that of the bulk sample. For the simulations reported in the study, the total sample thickness was held at 4 mm, the thickness of the intermediate layer was 0.5 mm and the top surface of the sample varied between 0 to 3.5 mm in thickness.

Monte Carlo simulations showed that the reflectance mode geometry led to a strong bias towards the surface layers of the sample – the signal intensity, obtained when the intermediate layer was placed at a depth of 1.5 mm through the sample, decreased to only 3% of the intensity seen when the layer was on the surface of the sample. Conversely, the corresponding transmission mode results showed that the layer position had only a small effect on the observed Raman intensity. Between depths of 0 and 3.5 mm, the Raman interlayer signal varied by only a factor of 2. From these numerical and experimental findings, Matousek and Parker concluded that transmission mode measurements were insensitive to the depth of impurity layers and hence provided a significantly more uniform way of probing the body of the sample compared to the conventional reflectance mode approach<sup>59</sup>.

As the application of Raman spectroscopy is extending to numerous fields and in turn numerous sample types (tablets<sup>60</sup>, bones<sup>112</sup> and cancerous cells<sup>113</sup>) it is important that a fundamental understanding of the technique is attained together with a solid knowledge of how light behaves in different media types. The literature reviewed has clearly demonstrated the importance of such investigations and has highlighted an area of great interest and importance that continues to be studied. Nevertheless, there is a gap in the current literature with respect to the effect physical properties (particle shape, size and density) have on the propagation of light through turbid media. Studies incorporating this topic would significantly add to the understanding of photon propagation and could in turn be applied to specific chemical systems to gain a detailed knowledge of how those systems affect analytical measurements. In this study, an experimental assessment of the effect of a moving impurity layer through loose powders on transmission Raman measurements was carried out; furthermore, the effect of the particle size and shape of loose powders on the recorded Raman spectra will be investigated. This experimental assessment complements the simulated study undertaken by Matousek and Parker<sup>59</sup>.



## 4.2 Experimental for Fundamental Studies

### 4.2.1 *Fundamental Transmission Mode Raman Studies*

Experiments were devised to assess the effect of the physical properties (particle size and shape) of two common pharmaceutical materials on transmission mode Raman measurements. Furthermore, Raman experiments were set up to investigate the origin of the signal in the transmission mode. In order to address this question two factors were investigated:

- The penetration power of the Raman signal of a ‘Raman active’ layer through a depth of bulk powder.
- The effect of the bulk sample on the
  - i. excitation of the Raman signal and,
  - ii. transmission of the Raman signal to the collection optics.

Figure 21 shows the sample configurations used in the experiments described above. The sample configurations shown in Figure 21 were supported using a glass slide attached to the underside of a 10 cm x10 cm stainless steel plate with a 6 cm diameter circular hole through which the laser light could penetrate. The bulk sample was layered to the required depths shown in Figure 21 using a series of stainless steel plates (10 cm x10 cm with a 6 mm diameter circular hole). The loose powder was carefully placed into the void and with minimum compaction was leveled off using a razor blade. The ‘Raman active’ layer containing flowers of sulphur was placed at the centre of the hole at the required depth within the bulk powder. The stack of stainless steel plates containing the powder and flowers of sulphur disk was then placed into the Kaiser Raman workstation such that the laser light passed through the centre of the stack ensuring contact with the ‘Raman active’ layer.

For all experiments described in this chapter the Kaiser Raman workstation together with the Kaiser Raman PhAT probe were used for analysis (details of their operation

can be found in section 2.5). All experiments were carried out in transmission mode unless otherwise stated. The illumination and collection optics provided a 3 mm spot size for all measurements, which involved use of 400 mW laser power, 3 s exposure time and 30 acquisitions. A dark current spectrum was acquired before each set of experiments and the HoloGRAMS software subtracted the dark current from each subsequent spectrum acquired. The spectra were converted to text files to allow the data to be processed and manipulated by independent software packages.

#### **4.2.2 *Materials***

The bulk materials used were loose Avicel (particle sizes 0-38, 53-106 and 150-212  $\mu\text{m}$ ) supplied by GlaxoSmithKline and aspirin (150-212  $\mu\text{m}$ ) supplied by Sigma Aldrich, UK. Materials were sieved to obtain the desired particle size range. The particle sizes ranges of Avicel were chosen to assess the effect of particle size on the transmission mode measurements. As aspirin particles are needles, whereas Avicel particles are granular in shape, inclusion of aspirin allowed the effects of particle shape to be investigated. Digital microscope images of the Avicel and aspirin materials were acquired to allow a visual comparison of the size and shape to be made (refer to Figure 27). The 'Raman active' layer used in the experiments was a 1 mm thick pressed disk of a 50:50 mixture of potassium bromide and flowers of sulphur. The disk was pressed using a conventional disk press, to a pressure of 25 tonnes to ensure an evenly pressed disk. Flowers of sulphur was chosen as it is a highly efficient Raman scatterer.

#### **4.2.3 *Data Analysis***

For analysis, all data were imported into Matlab version 7.0.2 (Mathworks Inc., Natick, Massachusetts, USA) using PLS Toolbox version 3.0.4 (Eigenvector Research Inc., Manson, Washington, USA). Spectra were converted to second derivative spectra using the Savitsky-Golay function – 51 point filter width, second order polynomial. A 51 point filter width was deemed acceptable as it was less than that of the square root of the number of points contained in an acquired spectrum.

#### ***4.2.4 Determination of the penetration power of the transmission Raman signal through powders of varying physical properties***

The penetration power of the transmission Raman signal through powders of varying physical properties, namely particle size and shape was assessed using the sample configurations shown in Figure 22, set-up A to E. Each sample configuration was analysed three times using each of the four materials: Avicel (0-38, 53-106, 150-212  $\mu\text{m}$ ) and aspirin (150-212  $\mu\text{m}$ ). The samples were prepared as detailed in section 4.2.1 and each of the positions (A to E) were analysed using the parameters stated in section 4.2.1.

#### ***4.2.5 Investigation to assess the effect of the bulk sample on the excitation of the transmission Raman signal and the propagation of the subsequent Raman signal to the collection optics***

The effect of the bulk sample (Avicel or aspirin) on the excitation of the transmission Raman signal and the transmission of the generated signal to the collection optics was investigated using the sample configurations P1 to P5 in Figure 21. Each position, P1 to P5, was analysed three times using Avicel (0-38, 53-106 and 150-212  $\mu\text{m}$ ) and aspirin (150-212  $\mu\text{m}$ ) as the bulk materials and the average sulphur signal was calculated. Sample configurations were prepared as described in section 4.2.1 and the 'Raman active' layer was progressively moved through the 4 mm depth of bulk powder as is shown in Figure 21.

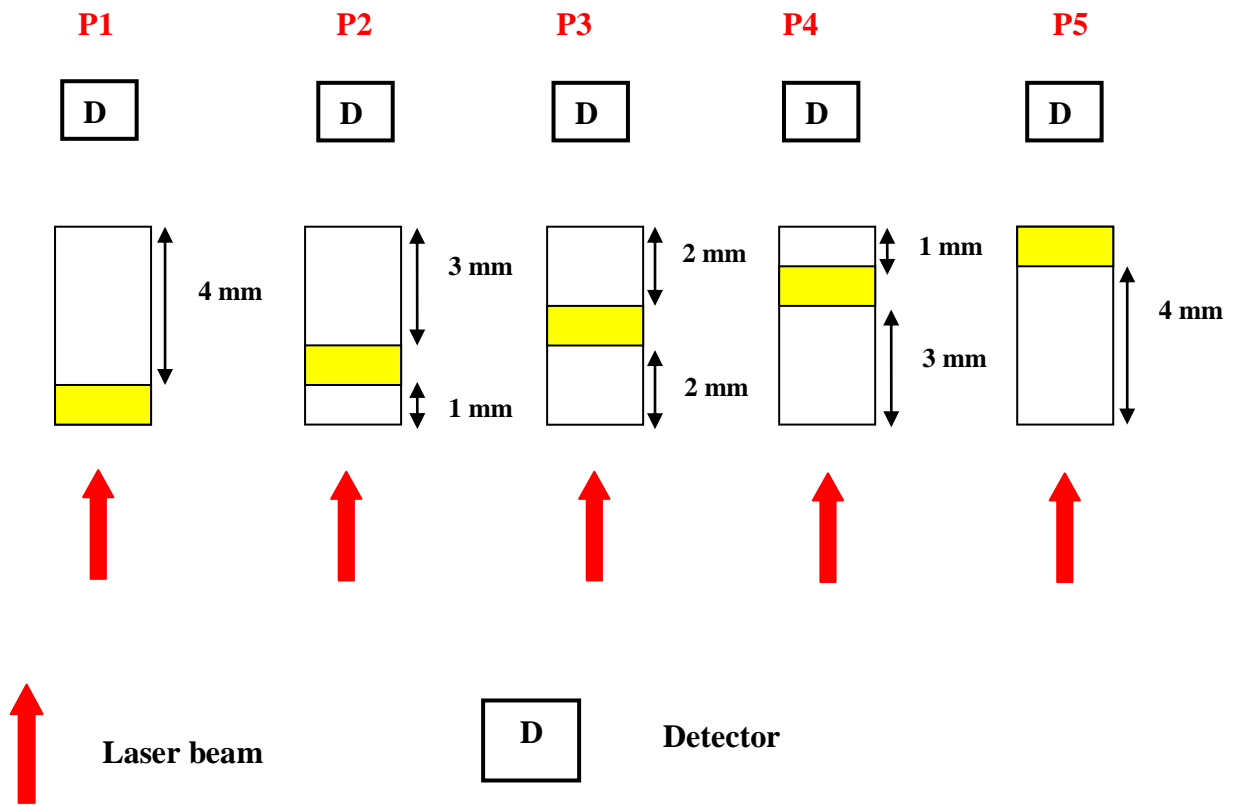


Figure 21 – Sample configuration for transmission mode Raman experiments to assess the effect of the bulk sample (white) on the excitation of the Raman signal of a ‘Raman active layer’ (yellow) and the transmission of the subsequent Raman signal to the collection optics.

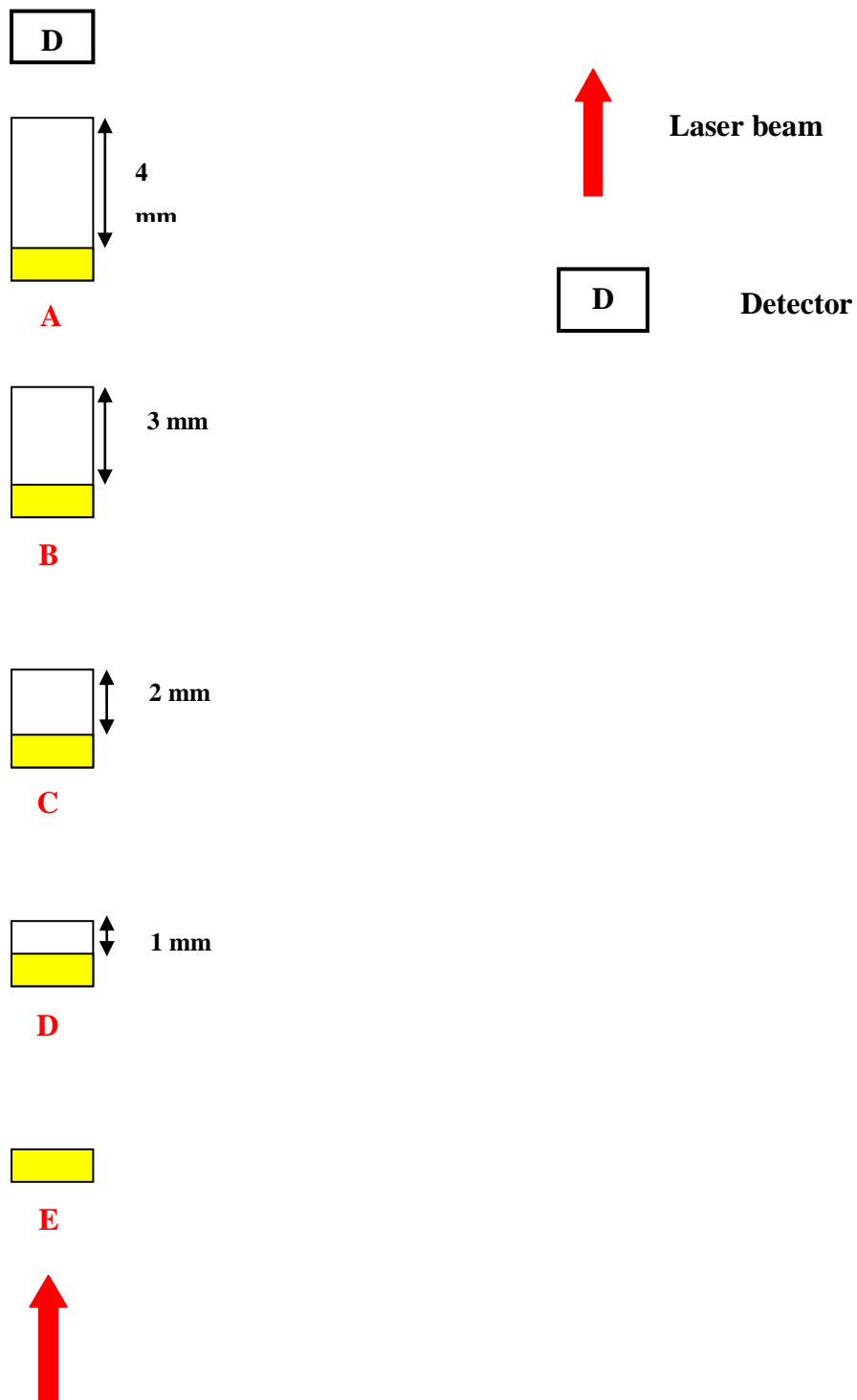
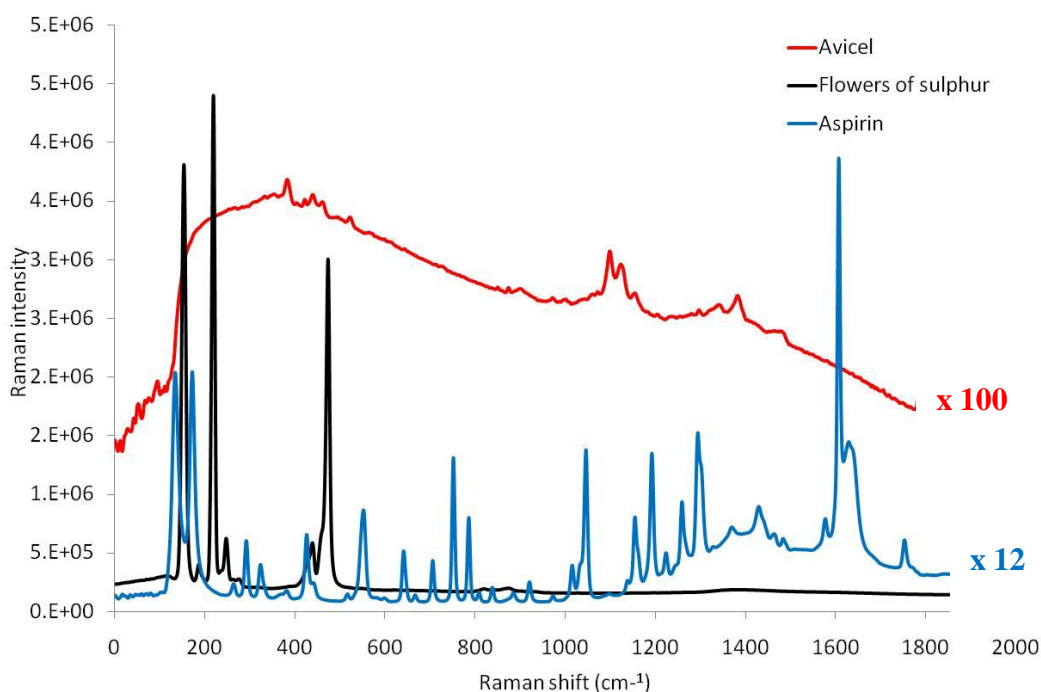


Figure 22 – Sample configuration for transmission mode Raman experiments to assess the penetration power of the Raman signal of a ‘Raman active layer’ (yellow) through powder (white) to the collection optics.

### 4.3 Results and Discussion

#### 4.3.1 Determination of the penetration power of the Raman signal through powders of varying physical properties

In order to assess the penetration power of the Raman signal generated from the flowers of sulphur disk through different depths of Avicel and aspirin, it was necessary to ensure that a strong Raman band from this layer could be studied without interference from the Avicel and aspirin bands. Figure 23 shows the transmission Raman spectra of Avicel, aspirin and flowers of sulphur; from the spectra it can be seen that Avicel exhibits a weak Raman spectrum on a slightly fluorescent background and furthermore, the signals for both Avicel and aspirin are significantly weaker than that of flowers of sulphur, indicating their relatively poor Raman scattering cross-sections. The analysis of all data in this section does not consider the possibility of beam shape deviations as the laser passes through the sample.



**Figure 23 – Transmission Raman spectra of Avicel (signal multiplied by 100), aspirin (signal multiplied by 12) powders and a compressed flowers of sulphur disk**

In order to remove the effects of the background in the Avicel spectrum and hence allow a comparison of the spectral peaks to be made, the second derivative Raman spectrum was calculated and plotted (see Figure 24).

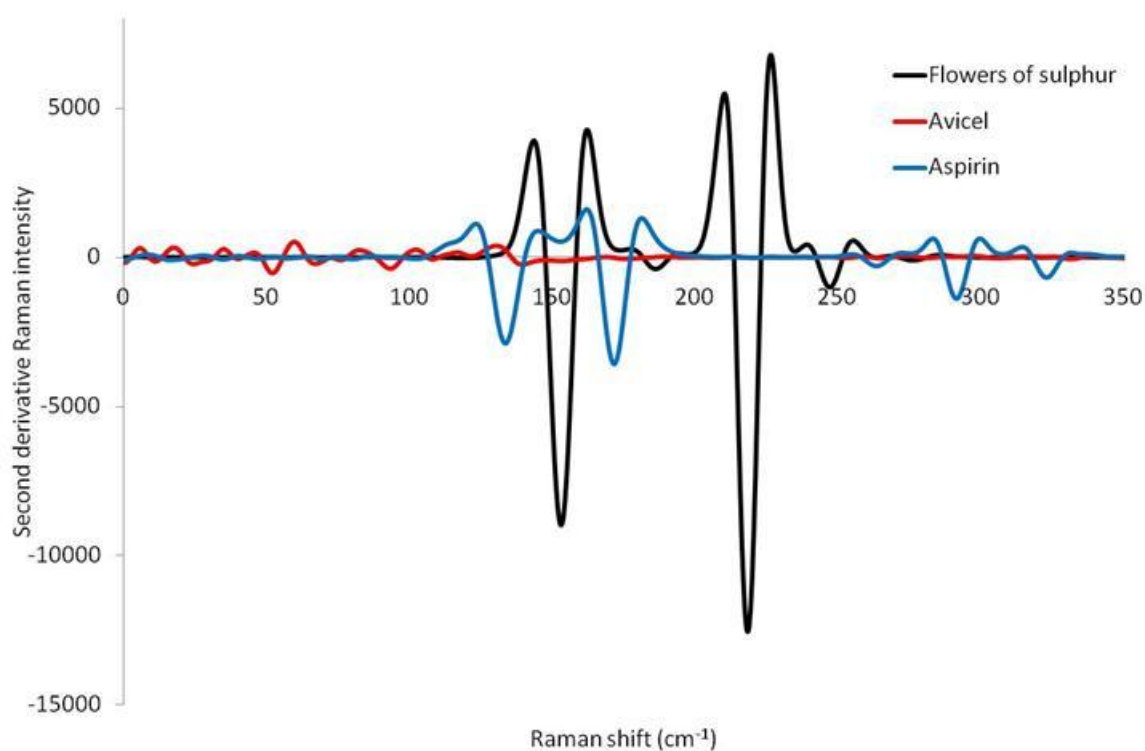


**Figure 24 – Second derivative Raman spectrum of Avicel (signal multiplied by 100), aspirin (signal multiplied by 12) powder and a compressed flowers of sulphur disk. X-axis reduced to show only 0-350  $\text{cm}^{-1}$  to highlight the region of interest.**

Figure 24 shows that there is a strong contribution from flowers of sulphur at approximately  $218 \text{ cm}^{-1}$  and furthermore there is no interfering contribution from either Avicel or aspirin in this region. Flowers of sulphur also exhibits a strong peak at  $155 \text{ cm}^{-1}$ , however owing to an overlapping response from aspirin in this region, it was decided to use the flowers of sulphur Raman peak at  $218 \text{ cm}^{-1}$  for all experiments. Specific aspirin and Avicel peaks were not required to be identified for analysis as the experiments described were designed to monitor the penetration of the sulphur signal through the bulk material (Avicel or aspirin).

To assess the penetration power of the sulphur Raman signal through Avicel of different particle sizes and aspirin, 1 mm increments of powder were stacked on top of the 1 mm thick sulphur disk (as is shown in Figure 22) to a total bulk powder depth of 8 mm. Figure 25 illustrates how the sulphur Raman signal decreases with the increasing depth of powder on the sulphur disk. Figure 26 is a Y-axis expanded version of Figure 25. Both figures show the average normalised Raman intensity, which was calculated from six replicate measurements and values were normalised to the sulphur disk intensity when no powder was placed on top of it (refer to Figure 21 position E).

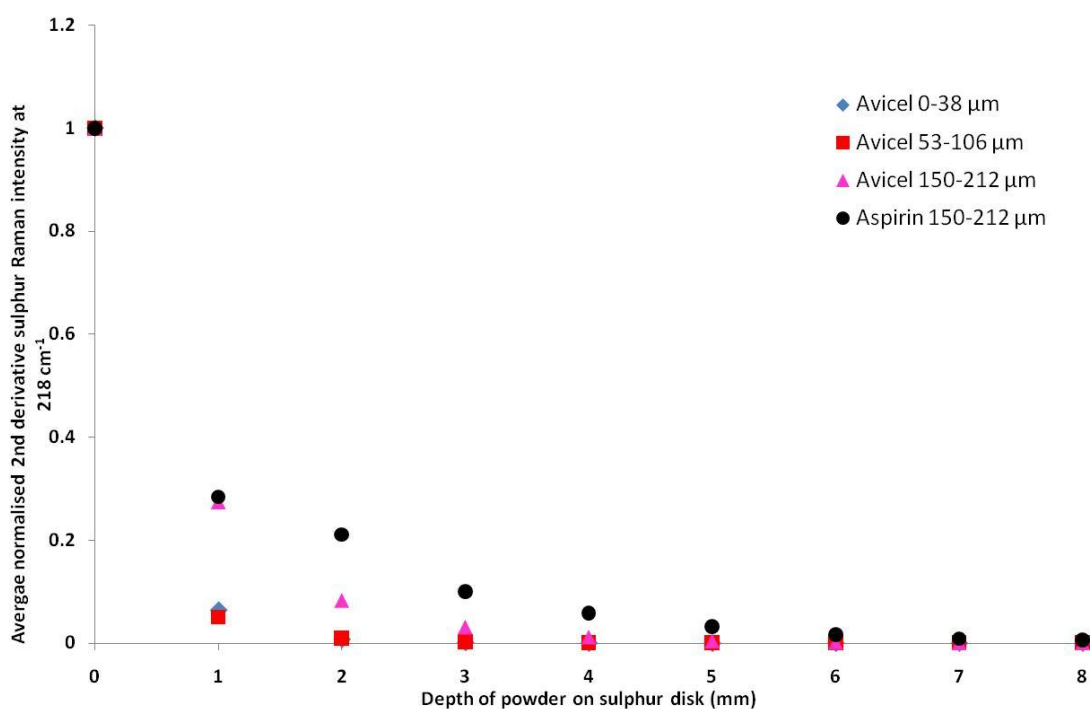


**Figure 25 – Plot of the change in the average normalised second derivative transmission Raman intensity of the sulphur peak at  $218\text{ cm}^{-1}$  with the increasing depth of Avicel or aspirin powder on the sulphur disk**



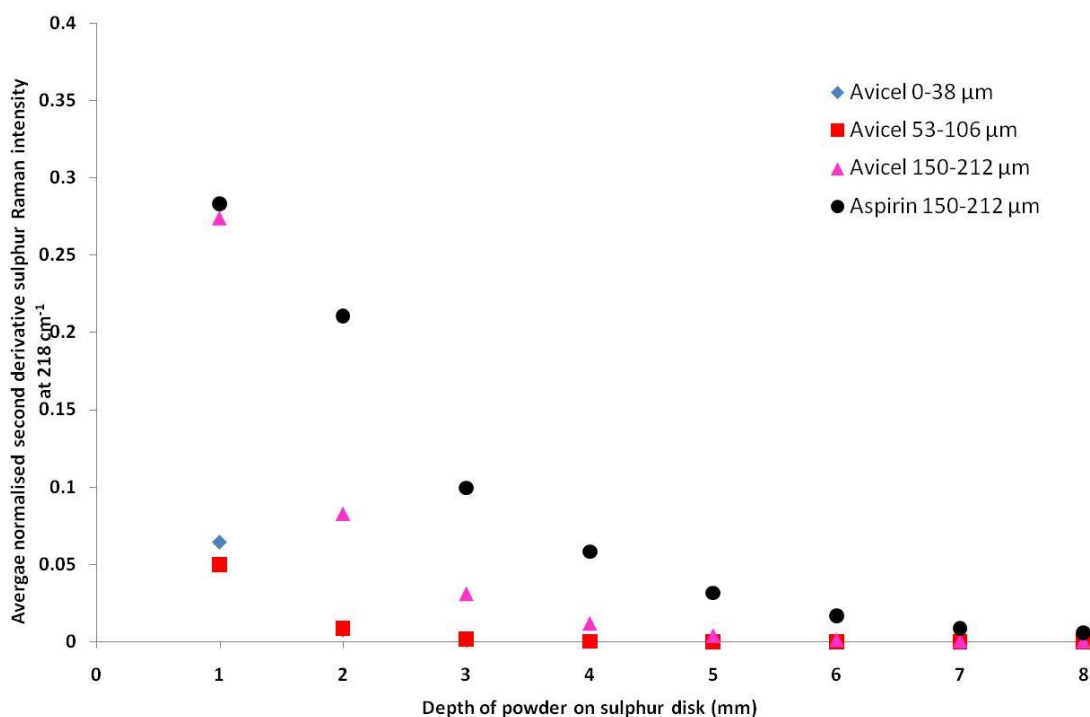


**Figure 26 – Y-axis expanded plot of the change in the average normalised second derivative transmission Raman intensity of the sulphur peak at  $218\text{ cm}^{-1}$  with the increasing depth of Avicel or aspirin powder on the sulphur disk**

Both figures show, as expected, that as the depth of powder on top of the sulphur disk is increased, the detected sulphur signal decreases. This illustrates the extent to which penetration of the generated sulphur signal is hindered by the surrounding powder. Figure 26 illustrates clearly that the rate of decay of the sulphur Raman signal differs with increasing particle size. When only 1 mm of Avicel 0-38 and 53-106  $\mu\text{m}$  is placed on top of the sulphur disk, the sulphur signal recorded decreases by a factor of 16 and 20, respectively, compared to the intensity when no powder is present on the disk. Furthermore, at Avicel depths  $\geq 5\text{ mm}$ , the Raman signal of sulphur is essentially blocked from reaching the detection system. Owing to the small particles sizes of the Avicel, the particles pack closely together and hence the sulphur Raman photons generated from the bottom layer will collide many times with the tightly packed Avicel particles and many of the Raman photons will fail to propagate through the mass of powder; consequently the sulphur signal is significantly attenuated by only a few millimeters of the powder. Furthermore, as the monitored signal originates exclusively from the bottom layer of the sample, there

are no further opportunities at different depths within the sample for the continued generation of sulphur Raman photons.

The trend observed for the largest Avicel particle size range is surprisingly different to that of the smaller Avicel particle size ranges. Whereas the smaller particles attenuate the sulphur Raman signal significantly even when only shallow depths are used, the detected sulphur Raman signal through 1 mm of Avicel 150-212  $\mu\text{m}$  is approximately five times greater than that seen with the other Avicel size ranges. This occurs because the larger particles are less tightly packed and consequently the powder will attenuate the Raman photons to a lesser extent owing to fewer collisions. Furthermore, the sulphur Raman photons can more readily propagate through a larger depth of powder via the gaps between the particles. Owing to the significant difference in the Raman intensity recorded after 1 mm of Avicel 150-212  $\mu\text{m}$  was placed on the sulphur disk compared to the other Avicel fractions (Figure 26), the Raman spectrum for this configuration was repeated over several days; the data were consistent at each acquisition.

The effect of particle shape on the packing of particles is illustrated when the results for 150-212  $\mu\text{m}$  particles of Avicel and aspirin are compared. At depths of 2-4 mm of powder on the sulphur disk, the sulphur signal seen when using Avicel is approximately 50-75% less than when using the equivalent depth of aspirin. At aspirin depths greater than 4 mm measureable Raman signals are obtained, where as for Avicel there is almost no transmitted Raman intensity. Figure 27 shows digital microscope images of Avicel and aspirin (both 150-212  $\mu\text{m}$ ) taken using a standard Nikon Eclipse TE2000-U microscope. All images were taken with a magnification factor of 150 and recorded using a Nikon CoolPIX 5400, 5.1 mega pixel camera attached through a screw port.

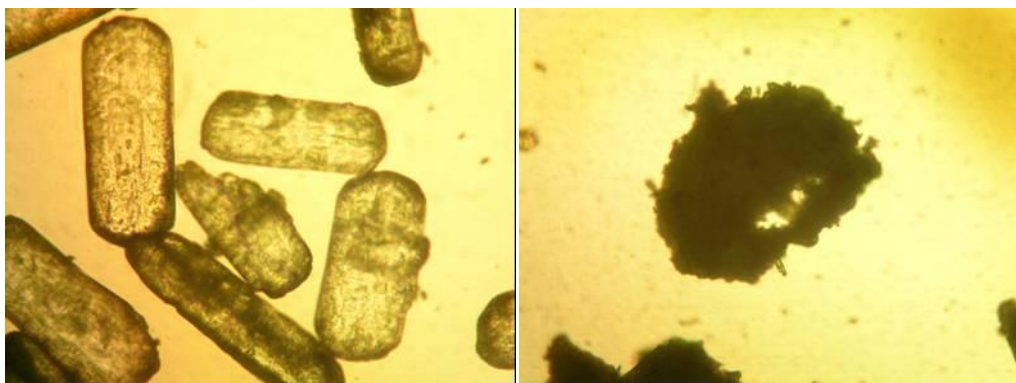


**Figure 27 – Digital microscope images of aspirin 150-212  $\mu\text{m}$  (left) and Avicel 150-212  $\mu\text{m}$  (right) taken using a standard Nikon Eclipse TE2000-U microscope.**

Figure 27 illustrates the different particle shapes of Avicel and aspirin. As aspirin particles are low aspect ratio needles<sup>114</sup> they will pack less efficiently in loose powder than the more granular Avicel particles, consequently, the Raman photons from the sulphur disk will propagate through the depth of aspirin powder more efficiently than with Avicel and hence the detected sulphur Raman signal would be expected to be greater when aspirin is used as the bulk powder, as shown in Figure 26. Based on the results summarised in Figure 26, it was decided to carry out further experiments with a maximum powder depth of 4 mm, resulting in a total sample depth of 5 mm (as shown in Figure 21 and Figure 22).

Repeatability studies were carried out at all powder depths using all materials: six replicate measurements were made without removing the sample (measurement variation), and six replicate measurements were also made removing the sample after each acquisition (positional variation). The results in Table 8 show that there is no detrimental effect on the precision of Raman intensities when the sample is removed and replaced between measurements.

**Table 8 - % CV values for transmission Raman measurement of sulphur at 218 cm<sup>-1</sup>, through Avicel or aspirin powder at depths of 1, 4 and 8 mm, when the sample was left in position (measurement CV) and when it was removed and replaced (positional CV); n=6.**

|                     | Measurement<br>%CV |     | Positional<br>% CV |     |
|---------------------|--------------------|-----|--------------------|-----|
|                     | 1                  | 4   | 1                  | 4   |
| Material depth / mm | 1                  | 4   | 1                  | 4   |
| Avicel 0-38 µm      | 0.3                | 3.3 | 0.2                | 4.3 |
| Avicel 53-106 µm    | 0.1                | 2.8 | 0.1                | 2.1 |
| Avicel 150-212 µm   | 0.3                | 0.1 | 0.4                | 0.2 |
| Aspirin 150-212 µm  | 0.1                | 0.1 | 0.1                | 0.1 |

The results in Table 8 also support the decision to limit the depth of powder on the sulphur disk to 4 mm; although the intensities recorded at 4 mm are small, the % CV values are fairly low, demonstrating robust measurements have been made.

For comparison, the experiments were also carried out in reflectance mode using a 3 mm illumination and collection spot size with the same flowers of sulphur disk and powders as described above. The sample set-up was the same as that used for transmission measurements (see Figure 22, A-E) and the maximum powder depth used was 7 mm. For reflectance mode measurements a 2 s exposure time and 10 acquisitions were used. Figure 28 shows how the reflectance Raman sulphur intensity changes as the depth of powder on the sulphur disk increases and Figure 29 shows a Y-axis expanded version of Figure 28.

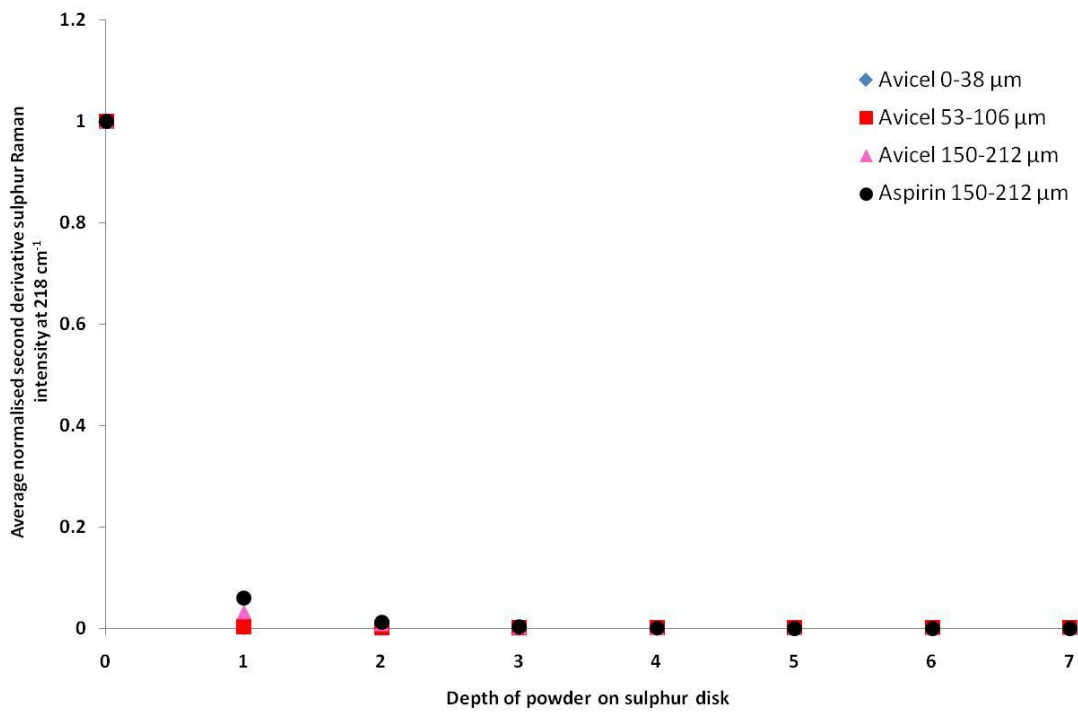


**Figure 28 - Plot of the change in the average normalised second derivative reflectance Raman intensity of the sulphur peak at  $218\text{ cm}^{-1}$  with the increasing depth of bulk powder on the sulphur disk**

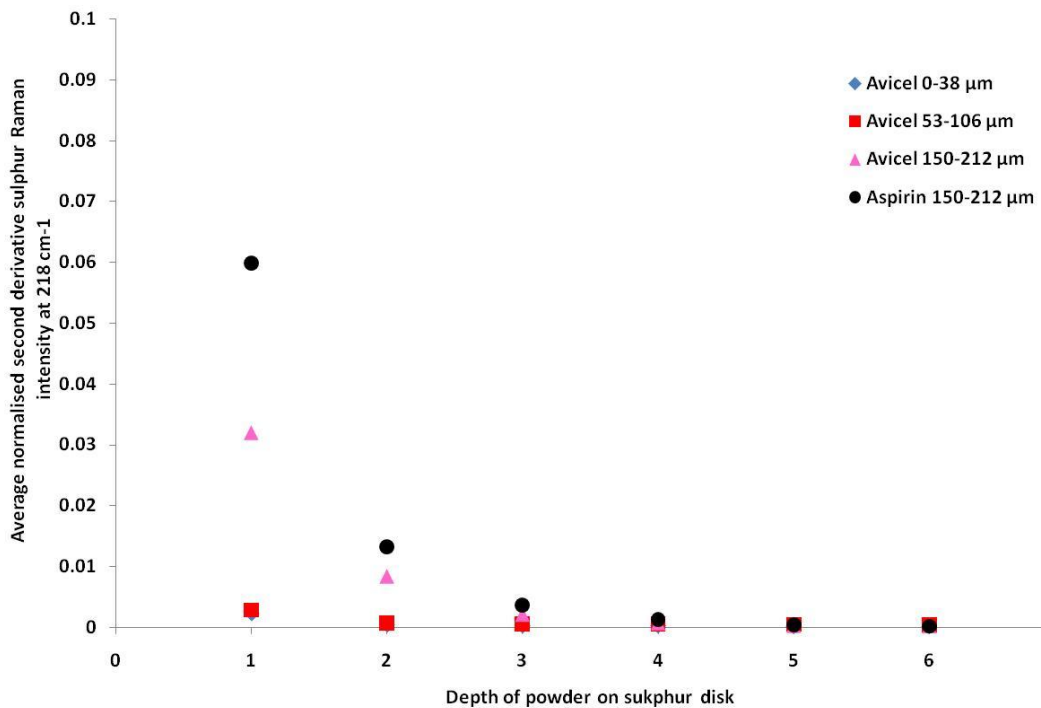


**Figure 29 – Y-axis expanded plot of the change in the average normalised second derivative reflectance Raman intensity of the sulphur peak at  $218\text{ cm}^{-1}$  with the increasing depth of bulk powder on the sulphur disk**

The normalised sulphur Raman signals detected in the reflectance Raman experiments, regardless of the bulk material on top of the sulphur disk are much smaller than those seen when the same depths of powder are used in transmission mode. This arises owing to the different sampling geometries used for transmission and reflectance mode measurements - Figure 30 illustrates these differences.

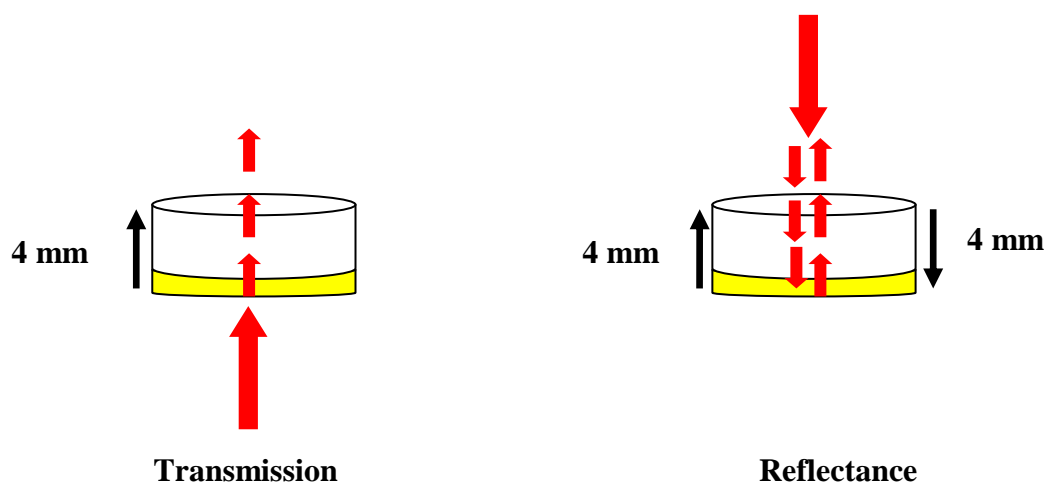


**Figure 30 – Schematic illustrating the propagation path of the laser light and Raman photons in transmission and reflectance Raman spectroscopy through a 4 mm thick bi-layer sample of a 3mm depth of powder (white) and a 1 mm thick pressed flowers of sulphur disk (yellow)**

From Figure 30 it can be seen that in the transmission mode, the laser first strikes the sulphur disk, generating Raman photons which subsequently must propagate through the 3 mm depth of powder to reach the detector. The reflectance geometry however requires the laser to first pass through 3 mm of powder before coming into contact with the sulphur disk and consequently the laser light that strikes the disk will be significantly attenuated by the powder. As a result there will be less efficient excitation of the sulphur disk than in the transmission mode and furthermore, the generated photons must then pass through 3 mm of powder to reach the detector. This therefore accounts for the significantly lower signals seen for the reflectance mode experiments and may also contribute to the difference in particle size effects seen in the two experiments.

Repeatability studies were carried out for the reflectance mode measurements similar to those made in transmission. The results in Table 9 show that there is no significant difference when the sample is moved and replaced, as was also seen with transmission mode measurements. However, owing to the lower intensities measured, the % CV values are considerably higher than shown in Table 8, except for aspirin.

**Table 9 -% CV values for reflectance Raman measurements of sulphur at 218 cm<sup>-1</sup>, through Avicel or aspirin powder at depths of 1, 4 and 7 mm, when the sample was left in position (measurement CV) and when it was removed and replaced (positional CV); n=6.**

|                    | Measurement<br>% CV |      | Positional<br>% CV |      |
|--------------------|---------------------|------|--------------------|------|
|                    | 1                   | 4    | 1                  | 4    |
| Material depth/mm  |                     |      |                    |      |
| Avicel 0-38 µm     | 1.6                 | 21.5 | 4.1                | 20.1 |
| Avicel 53-106 µm   | 0.8                 | 23.8 | 2.8                | 19.9 |
| Avicel 150-212 µm  | 0.2                 | 19.2 | 0.4                | 21.1 |
| Aspirin 150-212 µm | 0.2                 | 2.1  | 0.1                | 1.4  |

#### ***4.3.2 Investigation to assess the effect of the bulk sample on the excitation of the transmission Raman signal and the propagation of the subsequent sample to the collection optics***

To understand more fully the propagation of light in transmission mode through diffusely scattering media, such as pharmaceutical solids, transmission mode experiments were devised to assess the effect of the bulk sample on:

1. The excitation of the Raman signal.
2. The transmission of the Raman signal to the collection optics.

Figure 31 illustrates the sample configurations used for this experiment, each position (P1-P5) was repeated using the four bulk materials and the Raman active layer described in section 4.2.2. As can be seen from Figure 31 the sulphur disk was progressively moved through the entire thickness of the sample in 1 mm increments to assess the resulting effect on the detected sulphur Raman signal. By doing this, the capability of the transmission Raman geometry to detect an ‘impurity’ (in this case a sulphur disk) at different depths within a sample could be assessed whilst establishing the ‘origin’ of the transmission mode signal.

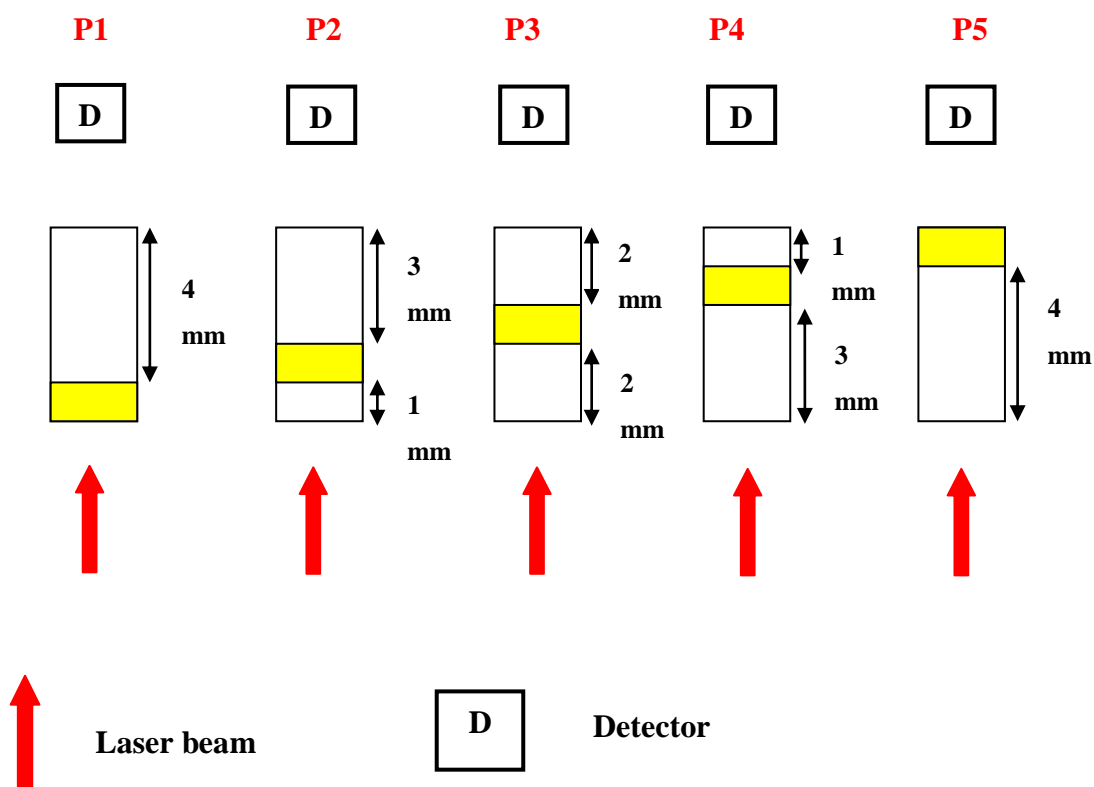
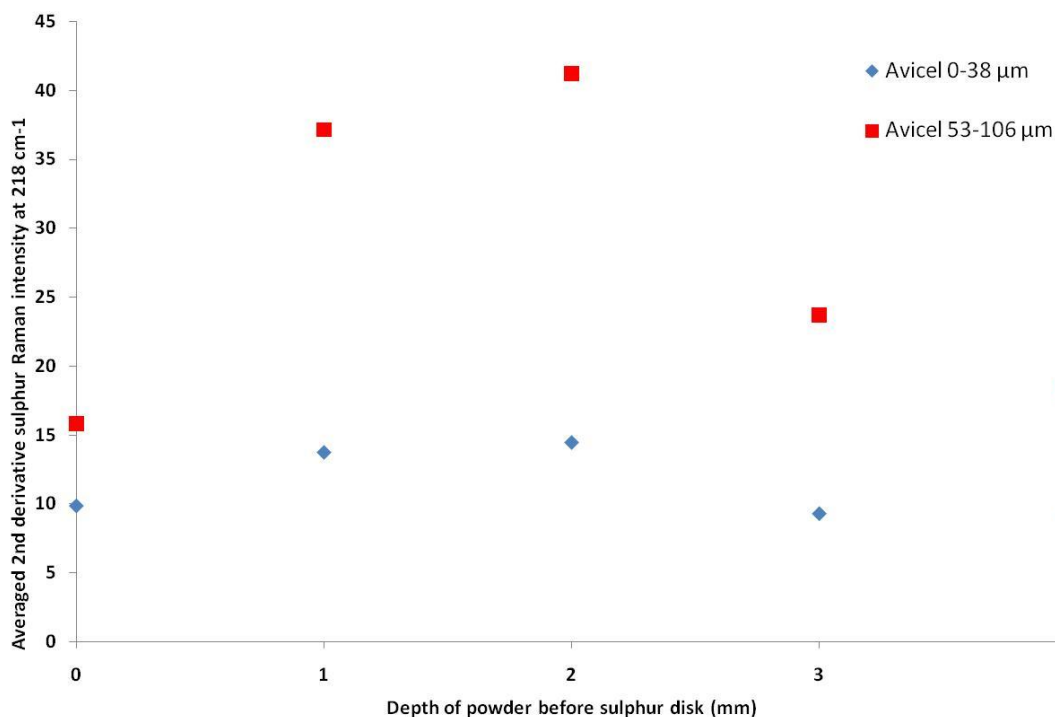


Figure 31 - Sample configuration for transmission mode Raman experiments to assess the effect of the bulk sample (white) on the excitation of the Raman signal of a ‘Raman active layer’ (yellow) and the transmission of the subsequent Raman signal to the collection optics.



Position 1 in Figure 31 allows investigation of the effect of the selected powder on the transmission of the excited Raman spectrum of sulphur. In contrast, P5 permits assessment of the effect of the powder on the exciting intensity that generates the Raman spectrum from the disk. With P2-P4 the powder has an effect on both the intensity of the exciting radiation and the Raman spectrum to different extents. By analysing each position using different materials information was also collected regarding the effect of particle size and shape on the propagation of the Raman signal to the detector. The same normalisation method used previously was applied to the data (refer to 4.3.1). Figure 32 and Figure 33 show how the sulphur Raman intensity changes as the disk is progressively moved through 4 mm of different loose powdered materials. Data points at 0, 1, 2, 3 and 4 mm of loose powder shown in both figures correspond to positions P1, P2, P3, P4 and P5, respectively (see Figure 31). Each data point is an average of three replicate measurements. By following the previously defined protocol the effect of measurement and positional variation was assessed, giving CV values of 1.8% and 1.9%, respectively.



**Figure 32 – Plot of the change in the normalised second derivative transmission sulphur signal at  $218\text{ cm}^{-1}$  as the sulphur disk is progressively moved through 4 mm of Avicel particles in the range 0-38 or 53-106  $\mu\text{m}$**

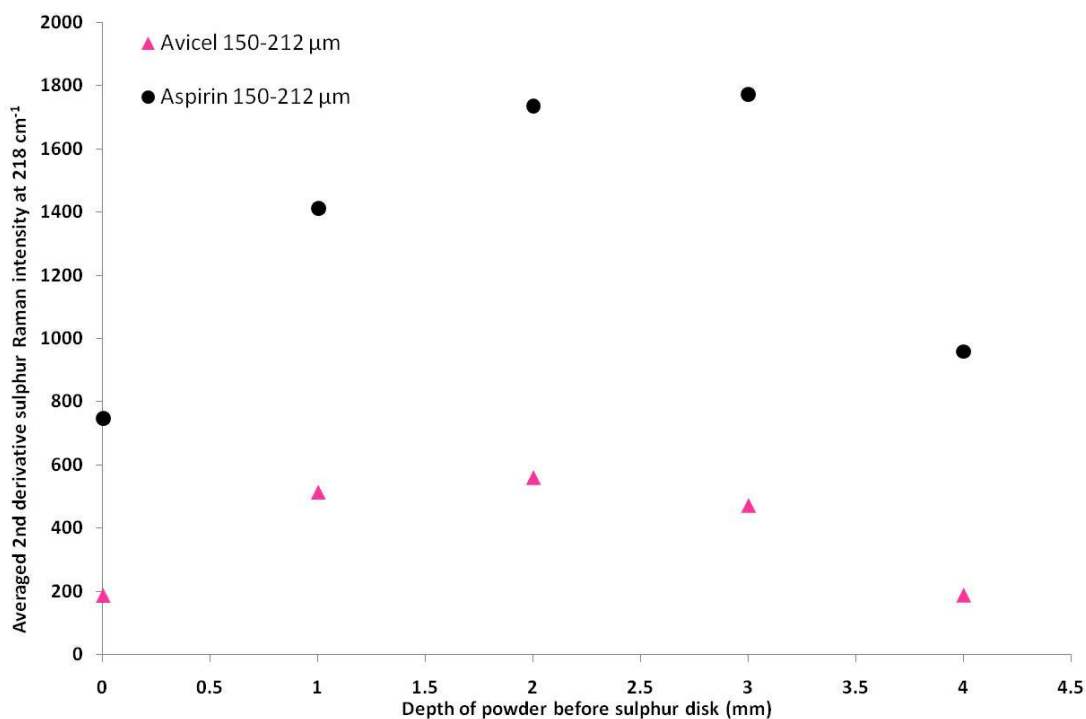


**Figure 33 - Plot of the change in the normalised second derivative transmission sulphur signal at  $218\text{ cm}^{-1}$  as the sulphur disk is progressively moved through 4 mm of Avicel or aspirin particles in the range 150-212  $\mu\text{m}$**

Both figures show that as the sulphur disk is moved through each of the bulk materials, there is a different Raman response at each depth. Each material shows the same basic trend, that is an increase in the Raman intensity of the sulphur disk as it is moved through the powder, reaching a maximum and thereafter the signal intensity decreases. The depth at which the signal reaches a maximum is the same for each size range of Avicel (2 mm), but is slightly greater (3 mm) for aspirin. As would be expected, the larger particle size materials show greater sulphur Raman intensities, which agrees with the observations seen in previous experiments (refer to section 4.3.1). This was also the case in other experiments regarding the penetration power of the sulphur Raman signal through depths of powder and was attributed to the difference in the particle shape of the two materials.

The trends shown in Figure 32 and Figure 33 are a consequence of the effect of the powder on the excitation efficiency and the efficiency of the transmission of the Raman photons to the detector. When the sulphur disk is below the 4 mm depth of powder (P1), there is efficient excitation of the sulphur disk however the generated Raman signal must pass through 4 mm of powder before reaching the detector and in doing so the signal becomes significantly attenuated by the powder. Consequently, the resulting intensity at position 1 will be relatively small. At position 2 the Raman signal of the sulphur disk is greater than at position 1. The 1 mm powder barrier that the laser must penetrate before coming into contact with the sulphur disk will result in less efficient excitation of the disk however, as there is a smaller depth of powder for the generated Raman photons to propagate through, the signal is less attenuated by the powder than in position 1 and consequently an increased signal is observed. At position 3, there is an equal depth of powder above and below the sulphur disk however an increase in the Raman signal is again observed. This therefore suggests that generated Raman photons (although fewer owing to the attenuation of the laser beam by the 2 mm of powder) can more readily penetrate the 2 mm of powder on the surface of the sulphur disk to reach the detector than the 3 mm of powder in position 2.

After position 3, the shape of the profiles in Figure 32 and Figure 33 change, as a decrease in the observed Raman signal is recorded. In position 4, the laser must pass through 3 mm of powder before impacting the sulphur disk. This therefore significantly reduces the laser power striking the disk and consequently attenuates the laser beam resulting in poor excitation of sulphur Raman photons. Despite only having a 1 mm powder barrier to pass through to reach the detector, the smaller number of Raman photons generated results in an overall decrease in the Raman signal. Position 5 is similar to position 4 – the excitation efficiency of the sulphur disk will be severely hampered owing to the high degree of attenuation of the laser beam and so the unblocked pathway between the surface of the sulphur disk and the detector is not advantageous as the generated Raman signal is so weak that fewer Raman photons are detected and the signal therefore decreases.

In 2006, Matousek and Parker used Monte Carlo simulations to determine how the transmission Raman signal would be affected by a moving inter-layer within a bulk medium (section 4.1 details the assumptions that were used to generate the model). This study reported that for the transmission Raman geometry there is only a weak dependence of the Raman signal on the position of the active layer within the sample. Furthermore, it was reported that between depths of 0 to 3.5 mm, the Raman signal of the interlayer varied only by a factor of two; this finding was supported by the present study which reports a Raman signal variation of less than a factor of three over the same interlayer depths. The simulated plots also showed an overall decreasing trend of the Raman intensity after the signal maximum (0.5 mm), as the depth of the inter-layer through the sample increased, in contrast to the more regular ‘parabolic’ profile reported in this study<sup>59</sup>. The current study shows a gradual increase in the intensity of the sulphur disk to the maximum value (at 2 mm) as it is moved through the 4 mm depth of bulk powder, conversely, despite carrying out a similar study, Matousek and Parker reported a signal maximum at a much shallower depth of 0.5 mm .

The differences in the trends could potentially be attributed to a number of variations between the two studies, namely material and wavelength differences. The materials used in the current study (Avicel and aspirin) have densities of 0.32 g/mL and 1.40 g/mL, respectively<sup>114</sup> and the density of trans-stilbene, used in the study by Matousek and Parker lies in between these values, at 0.97 g/mL<sup>115</sup>. From Figure 33 it can be seen that the inter-layer depths at which the maximum sulphur intensity is seen differ slightly when aspirin is used instead of Avicel (3 mm and 2 mm, respectively), despite both materials having the same particle size range of 150-212  $\mu\text{m}$ . As aspirin and Avicel do not have similar densities, the difference seen in the depth at which the maximum signal intensity is reached, could be a consequence of this. From Figure 33 it can be seen that the depth at which the maximum Raman signal is reached increases as the density of the bulk material increases and hence as the density of trans-stilbene is in between that of Avicel and aspirin, it would be expected that a signal maximum, when using trans-stilbene, would lie between 2 and 3 mm (assuming density is a contributing factor) - this however was not found to be the case by Matousek and Parker.

In addition to using different materials, both studies differ with respect to the laser irradiation wavelengths used and the regions of the Raman spectrum that are of interest. The present study utilised a 785 nm laser to investigate the response of a sulphur peak at  $218\text{ cm}^{-1}$ , which equates to a wavelength of 798.6 nm. The Matousek and Parker study utilised an 827 nm laser to investigate spectral regions between  $900$  and  $1700\text{ cm}^{-1}$ , consequently the Stokes Raman peaks of interest corresponded to wavelengths between 893 and 926 nm. Bellamy et al. demonstrated that the information depth of NIR radiation increased with increasing wavenumber (decreasing wavelength), owing to the greater extent of absorption at lower wavenumbers (higher wavelengths)<sup>116</sup>. The shallow depth at which the signal maximum is seen in the study by Matousek and Parker could therefore be a consequence of the wavelengths used in the study, exhibiting a greater extent of absorption than would be expected in the current study which utilised shorter wavelengths and hence would benefit from greater penetration depths. Furthermore, it is important to highlight that a major difference between the studies is the method

by which the data was acquired. The present study reports physically acquired experimental data whereas Matousek and Parker report simulated data derived from a number of assumptions.

Despite the differences discussed, the two studies show a number of similarities. Both reported trends show that when the interlayer is sandwiched between a bulk medium, with both faces of the interlayer in contact with the bulk medium (refer to Figure 31, P2 to P4), the recorded Raman intensity of the inter-layer is greater at all the depths studied compared to the intensity seen when only one face of the inter-layer is in contact with the bulk sample (refer to Figure 31, P1 and P5, Figure 32 and Figure 33). This supports the suggestion that the trends shown in Figure 32 and Figure 33 are a consequence of the relationship between the excitation efficiency of the Raman active layer and the propagation of the generated Raman signal to the collection optics. Nevertheless, the trends from both studies suggest that the depth of powder between the Raman active layer and the collection optics is the dominant parameter in affecting the success of photon collection. From Figure 33 it can be seen that as the depth of powder through which the laser must pass before reaching the sulphur disk is increased and by default the depth of powder between the sulphur disk and the collection optics is decreased, the Raman signal of the sulphur disk is always greater than that recorded in position 1 or position 5. This shows that despite the presence of powder impeding the excitation efficiency of the sulphur disk, the dominating factor is the ability of the Raman signal to pass to the detector and hence, the configuration of the upper section of the sample. As previously indicated, this is not the case for when the sample is analysed in position 1 or position 5; this suggests that a 4 mm depth of powder, regardless of its position on the disk, hinders the excitation of the disk or the collection efficiency of the Raman photons more significantly than when the depth of powder encompasses the disk therefore providing a less significant barrier to both processes rather than a large barrier to one. These results suggest a significant dependence of the Raman signal on the sulphur disk position – the opposite conclusion to that drawn in 2006<sup>59</sup>.

Despite carrying out a similar study to that reported in this thesis, Matousek and Parker did not assess the effect of the material properties on the tested system; their study investigated the effects of one material on the transmission Raman signal<sup>59</sup>. The current study investigates the effects of the particle size and shape of two materials therefore providing a more rigorous assessment. From Figure 32 and Figure 33, it can be seen that the intensity of the sulphur disk varies by a factor of approximately 1.5, 2.6, 3.0 and 2.4 when using Avicel 0-38, 53-106, 150-212  $\mu\text{m}$  and aspirin 150-212  $\mu\text{m}$ , respectively and hence confirms that particle size of the material affects the propagation of light in transmission mode Raman measurements. The effect of particle size was not investigated by Matousek and Parker in their study<sup>59</sup>. Despite both aspirin and the largest Avicel fraction having the same particle size range, the variation in the Raman signal of the sulphur layer is different for both materials, which suggests an effect of particle shape; the packing in loose powders is dependent upon the shape and size of the particles. The intensity of the sulphur layer varies more when Avicel 150-212  $\mu\text{m}$  is used as the bulk medium and the intensity variation seen when aspirin is used is in fact more similar to that attained with the Avicel 53-106  $\mu\text{m}$  fraction. Nevertheless, the magnitude of the Raman intensities shown in Figure 32 and Figure 33 for both of these materials are very different.

In addition to simulated data, Matousek and Parker also discussed experimental data that was physically acquired in the 2006 study; the transmission Raman signal of the same sample used in the simulated experiments was acquired, when the interlayer was positioned on the top and the bottom of the bulk sample<sup>59</sup> (refer to Figure 31 P1 and P5 for analogous configurations). Data showed that transmission mode measurements could not distinguish between the two geometries, giving very similar signal intensities for both sample configurations. This finding is supported by data presented in the current study. Figure 32 and Figure 33 show that when Avicel (all particle sizes) is used as the bulk medium, regardless of whether the sulphur disk is on the bottom or the top of the sample (position 1 and position 5, respectively) the Raman signal is the same and clearly identifiable. This however was not seen when aspirin was used as the bulk medium, the signal recorded at position 5 was greater than that for position 1 but still less than the intensity acquired at position 4; the

different trend seen for aspirin could be attributed to the difference in the particle shape of the material. The trends seen with Avicel however, demonstrate the ability of the transmission mode geometry to detect equally the presence of an ‘impurity’ irrespective of its location, front or back of the sample. Although this was also demonstrated by Matousek and Parker, they also stated that as a consequence of their reported results, the transmission Raman geometry exhibited a gross insensitivity to the location of the ‘impurity’ or inter-layer<sup>59</sup>. This statement is not supported by the findings of the present study which clearly shows (refer to Figure 32 and Figure 33) that the position of an inter-layer of a different Raman signature to that of the bulk material of the sample, will significantly affect the Raman signal observed as the depth of the inter-layer is altered.

#### **4.3.3 *Calculation of the attenuation of the laser beam***

From the schematics in Figure 22 it can be seen that sample configurations A to E investigate the decay of the Raman signal generated from the sulphur disk as the Raman photons propagate through the increasing depth of powder on the disk; the resulting decay profiles have been plotted and can be seen in Figure 25 and Figure 26. The Raman response generated from sample configurations P2 to P4 (Figure 21 and Figure 31) will be a combined effect of the attenuation of the laser beam by the depth of powder before the sulphur disk and also the decay of the generated Raman signal as it passes through the remaining powder. By comparing the correct sample configuration describing the decay of the Raman signal with the corresponding ‘combined effect’ sample configuration, the attenuation of the laser by the depth of powder below the sulphur disk can be determined.



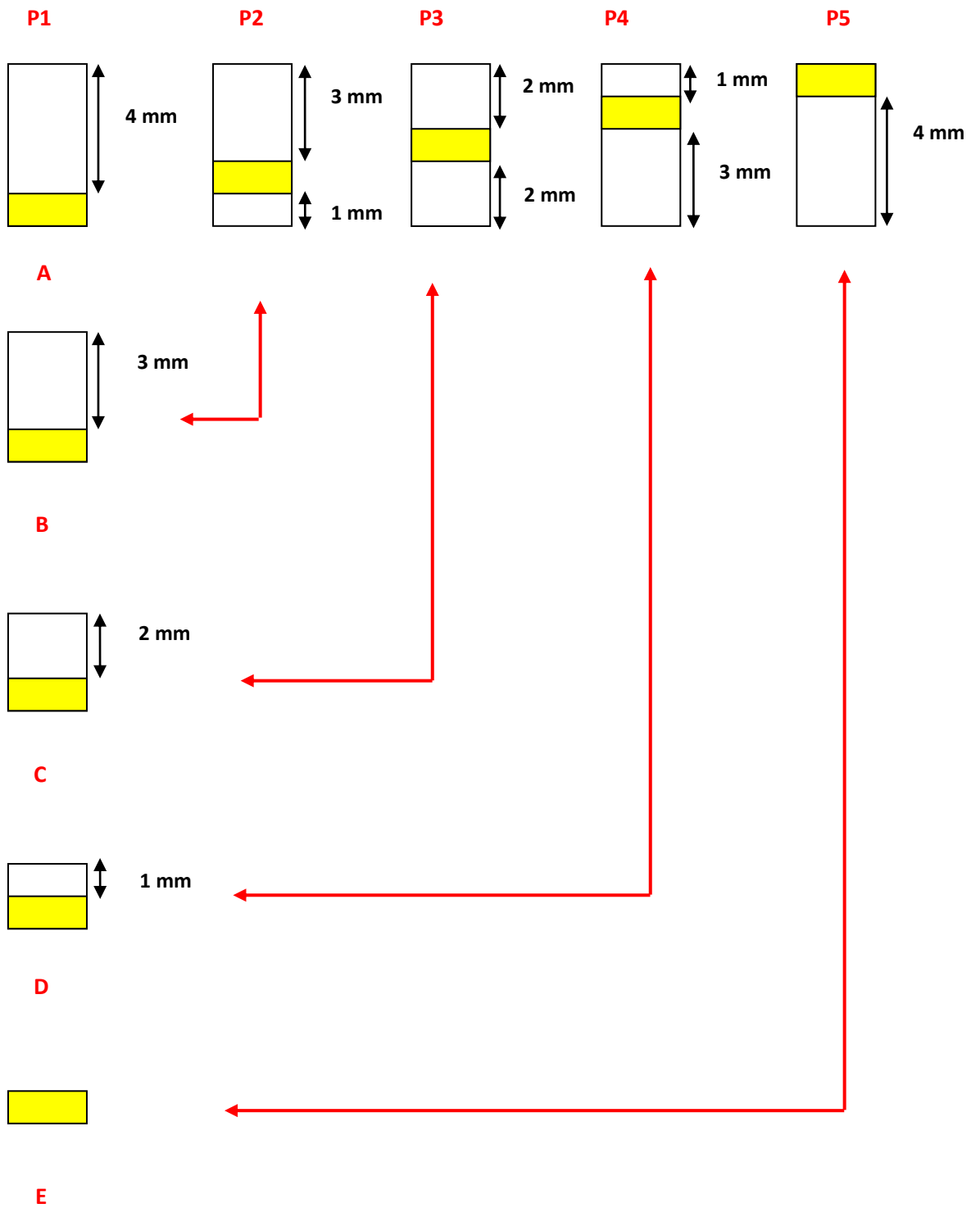


Figure 34 – Schematic highlighting the sample configurations to be compared in order to calculate the attenuation of the laser beam by the depth of powder (white) below the sulphur disk (yellow).

Figure 34 shows the sample configurations that should be compared. For example, a comparison of configurations P2 and B can be made; configuration P2 differs from B only by a 1 mm depth of powder before the sulphur disk. By comparing these two configurations, the effect of this powder on the laser light can be calculated. Similarly, the difference between configuration E and P5 is the presence of 4 mm of powder before the sulphur disk hence comparing these two configurations will allow the effect of 4 mm of powder on the laser intensity to be calculated. Furthermore, Figure 34 shows that in both sets of sample configurations, the common factor is sample configuration P1 or A. Consequently, it was decided that all Raman intensities acquired from experiments utilising configurations P1 to P5 would be normalised to P1 and similarly, data acquired using samples A to E would be normalised to position A. This is illustrated in Table 10 and Table 11 for Avicel particles in the range 150-212  $\mu\text{m}$ , for positions A-E and P1 – P5, respectively. For the purpose of this chapter, experimental configurations P1 to P5 will be referred to as ‘combined intensity’ and configurations A to E, ‘Raman decay intensity’.

**Table 10 – Data corresponding to the change in the sulphur Raman signal as the depth of Avicel 150-212  $\mu\text{m}$  on the disk is increased**

| Depth of Avicel 150-212 $\mu\text{m}$ on the sulphur disk (mm) | Sample configuration identity (refer to Figure 34) | Average 2 <sup>nd</sup> derivative sulphur Raman intensity at 218 $\text{cm}^{-1}$ | Normalised average 2 <sup>nd</sup> derivative sulphur Raman intensity* |
|--|--|--|--|
| 0  | E  | 12743.17   | 84.80  |
| 1  | D  | 3493.75  | 23.25  |
| 2  | C  | 1055.82  | 7.03   |
| 3  | B  | 395.22   | 2.63   |
| 4  | A  | 150.263  | 1  |

\*Data normalised to position A.

**Table 11 - Data corresponding to the change in the sulphur Raman signal as the sulphur disk is moved through the 4 mm depth of Avicel 150-212  $\mu\text{m}$**

| Depth of Avicel 150-212 $\mu\text{m}$ below the sulphur disk (mm) | Sample configuration identity (refer to Figure 34) | Average 2 <sup>nd</sup> derivative sulphur Raman intensity at 218 $\text{cm}^{-1}$ | Normalised average 2 <sup>nd</sup> derivative sulphur Raman intensity* |
|---|--|--|--|
| 0   | P1   | 188.37   | 1  |
| 1   | P2   | 515.50   | 2.74   |
| 2   | P3   | 561.22   | 2.98   |
| 3   | P4   | 473.09   | 2.51   |
| 4   | P5   | 189.64   | 1.01   |

\*Data normalised to position 1.

To calculate the attenuation of the laser by the powder (referred to as corrected intensity, CI) the following equation was used.

$$CI = \frac{\text{Norm. intensity of } E}{\text{Norm. Raman decay intensity } X} \times \text{Norm. combined intensity } Y \quad (21)$$

where,

X is the sample configuration identity (A to E)

Y is the sample configuration identity (P1 to P5)

An example is detailed below, comparing sample configurations P2 and B using Avicel 150-212  $\mu\text{m}$  as the bulk material:

$$CI = \frac{\text{Norm. intensity of } E}{\text{Norm. Raman decay intensity } B} \times \text{Norm. combined intensity } P2$$

Therefore by substituting the corresponding values from Table 10 and Table 11,

$$CI = \frac{84.8}{2.63} \times 2.74 = 88.35$$

These calculations were carried out for all sample combinations – P1 and A, P3 and C, P4 and D and P5 and E.

**Table 12 – Calculated corrected intensity values using Avicel 150-212 µm as the bulk medium**

| Sample configurations being compared (refer to Figure 34) | Depth of Avicel 150-212 µm below the sulphur disk (mm) | Calculated corrected intensity values |
|---|--|---------------------------------------|
| P1 and A  | 0  | 84.81                                 |
| P2 and B  | 1  | 88.24                                 |
| P3 and C  | 2  | 35.96                                 |
| P4 and D  | 3  | 9.16                                  |
| P5 and E  | 4  | 1.01                                  |

The calculated corrected intensity values in Table 12 were normalised to P1(84.81) and are shown in Table 13. Similarly, the normalised intensities corresponding to the Raman decay experiments (refer to Table 10 column 4) were normalised to position A (84.80) and the values are given in Table 14. This additional normalisation allowed a comparison of the decay of the sulphur Raman signal and the attenuation of the laser light by the powder to be made.

**Table 13 – Normalised calculated corrected intensity values corresponding to the attenuation of the laser beam by Avicel 150-212  $\mu\text{m}$**

| Sample configurations being compared (refer to Figure 34) | Depth of Avicel 150-212 $\mu\text{m}$ below the sulphur disk (mm) | Normalised calculated corrected intensity values* |
|---|---|---|
| P1 and A  | 0   | 1   |
| P2 and B  | 1   | 1.04  |
| P3 and C  | 2   | 0.42  |
| P4 and D  | 3   | 0.11  |
| P5 and E  | 4   | 0.01  |

\*Data normalised to P1

**Table 14 - Normalised calculated Raman intensity values corresponding to the decay of the sulphur Raman signal as it passes through increasing depths of Avicel 150-212  $\mu\text{m}$**

| Sample configuration identity (refer to Figure 21) | Depth of Avicel 0-38 $\mu\text{m}$ on the sulphur disk (mm) | Normalised calculated Raman intensity corresponding to decay of Raman signal* |
|--|---|---|
| E  | 0   | 1   |
| D  | 1   | 0.27  |
| C  | 2   | 0.08  |
| B  | 3   | 0.03  |
| A  | 4   | 0.01  |

\*Data normalised to E

The same exercise was completed for the data obtained for each powder (Avicel and aspirin). Figure 35 shows a comparison of the calculated attenuated laser intensities for all materials (this is based on the data in Table 13 and similar information derived for the other powders).

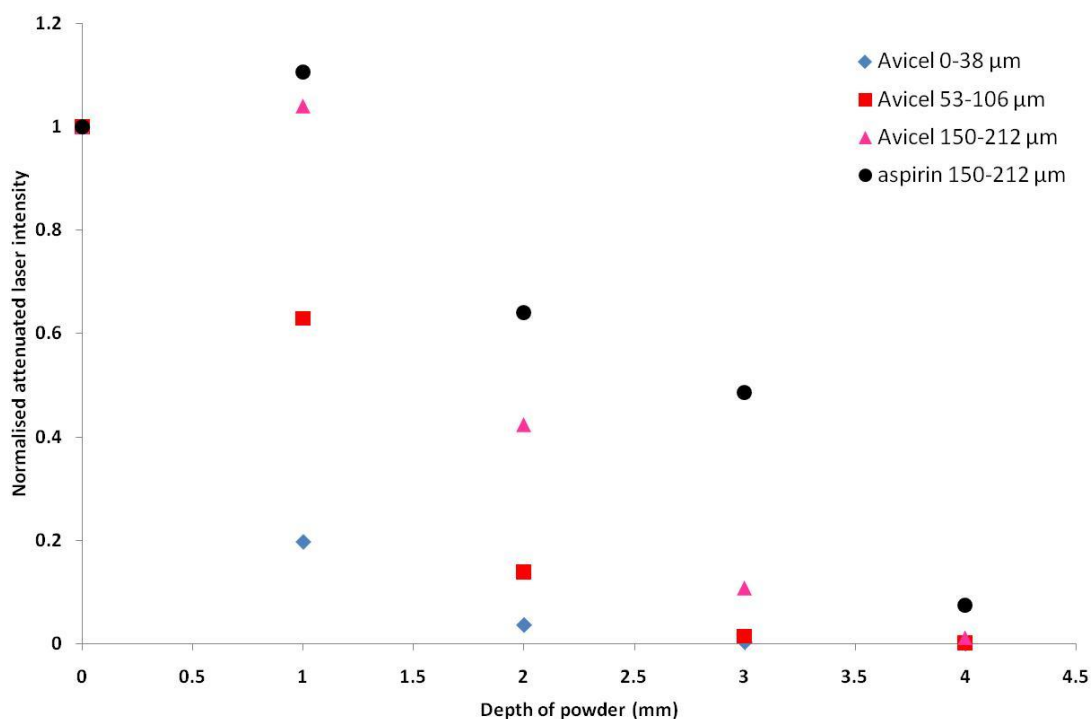


**Figure 35 – Plot showing the degree of attenuation of the laser when passing through increasing depths of powders of different particle size ranges**

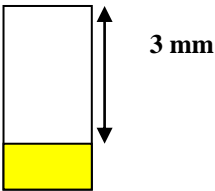
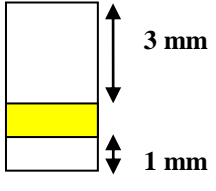
Figure 35 shows that the laser is significantly attenuated when passing through increasing depths of powder and that the extent to which the laser light is attenuated is dependent on the particle size of the material through which it is travelling. For example, after the laser light has passed through 3 mm of Avicel 150-212 µm, the intensity seen is 89% less than when there is no powder for the laser to pass through. When smaller Avicel particles are used (53-106 µm), the laser light is almost entirely attenuated by the 3 mm of powder – the calculated intensity is 99% less than when no powder is present.

Furthermore, Figure 35 illustrates the same trend that was seen in Figure 26 regarding Avicel and aspirin particles in the range 150-212 µm. Despite having the same particle size range, the degree of attenuation of the laser is significantly different when it passes through both materials (at depths greater than 1 mm). After passing through 3 mm of Avicel (150-212 µm), the laser has been attenuated by 89% whereas after passing through the same depth of aspirin, the laser is attenuated by

only 51% (relative to the laser intensity when no powder is present). This therefore supports the suggestion made in previous sections that owing to the difference in the packing efficiency of the granular Avicel and needle aspirin particles, light will propagate through these materials differently; the more tightly packed Avicel particles hinder the penetration of the photons through the material more than the less ordered and more loosely packed aspirin particles.

When comparing sample configurations P2 and B, it was found that, as would be expected, the Raman intensities recorded for configuration P2 were smaller than those for configuration B when Avicel 0-38 and 53-106  $\mu\text{m}$  were used as the bulk materials. Conversely, when Avicel 150-212  $\mu\text{m}$  and aspirin were used there was little difference seen between the intensities recorded for each sample configuration (see Table 15). When the laser radiation impinges on the sample some of the photons will be reflected (specular reflection) and some will suffer diffuse reflection and pass through the gaps in the particles (see Figure 36). It is possible that with 1 mm of the larger particles (150-212  $\mu\text{m}$  Avicel or aspirin) there is less specular reflection than occurs when the laser impinges directly on the sulphur disk, together with minimal attenuation such that the effective exciting intensity that reaches the disk is similar to that for configuration B (see Table 15). With 1 mm of smaller sized particles in configuration P2, closer packing of the particles result in increased specular reflection and greater attenuation of the photons, causing a lower effective exciting intensity than the equivalent configuration B arrangement.

**Table 15 – Comparison of the normalised second derivative sulphur Raman intensities recorded for sample configurations P2 and B, using different bulk materials**

| Material through which laser propagates | Normalised second derivative sulphur Raman intensity of sample configuration B<br> | Normalised second derivative Raman intensity of sample configuration P2<br> |
|---|---|--|
| Avicel 0-38 $\mu\text{m}$               | 7.1   | 1.4  |
| Avicel 53-106 $\mu\text{m}$             | 3.7   | 2.4  |
| Avicel 150-212 $\mu\text{m}$            | 2.6   | 2.7  |
| Aspirin 150-212 $\mu\text{m}$           | 1.7   | 1.9  |

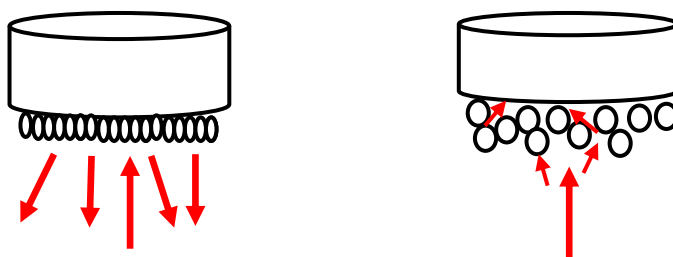


**Figure 36 – Schematic illustrating the effect of material particle size on the propagation path of the laser light (red arrows). Small particles (left), large particles (right).**

Figure 37 and Figure 38 show Y-axis expanded plots comparing the attenuation of the laser beam and the decay of the sulphur Raman signal with the increasing depth of Avicel 0-38 and 53-106  $\mu\text{m}$ , respectively. Figure 39 and Figure 40 show full scale plots comparing the attenuation of the laser beam and the decay of the sulphur Raman signal with the increasing depth of Avicel and aspirin 150-212  $\mu\text{m}$ ,



respectively. The plots for the attenuation of the laser radiation are taken from Figure 35.

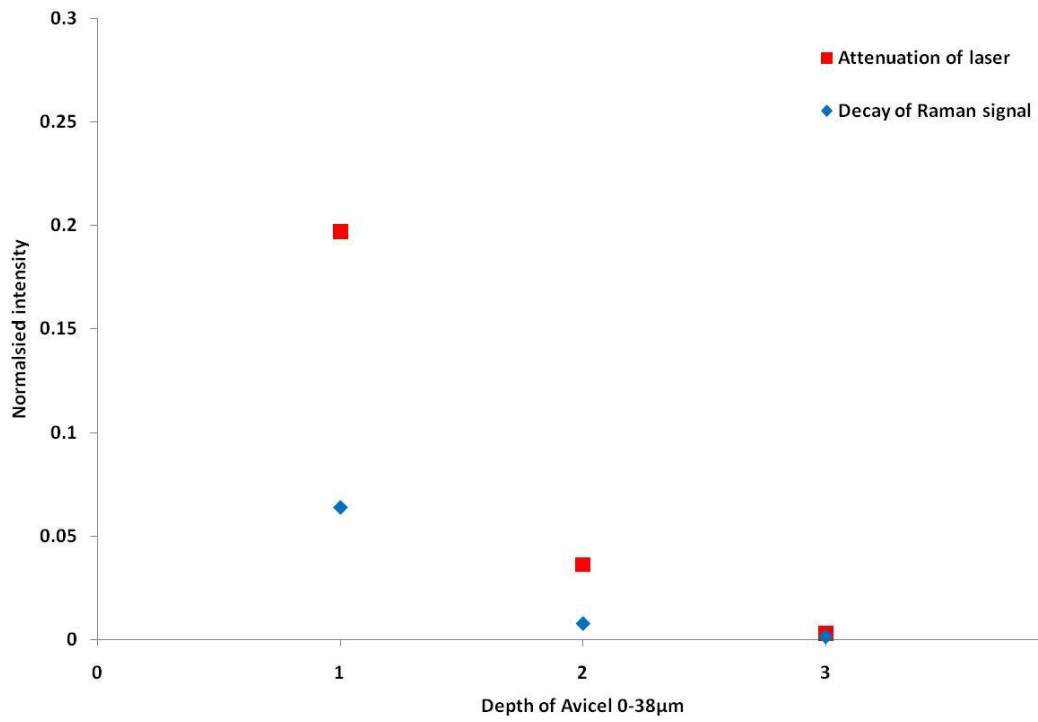


**Figure 37 – Y-axis expanded plot comparing the laser attenuation and decay of the Raman signal in transmission mode when Avicel 0-38 µm is used**

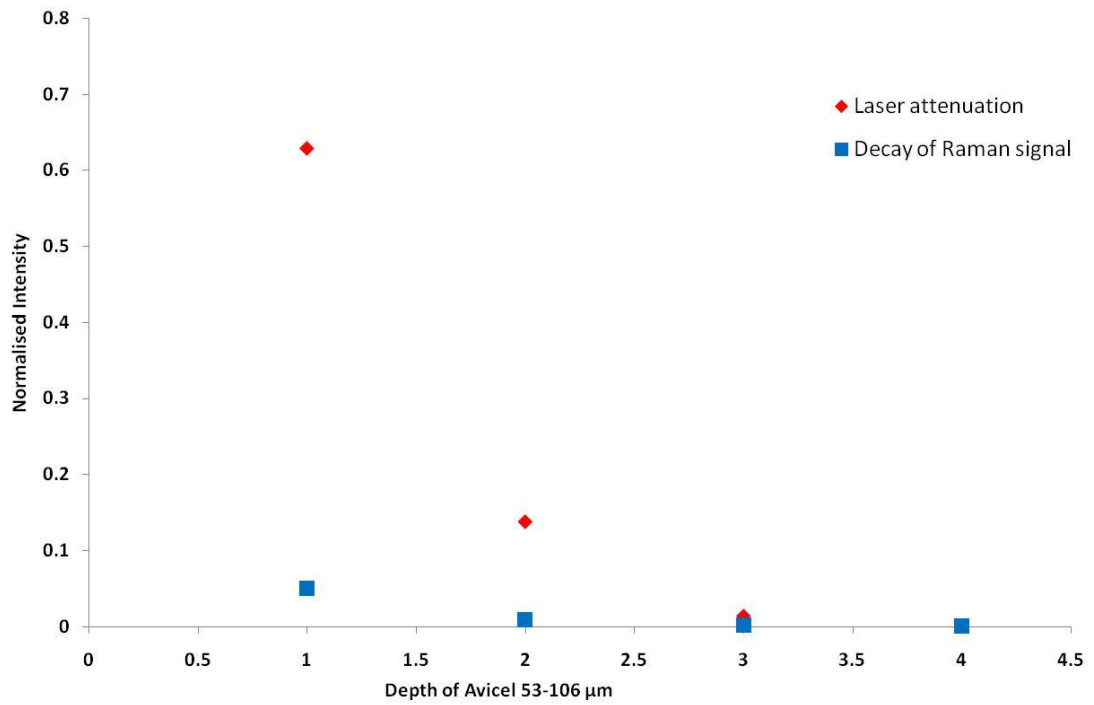


**Figure 38 - Y-axis expanded plot comparing the laser attenuation and decay of the Raman signal in transmission mode when Avicel 53-106 μm is used**

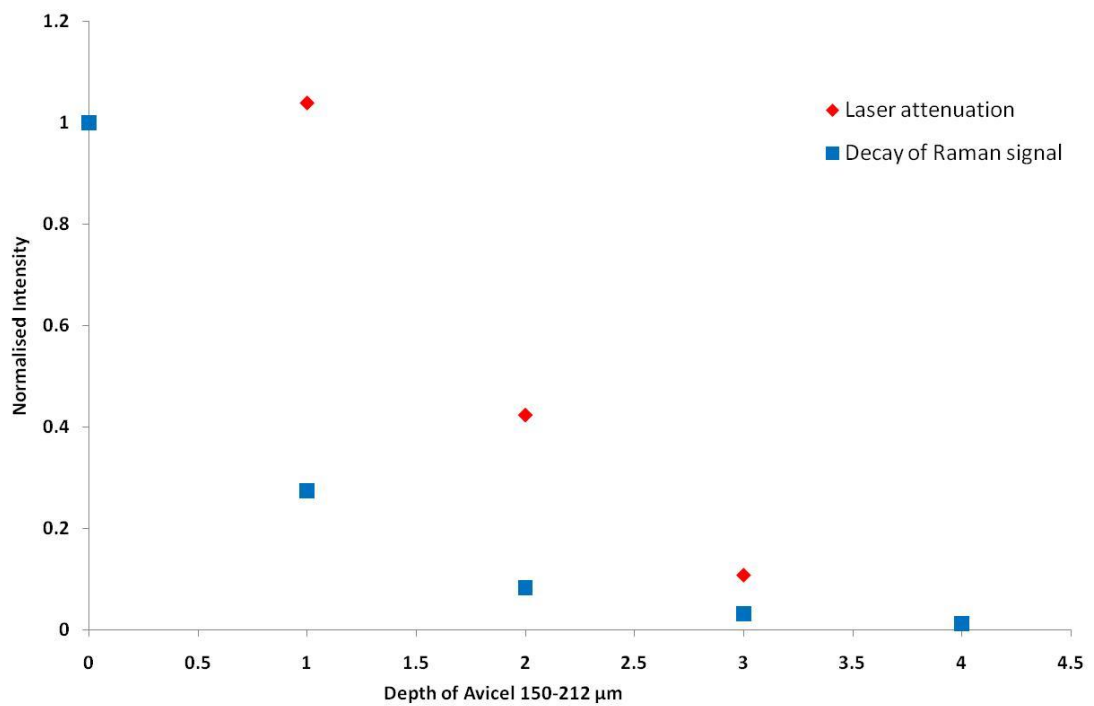


**Figure 39 - Plot comparing the laser attenuation and decay of the Raman signal in transmission mode when Avicel 150-212 μm is used**

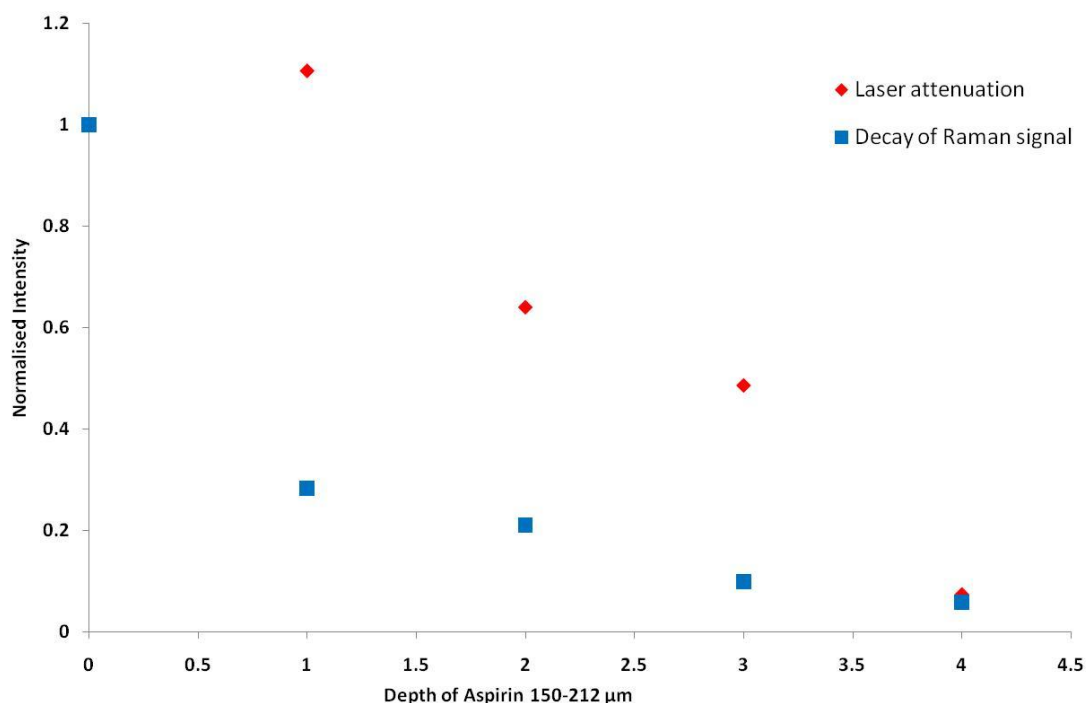


**Figure 40 - Plot comparing the laser attenuation and decay of the Raman signal in transmission mode when aspirin 150-212  $\mu\text{m}$  is used**

From the plots in Figure 37 to Figure 40 it is clear that the attenuating effect of 1 mm of powder on the decay of the Raman signal is much greater than the effect on the laser attenuation. The presence of the powder between the disk and the detector means that the collection of the Raman photons will be less efficient than if the powder was not present, as a large number of the photons will be scattered by the powder in many directions out with the collection area. However, as indicated in Table 16 and Table 17, for powder depths greater than 1 mm the percentage change in the signal is more similar for the attenuation of the laser and Raman intensities for each additional mm of powder.

**Table 16 - % change in the calculated laser intensity as the depth of Avicel or aspirin powder below the sulphur disk is increased (the % changes are based on the effect of the next mm of powder on the measured intensity).**

| Depth of powder below the sulphur disk (mm) | % change in laser intensity using Avicel<br>0-38 $\mu\text{m}$ | % change in laser intensity using Avicel<br>53-106 $\mu\text{m}$ | % change in laser intensity using Avicel<br>150-212 $\mu\text{m}$ | % change in laser intensity using aspirin<br>150-212 $\mu\text{m}$ |
|---|--|--|---|--|
| 0   | 0  | 0  | 0   | 0  |
| 1   | <b>-80</b>   | <b>-37</b>   | <b>+4</b>   | <b>+11</b>   |
| 2   | -81  | -78  | -59   | -42  |
| 3   | -92  | -90  | -77   | -24  |
| 4   | -94  | -96  | -89   | -85  |

**Table 17 - % change in the sulphur Raman signal at 218  $\text{cm}^{-1}$  as the depth of Avicel or aspirin powder below the sulphur disk is increased (the % changes are based on the effect of the next mm of powder on the measured intensity).**

| Depth of powder on the sulphur disk (mm) | % change in sulphur Raman signal using Avicel<br>0-38 $\mu\text{m}$ | % change in sulphur Raman signal using Avicel<br>53-106 $\mu\text{m}$ | % change in sulphur Raman signal using Avicel<br>150-212 $\mu\text{m}$ | % change in sulphur Raman signal using aspirin<br>150-212 $\mu\text{m}$ |
|--|---|---|--|---|
| 0  | 0   | 0   | 0  | 0   |
| 1  | <b>-94</b>  | <b>-95</b>  | <b>-73</b>   | <b>-72</b>  |
| 2  | -88   | -82   | -70  | -26   |
| 3  | -83   | -81   | -62  | -53   |
| 4  | -85   | -73   | -65  | -41   |

The data shown in Table 16 and Table 17 suggests that the decay of the Raman signal and the laser light is essentially the same for each material through which the photons pass after the first mm. This is supported by plots of the natural logarithm of the intensity versus powder depth shown in Figure 41 and Figure 42 for the laser and Raman intensities, respectively, which provide decay constants derived from the slopes of the plots of ln intensity versus depth of powder.

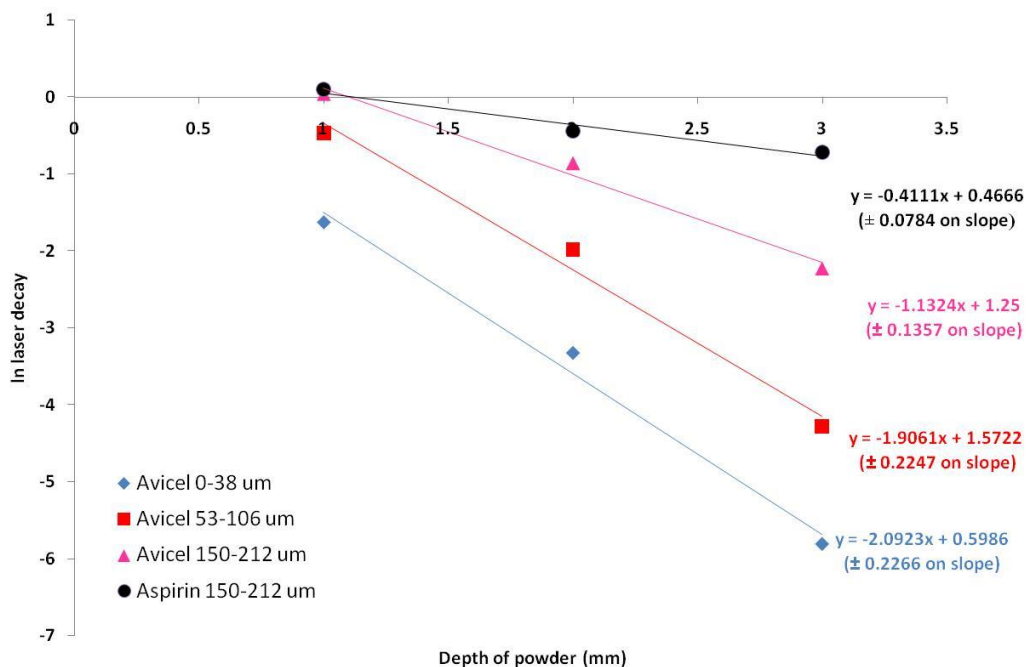
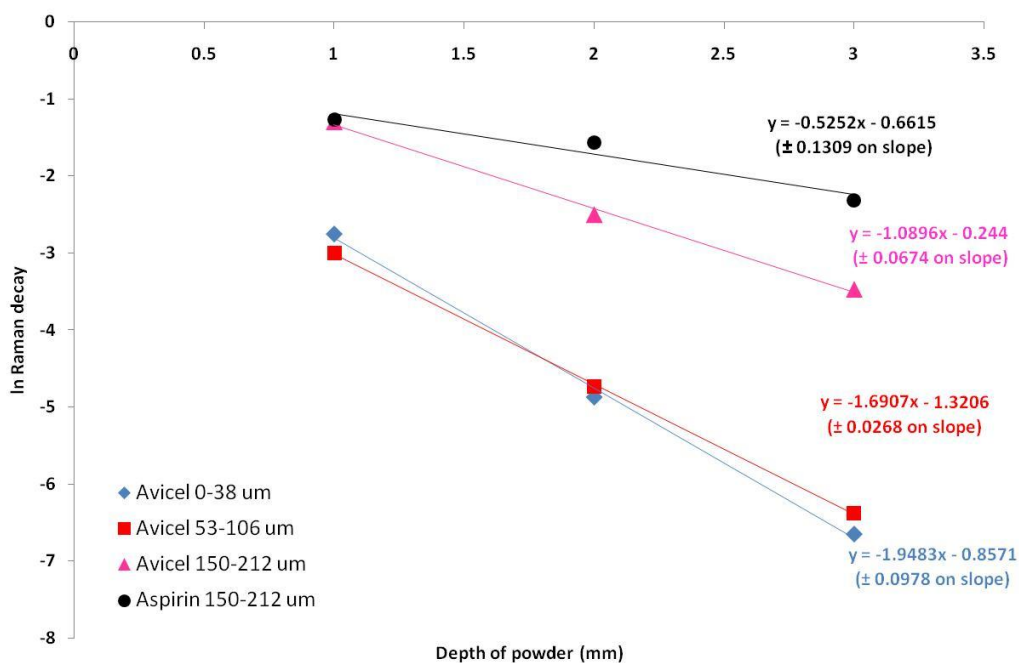


Figure 41 – Plot showing the change in the log of the calculated laser intensity with the increasing depth of powder under the sulphur disk



**Figure 42 - Plot showing the change in the log of the transmission Raman intensity at  $218 \text{ cm}^{-1}$  with the increasing depth of powder on the sulphur disk**

The slope of the plots from Figure 41 and Figure 42 are tabulated in Table 18 along with the error in each slope calculated using the Linest function in Excel. For each material, the slopes of the data points for both the laser and Raman decay are similar, supporting the conclusion that for the system analysed, the rate of decay of the laser and Raman photons is essentially the same after the initial 1 mm of powder.

**Table 18 – Slope of plots and associated errors calculated from the change in the natural log of the laser intensity and Raman intensity with the increasing depth of powder under the sulphur disk**

| Material                      | Slope of laser intensity (Figure 41) | Error of slope measurement | Slope of Raman intensity (Figure 42) | Error of slope measurement |
|-------------------------------|--------------------------------------|----------------------------|--------------------------------------|----------------------------|
| Avicel 0-38 $\mu\text{m}$     | -2.1                                 | 0.23                       | -1.9                                 | 0.1                        |
| Avicel 53-106 $\mu\text{m}$   | -1.9                                 | 0.22                       | -1.7                                 | 0.03                       |
| Avicel 150-212 $\mu\text{m}$  | -1.1                                 | 0.14                       | -1.1                                 | 0.07                       |
| aspirin 150-212 $\mu\text{m}$ | -0.4                                 | 0.08                       | -0.5                                 | 0.13                       |

The greater decay rates seen with smaller particles compared larger particles can be attributed to the packing efficiencies of the materials: smaller particles pack more tightly and hence will attenuate the Raman and laser photons more significantly than larger particles which pack less efficiently, with more gaps between the particles, allowing photons to bounce, achieving greater penetration into the sample (refer to Figure 36). Furthermore, the data in Table 18 indicates that particle shape has a major effect on the decay constant with the slope values for 150-212  $\mu\text{m}$  aspirin roughly half those of Avicel of the same particle size. As suggested previously, the looser packing of the needle shaped aspirin particles causes less attenuation of the photons.

In 2001 Everall et al. reported that Raman experiments carried out using a powdered sample of trans-stilbene revealed that the corresponding Rayleigh and Raman signals decayed over different time periods and that the Rayleigh component decayed at a faster rate than the Raman signal<sup>106</sup>. The current study reports contradictory results that show the rate of decay of the Raman and Rayleigh components to be approximately the same (refer to Figure 37-Figure 40). Everall described a system using short, pico-second measurements and a single component sample, and did not consider a dual component system where both layers exhibited different Raman signatures (as was considered in the present study). Despite producing opposing results, the findings from both studies can be explained. In the current study, the samples analysed were comprised of two materials of differing structures and hence different Raman signatures – one of which was used as a bulk medium and the other as a compressed Raman active layer. The sample configurations used contain the ‘active layer’ below or in between depths of the bulk medium (refer to Figure 21) and therefore the generation of Raman photons is confined to one specific region of the sample (the region in which the ‘active layer’ is present). As there are no opportunities for the further generation of Raman photons within the remaining sample depth, the generated Raman signal can only decay as it passes through the bulk medium to reach the detector. Similarly, the laser photons, once in contact with the sample can only be attenuated as they propagate through the depth of powder and consequently as both components have no opportunity for regeneration, the photons would be expected to decay at approximately the same rate.

Conversely, when a single component sample is used (as in the study carried out by Everall et al.<sup>106</sup>), the whole sample is the ‘active layer’ and hence through the entire thickness of the sample there are opportunities for the continued generation of Raman photons and furthermore, there is no ‘inactive material’ present to hinder the collection of the generated Raman photons. Moreover, the Rayleigh light can only be attenuated as it passes through the sample, it cannot be regenerated as the Raman photons can and consequently in comparison to the dual component configuration described in the current study, the Raman photons will decay slower than the Rayleigh component.



Whilst the findings from both studies can be explained, it is important that the concluding statements are understood to be valid for only the sample analysed; Everall et al. stated that the Raman component decays substantially slower than the Rayleigh light – this statement only holds true within the experiment carried out. Furthermore, Everall et al. did not assess the effect of the material particle size or shape on the decay profiles calculated and consequently the present study provides a more rigorous assessment of the nature of the decay of Raman and Rayleigh photons.

It is clear from this discussion that the propagation of Rayleigh and Raman photons through solids is dependent upon the system that is being interrogated and also whether compressed or loose particles are involved. Whilst the number of publications regarding photon propagation continue to grow, it is important to realise that as with manufacturing processes, different solid sample types (one component, bi-layer, spherical particles, small particles) behave differently, despite being analysed by one specific method. It is therefore important that research continues in this field, to encompass as wide a range of samples, physical properties and variations as possible, to expand and aid the fundamental understanding of Raman spectroscopy.

#### **4.4 Conclusions**

An experimental assessment of the effect of a moving Raman active layer through different loose powders on the recorded transmission Raman measurements has been undertaken. The study highlighted several important points:

- When a compressed Raman active layer was placed on top or below a 4 mm depth of loose powder (Avicel 0-38, 53-106, 150-212  $\mu\text{m}$  and aspirin 150-212  $\mu\text{m}$ ) little difference to the measured transmission Raman intensity was seen. Matousek and Parker also found that similar transmission Raman intensities were achieved when a Raman active material was placed on the top or bottom of a bulk material.

- When the Raman active layer was embedded in the loose powder, the signal recorded in transmission mode was always greater than when the layer was on the top or bottom of the bulk powder.
- The magnitude of the transmission Raman signal obtained for any position of the Raman active layer within or on the surface of the loose powder was dependent upon the size and shape of the particles of the loose powder which will affect the packing of the particles.
- For Avicel, the intensity obtained at each particle size range when 1 mm of powder is before the Raman active layer is greater than when 1 mm of powder is after the active layer. Conversely, for the single size range of aspirin studied, the reverse was found to be true.
- Matousek and Parker used Monte Carlo simulations to study the effect of the position of a Raman active layer within a bulk medium, on the transmission Raman intensity observed. The study concluded that transmission Raman measurements were insensitive to the location of the active layer; the opposite conclusion to that drawn from the experimental data discussed in this chapter.

## **5. Non-invasive analysis of Chlortrimeton tablets by Raman spectrometry**

Chapter 3 gives details of the analysis of Chlortrimeton tablets for the active pharmaceutical ingredient (API) chlorpheniramine maleate, using high performance liquid chromatography (HPLC). This technique has many advantages but its main disadvantages are the time involved in completing the analysis and the destructive nature of the method. Direct, non-invasive analysis of tablets would overcome both of these disadvantages and in this part of the study, Raman spectrometry is investigated for the determination of chlorpheniramine maleate.

### **5.1 Review of literature on the direct analysis of tablets**

Owing to the FDA PAT initiative, there is an increasing demand for high levels of quality control within both pharmaceutical development and manufacturing, and as a result, faster, more robust analytical techniques are being sought to fulfill this need. The majority of drugs are formulated and delivered as solid dosages, typically tablets and capsules. It is well known that the solid state properties of a drug substance impact the bioavailability and stability of the drug and consequently the identification, quantification and characterisation of these drug substances are necessary<sup>117</sup>. It has been recognised that drug substances can undergo transitions during the processing or storage stages of the formulation and hence although the bulk drug substance may be well characterised, this is not necessarily true of the end product. In recent years there has been an increased demand for rapid and robust at-, on- and in-line analyses for the pharmaceutical industry<sup>118</sup>; this together with stringent regulatory control results in the need for large numbers of quality control analyses to be regularly performed to verify the API content and the uniformity of its distribution within manufactured tablets. The traditional techniques used for tablet analysis (for example HPLC) often require complicated pretreatment procedures and are time consuming. Moreover, the use of such wet chemistry methods does not allow for the acquisition of physical property information concerning the API and sample matrix.

Non-invasive, non-destructive optical spectroscopic techniques provide advantages over the traditional wet chemistry techniques that are currently the analysis methods of choice for tablets. As commercial demand and patient requirement for prescription drugs increases, there is a need to increase the speed of pharmaceuticals to market and consequently, the pharmaceutical industry can no longer solely rely on the traditional labour intensive technologies that have been used for many years. Generally, spectroscopic techniques can provide rapid, non-destructive analysis of samples in their native state with no sample preparation<sup>119</sup>. The importance of non-destructive analysis has in recent years been warranted owing to the increased interest and significance of the solid state properties of pharmaceutical materials and their consequent characterisation<sup>117</sup>.

In addition to the quantification of the API within a tablet, quality control is also concerned with the rapid and non-destructive acquisition of analytical measurements that will allow for the non-invasive quantification of polymorphs, impurities and starting materials within the product. The requirement for such rapid, non-destructive analysis arises from the practicalities of applications such as production line quality monitoring and the determination of the shelf life of a product. Analytical methods such as X-ray diffraction and terahertz spectroscopy can be used in these applications, however, both techniques are expensive and slow making them less adaptable for on-line use<sup>120</sup>.

Near infrared spectrometry (NIRS) has also been shown as a useful tool in the pharmaceutical industry, where it has been utilised in the production sector with respect to raw materials identification<sup>121</sup>, process control<sup>122</sup> and the qualitative and quantitative analyses of end products such as tablets<sup>123</sup>. Nevertheless, for many years such applications of NIRS have been carried out in diffuse reflectance mode, which suffers from the problem of sub-sampling, where only shallow surface layers of the sample are represented by the resulting spectra. The diffuse reflectance NIR approach is therefore seen as inadequate for the probing of pharmaceutical tablets as representative measurements cannot be guaranteed with this method. In order to

address this problem, diffuse transmittance NIR measurements have been explored. The advantage of this approach compared to the reflectance mode counterpart is that the NIR radiation interacts with an increased sample volume and hence the resulting spectra contain more detailed information regarding the sample as a whole. Studies comparing both geometries have reported lowered prediction errors with transmittance compared to reflectance NIRS<sup>124, 125</sup>. The advantages gained using transmittance mode NIRS have resulted in this mode being more widely used and as a result a number of studies detailing the quantification of different active ingredients in pharmaceutical tablets using this approach, have been reported<sup>124-127</sup>.

Despite the advantages of the transmittance approach, NIRS has a number of limitations. One of the major disadvantages is that it is sensitive to variations in the physical characteristics of the sample<sup>125</sup>. As the measured absorbance in NIRS follows the Beer-Lambert law, it is dependent upon the concentration of the analyte being quantified but also on the path length of the light passing through the sample. The path length of the penetrating light, however, is affected by the physical properties of the sample i.e. particle size distribution, particle shape and sample thickness. As a result of this, it has been shown that when analysing a tablet by NIRS, the extent of scattering is 1000 times greater than the absorption<sup>128</sup> of the source radiation and consequently a small change in the physical properties of the sample can change the resulting spectrum to a greater extent than would occur due to analyte concentration variations. Furthermore, NIRS can in many cases lack the ability to detect subtle differences in the spectra owing to compositional variations, as a result of the broad overlapping spectral features that typify the technique.

Raman spectroscopy is an alternative technique to NIRS for the analysis of pharmaceutical tablets. Raman spectroscopy provides a greater chemical specificity, larger penetration depths into the sample and sharper spectral features compared to NIRS. Furthermore, common non-aromatic, non-crystalline excipients are generally poor Raman scattering materials in comparison to drug substances that are often small aromatic heterocycles. Identifying active ingredient peaks, even if present in

very low concentrations compared to the excipient, is therefore more likely to be achieved with Raman spectrometry, compared with NIR spectrometry.

Traditional confocal reflectance Raman spectroscopy has been widely used for the composition monitoring of pharmaceutical tablets<sup>100, 101, 129-134</sup>. In 2000, Bell et al. demonstrated that the Raman spectrum of a seized ecstasy tablet had the potential to provide a more complete compositional profile of the tablet than the more established gas chromatography-mass spectrometry (GC-MS) technique that is the method of choice for criminal prosecutions<sup>132</sup>. Bell used a large sub-sample set of 400 ecstasy tablets from more than 50 000 seized tablets. The 400 tablets analysed originated from eight different bags of tablets found at the same source; 50 tablets from each bag were collected randomly and all tablets had the same physical appearance. Raman analysis of the tablets showed no composition variation within bags, however it was identified that the eight bags consisted of either sorbitol, cellulose or glucose based tablets. Three bags of sorbitol based tablets were found to be very similar in composition except for one bag which differed with respect to the ratio of ecstasy to sorbitol. Furthermore, two bags of cellulose based tablets exhibited a broad range of drug to excipient ratios and moreover these tablets were found to contain ecstasy with a hydration intermediate that was between that found in the sorbitol and glucose based tablets. Additionally, one bag of tablets showed a significantly different degree of hydration and a significantly narrower range of ecstasy to glucose ratios than the other tablets analysed and consequently this suggested these tablets had been carefully manufactured. Bell concluded that simply noting the physical appearance of a seized tablet and identifying and quantifying the API, as is done with the traditional GC-MS approach, overlooks important information that highlights differences in seemingly similar tablets and furthermore, that Raman spectroscopy facilitates the acquisition of such information.

In 1997, Wang et al. assessed the potential of reflectance Raman spectroscopy for the direct assay measurement and shelf life monitoring of aspirin tablets and compared the spectroscopic data to that acquired by HPLC<sup>130</sup>. Raman measurements were

carried out on both tablets (90% w/w API) and powdered tablets. Tablets were analysed directly on a rotating platform to assess the extent of sample degradation; measurements were taken at four time points over a period of eight weeks. For the quantification of aspirin, 20 tablets were ground by hand and homogenised before being poured into a sample holder. The study reported that the peak shapes of the Raman spectra were unaffected by the particle size variations encountered however, peak intensities were affected and consequently control of sample packing would be necessary for quantitative work. Raman measurements showed clearly that over an eight week period, there was a significant increase in the intensity of the salicylic acid peak in the Raman spectrum, confirming that sample degradation had taken place. Quantitative data acquired from both Raman and HPLC measurements, using powdered tablets, confirmed this. On the whole, the study showed a good agreement between the quantitative HPLC and Raman results except for the zero storage time set corresponding to the lowest percent salicylic acid. This was attributed to aspirin hydrolysis occurring during the HPLC analysis. Wang concluded that Raman spectroscopy was a feasible method for the assay determination of aspirin tablets and the major degradation product salicylic acid and furthermore that the technique provided important additional information regarding the samples that could not be attained from the conventionally used methods of analysis.

Szostak and Mazurek also assessed Raman spectroscopy for the quantitative determination of aspirin and paracetamol in tablets<sup>134</sup>. The study used powdered commercial tablets of API concentrations ranging 33.2-90.9 % w/w and confirmed the potential of Raman spectroscopy when combined with chemometric methods (partial least squares and principal component regression) for the quantitative analysis of pharmaceuticals. Furthermore, Szostak and Mazurek concluded that it was possible to precisely determine the amount of target compounds in complex solid mixtures, even when only the partial composition of the sample is known. They did state, however, that a rotating sample holder was needed to ensure rapid representative analysis and moreover, further method development would be required for analysis of preparations with lower API concentrations.

NIR transmittance and NIR reflectance Raman spectroscopy were compared for the quantitation of active substances in pharmaceutical tablets by Dyrby et al<sup>100</sup>. Chemometric calibrations of the API content of pharmaceutical tablets were developed using partial least squares for both analysis methods. Despite analysing samples containing highly Raman active nitrile functional groups, the best results were obtained for NIR transmittance. Tablets of four dosages (5, 10, 15 and 20 mg) with only two different API concentrations (5.6 and 8.0 % w/w) were used and a calibration model based on all four dosages resulted in a prediction error of 0.3 % w/w for the NIR transmittance model; the corresponding error for the Raman measurements was 0.56 % w/w. Dyrby et al. attributed the higher prediction error associated with the Raman measurements to the sampling conditions of the analysis method and stated that the inherently small sample volume measured with reflectance Raman spectroscopy made it inferior to NIR transmittance spectroscopy with respect to quantitative measurements. Similarly, in a separate study, the small sampling volume of conventional Raman systems was stated as the largest source of error in a study that investigated the use of Raman spectroscopy for the determination of the bucindolol concentration of intact capsules contained in blister packs<sup>135</sup>.

In 2005, Johansson et al. addressed the effect of varying the laser irradiation method for reflectance Raman spectroscopy measurements, on the quantitative determination of the API in tablets<sup>102</sup>. The tablets used contained API concentrations varying between 28.6 and 35 % w/w. The study examined four different laser irradiance patterns to assess the effect of sub-sampling: point irradiation where five points on each side of the stationary tablet were measured; small (2.5 mm diameter) and large circle (5 mm diameter) irradiation, where the tablets were rotated to create a circular pattern; and area irradiation (5 mm) which was achieved by simultaneously rotating and translating the tablets to achieve a spiral motion of the laser beam on the tablet surface. The study reported results as the difference between two evaluations from each side of the tablet and the data showed that by increasing the area of the tablet



sampled, the sub-sampling error was lowered. Furthermore, the study showed that no improvement was attained when going from a 5 mm circle pattern (large circle irradiance) to a 5 mm area pattern and consequently Johansson et al. concluded that there was no benefit in scanning a 5 mm diameter of a sample compared to a 5 mm circumference.

Additional studies have been reported, demonstrating the advantages of large area illumination Raman probes compared to conventional small spot size systems. In 2006, Kim et al. reported the use of a wide area illumination reflectance Raman system for the non-destructive analysis of pharmaceutical tablets<sup>136</sup>. The study compared a Raman system developed by Kasier Optical Inc. (Ann Arbor, MI, USA) utilising a 6 mm diameter spot size with a conventional Raman system using a spot size of 100  $\mu\text{m}$ , to quantitatively determine naproxen in tablets over the concentration range of 58-79 % w/w. When replicate measurements were made on the same tablet using both methods, a significant improvement in the repeatability of the analyte peak area was seen with the large spot size approach compared to that with the conventional approach. A separate study illustrated the benefits of wide area illumination Raman measurements for the non-invasive, quantitative determination of povidone in commercial eyewash solutions, directly through plastic bottles<sup>137</sup>. The study compared results obtained using a spot size of 6 mm in diameter (focal length 248 mm) with a conventional 80  $\mu\text{m}$  spot size (focal length 10 mm); 20 spectra of a 2% povidone solution were collected using both spot sizes, with the sample bottle removed and repositioned after each measurement to simulate a routine measurement. The ratio of the plastic bottle peak at 1063  $\text{cm}^{-1}$  and the povidone peak at 936  $\text{cm}^{-1}$  was calculated for each recorded spectrum and the results showed a % RSD of 32.5 for the conventional small spot size approach compared to a 3.2 for measurements acquired using a 6 mm spot. This marked difference was attributed to the smaller sampling area and shorter focal length of the 80  $\mu\text{m}$  spot configuration, which resulted in a greater sensitivity to slight variations in the distance between the Raman probe and the sample bottle (occurring after repositioning the bottle). Wide area illumination Raman analysis was also shown to be successful for the quantitative measurement of the API in an intact capsule

formulation<sup>138</sup>. A laser spot of 6 mm in diameter was used to determine the ambroxol content in capsules and the results were compared to those obtained by NIR transmittance spectroscopy and Raman spectroscopy using a small spot size. The resulting standard error of prediction using the large spot size Raman system was comparable to that obtained with transmittance NIR measurements, however, NIR measurements were acquired on powdered material removed from the capsule shell. Furthermore, compared to conventional small spot size Raman spectroscopy, measurements acquired with a 6 mm spot decreased the spectral variation among empty capsules; consequently measurement variations originating from the capsule shell did not influence the accuracy of the determination of the ambroxol concentrations when a large spot size was used.

Despite the reported advantages of wide area illumination Raman probes compared to conventional confocal Raman spectroscopy, the reflectance Raman spectra produced still fail to represent the entire sample body, rather they contain mainly information from the surface layers of the sample. In 2006, Matousek and Parker reported that even with a sample spot size of 4 mm, 88% of the reflectance Raman signal from a 4 mm thick tablet was generated in the top 1 mm layer and only 12% of the signal originated from the remaining 3 mm of sample<sup>59</sup>. These findings illustrated the strong bias of reflectance Raman spectroscopy towards the surface layers of samples and hence highlighted its sensitivity to both fluorescence and Raman contributions emanating from shallow layers of the sample.

The problems associated with reflectance Raman spectroscopy are further intensified by the current drive for an increased understanding of manufacturing processes and in turn, the quality of the end products produced. A number of analytical applications require the non-invasive probing of the bulk material within tablets or capsules, to understand the overall content and distribution of constituents within the body of the tablet rather than simply acquiring a ‘snap shot’ of a small volume of the sample. This has arisen from the need to understand the overall content of a tablet accurately so that when it is delivered to the patient, one can be sure that undesirable

components (e.g. polymorphs, solvates, starting materials) concealed within the body of the sample that may produce harmful effects, are not present. Additionally, acquiring representative data allows information to be obtained regarding the content uniformity of an API or series of ingredients; such information is imperative to achieve process control and in turn good, consistent quality control of the product. These driving forces are reinforced by the FDA's PAT initiative, which encourages manufacturers of pharmaceuticals to adopt innovative changes to improve the performance monitoring of manufacturing processes for ensuring end product quality<sup>7</sup>. Despite the merits of reflectance Raman spectroscopy (as previously discussed), the technique is unable to provide a complete picture of the sample make up, even with the use of large area illumination probes<sup>59</sup> and consequently information regarding the content uniformity of a sample and the presence of deeply buried impurities within the sample body, cannot be attained by this technique.

Recent research into Raman photon migration<sup>106, 107</sup> and novel sampling configurations for Raman spectroscopy<sup>105, 110</sup> (previously discussed in section 4.1) has identified a sampling geometry that has been reported to be suitable for the determination of the bulk content of samples such as pharmaceutical tablets<sup>57, 59, 60</sup>. As discussed in section 4.1, the transmission mode geometry requires the laser beam to be incident on the opposite side of the sample from which the generated photons are collected and consequently the laser beam penetrates the entire thickness of the sample, allowing the collection of photons from different depths within the sample. As previously discussed, the problems of sub-sampling and the significant bias of conventional Raman spectroscopy towards surface emanating signals and hence sensitivity to fluorescence, have been major limitations for the use of conventional confocal and wide area illumination reflectance Raman spectroscopy in probing the content of pharmaceutical samples<sup>59, 108</sup>. Complicated rotating sampling devices have been used to attempt to overcome these limitations however, the transmission Raman geometry has been reported to eliminate the need for such devices by rapidly acquiring spectra representative of the bulk content of the sample.

The absence of the sub-sampling limitation in transmission Raman spectroscopy was demonstrated by both simulated and experimental data in 2006<sup>59</sup>. The study showed that simulating the relocation of an impurity layer from the sample surface to a depth of 3 mm within a tablet medium, decreased the conventional reflectance mode Raman signal by a factor four whereas the equivalent transmission mode experiments exhibited a much less variable signal, changing by less than a factor of two. Similar transmission mode results have been reported in the current study (refer to section 4.3.2), where experimental data describing the relocation of an impurity layer showed the variation in the Raman intensity to be less than a factor of 3. In addition to simulated data, the study also demonstrated the elimination of the sub-sampling problem experimentally using a paracetamol tablet with an impurity layer of trans-stilbene powder located in front or behind the tablet relative to the incident laser beam. In both configurations, the reflectance spectra exhibited the Raman signature of the surface layer but not the sub-surface layer, whereas the spectra acquired using the transmission geometry contained spectral features of both the impurity layer and the paracetamol tablet. The similarity of the spectra in both sample configurations demonstrated that the transmission geometry was not susceptible to sub-sampling, unlike the conventional reflectance mode approach.

Many pharmaceutical tablets and capsules are brightly coloured and hence fluoresce strongly even under NIR excitation; consequently when analysed by conventional Raman spectroscopy, information regarding the inner composition of the sample is obscured by the strongly fluorescent signals emanating from the sample surface. In 2007, the insensitivity of transmission Raman spectroscopy to surface Raman signals and fluorescence, compared to the conventional reflectance Raman approach, was demonstrated<sup>139</sup>. The study compared reflectance and transmission geometries for the analysis of variously coloured pharmaceutical capsules. The reflectance mode measurements showed that the detected fluorescent signals were adversely affecting the signal to noise ratio of the measured spectra of the material within the capsule. The use of the transmission geometry, however, eliminated to a large extent this interference and allowed much more sensitive measurements of the bulk material within the capsule to be made. Furthermore the study compared reflectance and

transmission mode Raman with spatially off-set Raman spectrometry (SORS); the resulting spectra highlighted that SORS was also capable of rejecting surface layer signals, however not to the same extent as transmission mode measurements. Nevertheless, both the SORS and transmission geometry permitted the observation of the bulk material within the capsule despite these spectral features being completely obscured by fluorescence originating from the capsule shell in the conventional reflectance mode spectra. The different results shown using the both geometries were explained with respect to the thickness of the capsule shell and the differences in the sample orientations in both measurements. As the shell thickness of a capsule is significantly less than the underlying pharmaceutical material, it was concluded that its contribution to the overall signal would be very low when acquiring transmission measurements compared to reflectance measurements, where owing to its strong bias towards the surface layers of a sample, the capsule signals would be emphasised. Moreover as the capsule shell is located at the surface of the probed sample and the detector is placed at the opposite side of the sample (when using the transmission geometry), the authors concluded that there would be a greater loss of laser and Raman photons at the sample to air interface than its inner parts. These explanations were extrapolated from data previously reported by the authors<sup>59</sup>.

The ability of the transmission Raman geometry to quantify the API as well as determine the signature of the internal composition of pharmaceutical tablets has been experimentally demonstrated by Johansson et al<sup>60</sup>. This study analysed 20 test tablets (3.3 mm thick), prepared in the laboratory to contain an API concentration of between 16 and 24 % w/w. The samples were analysed using both transmission and reflectance Raman geometries and in each case a laser power of 400 mW, a laser excitation wavelength of 785 nm and a large spot size of 6 mm in diameter were utilised. The API was quantified using transmission mode measurements with a relative root mean square error of  $\pm 2.2$  % and  $\pm 2.9$  % for reflectance mode measurements; the latter yielding a lower relative accuracy (despite exhibiting greater signal intensities) which was attributed to a significant sub-sampling effect. This was confirmed by the analysis of an outlier spectrum acquired with the reflectance mode. The outlier exhibited a significant deviation from the expected

peak intensities for the API for the concentration range and this deviation was explained as an inhomogeneity within the region probed. A corresponding outlier was not identified by transmission Raman measurements and this was explained with respect to the nature the measurement - sampling the entire content of the tablet and averaging any inhomogeneous regions. The study also stated that the transmission mode Raman had the potential to give simpler more robust calibration models for the API in solid pharmaceutical tablets compared with reflectance Raman. This was primarily attributed to the more representative measurements achieved with transmission Raman spectroscopy and this was demonstrated in the study by a lower prediction error and the requirement for fewer PLS components to explain the variance of the data, compared to reflectance mode equivalents.

A parallel study which investigated the feasibility of quantifying the API in pharmaceutical capsules coated in a highly fluorescent material, was carried out by Eliasson et al<sup>57</sup>. The study analysed a sample set of 150 capsules with API concentrations ranging from 27 to 33 % w/w. Eliasson compared the performance of four Raman systems for the analysis of the capsules: three reflectance mode systems (a confocal, a defocused and a large spot size system) and a transmission Raman system. The spectra acquired using the confocal system contained strong spectral features from the fluorescing capsule shell, similarly the defocused and large illumination area reflectance systems also suffered from strong capsule shell contributions, however, defocusing and increasing the sampling area reduced the intensity of the shell signals by half. A dramatic reduction in the capsule shell signal was seen when the transmission mode measurements were deployed; the Raman signal of the capsule relative to that of the capsule interior was suppressed by a factor of 33, however, it was not entirely removed. The significant improvement seen with transmission mode measurements allowed the API to be accurately quantified with a relative root mean square error of  $\pm 1.2\%$  when using a 5 s acquisition time and  $\pm 1.8\%$  when using a 1 s acquisition time.

The studies discussed in this section indicate that Raman spectroscopy, particularly in the transmission mode, is well suited for the quantitative, non-invasive analysis of pharmaceutical tablets. The suitability of transmission Raman spectroscopy for the probing of the bulk content of a pharmaceutical sample has been commented on in all of the reviewed studies and likewise the studies have reported the use of this technique with samples of relatively high API concentrations (16-33 % w/w). Whilst the applicability of transmission Raman spectroscopy for the analysis of such samples has been clearly investigated, there is a lack of reported studies regarding the use of transmission Raman for the quantitative analysis of low concentration APIs in pharmaceutical tablets. Furthermore, whilst the capabilities of reflectance and transmission mode Raman measurements for the analysis of highly concentrated samples have been compared, comparisons have not been made for samples containing small amounts of API; moreover, with the exception of the study carried out by Eliasson et al.<sup>57</sup>, the tested sample sizes have been small for both reflectance and transmission mode investigations.

As was discussed in section 4.4, changes in the physical properties of the materials being analysed significantly affect the nature of photon propagation through solids and hence the properties of the interrogated system must be known and understood to ensure the subsequently acquired information is reported and handled in the appropriate manner. As transmission mode measurements have been shown to investigate the body of the sample rather than just the surface regions, the measurements consequently involve the migration of photons (Rayleigh and Raman) through the entire depth of the sample. It is a sensible assumption, therefore, that changes in the physical properties of the samples analysed will also affect the calibration models used for the quantitative assessment of pharmaceutical tablets and hence its success - the effect of such properties on Raman measurements, both transmission and reflectance has not been widely reported. The forthcoming sections will describe a rigorous assessment of the capabilities of both reflectance and transmission mode Raman measurements for the quantitative determination of a large sample set of over-the-counter, low concentration pharmaceutical tablets and will address the effect of the material particle size on the resulting data. Chapter 4

has discussed the Raman effects seen with powdered materials of varying particle size and shape and chapter 5 will analyse compacted material.

## 5.2 Experimental

### 5.2.1 *The quantitative determination of chlorpheniramine maleate as an example of a low concentration API pharmaceutical tablets by reflectance and transmission Raman spectroscopy*

Chapter 3 discussed the analysis of a large sample set of Chlortrimeton tablets by HPLC. Results showed the mean calculated API mass to be in good agreement with the API mass stated by the manufacturers. Nevertheless, several tablets were identified to be outliers with respect to deviations in the expected API mass and whole tablet mass values seen. Furthermore, the outlier samples identified did not exhibit a correlation between the fluctuating tablet and API masses. Owing to the limitations associated with HPLC, the analysis of such sample sets could be improved by the use of non-invasive, non-destructive spectroscopic techniques. Consequently, experiments were devised to investigate the potential of transmission and reflectance Raman spectroscopy for the quantitative determination of chlorpheniramine maleate. A sample set of 383 Chlortrimeton tablets were analysed in both Raman modes and the analyte mass values were predicted from a synthetic calibration tablet set. Mapping (using confocal, small spot size and PhAT large spot mapping techniques) was used to investigate outlier calibration tablets showing contradictory results from the reflectance and transmission Raman modes.

The Kaiser Raman workstation together with the Kaiser Raman PhAT probe were used for analysis in both the reflectance and transmission modes; refer to section 2.5 for details regarding the instrumentation used. The illumination and collection optics utilised provided a 3 mm spot size (used for all measurements unless otherwise stated). A 400 mW laser power was used together with a 20 s exposure time and 3 acquisitions for reflectance mode measurements, and a 60 s exposure time and 3 acquisitions were used for transmission mode measurements. The HoloGRAMS software used with the Kaiser instrumentation subtracted the dark current from each



subsequent spectrum acquired. The spectra were converted to text files to allow the data to be manipulated by independent software packages.

### 5.2.2 *Materials*

The Chlortrimeton antihistamine tablets (Schering-Plough HealthCare Products, Inc., Memphis, TN, USA) previously discussed in section 3.2.1 were used; they contained chlorpheniramine maleate (active pharmaceutical ingredient), corn starch, D&C yellow No 6&10, lactose monohydrate and magnesium stearate. Chlorpheniramine maleate (99.8 % purity) was purchased from Sigma Aldrich and microcrystalline cellulose (Avicel PH-101, 105 and 200) was obtained from GSK, Irvine (refer to table for the physical properties of the different grades of Avicel used).

**Table 19 – Physical properties of Avicel PH-101, 105 and 200<sup>114</sup>**

|                                   | <b>Avicel PH-101</b> | <b>Avicel PH-105</b> | <b>Avicel PH-200</b> |
|-----------------------------------|----------------------|----------------------|----------------------|
| <b>Average particle size (µm)</b> | 50                   | 20                   | 180                  |
| <b>Particle size range (µm)</b>   | 19.6-139.7           | 7.3-50.9             | Unknown              |
| <b>Particle shape</b>             | Granular             | Granular             | Granular             |

### 5.2.3 *Data Analysis*

For analysis, all data were imported into Matlab version 7.0.2 (Mathworks Inc., Natick, Massachusetts, USA) using PLS Toolbox version 3.0.4 (Eigenvector Research Inc., Manson, Washington, USA). Spectra were converted to second derivative spectra using the Savitsky – Golay function with a 51 point filter width and second order polynomial.

#### **5.2.4 Preparation of calibration tablets**

Tablets of known concentrations of chlorpheniramine maleate were prepared to form a calibration set which would be used to predict the API content of the Chlortrimeton sample tablets. Schering-Plough were contacted in an attempted to acquire additional details regarding the composition of the Chlortrimeton tablets, however the company would not provide the information and consequently the calibration tablets prepared were comprised of accurately weighed masses of active ingredient and Avicel. Despite the absence of Avicel in the Chlortrimeton tablets, it was used as the excipient in the calibration tablets owing to its wide use as a pharmaceutical material and furthermore, even though the inactive materials of the Chlortrimeton tablets were known, it was not possible to mimic the true make up of the samples. Moreover, the spectral features of Avicel did not interfere with the spectral region of interest of the API (refer to Figure 43).

Initially seven mixtures of API and Avicel were prepared covering the range 0-8 mg of API. Before tableting, each mixture was blended for 10 minutes in a tumbler blender to ensure, as far as possible a resulting homogeneous blend. From each blend four tablets were pressed. Each tablet was weighed and from this mass the API content of each tablet was calculated. For the purposes of this report, this calibration set will be referred to as the 'primary calibration set'. As the experimentally calculated masses of chlorpheniramine maleate from the HPLC study described in chapter 3 covered the range of 3.36 – 4.81 mg, it was decided to make an additional set of calibration tablets covering this range. Eight blends covering 3.36-4.81 mg of chlorpheniramine maleate were prepared in the same ways as previously described and four tablets were pressed from each blend. For the purposes of this report, this calibration set will be referred to as the 'reduced range calibration set'. Primary and reduced range calibration sets were prepared using three grades of Avicel (properties detailed in section 5.2.2). The thickness and mass of each tablet were measured and recorded.

### 5.2.5 Raman mapping of tablets

Raman mapping was used to confirm the degree of homogeneity of the outlier calibration samples identified by Raman spectroscopy. Two types of Raman mapping were used: PhAT mapping utilising a large spot size, and traditional confocal small spot size mapping (micro-mapping). Sample mapping was carried out on both sides of the calibration samples analysed.

Micro-maps were acquired using the Kaiser Raman workstation with a confocal Raman Mark II probe head (Kaiser Optical Systems Inc). By definition, micro-maps only cover a small area of the sample surface and penetration of the laser into the sample is limited owing to the confocal nature of the probe. A 20 x objective together with a 50  $\mu\text{m}$  illumination fibre, a 100  $\mu\text{m}$  collection fibre and a 20 s exposure time were used for analysis and the automated stage was programmed to collect data over an area of 250  $\mu\text{m}$  x 350  $\mu\text{m}$  in 30  $\mu\text{m}$  steps.

In order to investigate the benefits provided by mapping the entire area of the sample surface, PhAT maps of the samples were also acquired. The Kaiser Raman PhAT probe was used in conjunction with the Kaiser Workstation; a 1 mm spot size was utilised to map the entire tablet sample area in step sizes of 1 mm, with a 4 s acquisition time.

The resulting maps using both methods were treated using Pearson's baseline correction followed by multivariate curve resolution (MCR) over the region 850-1720  $\text{cm}^{-1}$  using the HoloMAP software provided with the instrument. The colour scale used was set to represent the active ingredient as red and the remaining tablet constituents as blue. The acquired maps were interpolated to show shades of colours in between red and blue; the information obtained from the maps is not intended to be quantitative.

## 5.3 Results and discussion

### 5.3.1 Raman spectra of Avicel, Chlortrimeton sample tablets and the active pharmaceutical ingredient (chlorpheniramine maleate)

Figure 43 illustrates an overlay of the transmission and reflectance Raman spectra of a sample Chlortrimeton tablet, a powdered sample of the API and Avicel powder. Figure 44 is a y-axis expanded version of Figure 43 highlighting the region 1500-1750  $\text{cm}^{-1}$ .

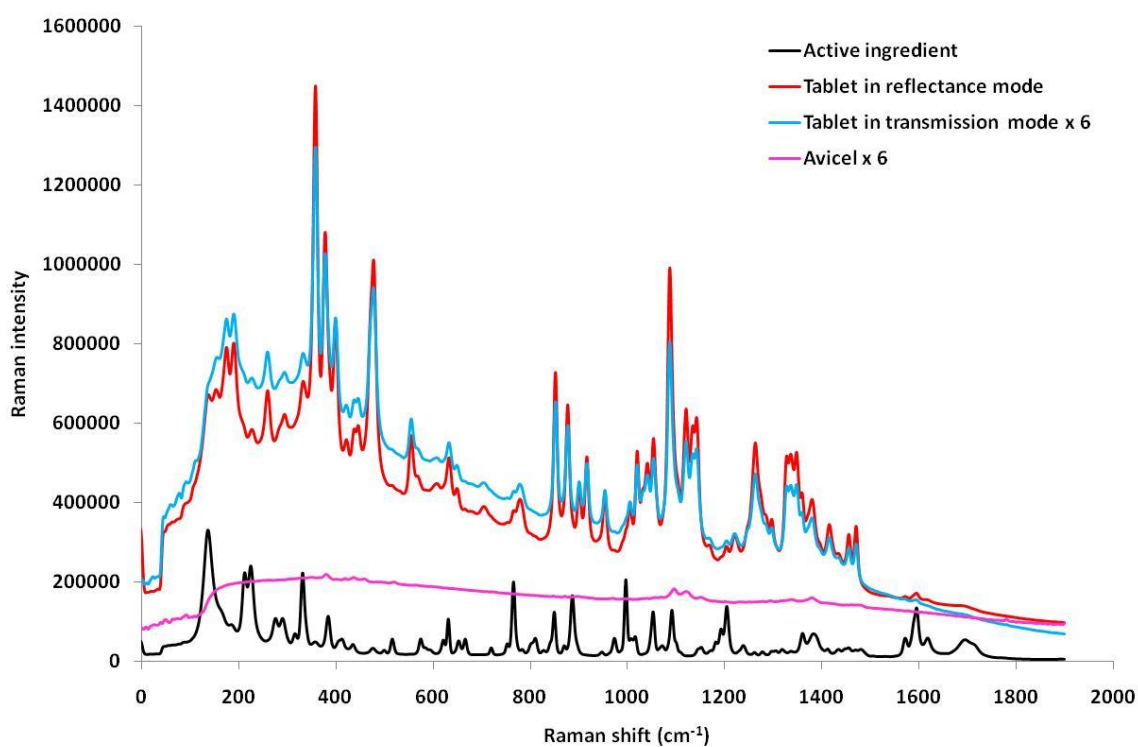


**Figure 43 – Overlaid Raman spectra of a Chlortrimeton tablet (reflectance mode), a powdered sample of the active pharmaceutical ingredient (reflectance mode), a Chlortrimeton tablet (transmission mode, signal multiplied by 6) and a sample of Avicel powder (transmission mode, signal multiplied by 6).**

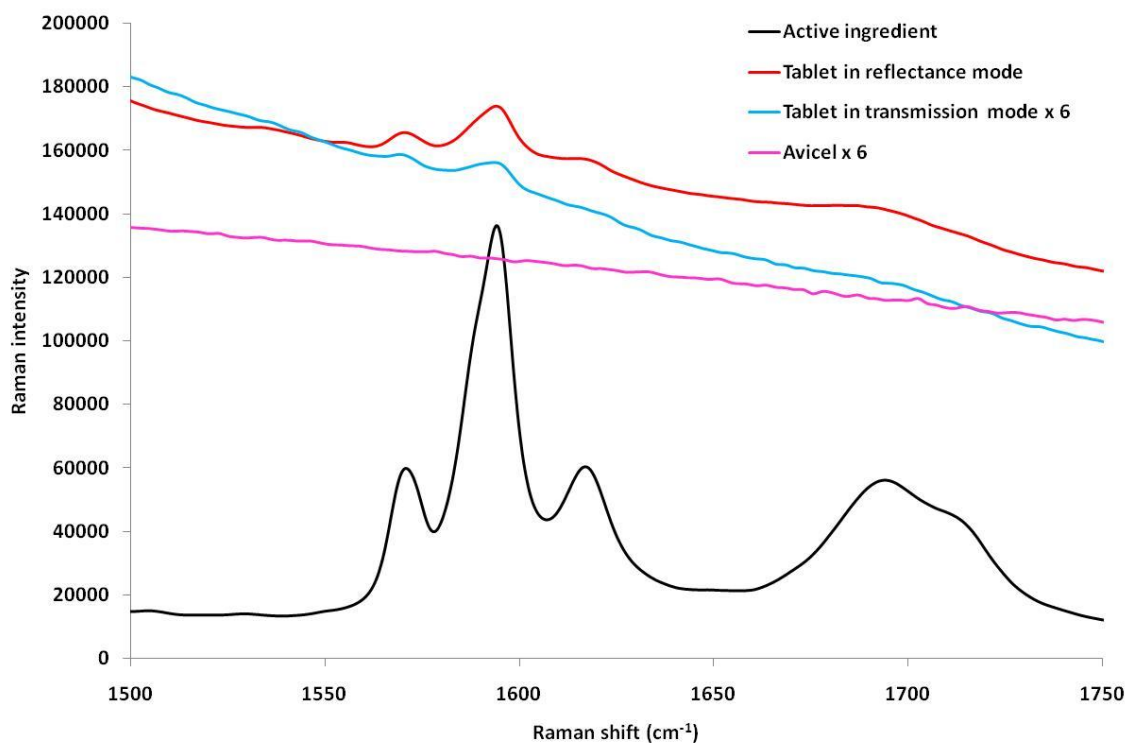


**Figure 44** – A y-axis expanded plot of the region 1500-1750  $\text{cm}^{-1}$  showing the overlaid Raman spectra of a Chlortrimeton tablet (reflectance mode), a powdered sample of the active pharmaceutical ingredient (reflectance mode), a Chlortrimeton tablet (transmission mode, signal multiplied by 6) and a sample of Avicel powder (transmission mode, signal multiplied by 6)

From Figure 44 it can be seen that the strong peak in the API spectrum at  $1594 \text{ cm}^{-1}$  (arising from the benzene derivatives present in the API molecule (refer to Figure 14)) is also visible in the Chlortrimeton tablet spectra taken in both reflectance and transmission modes. Furthermore, it can be seen that there is no response from Avicel in this region and hence no interference with the determination of the API peak will occur for calibration tablets prepared using Avicel. As expected, the API contributions at  $1594 \text{ cm}^{-1}$  in the transmission and reflectance mode spectra of the sample tablet, shown in Figure 43 and Figure 44 are significantly weaker than the response that can be seen from the pure API spectrum; the concentration of chlorpheniramine maleate in the tablets analysed is approximately 2% w/w. Furthermore, the transmission mode spectra of the sample tablet and Avicel powder have been multiplied by six in order to display these spectra on the same scale as the

reflectance mode measurements. The significantly lower intensity of the transmission mode data is a consequence of the different sampling geometries utilised by the two measurement types. Reflectance mode measurements illuminate the sample and collect the resulting Raman photons from the same side of the sample. Conversely, the illumination and collection optics are placed at opposite sides of the sample in the transmission geometry and consequently most of the highly intense Raman signal originating from the surface of the sample is not collected by the detector.

#### ***5.3.1.1 Instrument repeatability***

Owing to the low concentration of the API in the sample tablets and consequently, the small intensity of the corresponding peak in the Raman spectrum, the following repeatability studies were carried out. For each study the same Chlortrimeton tablet was used and the values reported are the average of six replicate measurements. In the first study, six consecutive measurements of the same tablet were made without moving the tablet position between measurements (measurement CV). In study two, six consecutive measurements of the same tablet were made, removing and replacing the tablet after each measurement (positional CV). Both study 1 and 2 were repeated 24 hours later to assess the effect of day to day variation.

The results in Table 20 show that there is no detrimental effect on the precision of the reflectance or transmission mode Raman intensities when the sample is removed and repositioned in the sample holder between measurements. Furthermore, the results also suggest there is no significant difference in the degree of repeatability achieved on different days.

**Table 20 - % CV values for transmission and reflectance Raman measurements of the API peak at 1594 cm<sup>-1</sup> in a Chlortrimeton sample tablet when the sample was left in position (measurement CV), when it was removed and replaced (positional CV) and when the studies were repeated on a separate day (day to day CV); n = 6**

|                                  | <b>Reflectance mode<br/>% CV</b> | <b>Transmission mode<br/>% CV</b> |
|----------------------------------|----------------------------------|-----------------------------------|
| <b>Measurement CV</b>            | 4.7                              | 4.9                               |
| <b>Measurement CV day to day</b> | 3.7                              | 4.1                               |
| <b>Positional CV</b>             | 4.9                              | 5.6                               |
| <b>Positional CV day to day</b>  | 3.8                              | 5.1                               |

## 5.3.2 Reflectance mode measurements

### 5.3.2.1 Information depth studies

It has been widely reported that transmission Raman measurements achieve a more representative measurement of the sample than those made in reflectance mode<sup>57, 59, 60</sup> and that owing to the small spot size and confocal nature of conventional Raman instruments, analysis by reflectance Raman does not probe deep into the sample<sup>43</sup>. Consequently reflectance Raman information depths have been reported to be limited to 1 mm in some cases<sup>43</sup> and furthermore, reflectance Raman spectra have been shown to be mainly comprised of highly intense surface generated Raman signals<sup>59</sup>. With the introduction of wide area illumination probes utilising an essentially collimated, rather than a tightly focused beam (e.g. the Kaiser Raman PhAT probe) a greater achievable field of depth and a longer working distance compared to confocal systems, can be achieved<sup>82</sup>; this introduces the potential for greater information depths (refer to Figure 45)

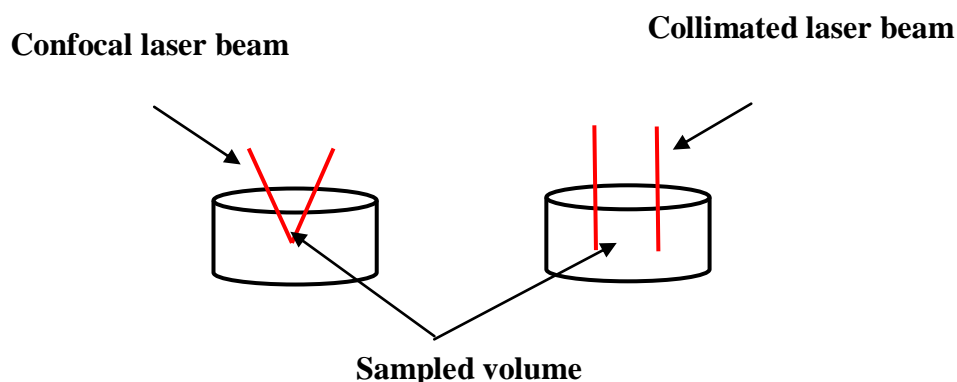


**Figure 45 - Schematic showing the differences between the sampling areas achieved by using a confocal laser beam compared to a collimated laser beam**

In order to determine the information depths that could be achieved in reflectance mode with the Kaiser Raman PhAT probe using a collimated laser beam 3 mm in diameter, Raman spectra of the sample configuration shown by Figure 46 were acquired. A 3.94 mm thick Chlortrimeton tablet was placed on a layer of flowers of



sulphur and analysed in reflectance mode using a 10 s acquisition time. The sulphur layer underneath the tablet was narrower than the tablet diameter in order to ensure that any sulphur present in the resulting spectra was detected from the underside of the tablet and not from over spill onto the sides of the sample holder. Three replicate measurements of a sample tablet with and without sulphur were acquired. Example spectra for both sample arrangements are shown in Figure 47. Flowers of sulphur was chosen owing to its high Raman scattering cross section<sup>64</sup>, exhibiting a strong Raman response at approximately 155 and 218  $\text{cm}^{-1}$ .

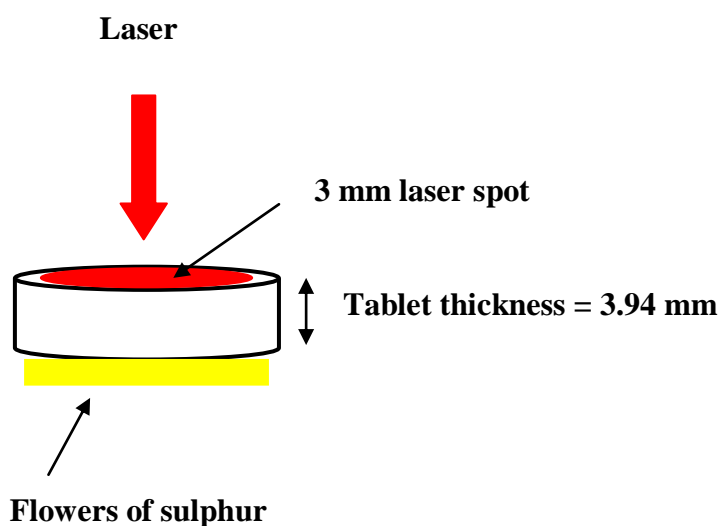


**Figure 46 – Schematic illustrating the sample analysed (3.94 mm thick Chlortrimeton tablet sitting on a layer of flowers of sulphur) to determine the achievable information depth when reflectance Raman measurements are made using a collimated, large area laser beam**

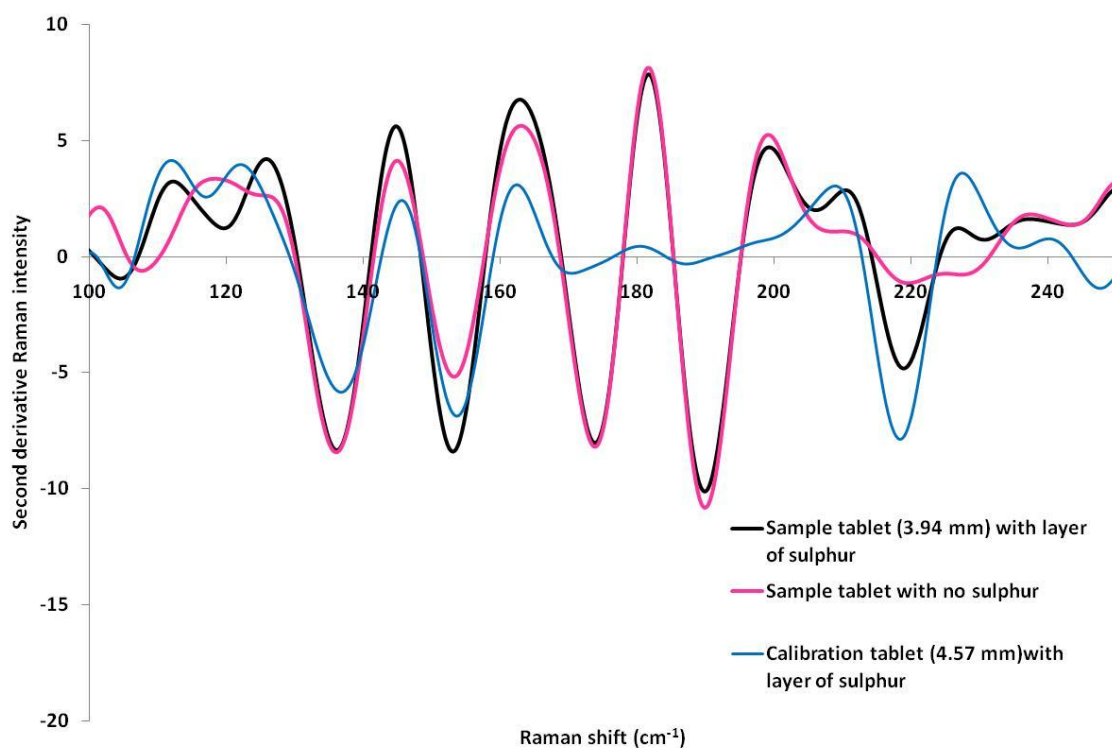


**Figure 47 – Second derivative reflectance spectra in the region 100 – 240  $\text{cm}^{-1}$ , of a 3.94 mm thick sample tablet with and without a layer of sulphur and a 4.57 mm thick calibration tablet with a layer of sulphur**

From Figure 47, it can be seen that the sample tablet with no layer of sulphur shows a response at  $154 \text{ cm}^{-1}$ , the Raman shift of a characteristic sulphur peak. Nevertheless, the intensity of this peak is greater when the sulphur layer is present under the tablet. Furthermore, the sample tablet shows no significant Raman response at  $218 \text{ cm}^{-1}$ , however, when a sulphur layer is present a strong spectral response at this Raman shift is observed. Figure 47 also shows the Raman spectrum acquired when a layer of sulphur was placed under a 4.57 mm thick tablet; the spectrum shows a significant response at  $218 \text{ cm}^{-1}$  from the sulphur layer. Consequently it has been shown that in reflectance mode, using a collimated, large sampling area laser beam it is possible to achieve information depths of at least 3.94 and 4.57 mm through a real and calibration tablet, respectively.

Wikstrom et al. reported information depths of 300 and 600  $\mu\text{m}$  for studies carried out with two confocal Raman probes and information depths of between 1.7 and 2 mm acquired with the PhAT system<sup>43</sup>. The spectra in Figure 47 show information depths approximately 2.6 mm greater than has been previously reported however it is important to acknowledge that the effective information depth will depend on the intensity of the Raman band of interest. Materials with a high Raman scattering cross section will exhibit greater information depths than materials exhibiting a weaker Raman scattering cross section. Consequently, it is not possible to make a rigorous comparison of information depths unless the same Raman active material is used.

#### ***5.3.2.2 Reflectance Raman analysis of a calibration sample set to be used for the prediction of the active ingredient mass in Chlortrimeton tablets***

As a key aim of the investigation involved assessing the degree of variation of the API within the Chlortrimeton and calibration sample sets and furthermore the degree of inhomogeneity of the identified tablets, it was decided to analyse both sides of the calibration tablets in order to obtain a true measurement of the API content. Furthermore, including data from both sides of the tablets would ensure that a good quality calibration model was produced, eliminating any false results from analysing only one side of an inhomogeneous tablet. Data were analysed as described in section 5.2.3; Figure 48 and Figure 49 shows the second derivative reflectance Raman spectra of calibration and sample tablets between 1565 and 1610  $\text{cm}^{-1}$ .

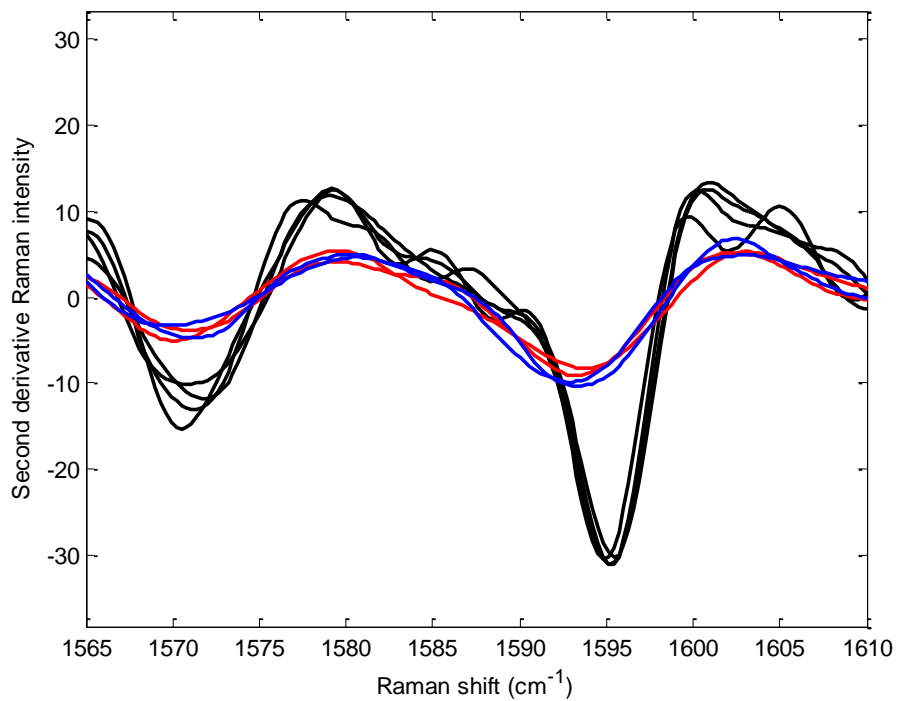


**Figure 48 – Second derivative reflectance Raman spectra highlighting the region 1565-1610 cm<sup>-1</sup> of two calibration tablets (blue and red) and four sample tablets (black)**

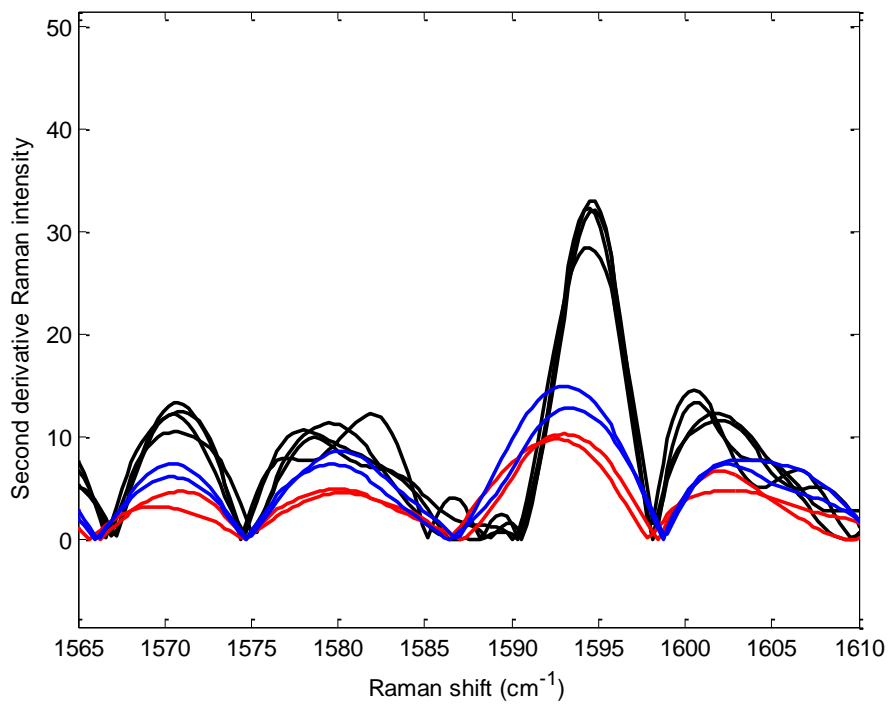


**Figure 49 – Positively plotted second derivative reflectance Raman spectra highlighting the region 1565-1610 cm<sup>-1</sup> of four sample tablets (black) and two calibration tablets (blue and red).**

Figure 48 and Figure 49 show the presence of the chlorpheniramine maleate peak at approximately  $1594\text{ cm}^{-1}$  in the 2<sup>nd</sup> derivative spectra of the sample and calibration tablets. Furthermore, the reflectance spectra of the calibration tablets show that differences in the Raman intensities of the analyte peak on each side are apparent, which supports the decision to include both sides of the tablets in the calibration models to compensate for an inhomogeneity that was caused during preparation of the tablets.

In order to determine whether the analyte mass calculations should be based on analyte peak areas or peak intensities, calibration plots were constructed from both the peak area and intensity at  $1594\text{ cm}^{-1}$  recorded in the 2<sup>nd</sup> derivative reflectance Raman spectra of the primary and reduced range calibration sets. The primary calibration plots are shown in Figure 50 and Figure 51 and the reduced range calibration plots are shown in Figure 52 and Figure 53. The correlation values were calculated to be 0.996 and 0.989 for the primary calibration plots constructed using the peak areas and intensities, respectively. Prior to preparation of the calibration plots, the peak areas and intensities of the chlorpheniramine maleate were normalised to account for any laser intensity fluctuations. As the composition of the calibration and Chlortrimeton tablets differ and only have the API in common, the API peak was normalised to different response regions for both tablet types. The normalising peaks for the calibration and Chlortrimeton tablets were chosen to be  $1095.5$  and  $1142.5\text{ cm}^{-1}$ , respectively. These peaks were chosen as they corresponded to excipient material and hence would not change significantly between samples. Nevertheless, it was expected that a small degree of change would be seen as, with an increase or decrease in the API mass (from the target amount), a corresponding increase or decrease in the amount of inactive material should also occur. Consequently a correction factor was applied to the normalisation process

$$\text{Laser intensity correction} = \frac{\text{area RP in S1}}{\text{area RP SX}} \times \text{area AP SX} \quad (22)$$

where,

RP is the reference peak (1095.5 or 1142.5  $\text{cm}^{-1}$  for the calibration or Chlortrimeton tablets, respectively)

AP is the analyte peak (1594  $\text{cm}^{-1}$  corresponding to the API)

S1 is the first spectrum acquired on the day of analysis of the tablet set

SX is the spectrum of interest

The primary calibration set prepared using Avicel PH-101 was analysed and one tablet at each concentration point (tablets 0 to 6) was selected to form the calibration graph. It was evident from the resulting spectra that all preparations from calibration tablet 5 were exhibiting signal intensities both significantly higher and lower than the calibration samples to either side of them. This was attributed to tableting an inhomogeneous blend of powders and consequently this concentration point was removed from the reflectance mode calibration graph. As the API mass corresponding to this concentration point was 50% greater than the stated API mass by the manufacturers, the removal of this sample from the calibration plot was not expected to adversely affect the resulting API mass predictions. The presence of outlier calibration tablets highlights the difficulties associated with preparing tablet standards; the calibration tablets used in the calibration plots were selected based on the similarity of the reflectance Raman intensities from both sides.

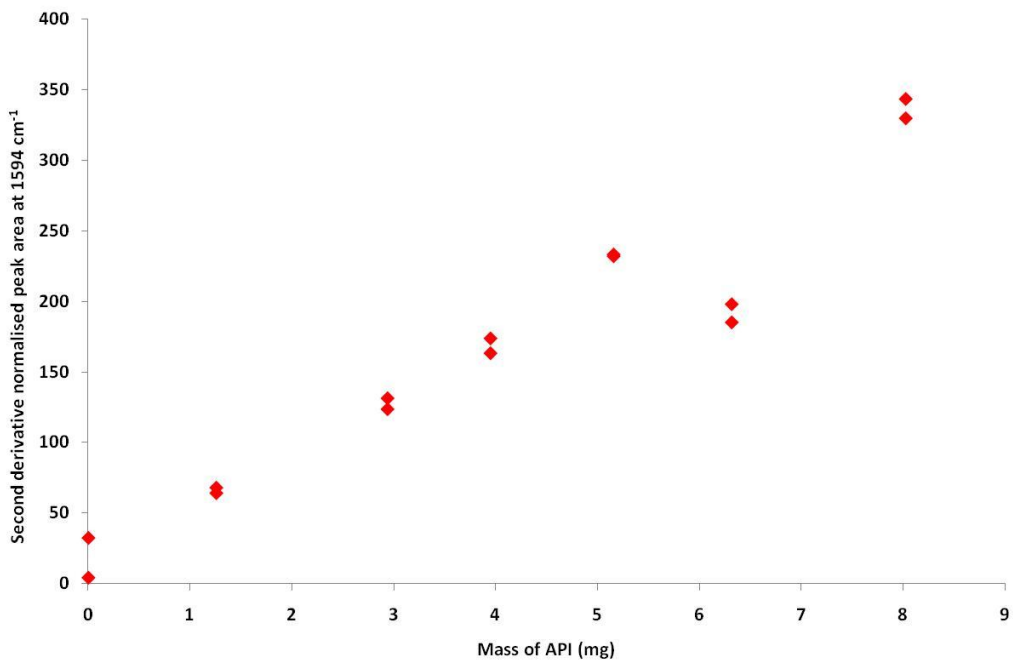


**Figure 50 – Calibration plot constructed from the primary calibration set containing chlorpheniramine maleate (API) and Avicel PH-101, showing the change in the second derivative normalised reflectance Raman peak area at 1594 cm<sup>-1</sup> for both sides of the tablet, as the mass of the API is increased**

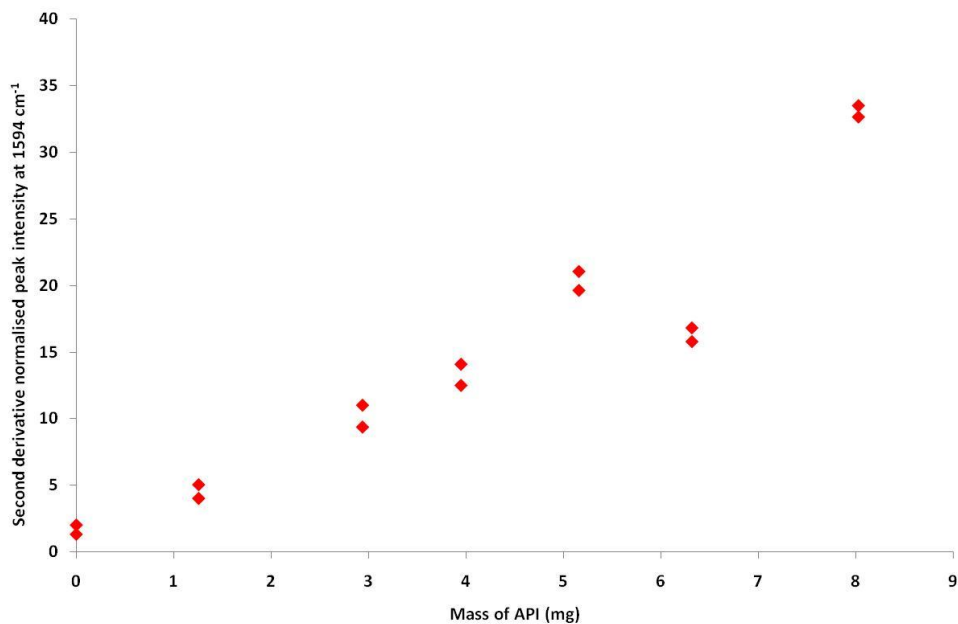


**Figure 51 – Calibration plot constructed from the primary calibration set containing chlorpheniramine maleate (API) and Avicel PH-101, showing the change in the second derivative normalised reflectance Raman peak intensity at 1594 cm<sup>-1</sup> for both sides of the tablet, as the mass of the API is increased**

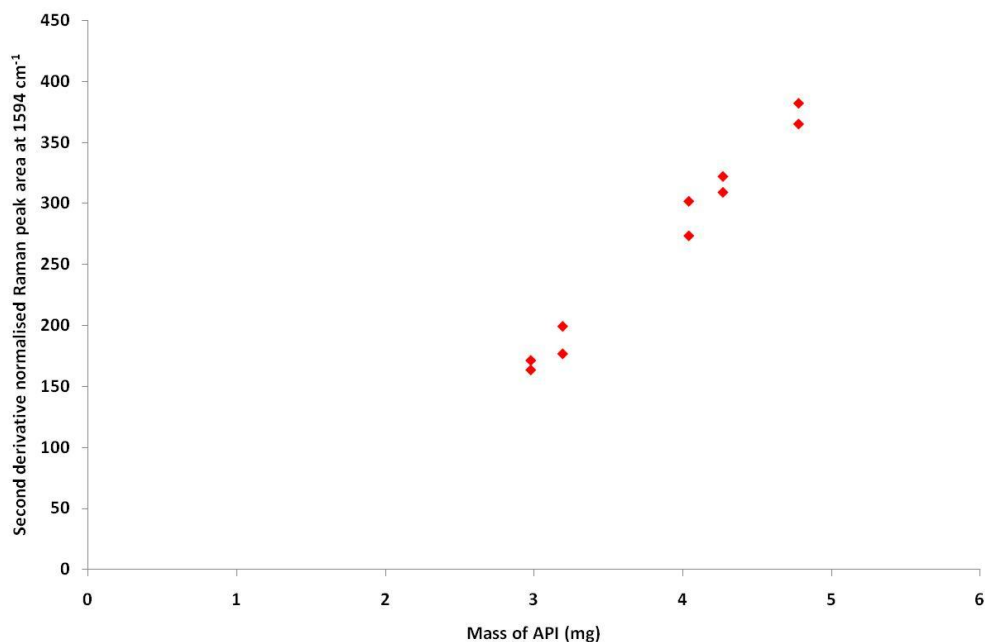


**Figure 52 – Reduced range calibration plot constructed from a calibration set containing Chlorpheniramine maleate (API) and Avicel PH-101, showing the change in the second derivative normalised reflectance Raman peak area at 1594 cm<sup>-1</sup> for both sides of the tablet, as the mass of API is increased**

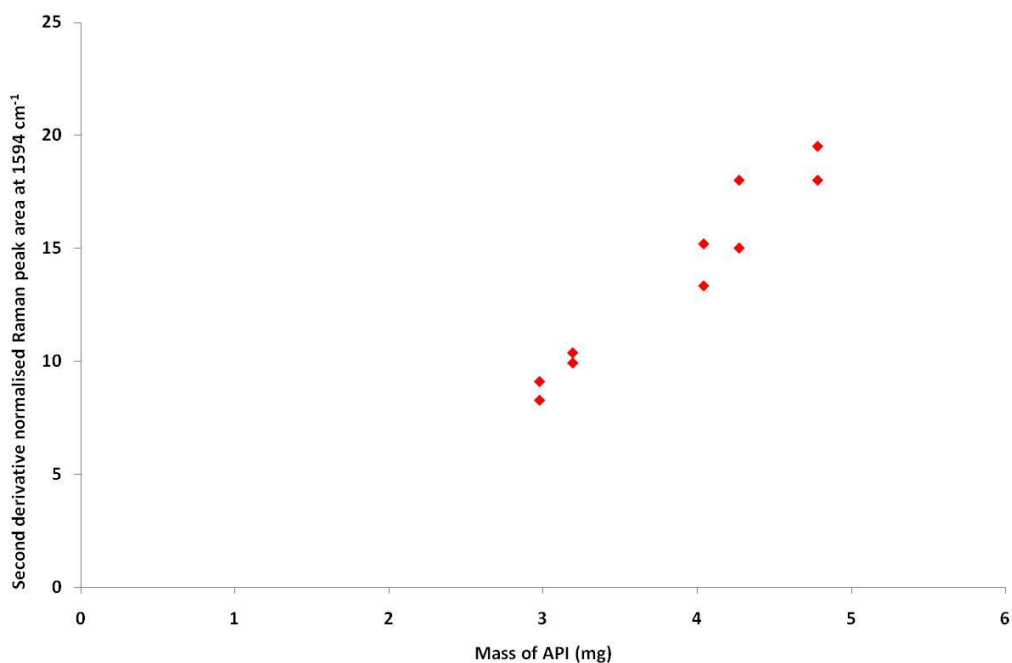


**Figure 53 – Reduced range calibration plot constructed from a calibration set containing chlorpheniramine maleate (API) and Avicel PH-101, showing the change in the second derivative normalised reflectance Raman peak intensity at 1594 cm<sup>-1</sup> for both sides of the tablet, as the mass of the API is increased**



Figure 54 shows the predicted mass values of chlorpheniramine maleate in 90 Chlortrimeton samples obtained using the second derivative normalised peak area data and Figure 55 shows the predicted mass of chlorpheniramine maleate using the second derivative normalised peak intensity data.

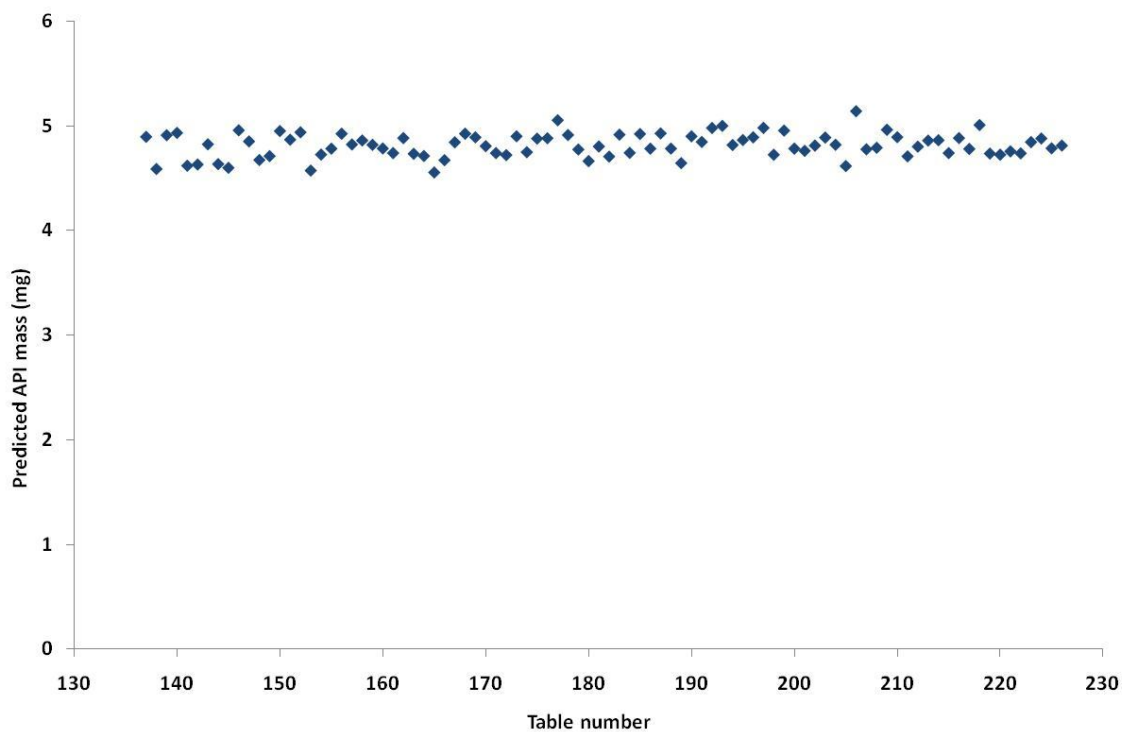


**Figure 54 – Plot of the predicted Chlorpheniramine maleate mass in Chlortrimeton tablets, calculated from the second derivative peak area at  $1594\text{ cm}^{-1}$  using the primary calibration set**

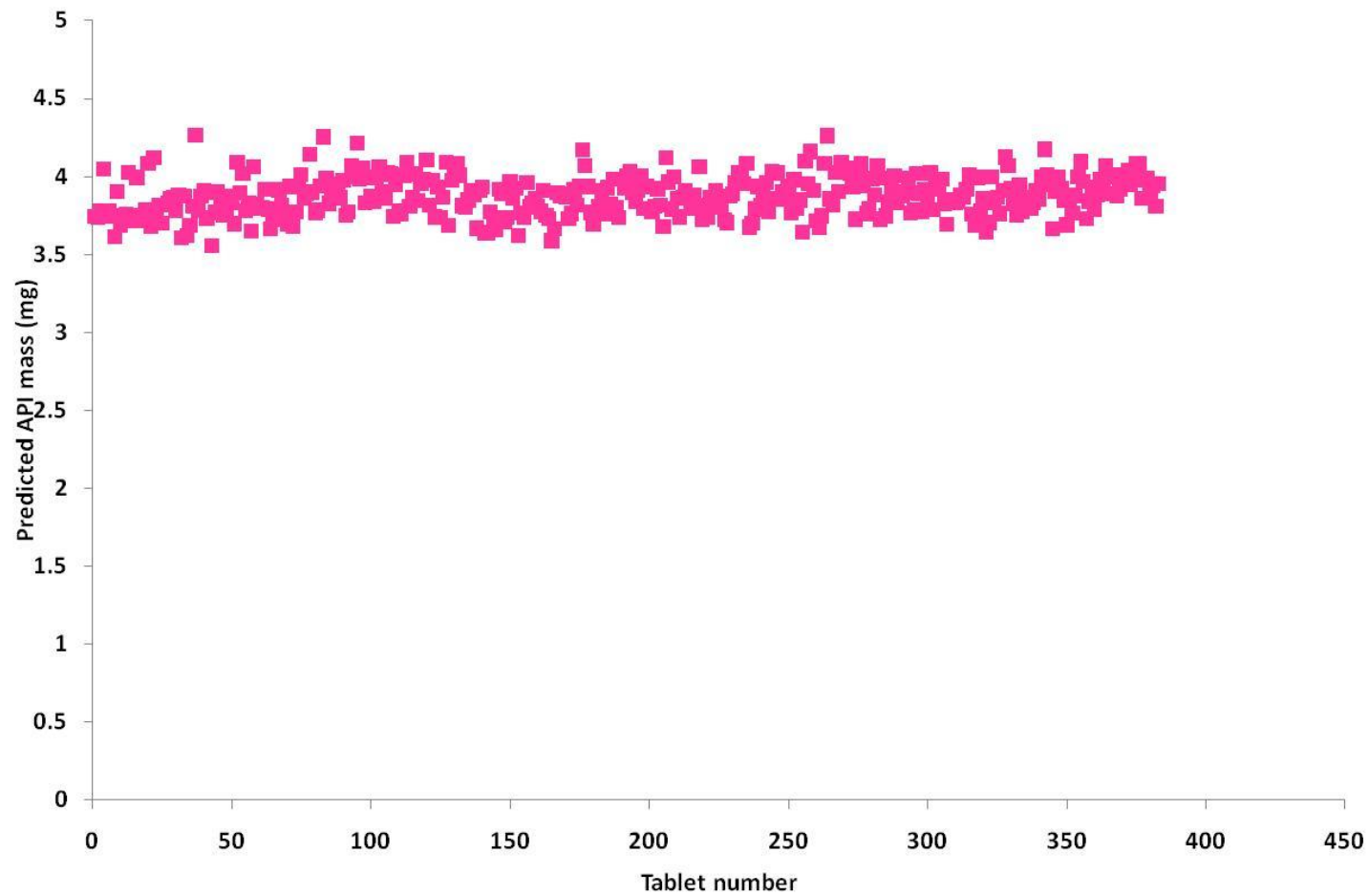


Figure 55 – Plot of the predicted mass of chlorpheniramine maleate in Chlortrimeton tablets, from the second derivative reflectance mode, normalised peak intensity at  $1594\text{ cm}^{-1}$  using the primary calibration set

The average API and % CV values calculated from the data points shown in Figures 54 and 55 were found to be 4.82 mg, with a CV of 2.4 %, and 3.86 mg with a CV of 3.3 %, for peak area and intensity measurements, respectively. From this data it is apparent that the predictions obtained using the peak area data were significantly closer to the stated API mass than those produced using the intensity data. This could be attributed to the differing spectral features of the analyte peak at approximately  $1594\text{ cm}^{-1}$ , in the sample and calibration spectra (refer to Figure 48 and Figure 49). Figure 49 shows that the chlorpheniramine maleate peak in the calibration tablets extends below  $1590\text{ cm}^{-1}$  whereas, the corresponding analyte peak in the Chlortrimeton tablets does not and furthermore, Figure 48 and Figure 49 show a broader analyte peak width for the calibration tablets compared to the samples. These differences however, are not seen when comparing the peak at  $1570\text{ cm}^{-1}$  for the calibration and sample tablets. The poorer predictions obtained using the peak area data could be a consequence of these spectral differences. As the API mass predictions obtained using peak intensity data were in good agreement with the stated API mass of the Chlortrimeton tablets, it was decided to use only peak intensities.

As the initial HPLC study (discussed in chapter 3) demonstrated that the calculated mass of chlorpheniramine maleate in the 254 Chlortrimeton tablets analysed ranged between 3.36 and 4.81 mg, it was decided to re-predict the API mass values of the second set of Chlortrimeton tablets using a reduced mass calibration set (refer to section 5.2.4 for tablet preparation details). The correlation value calculated for the reduced range calibration plot constructed from normalised peak intensities was 0.982. Figure 56 illustrates the effect of the reduced range calibration set on the predicted mass values of chlorpheniramine maleate when using peak intensities.

By using a reduced range of concentrations in the calibration, the variability in the range of chlorpheniramine maleate masses predicted has lowered (see Table 21 for % CV values). Furthermore, the average predicted API mass obtained when using the reduced range calibration model based on normalised peak intensities is closer to that

of the states API mass (Figure 56). The average mass values for the API and the % CV values are summarised in Table 21.

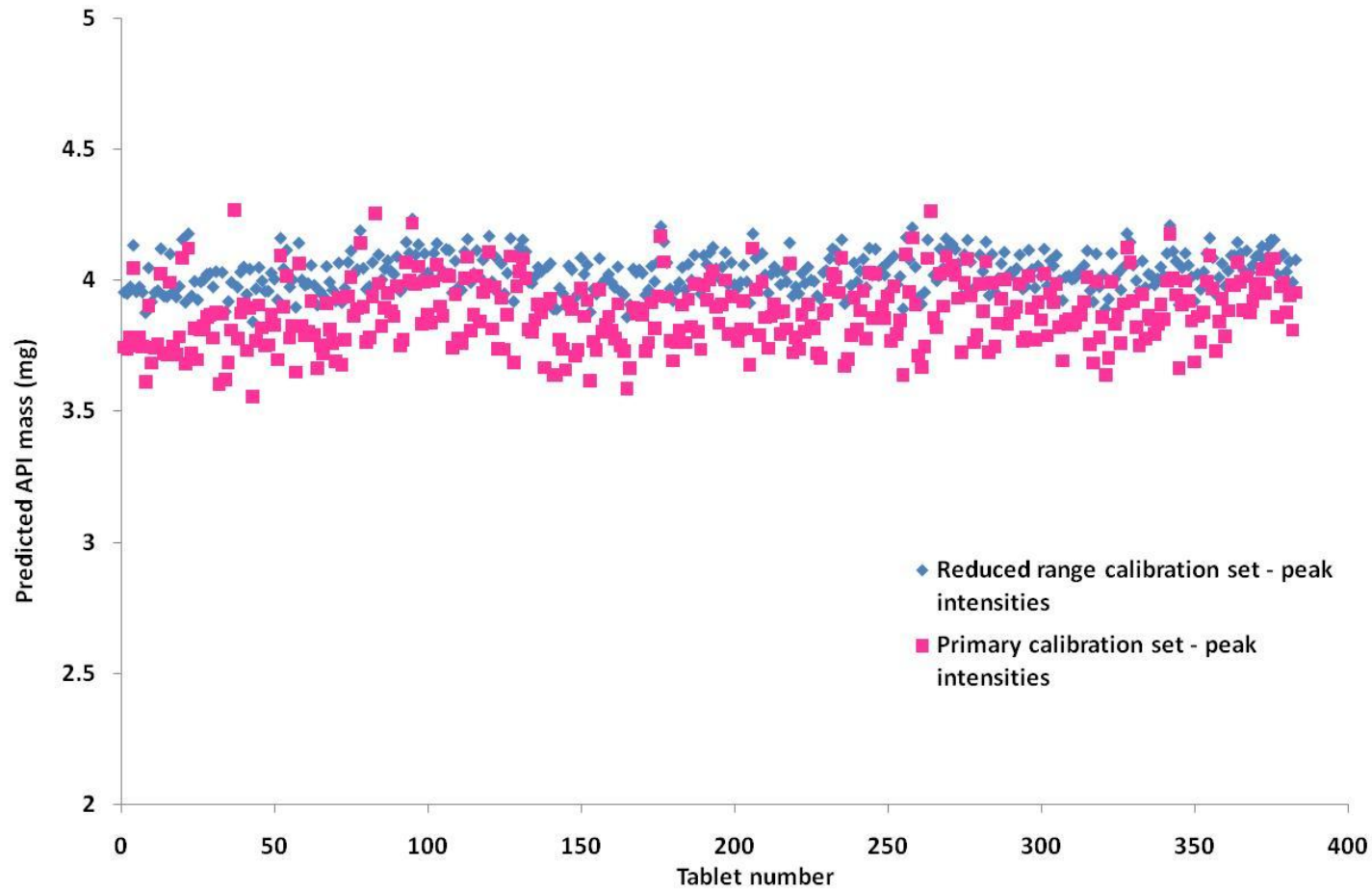


Figure 56 – Comparison of the predicted mass of chlorpheniramine maleate (API) in Chlortrimeton tablets calculated from the primary and reduced range calibration sets, using normalised peak intensities

**Table 21 – Average predicted API mass and calculated CV values using the primary and reduced range calibration models based on reflectance mode peak areas and intensities at 1594 cm<sup>-1</sup>;for intensity and area data n=383 and 90, respectively**

| Calibration model used                           | Average predicted API mass (mg) | % CV |
|--|---------------------------------|------|
| Primary calibration set – peak areas             | 4.8                             | 2.4  |
| Reduced range calibration set – peak areas       | n/a                             | n/a  |
| Primary calibration set – peak intensities       | 3.9                             | 3.3  |
| Reduced range calibration set – peak intensities | 4.0                             | 1.9  |

### ***5.3.2.3 Initial reflectance mode conclusions***

It has been shown that information depths of up to 4.57 mm can be achieved in reflectance mode when using flowers of sulphur, a collimated laser beam and a laser spot size of 3 mm. Furthermore, the discussed data has demonstrated the suitability of wide area illumination reflectance Raman spectroscopy for the determination of low concentration pharmaceutical tablets. Univariate prediction models based on external synthetic calibration sets covering the range 0- 8 mg API predicted the average API mass of the sample set to be 4.8 and 3.9 mg when using peak areas and peak intensities, respectively. It was found that reducing the calibration range improved the peak intensity calibration model slightly, providing an average predicted API mass of 4 mg and reducing the % CV of the measurements from 3.3 to 1.9 %; this was in good agreement with the average predicted mass of 3.98 mg reported from HPLC data (chapter 3) and furthermore, showed significantly lower CV values (6.3 % from HPLC data). Owing to the poor predicted values of the API

mass when using peak areas and furthermore, the differing spectral features of the analyte peak in the sample and calibration tablets, area data was not suitable for use in the prediction models.

It has therefore been demonstrated that univariate calibrations based on the change in the API peak intensity of a synthetic calibration set, covering the range 2.9-4.8 mg API produced the optimum predictions and moreover predicted API masses in good agreement with the stated API mass. Whilst previous studies have illustrated the advantages of wide area illumination Raman spectroscopy for the determination of pharmaceutical tablets, the majority of the investigations were concerned with samples containing approximately 30 – 90 % w/w API. The current study shows that the capabilities of this technique can be extended to samples containing as little as 2% w/w API and furthermore, this has been demonstrated using a sample size of > 380 tablets.

### 5.3.3 *Transmission Raman analysis of a calibration sample set to be used for the prediction of active ingredient mass in Chlortrimeton tablets*

In a similar fashion to the reflectance mode measurements, it was decided to analyse both sides of the calibration tablets in order to obtain a true measurement of the API whilst ensuring good quality calibration models were produced, eliminating any false results from analysing only one side of an inhomogeneous tablet. Figure 57 shows the transmission Raman spectra of both sides of a calibration tablet containing 4 mg chlorpheniramine maleate.

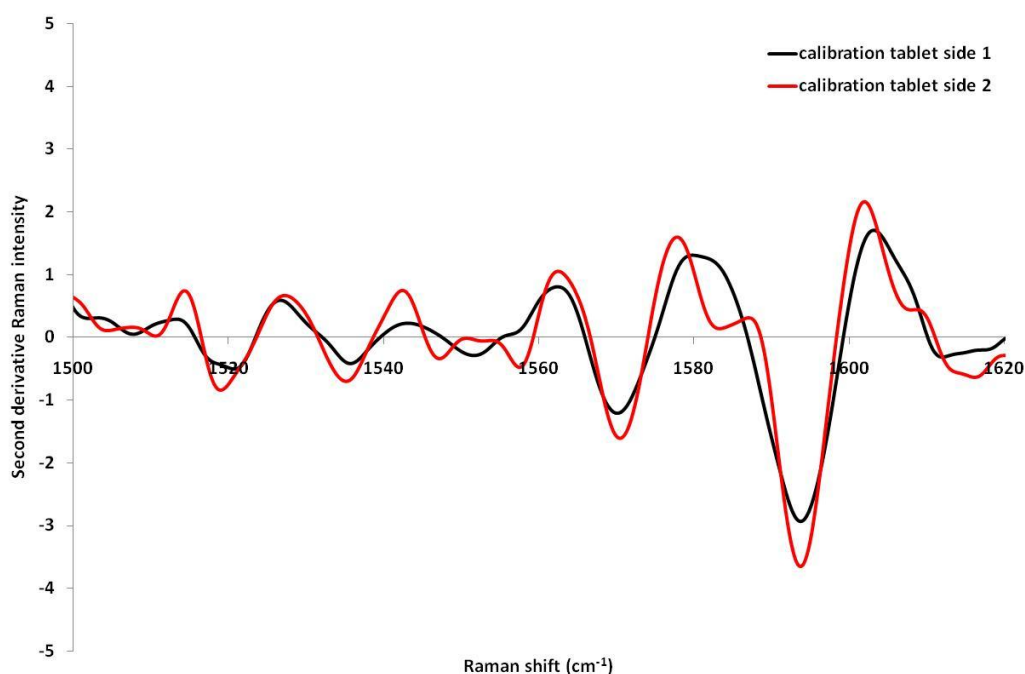


**Figure 57 – Second derivative transmission Raman spectra of both sides of a calibration tablet containing 4 mg of chlorpheniramine maleate**

Figure 57 shows the presence of the analyte peak at  $1594\text{ cm}^{-1}$  in the 2<sup>nd</sup> derivative Raman spectra of both sides of the calibration tablet. Furthermore, the spectra show that differences in the Raman intensities of the analyte peak are apparent which raises a question about how homogeneous the analyte is distributed in the tablet, and supports the decision to include both sides of the tablets in the calibration models; this was also found in the reflectance mode spectra of the same calibration tablet (refer to Figure 48).



Calibration plots constructed from the primary calibration set did not show a linear response and consequently API mass predictions were based on the reduced range calibration set (Figure 58). The peak intensities of chlorpheniramine maleate were normalised in both the calibration and Chlortrimeton tablets to account for any laser intensity fluctuations, as described for the reflectance mode data in section 5.3.2.2.

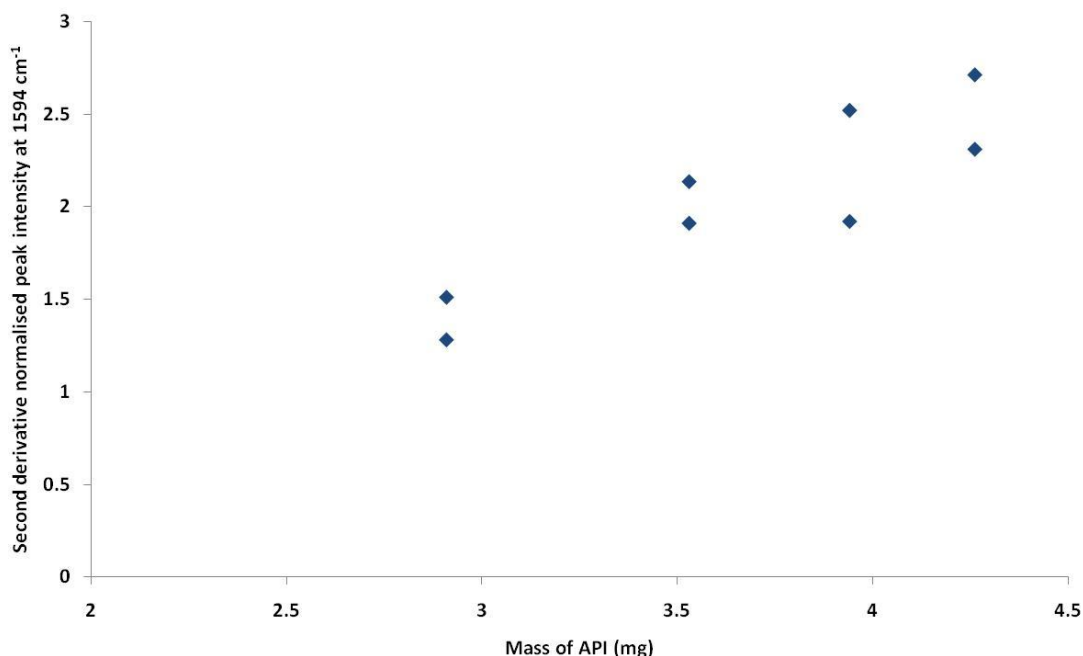


**Figure 58 - Calibration plot constructed from the reduced range calibration set containing chlorpheniramine maleate (API) and Avicel PH-101, showing the change in the second derivative normalised transmission Raman peak intensity at 1594 cm<sup>-1</sup> for both sides of the tablet, as the mass of the API is increased**

From Figure 58 it can be seen that the calibration graph constructed from the transmission mode reduced range calibration set data are not as successful as those constructed using reflectance mode data. There is a greater relative difference in the transmission Raman intensities from both sides of the tablet than obtained in reflectance mode. The observation that there is a marked difference in the intensity of the chlorpheniramine maleate depending on what side of the tablet is irradiated is interesting as it would be expected that more similar intensities would be obtained from transmission measurements as all of the tablet is analysed, whereas in

reflectance mode the signal is dominated by the initial 1 mm or so of the tablet<sup>59</sup>. The reduced range calibration tablet set was analysed and data are shown in Figure 59.

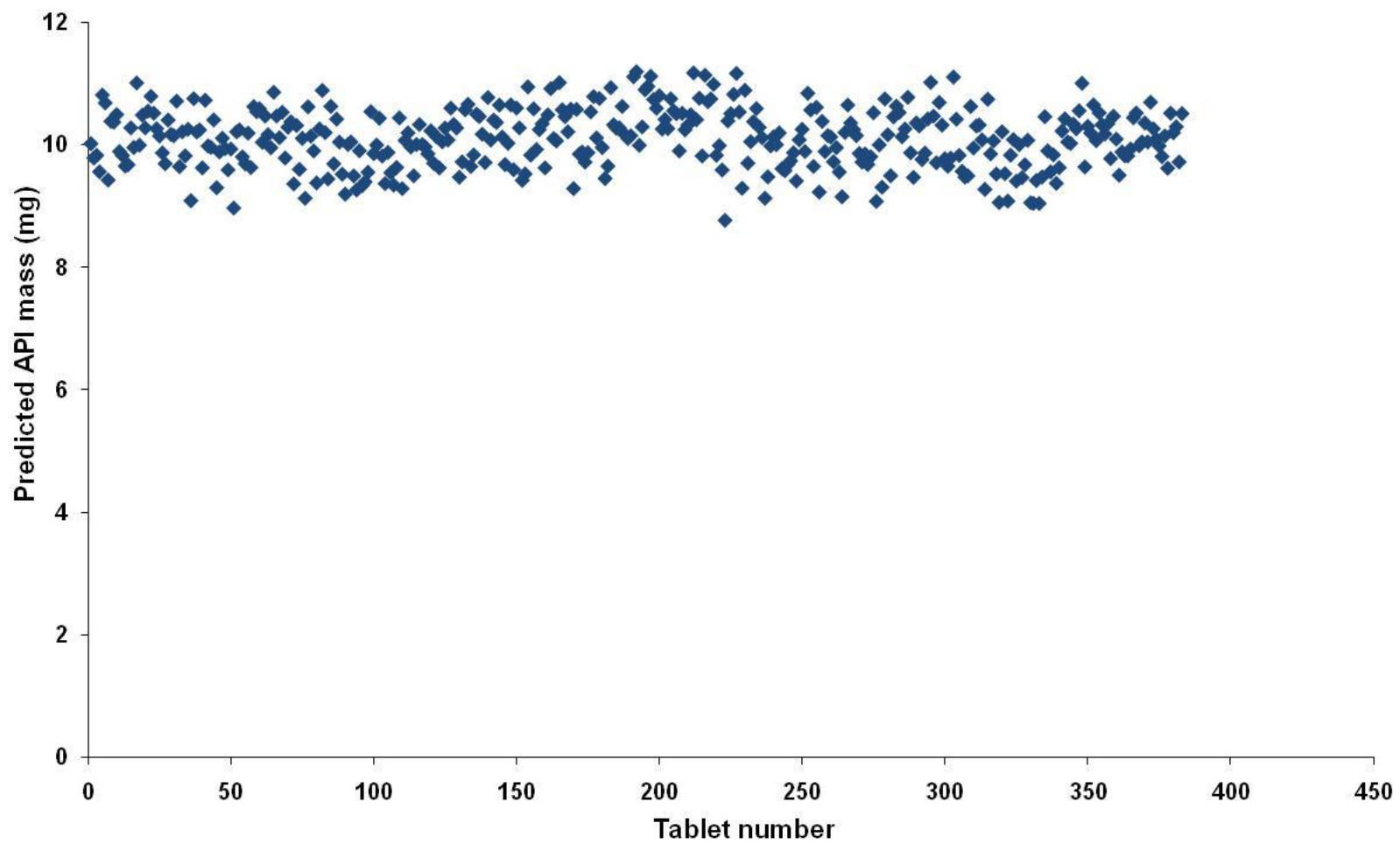
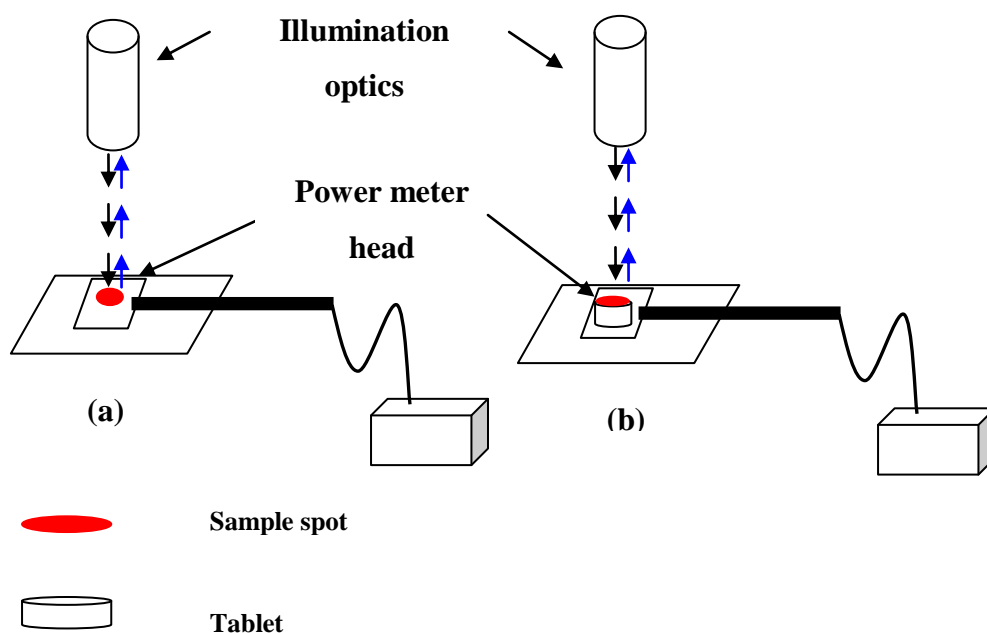


Figure 59 - Plot showing the predicted active ingredient mass in Chlortrimeton tablets from the second derivative transmission mode, normalised peak intensity at 1594  $\text{cm}^{-1}$  of the reduced range calibration set

From Figure 59 it is apparent that the API prediction is significantly greater than the stated API mass of 4 mg per tablet; the average predicted API mass and % CV were calculated to be 10.1 and 4.7 %. The masses of chlorpheniramine maleate in the Chlortrimeton tablets predicted from transmission Raman measurements are more than twice the values obtained from reflectance Raman spectrometry. As the results from reflectance Raman are more accurate (compared to the HPLC results and stated mass per tablet from the manufacturer), it may be surmised that the intensities of the transmitted Raman spectra of chlorpheniramine maleate in the standards are lower than expected compared to the samples; this suggests that the propagation of the Raman photons in transmission mode is different for the standards compared to the Chlortrimeton tablets.

The results discussed in chapter 4 demonstrated that the propagation of photons in transmission mode varied with the physical properties of the solids through which they penetrated. It was shown that when propagating through a body of small, granular particles that could pack efficiently, the penetration power of the Raman and Rayleigh photons was impeded more than when they propagated through larger particle size fractions of the same material. Furthermore, it was shown that granular particles in the range 150-212  $\mu\text{m}$  attenuated both Raman and Rayleigh photons to a greater extent than needle shaped particles in the same size range. The effect of the sample physical properties on the propagation of Raman photons in reflectance mode was also investigated. Whilst data showed similar trends to those seen with the transmission mode measurements, the particle size and shape effects were less obvious, only minor differences in the reflectance Raman response were recorded when the particle size of the sample material was increased. It was concluded from this data that owing to the nature of transmission mode measurements, the recorded responses are greatly affected by the particle size and shape of the sample material, much more so than for the reflectance mode measurements which are mainly comprised of surface generated Raman signals rather than those originating from deep within the sample body<sup>59</sup>.

Owing to the conclusions drawn from the data discussed in chapter 4, it was thought that the poor transmission mode predictions could be attributed to a mismatch of the composition and particle sizes of the Chlortrimeton and calibration tablet constituents, therefore resulting in differences in the propagation of the Raman photons through the material. Furthermore, based on the data discussed in chapter 4, it would be expected that the reflectance mode predictions of chlorpheniramine maleate mass would be much less sensitive to variations in the physical properties of the materials. To investigate the effect of the particle size of the sample materials, a comparison of the propagation of light through a series of calibration tablets made from different particle size ranges of Avicel and a Chlortrimeton tablet was made in both reflectance and transmission Raman modes using the configurations illustrated in Figure 60 and Figure 61.



**Figure 60 – Schematic of the reflectance mode experimental set-up to assess the effect of particle size on the propagation of light through a tablet; (a) configuration with no sample, (b) configuration with sample.**

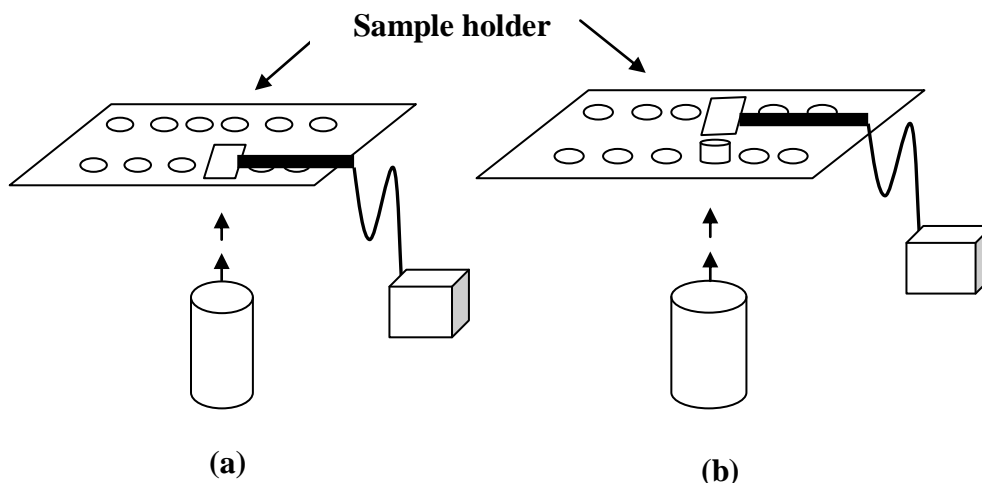


**Figure 61 - Schematic of the transmission mode experimental set-up to assess the effect of particle size on the propagation of light through a tablet; (a) configuration with no sample, (b) configuration with sample.**

Before measurements were made using the reflectance mode set-up shown in Figure 60, a power meter head was placed onto the sample tray and the laser was turned on, with the laser beam positioned on the centre of the power meter head. The position of the power meter head was adjusted until the maximum reading was obtained and the power meter was then taped to the sample tray to maintain a constant position. The value shown on the power meter when the laser beam was directed onto the power meter head but no sample was present, was recorded. To assess the effect that calibration tablets comprised of particles of different size, had on the power meter reading, the laser was turned on and the resulting power was recorded when tablets were placed on top of the power meter head. This was repeated three times and an average reading for each sample was calculated. Equivalent transmission measurements were also made (refer to Figure 61). To measure the power through a calibration tablet in the transmission configuration, the tablet was placed into the sample holder and the power meter head was placed on top of the tablet. The value shown on the power meter was recorded. This was repeated three times for each sample and an average value was calculated. A sample spot size of 3 mm was used for both the reflectance and transmission measurement configurations.

The data presented in Table 22 demonstrates that there is no significant difference in the power measured through calibration tablets made from different grades of Avicel when the reflection mode configuration is used. This is also the case for the transmission mode equivalent shown in Table 23.

**Table 22 – Reflectance mode power measurements recorded through calibration tablets containing Avicel of varying particle sizes and a Chlortrimeton tablet; acquired with a 3 mm laser spot size, n=3**

| Tablet  | Average particle size (µm) | Measured power (± 1 mW) |
|---|----------------------------|-------------------------|
| No sample   | n/a                        | 168.4                   |
| Calibration tablet comprised of Avicel PH-101 (3.94 mm thick) | 50                         | 0.6                     |
| Calibration tablet comprised of Avicel PH-200 (3.92 mm thick) | 180                        | 0.6                     |
| Calibration tablet comprised of Avicel PH-105 (3.89 mm thick) | 20                         | 0.6                     |
| Chlortrimeton   | Not known                  | 0.8                     |

**Table 23 - Transmission mode power measurements recorded through calibration tablets containing Avicel of varying particle sizes and a Chlortrimeton tablet; acquired with a 3 mm laser spot size, n=3**

| Tablet  | Average particle size (µm) | Measured power (± 1 mW) |
|---|----------------------------|-------------------------|
| No sample   | n/a                        | 249.4                   |
| Calibration tablet comprised of Avicel PH-101 (3.94 mm thick) | 50                         | 0.1                     |
| Calibration tablet comprised of Avicel PH-200 (3.92 mm thick) | 180                        | 0.2                     |
| Calibration tablet comprised of Avicel PH-105 (3.89 mm thick) | 20                         | 0.1                     |
| Chlortrimeton   | Not known                  | 0.4                     |

It is apparent from Table 22 and Table 23 that the measured power with no sample present is significantly different for the two sampling geometries; the power transmitted through a tablet in the transmission configuration is approximately 50% greater than that in the reflectance mode. This suggests that there are significant optical configuration differences at the laser delivery point from the transmission illumination unit compared to that of the reflectance mode PhAT probe illumination optics. Kasier Optical Systems Inc., confirmed the potential for differences in the illumination optics of the two geometries but would not provide details of any specific differences in the optical geometries.

In order to investigate the effect of material particle size on the reflectance and transmission Raman measurements, it was decided to re-predict the API masses of the Chlortrimeton sample set using primary calibration sets made with Avicel PH-105 (average particle size 20 µm) and Avicel PH-200 (average particle size 180 µm)



in order to provide examples of particle size ranges both smaller and larger than the primary calibration set constructed from Avicel PH-101 (average particle size 50  $\mu\text{m}$ ). Calibration plots were constructed using the API peak intensity at  $1594\text{ cm}^{-1}$  and both sides of each calibration tablet were analysed. Correlation values of 0.98 and 0.99 were calculated for the Avicel PH-105 and PH-200 calibrations, respectively, as is shown in Table 24.

**Table 24 – Calibration line equation for the calibration plots constructed from calibration tablets containing Avicel PH-105 and PH-200 using the transmission Raman peak intensity at  $1594\text{ cm}^{-1}$**

| <b>Calibration model</b> | <b>Calibration line equation</b> |
|--------------------------|----------------------------------|
| PH-105 peak intensities  | $y = 0.9531x + 0.4071$           |
| PH-200 peak intensities  | $y = 1.7121x + 0.6336$           |
| PH-101 peak intensities  | $y = 0.8047x - 0.9081$           |

Figure 62 shows the effect of the different Avicel grades on the predicted mass of chlorpheniramine maleate in the Chlortrimeton samples using the transmission Raman peak intensities. For comparison, analyte masses based on reflectance Raman measurements were obtained using calibration tablets comprised of Avicel PH-105 and PH-200. As it was previously shown that the predicted values from the peak intensity reflectance mode measurements were closer to that of the stated mass compared to those obtained from the peak area, only the predictions based on the peak intensity was plotted. Figure 64 shows a comparison of the resulting predicted API masses of the Chlortrimeton samples from calibration tablets comprised of Avicel PH-101, 105 and 200, using the reflectance Raman peak intensity at  $1594\text{ cm}^{-1}$ .

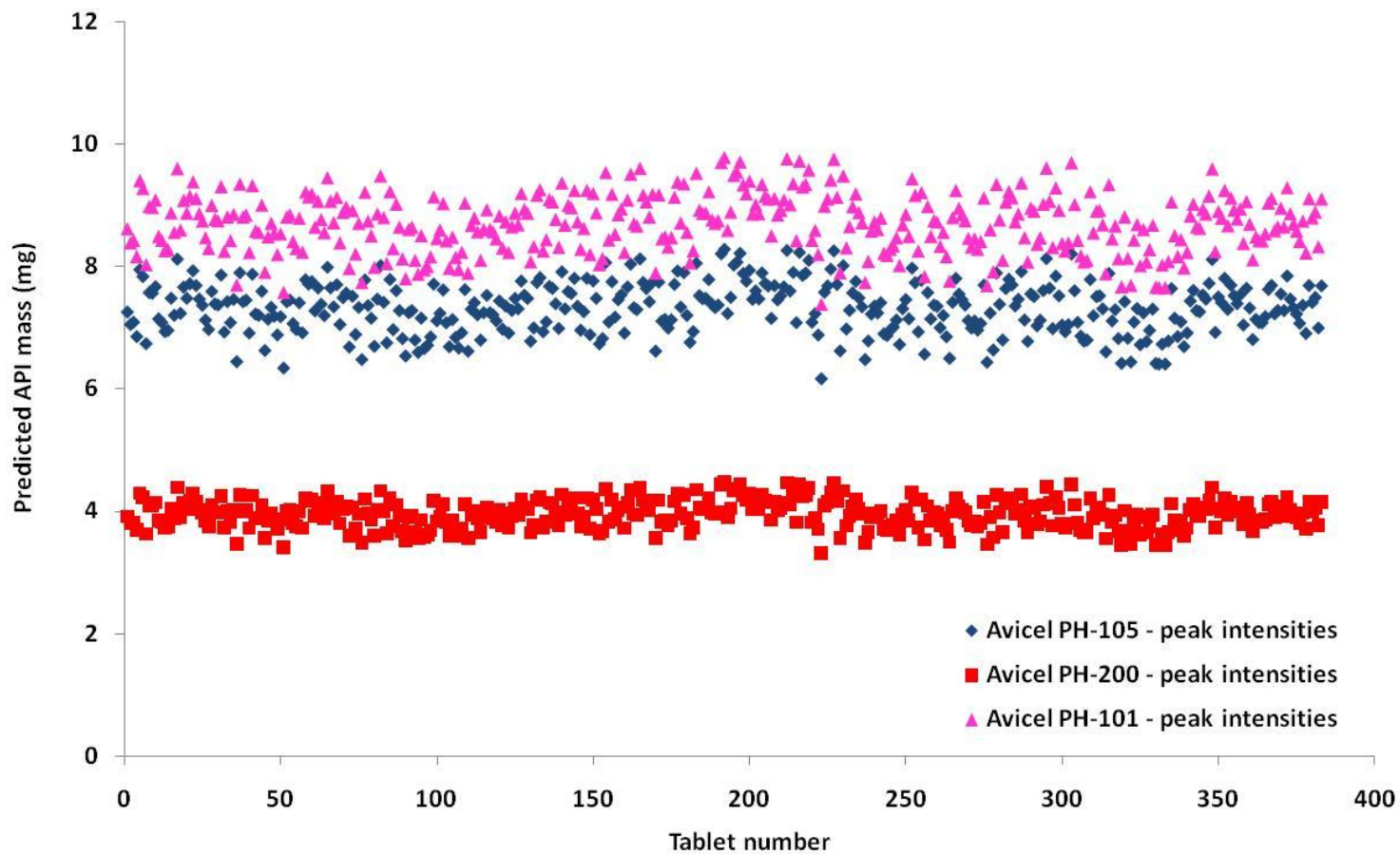
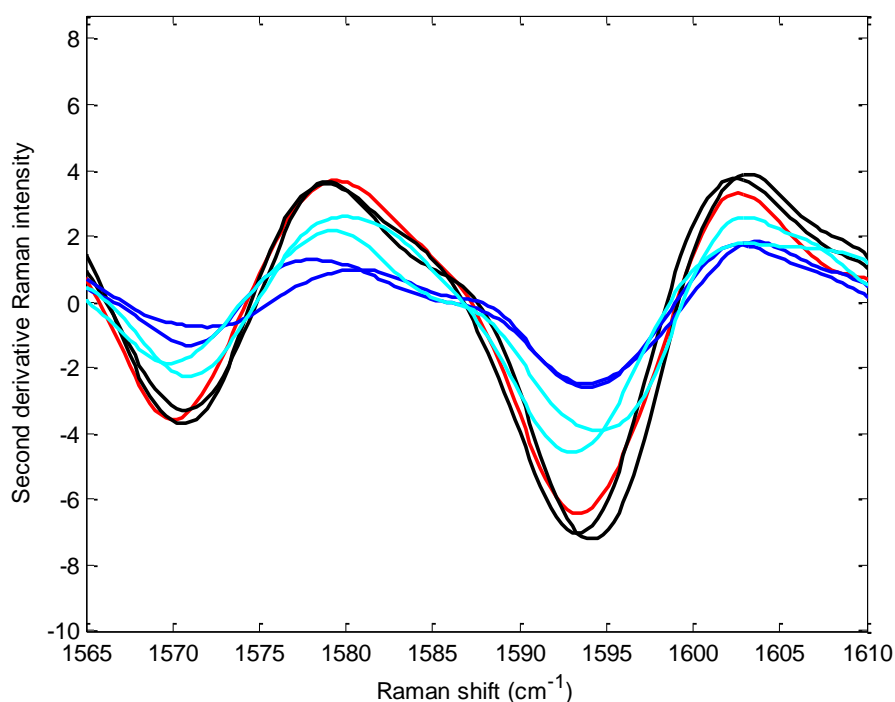


Figure 62 – Comparison of the predicted API mass values of a Chlortrimeton sample set from calibration tablets comprised of Avicel PH-101, 105 and 200 using the transmission mode peak intensity at  $1594\text{ cm}^{-1}$

Figure 62 shows a definite effect of particle size on the predicted API mass values in transmission mode and the data shown, illustrates that by increasing the average particle size of the Avicel used in the calibration tablets, the average predicted API mass is found to be in good agreement with the stated API mass (4 mg). This suggests that the calibration tablets made using Avicel PH-200 are most similar to the Chlortrimeton tablets, with respect to the material properties, in particular the material particle size; this is emphasised by the spectra shown in Figure 63.



**Figure 63 – Second derivative transmission Raman spectra showing the region 1565-1610  $\text{cm}^{-1}$  for calibration tablets containing approximately 4 mg of chlorpheniramine maleate, comprised of Avicel PH101 (dark blue), PH105 (light blue), PH200 (black) and a Chlortrimeton tablet (red)**

Figure 63 shows that even though the mass in each of the calibration tablets is the same, the intensities are very different. In comparison to the API peak in the spectrum of the Chlortrimeton tablet the peak intensities for the calibration tablets comprised of Avicel PH101 and 105 are significantly smaller which would result in an over estimation of the analyte mass. Conversely, the intensities of the API peak in the spectra corresponding to the Chlortrimeton tablet and the calibration tablet

comprised of Avicel PH200 are much more similar in size and consequently a predicted API mass close to that of the mass in the sample tablet would be obtained.

From Figure 62, it can be seen that the highest average mass prediction is observed when calibration tablets containing Avicel PH-101 are used. As the average particle size of Avicel PH-101 is greater than that of PH-105, it would be expected that predictions based on Avicel PH-105 calibration tablets would produce the greater mass value. This anomaly can be attributed to the overlapping particle size ranges of the two Avicel grades (refer to Table 19). Despite having different average particle sizes, these values only differ by 30  $\mu\text{m}$  and furthermore the range of particle sizes overlap significantly thus it would be expected that differences in the propagation of light through these materials would be negligible; the spectra shown in Figure 63 also show very similar peak shapes for the calibration tablets comprised of Avicel PH101 and 105. From Figure 62 it is clear that particle effects have an influence on transmission mode measurements, however it is important to note that particle size and shape may not be the only factors and that absorption characteristics of the materials in the tablets may have to be taken into consideration. It is possible that the absorption characteristics of Avicel and the Chlortrimeton tablets are significantly different such that by using Avicel PH200, the differences are compensated for; consequently it should not necessarily be assumed that the average particle of the material in the sample tablet is 180  $\mu\text{m}$  (the average particle size of Avicel PH 200).

**Table 25 – Comparison of the average predicted mass of chlorpheniramine maleate and % CV values obtained for transmission Raman measurements when calibration tablets containing different Avicel grades are used; n = 383; expected mass, 4 mg.**

| Prediction model        | Average predicted API mass (mg) | % CV |
|-------------------------|---------------------------------|------|
| PH-101 – peak intensity | 8.7                             | 5.4  |
| PH-105 – peak intensity | 7.3                             | 5.6  |
| PH-200 – peak intensity | 3.9                             | 5.8  |

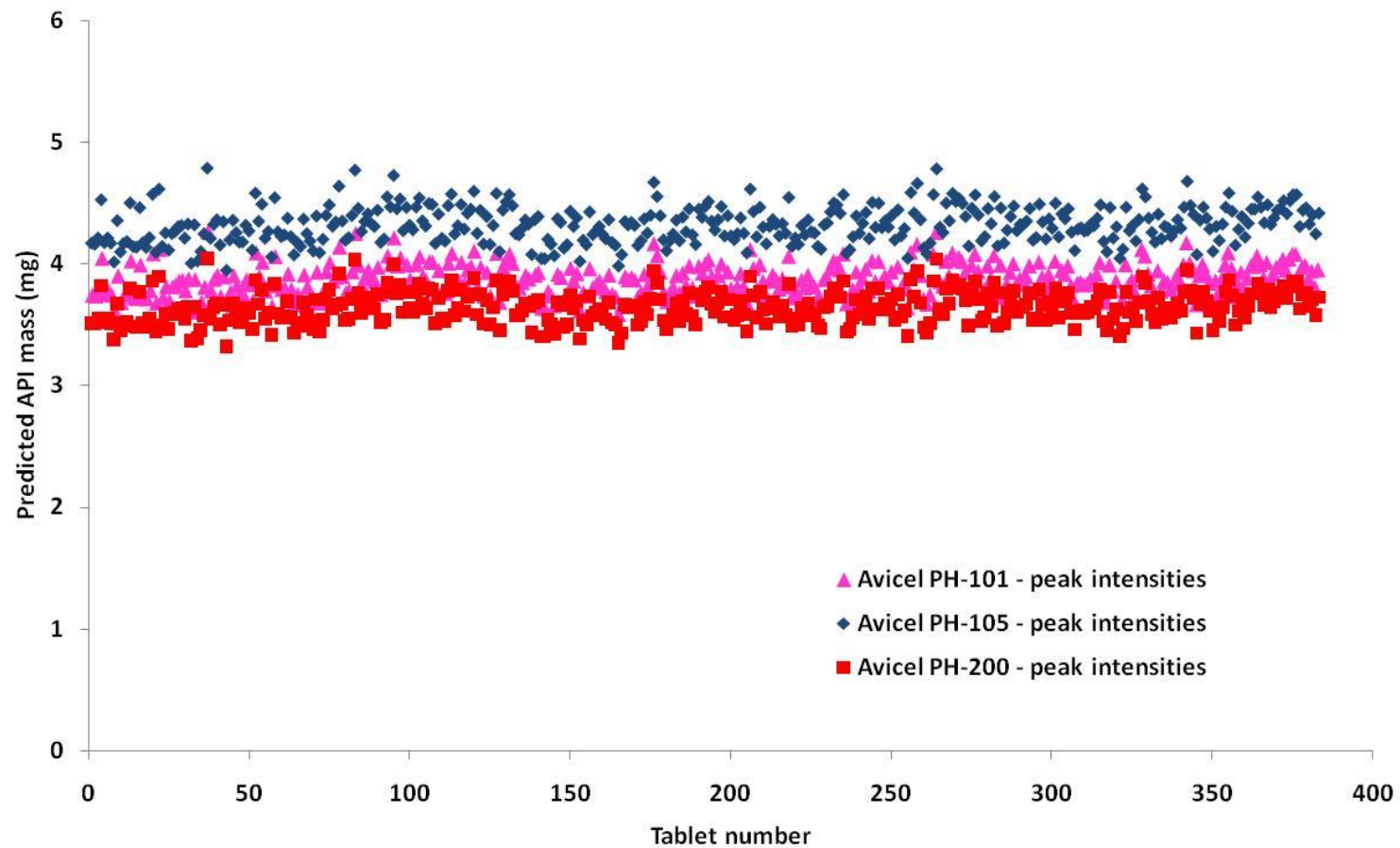


Figure 64 - Comparison of the predicted API mass values of a Chlortrimeton sample set from calibration tablets comprised of Avicel PH-101, 105 and 200 using the reflectance mode peak intensity at  $1594\text{ cm}^{-1}$

The data shown in Figure 64 suggests that reflectance mode Raman measurements are less sensitive to the material particle size than transmission mode measurements. It can be seen that regardless of the particle size range of Avicel used in the calibration tablets, the range of the predicted API masses is relatively small (3.6-4.3 mg) compared to those seen in the corresponding transmission mode data plots (3.9-8.0 mg). Furthermore, when calibration tablets comprised of Avicel PH101 are used in the reflectance Raman measurements, the predicted API mass values are closer to the stated mass than when calibration tablets comprised of Avicel PH200 are used; this suggests that the preferred material particle size used for the preparation of external calibration tablets would differ depending on the mode of Raman measurements used. This data is in good agreement with that discussed in chapter 4 which concluded that reflectance Raman measurements were only mildly sensitive to variations in the physical properties of sample materials and furthermore agrees with the power readings detailed in Table 22. Additionally, this effect can be explained by the findings of Matousek and Parker which stated that 88% of the reflectance Raman signal originates from surface generated Raman signals<sup>59</sup>. As transmission mode measurements are not strongly influenced by surface signals, rather the spectra are comprised of information from different depths within the sample body, the transmission mode Raman photons will be in contact with more of the sample and hence will be strongly influenced by their environment (particle size and shape). Conversely, the majority of the collected reflectance Raman photons do not emanate from deep within the sample and hence the sample characteristics will not affect (to the same extent) the resulting spectra.

In order to compare the data obtained from HPLC and both reflectance and transmission Raman measurements, 25 tablets from the sample set of 383 analysed by both Raman modes were chosen and analysed by HPLC using the method detailed in chapter 3. The average chlorpheniramine masses calculated from the three analysis techniques were compared using a t-test in order to determine if statistical differences in the calculated values existed. Table 26 and Table 27 show that the

transmission mode measurements yielded an average chlorpheniramine maleate mass closest to that of the stated mass of 4 mg however, the error associated with the transmission measurements was also the largest of the three analysis methods. Furthermore, it can be seen for Table 27 that the t-test results suggest statistical differences between the mean values calculated using HPLC and transmission Raman.

**Table 26 – Comparison of the average mass of chlorpheniramine maleate in 25 Chlortrimeton tablets acquired from HPLC, reflectance and transmission Raman spectrometry**

| Analysis technique | Average mass of chlorpheniramine maleate (mg) | Error ( $\pm$ 2 standard deviations) |
|--------------------|---|--------------------------------------|
| HPLC               | 3.85  | 0.105                                |
| Reflectance Raman  | 3.91  | 0.201                                |
| Transmission Raman | 4.03  | 0.239                                |

**Table 27 – Comparison of t-test data for the average calculated mass of chlorpheniramine maleate from 25 Chlortrimeton samples using three different analysis methods**

| Analysis methods being compared    | T-test result |
|------------------------------------|---------------|
| HPLC and reflectance Raman         | Pass          |
| Transmission and reflectance Raman | Pass          |
| HPLC and transmission Raman        | Fail          |

### ***5.3.3.1 Initial transmission mode conclusions***

- It is easier to use external, unmatched standard sets for reflectance mode measurements compared to transmission measurements.
- In transmission mode measurements, matrix effects (particle size, shape and absorption effects) have to be matched between the external standards and samples to achieve better accuracy.



### 5.3.4 Raman mapping of tablets

From the reflectance mode Raman analysis of the primary calibration set, different Raman responses were sometimes seen for each side of the same tablet, as illustrated in Figure 65.

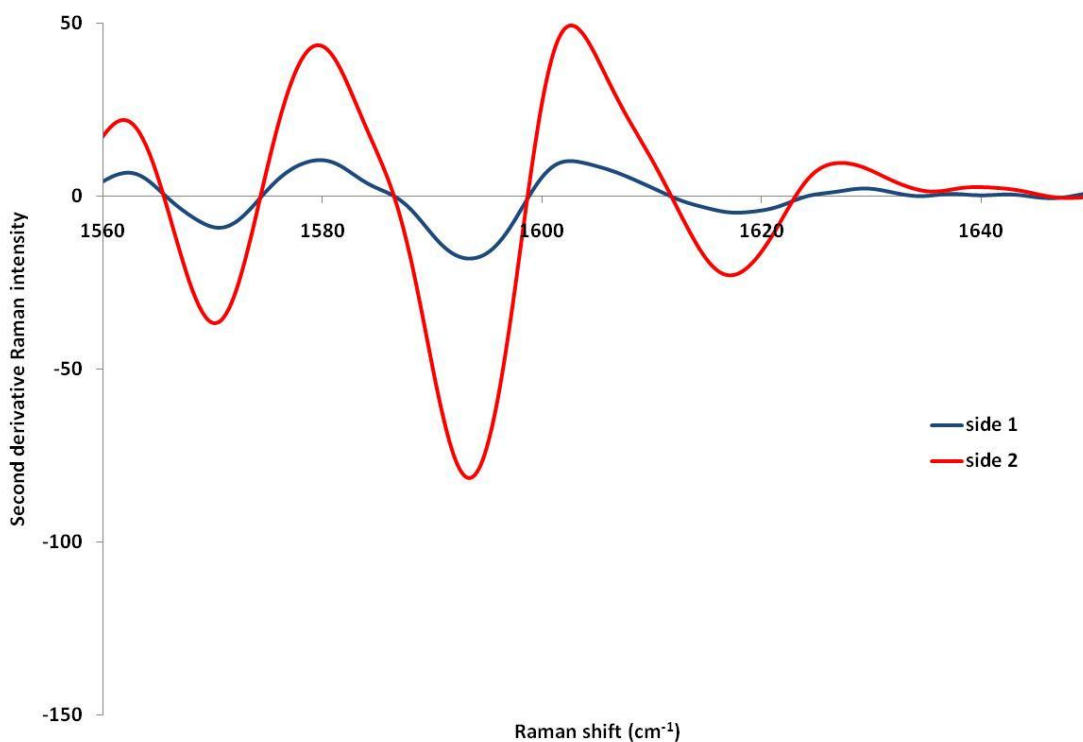


**Figure 65 – Second derivative reflectance Raman spectra of both sides of a calibration tablet showing the chlorpheniramine maleate peak at 1594 cm<sup>-1</sup>**

From Figure 65 it is apparent that there is a significant difference in the response in the API region of 1594 cm<sup>-1</sup> seen for sides one and two of the calibration tablet. Such a large difference would suggest the calibration tablet to be inhomogeneous, with more active ingredient present on one surface. Owing to the surface bias of reflectance Raman measurements, the spectra do not provide information regarding the degree of homogeneity of the sample body. If it was assumed that the spectra shown in Figure 65 imply an inhomogeneous distribution of the analyte, such a

calibration tablet would not yield good accuracy based on reflectance mode measurements. This emphasises the importance of choosing external standards for reflectance Raman where the responses from both sides are similar, if not the same. As can be seen from Figure 65, analysing both sides of a calibration tablet is a means of checking the success of its preparation. Figure 66 shows the transmission Raman response recorded for both sides of the same calibration tablet analysed in reflectance mode (Figure 65).

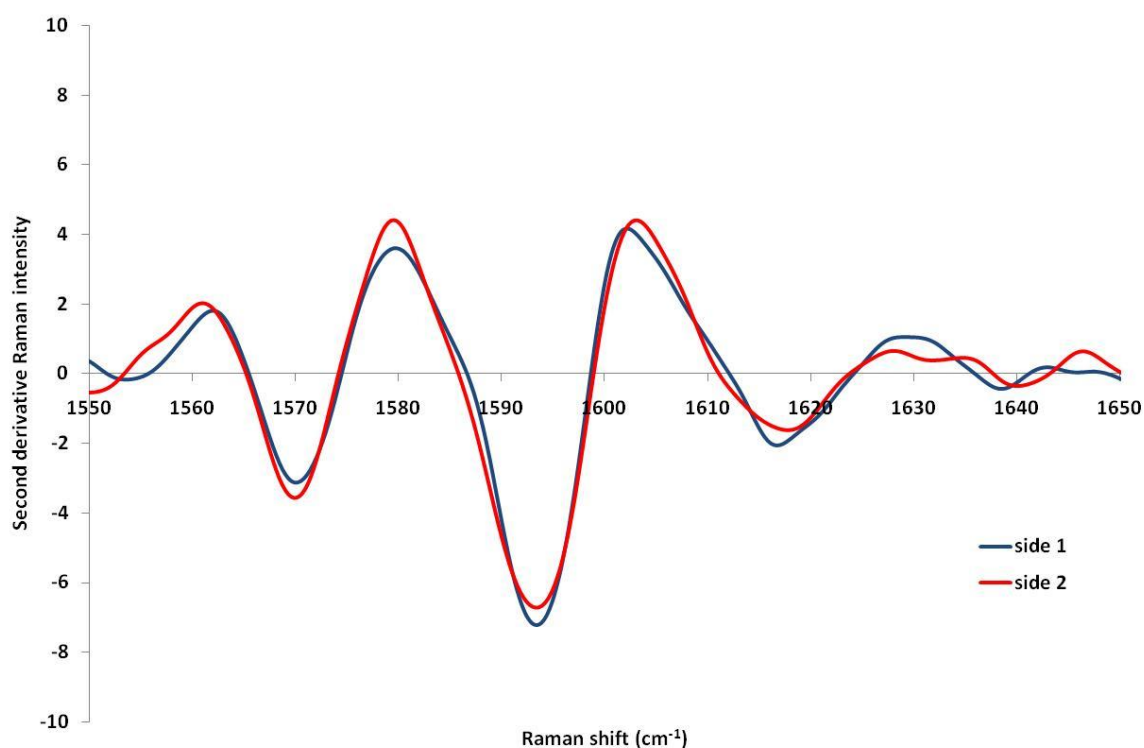


**Figure 66 - Second derivative transmission Raman spectra of both sides of a calibration tablet showing the API peak at 1594 cm<sup>-1</sup>**

The difference in the transmission Raman response of both sides of the calibration tablet shown in Figure 66 is much less than that was seen with the reflectance mode measurements. This reinforces that transmission and reflectance measurements yield different types of information and supports the findings detailed in section 5.3.3 and chapter 4. Furthermore, the marked differences between the reflectance and transmission spectra suggest that rather than the API being inhomogeneously distributed throughout the body of the sample, clumps of API are present on one

surface of the tablet. This is identified by the reflectance mode measurements which are biased towards surface generated Raman signals<sup>59</sup> but not by the transmission mode measurements which provide an overall picture of the entire sample body. The different responses shown by the two sampling configurations indicate the potential of Raman spectroscopy to provide rapid homogeneity screening of tablets however, reflectance mode measurements seem better than transmission measurements for indicating inhomogeneous distributions of the analyte if both sides are measured.

In order to confirm that the conclusions drawn from Figure 65 and Figure 66 were valid, the surface of both sides of the calibration tablet were mapped using a confocal Raman probe (refer to section 5.2.5). Figure 67 and Figure 68 show the micro-maps of side 1 and 2 of a calibration tablet, respectively.

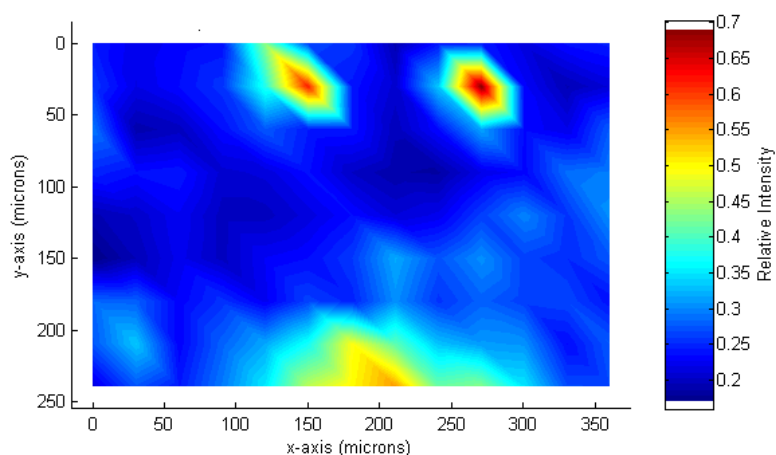


**Figure 67 – Micro-map of a 250 x 350  $\mu\text{m}^2$  area of side 1 of a calibration tablet containing approximately 6.6 mg Chlorpheniramine maleate**

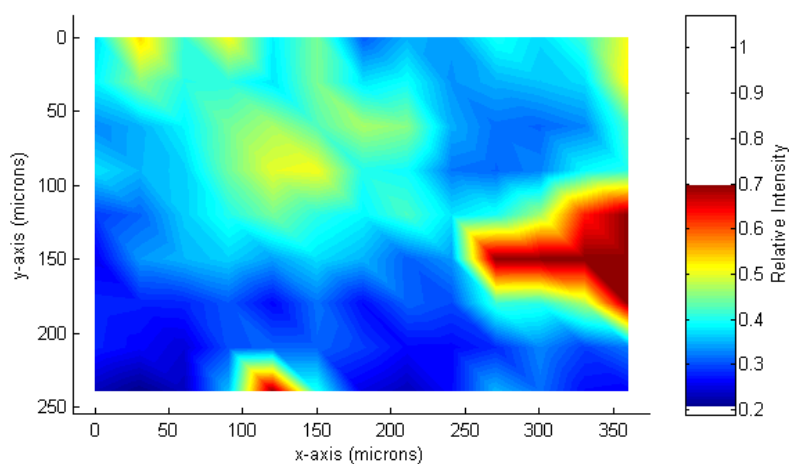


**Figure 68 - Micro-map of a 250 x 350  $\mu\text{m}^2$  area of side 2 of a calibration tablet containing approximately 6.6 mg Chlorpheniramine maleate**

From Figure 67 it can be seen that the micro-map of side 1 of the calibration tablet is dominated by excipient owing to the dark blue colour covering the majority of the map; this would be expected owing to the tablet being comprised of > 90% excipient. Analyte material (chlorpheniramine maleate), indicated by red areas can be seen as small discrete spots that are not evenly distributed throughout the map; this supports the presence of a low intensity analyte peak in the spectrum corresponding to side 1 of the tablet (refer to Figure 65). In comparison the micro-map of side 2, shown in Figure 68 highlights the presence of a large clump of analyte and whilst there is not an even distribution of red areas over this map, the dominating colours are lighter than those seen in Figure 67 which could suggest the presence of analyte under the surface layers of the sample that is not identified as red owing to the limited penetration depth and hence sampling volume of confocal Raman probe heads<sup>43</sup>. This therefore accounts for the large analyte peak in the spectrum of the second side of the calibration tablet (refer to Figure 65). In order to obtain a map of the entire tablet surface, PhAT maps of the same calibration tablet were acquired as is shown in Figure 69 and Figure 70.

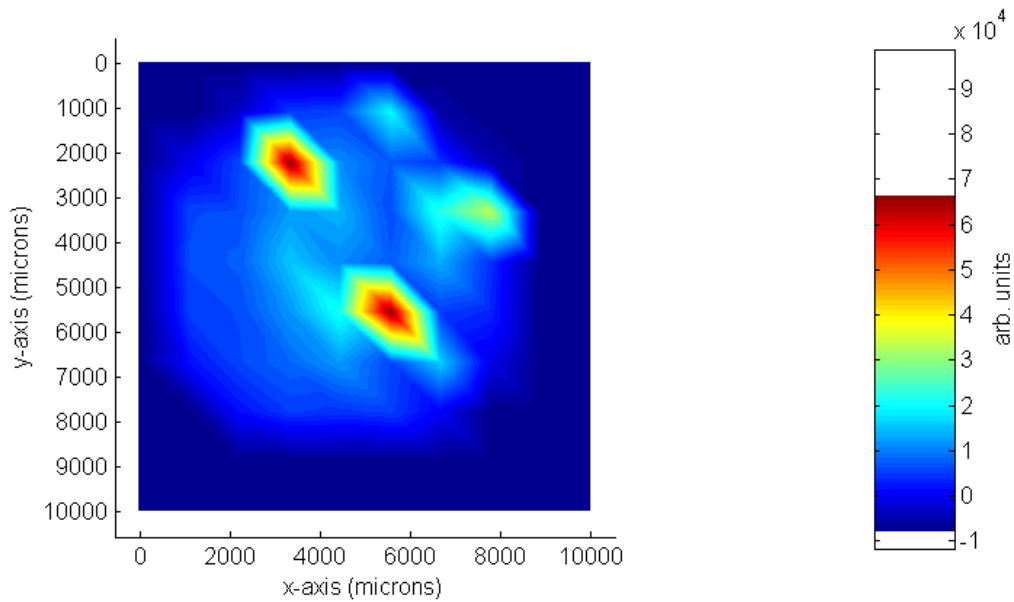


**Figure 69 – PhAT map of side 1 of an 8 mm diameter calibration tablet containing**

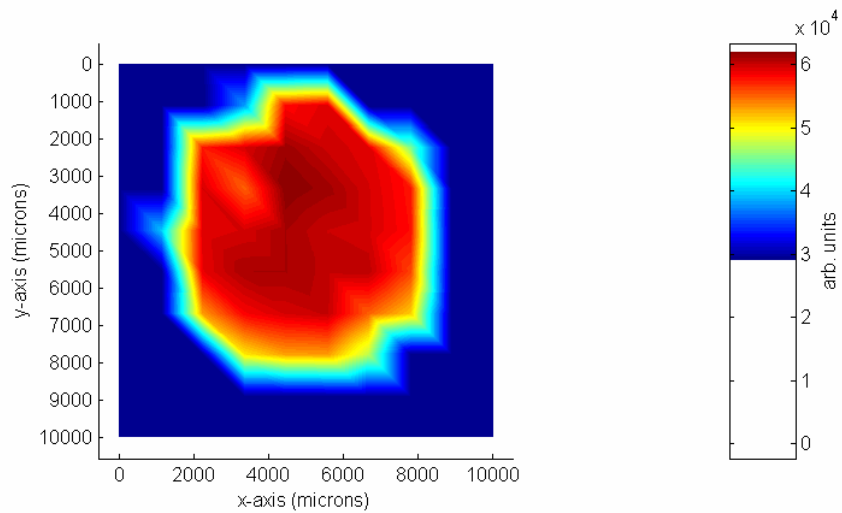


**Figure 70 - PhAT map of side 2 of an 8 mm diameter calibration tablet containing approximately 6.6 mg Chlorpheniramine maleate**

Figure 69 and Figure 70 show PhAT maps of a calibration tablet 8 mm in diameter – the maps are shown over a 10 x 10 mm area and the extra area mapped corresponds to the aluminum sample holder. Figure 69 shows, as would be expected, that side 1

of the tablet is mainly comprised of excipient material (owing to the blue colour dominating the map) and that similar to the micro-map, two discrete spots are shown, indicative of the analyte. This confirms that there is not a uniform distribution of the API over the surface of side 1 of the calibration tablet. Figure 70, however shows large amounts of active material are present on side 2 of the sample. Whereas the map shown in Figure 69 is dominated by excipient (as would be expected), the analyte is shown to dominate in Figure 70. Furthermore, the intensity of the red colour covering the surface of the map in Figure 70 varies which suggests that the amount of analyte present may be greater in some areas than other; this is supported by the large analyte clump seen in Figure 68. Furthermore, the larger proportion of analyte seen from the PhAT map corresponding to side 2 compared to side 1 explains the larger analyte peak present in the reflectance mode spectrum of side 1 of the tablet, shown in Figure 65.

#### ***5.3.4.1 Raman mapping conclusions***

Reflectance Raman spectra of a calibration tablet illustrated differences in the amount of API on both sides. Transmission mode spectra did not confirm this finding, rather it displayed essentially the same Raman response on both faces of the tablet; this was also identified in chapter 4 with a bi-layer sample comprised of a compressed sulphur disk and Avicel powder. This was thought to be a consequence of the different sampling methods of the two measurement types; surface biased reflectance measurements compared to ‘averaged’ transmission mode measurements. The different Raman responses identified by the reflectance mode measurements were confirmed by Raman micro-maps. Reflectance Raman mapping with the PhAT probe proved useful to examine inhomogeneities in the distribution of chlorpheniramine maleate in calibration tablets prepared from Avicel. The study has shown that the combination of reflectance Raman spectroscopy and PhAT Raman mapping is potentially suited for the rapid homogeneity screening of pharmaceutical tablets.

## 5.4 Conclusions

- Although transmission mode measurements give a more representative analysis of the tablet, either matrix matched calibration tablets or a previously analysed set of samples (as standards) are required for accurate analysis.
- Although reflectance Raman is less affected by a mis-match in the tablet composition between samples and standards, it is more susceptible to problems if the analyte is inhomogenously distributed in the tablets.
- Provided that tablet composition is taken into account for transmission measurements and inhomogeneities are absent for reflectance mode measurements, both modes can give accurate analysis for chlorpheniramine maleate at the 2 % w/w level.



## **6. The development of intracavity laser absorption spectrometry for trace liquid analysis**

High performance liquid chromatography (HPLC) is widely used for chemical analysis in many industries, including the pharmaceutical industry. The technique relies on having a sensitive detection method that is capable of quantifying the small amounts of separated compounds in sample components that elute from the chromatographic column. The most commonly used detector in HPLC is the UV-visible flow cell, such as that used in the tablet analysis study described in chapter 3. However, this detector relies on the separated compounds having a chromophore as part of the molecule, such as an aromatic ring that can absorb the UV-visible radiation. Analytes that do not possess a chromophore have to be chemically altered, either prior to analysis of the sample or after the compounds are separated. This derivatization step is time consuming and so is often not used, making HPLC less applicable to a number of applications. The purpose of derivatization in HPLC is to increase the absorptivity of the absorbing species, and in doing so, improve the sensitivity of the measured absorbance. An alternative way to increase the sensitivity is to increase the pathlength. In most applications, especially in HPLC, a significant physical increase in the pathlength of a conventional flow cell is not possible. However, there are procedures that can achieve increases in the effective pathlength, and one of these, intracavity laser absorption spectrometry, is evaluated in the preliminary investigation described in this chapter.

### **6.1 Introduction**

The potential to successfully analyse trace components within a process is essential for many different industries. As the presence of impurities in active pharmaceutical ingredients can have a significant impact on their quality and hence safety, the ICH guidelines specifically focus on ‘impurities in new drug substances’<sup>140</sup>. Furthermore, trace analysis has become increasingly important in the cleaning of chemical plants, where inadequate cleaning procedures may lead to a number of contaminants (such as degradation products of the API, solvents and micro-organisms) being present in the next manufactured batch. Consequently, as a regulatory requirement and a quality control measure, cleaning protocols are followed and chromatographic

techniques such as HPLC are commonly used to perform the analysis of cleaning swabs and rinse solutions collected from the reaction vessels. The ability to perform trace analysis in process environments also allows for less obvious advantages such as the facility to monitor the kinetics of a process rapidly, allowing potential problems to be detected quickly and furthermore, the ability to monitor low concentration side reactions also allows the control of undesirable products, detrimental to the success of the main reaction.

As molecular absorption techniques are governed by Beer's law, the absorbance is dependent upon the molar absorptivity and concentration of the analyte together with the pathlength utilised. Consequently, for a given molar absorptivity, the pathlength utilised will determine the concentration levels of analytes that can be used whilst still achieving measurable absorbances. This presents a problem when trace liquid analysis is required and alternatives to UV-visible spectrometry are sought. For example, quantitative trace analysis is not possible with NIRS owing to the low molar absorptivity values associated with the overtone transitions involved. Furthermore, trace analysis is also limited with MIRS as a result of the short pathlengths inherent with ATR technology used in in-line probes.

A number of techniques utilising large optical pathlengths have been investigated, including optical waveguide spectroscopy<sup>141-143</sup>, transient absorption spectroscopy<sup>144-146</sup> and cavity-ring-down spectroscopy (CRDS)<sup>147, 148</sup>. Whilst optical waveguide spectroscopy has shown to be useful for trace analysis by successfully measuring the absorption spectra of sub-monolayer films<sup>149</sup>, transient absorption spectroscopy has also demonstrated potential in this area, where the change in absorption is due to the production of photobleached or photoexcited molecules in photochemical and photobiological systems<sup>150</sup>. Until recently this technique was limited by the detection limits of the spectrometers it utilised, however, in 2004 Yoshihara reported the development of a spectrometer capable of detecting concentrations as low as 50 pM, corresponding to an absorbance of less than  $10^{-4}$ , a significant improvement on previous detection limits<sup>151</sup>. CRDS was first introduced in 1988 and is based on the time taken for a laser pulse to decay inside an optical cavity<sup>152</sup>. Since its

introduction, CRDS has been utilised in a wide variety of studies spanning spectral regions from the UV to IR; these include the examination of chemical species in gas cells<sup>147, 153, 154</sup>, plasmas<sup>148, 155</sup>, molecular beams<sup>156, 157</sup> and kinetic studies<sup>158, 159</sup>. Despite being a well established technique for gases<sup>160-162</sup>, only in the last few years has the technique been used for liquid applications<sup>163-165</sup> with a recent study reporting detection limits of 15-20 n mol in the visible region<sup>165</sup>.

Despite the diverse applications of CRDS, its practical applicability is limited by flaws in the set-up of the technique; CRDS employs a large cavity length consisting of a series of expensive highly reflective mirrors and advanced electronics necessary to achieve the nano second travel times required. As a consequence, its non-compact, costly design has prevented its wide application to trace analysis. In contrast, the development of optical techniques utilising low cost laser diodes and small cavity lengths, such as intracavity laser absorption spectrometry (ICLAS) have provided a potentially cheaper and simpler instrumental configuration<sup>166</sup>.

ICLAS is a multipass absorption technique whereby the sample is placed inside the cavity of laser; the multiple passes of laser light in a short time frame, through the sample increases the effective absorption path length and consequently allows lower analyte concentrations to be detected. For nearly 40 years, ICLAS has been recognised as one of the most sensitive techniques for gaseous detection<sup>167-169</sup> nevertheless, it is only recently that its potential has been recognised. In earlier years several drawbacks hindered the development of ICLAS: in the 1970s and 80s dye lasers were used rather than the cost effective diode lasers that are currently utilised, but ICLAS showed no advantages compared to other techniques such as laser induced fluorescence. Additionally, the enhancement factors provided by ICLAS compared to conventional single pass spectrometry were reported to be as low as ten<sup>170</sup> and as high as several million<sup>171</sup>, as well as many values in between, but the reason for such variation was not obvious. Moreover the fundamental principles of the technique were also unclear, with a variety of theories being offered to explain the sensitivity of lasers but each theory addressed the issue differently generating more uncertainty<sup>171-</sup>

<sup>174</sup>. Nevertheless, in recent years a better understanding of the theoretical and experimental aspects of the technique has allowed the acquisition of more reliable and repeatable results<sup>166, 175, 176</sup>.

The scope of this technique have recently been extended to include trace liquid detection: it has been reported that detection limits of 1 ppb and 20 ppt in the infrared can be achieved with a grating and mirror configuration, respectively<sup>166</sup>. Despite this, it is still apparent that ICLAS is prone to inconsistencies, providing significant intracavity enhancements in certain configurations yet with no obvious reason, failing to do so in others. In 1988, Kleist and Bettermann reported intracavity absorption measurements from aqueous solutions of Rhodamine 6G in an Ar<sup>+</sup> ion laser utilising a resonator length of 1.77 mm. Operation of the system at 488 nm achieved an absorbance of  $3.5 \times 10^{-9}$  for a  $1 \times 10^{-13}$  mol/L solution nevertheless the system could not be successfully operated at 514.5 nm owing to periodic intensity fluctuations seen within the system at that wavelength<sup>177</sup>. Unger and Patonay described the application of ICLAS to liquid samples using laser diodes and demonstrated that the ICLAS system could detect a 1.0 nmol/L solution of a cyanine dye compared to a concentration of  $4.49 \times 10^{-6}$  mol/L that could be detected by a commercial UV-visible spectrometer<sup>178</sup>. Nevertheless, the ICLAS system used was unable to detect equivalent concentrations of a second cyanine dye with similar extinction coefficients; a 20 nmol/L solution produced an output approximately 10 times less than that seen with the initial cyanine dye. Unger and Patonay concluded that mechanical perturbation caused by common laboratory events could be partially attributed to the differences seen, however, further research would be needed to confidently explain the differences. Furthermore, the authors commented that in order to minimise signal noise, frequent readjustment of the system optics was required. In 1996, Mank et al. investigated the possibility of on-line diode laser based intracavity absorption detection in liquid chromatography<sup>179</sup>. The reported data showed that despite the inherent stability of laser diodes compared to that of other lasers, little signal gain was observed when used in the liquid chromatography configuration; the detection limit obtained with mitoxantrone was  $7 \times 10^{-7}$  M

corresponding to an absorbance of  $1 \times 10^{-4}$ ; two orders of magnitude less favourable than those observed with double-beam absorption detection.

Regardless of the increased interest in the application of ICLAS to liquid samples, the studies discussed illustrate the associated difficulties despite its success with gaseous measurements, providing in some cases, sensitivity enhancements 2000 times greater than that of single pass analysis<sup>180</sup>. Despite using the same principles, it is apparent from the literature that the systems utilised for gaseous samples are significantly different; dye lasers are generally utilised together with large pathlength sample cells ranging from 15-69 cm<sup>55, 180, 181</sup> and cavity lengths as long as 1.77 m<sup>177</sup>. Furthermore, it has been suggested that the slight differences in the basic principles of operation with gaseous compared to liquid samples will affect the intracavity enhancement observed<sup>182</sup>. Three factors have been recognised as contributors to the sensitivity of ICLAS: (1) a multipass effect; (2) a threshold effect as close to the system threshold, a small change in loss in the cavity makes a large change in the number of photons in a laser mode and (3) mode competition occurs between the modes affected by the intracavity loss and the other laser modes. As liquid samples are in general broadband absorbers (with respect to the laser bandwidth), all modes are quenched equally hence mode competition is not a contributing factor for intracavity enhancement. Consequently, the intracavity enhancement for liquid analyte systems will not be as high as observed for narrow band absorbers in the gas phase; nevertheless, intracavity absorption measurements should be considerably more sensitive than those provided by conventional single pass spectrometry<sup>182</sup>.

The aim of this study was to construct an ICLAS system and assess its potential for analysis of liquid samples. The intention was to prove the idea that ICLAS could offer detection limit advantages over conventional absorption spectrometry that could be exploited, in due course, in possible flow cell configurations similar to HPLC UV-visible detection. Depending on the laser of the wavelength used, it was hoped that ICLAS detection could become feasible for a number of molecular absorption configurations, such as NIRS and MIRS, in the longer term. In this

preliminary study, however, a laser operating around 860 nm was used for quantitative analysis of solutions of a dye.

## 6.2 ICLAS Theory

### 6.2.1 General Principles of Operation

The transmittance of radiation through a sample and the absorption of radiation by a sample can be explained mathematically (refer to equations (23) and (24)).

$$T = \frac{I}{I_0} \quad (23)$$

$$A = \log \frac{I_0}{I} \quad (24)$$

where,

T is the transmittance of radiation through the sample

A is the absorption of radiation through the sample

$I_0$  is the incident radiation intensity

I is the intensity of the transmitted radiation

Furthermore, as the absorbance of a species at a known wavelength of radiation,  $A(\lambda)$  is proportional to the concentration,  $c$ , of the absorbing species, the absorbance can also be described as follows:

$$A(\lambda) = \epsilon cl \quad (25)$$

where,

$\epsilon$  is the molar absorptivity of the analyte ( $\text{dm}^3 \text{mol}^{-1} \text{cm}^{-1}$ )

l is the path length of radiation through the sample (cm)

$c$  is the concentration ( $\text{mol dm}^{-3}$ )

The absorption of a sample can be enhanced by increasing the effective absorption pathlength. In the 1970s it was discovered that a laser cavity and a laser with a large emission bandwidth were extremely sensitive to intracavity losses<sup>183</sup> and from this ICLAS was developed. By inserting the sample inside the laser cavity, multiple passes of light through the sample is achieved and hence the effective absorption path length is increased. The sensitivity of ICLAS is consequently based on the enhanced absorption as a result of the multipass effect through the sample and the delicate balance between the gain and the intracavity losses of the system; as lasers are extremely sensitive to small intracavity optical losses, it is possible that trace quantities of an absorber can quench the lasing action. Figure 71 illustrates how the multipass ICLAS effect is achieved using two highly reflective mirrors, a laser gain material and a sample.

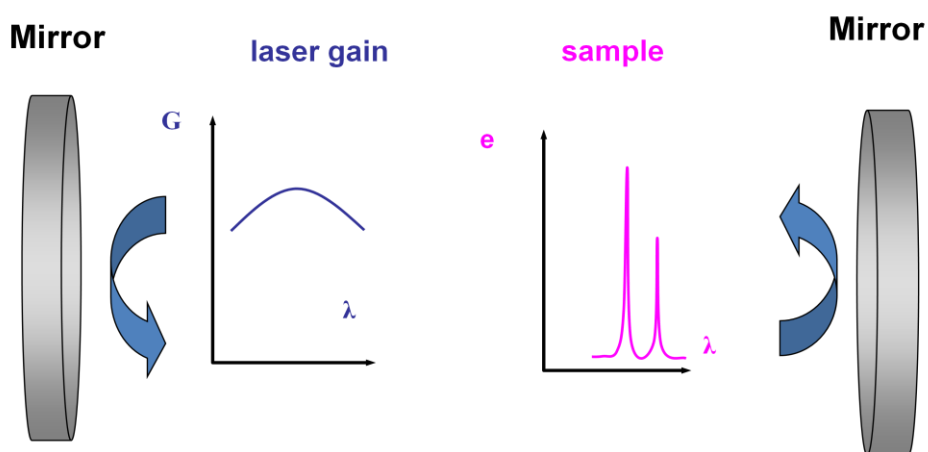
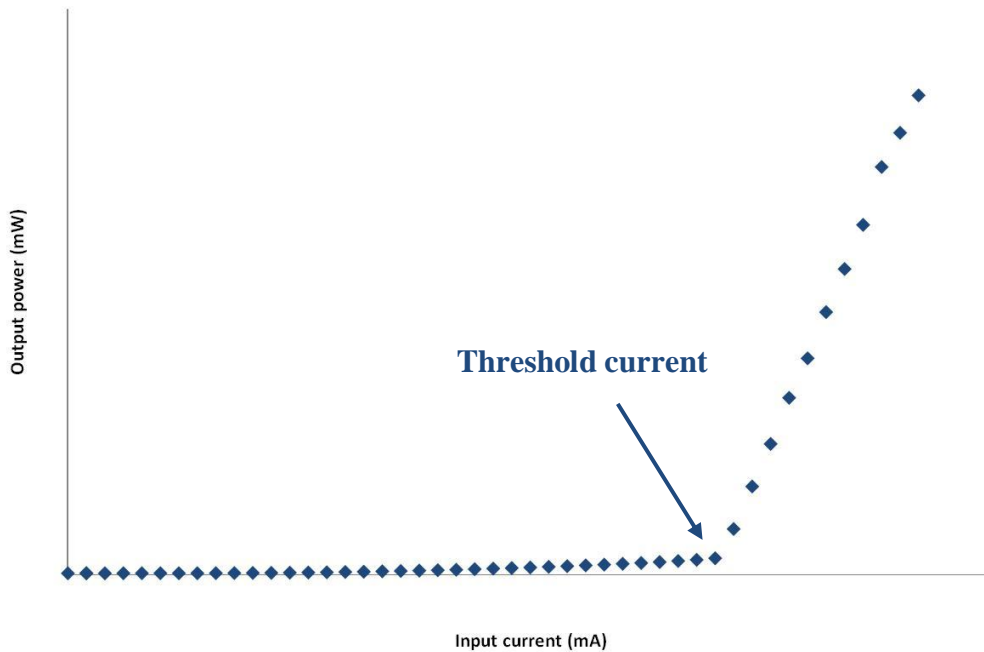


Figure 71 – Schematic of the basic components of an ICLAS system

### 6.2.2 Altering the dynamic range of the ICLAS system

An attractive advantage that ICLAS offers over other analysis methods is the ability to adjust the dynamic range of the technique to meet the requirements of the system being analysed. The dynamic range of the ICLAS system is determined by the threshold current of the system: the current at which the gain of the system overcomes the intracavity losses and facilitates lasing action (see Figure 72).



**Figure 72 – Schematic of a typical threshold current plot for an ICLAS system**

Figure 72 illustrates the change in the output power of a laser diode as the input current is increased. Initially as the input current is increased there is little change in the output power of the laser diode. This is owing to the intracavity losses in the system dominating compared to the gain of the system and consequently at this point lasing action is not achieved. Nevertheless, as the input current is increased further, the losses within the system no longer dominate to the same extent and the output power of the laser diode begins to increase; the current at which there is a definite change in the output power of the laser is known as the threshold current and



signifies the point at which the gain of the system is in excess compared to the intracavity losses and lasing action is achieved.

By setting the system to pre-determined levels above the threshold current (e.g. 1.3 times) it allows the dynamic range of the system to be tuned to the specific needs of the analysis. When the system is operated close to the threshold current, a small dynamic range can be utilised and conversely working further away from the threshold current allows for a larger dynamic range. It is important to understand that although the gain of the system at the threshold current is in excess compared to the intracavity losses, there is still a delicate balance between the two factors and hence the system is highly sensitive to even very small changes in the analyte concentration, as such changes will introduce intracavity losses that greatly affect the lasing capability of the system. Consequently, when analysis is performed at an input current close to that of the threshold current, the system will be optimised for sensitive trace analysis. When an input current significantly greater than the threshold current is used there is no longer a delicate balance between the gain of the system and the intracavity losses thus the system will not be sensitive to small concentration changes, rather a large dynamic range is available. The ability to tune the dynamic range and sensitivity of the ICLAS system to suit the needs of the analysis required, illustrates the flexible nature of the technique.

## 6.3 Experimental set-up

### 6.3.1 ICLAS configuration

The ICLAS system was constructed at the Institute of Photonics, University of Strathclyde using a grating to form the enhancement cavity; the experimental configuration is shown in Figure 73. This set-up was previously optimised by the Institute of Photonics and was discussed in a publication in 2007<sup>166</sup>. An antireflection coated laser diode (Toptica Photonics AG, Graefelfing, Germany) tuneable from 810-890 nm was mounted in a copper block which was temperature controlled with a Peltier element and a controller (Model 350, Newport Inc, Irvine, California) and the laser input current was altered using a precision current driver (Model LDC402B, Profile GmbH, Munich, Germany). The NIR radiation from the laser diode was collimated using a lens with a 0.49 numerical aperture and 4.5 mm focal length (Olympus Inc., Melville, New York); the radiation was split using a beam splitter which allowed the light to be fed into both the photodiode detector (Ocean Optics) and the spectrometer (Ocean Optics).

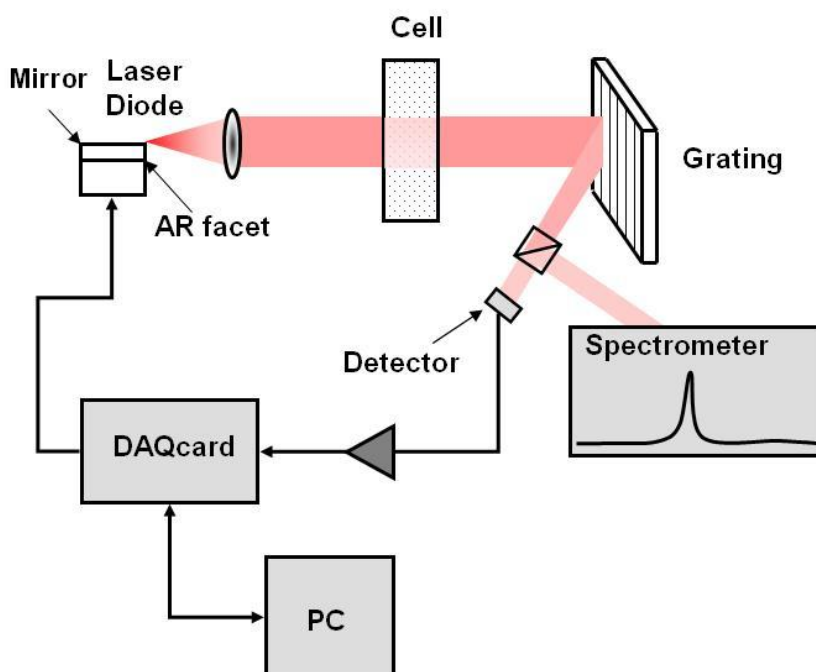


Figure 73 – Schematic of the configuration of the ICLAS system comprised of a laser diode with an antireflection coated (AR) facet, a sample cell, grating, detector, spectrometer, data card (DAQ card) and personal computer (PC).

Figure 73 shows a laser cavity (25 cm in length and 15 cm wide) formed by the diode laser back facet and a grating (1200 lines per mm); this formed a wavelength selective external cavity diode laser tuneable from 810 nm to 890 nm; the system was operated at 860 nm as the laser showed optimum performance at this wavelength. Some of the diffracted light was reflected back into the laser diode, whilst the rest was monitored by the photodiode detector and the spectrometer, the wavelength could be tuned by tilting the grating. The spectrometer was used solely to monitor the shape and wavelength of the lasing peak and the photodiode detector measured the changes in the power of the output beam after passing through the absorbing sample positioned inside the cavity, between the laser diode and the grating is a quartz cuvette (1 cm path length, Hellma, Mulheim, Germany).

### **6.3.2 *Sample preparation***

Standard solutions of IR-140 dye (SI053002, Exciton, Dayton, Ohio ) in ethanol were prepared over the range 0.73-2.92 mg L<sup>-1</sup> ; this compound was selected as it exhibited significant absorption at 860 nm and furthermore was chemically stable. Ethanol was used as the diluents for all standard solutions as it exhibited no absorption at 860 nm.

### **6.3.3 *Data Analysis***

A LabVIEW (National Instruments Inc) program was developed by the Institute of Photonics, University of Strathclyde, with a National Instruments data acquisition card (DAQPad-6015) to control the laser diode emission and to read the output of the photodiode detector. To determine the laser threshold current, the laser diode input current was varied from 0 mA to 180 mA, and the recorded output power was plotted versus the input current. From this plot the threshold and slope of the characteristic curves were calculated. The input current for the chosen pump power was then determined, usually at a multiple value of the threshold current, and fixed. The output power for a range of concentrations, at the fixed input current, was then

recorded. The absorbance was calculated using equation (24) ;  $I_0$  was defined as the measured intensity of the blank (ethanol) at the chosen input current. The sensitivity enhancement achieved by ICLAS compared to conventional single pass spectrometry was determined by plotting the ICLAS absorbances versus the dye concentration and comparing the plot to those obtained with a conventional UV/VIS absorption spectrometer (S. I. Photonics 420 series)

## 6.4 Results and Discussion

### 6.4.1 Investigation of the effect of the input current on the measured absorbances of a series of IR-140 dye standards

Preliminary experiments were carried out to investigate the optimum experimental parameters of the ICLAS system; a diluent blank (ethanol) and four IR-140 standard solutions in the range  $0.73\text{-}2.92\text{ mg L}^{-1}$  were analysed at different multiples above the threshold current (1.05, 1.25 and 1.5). Figure 74 shows a plot of the change in the output power as the input current of the laser diode is increased; a threshold current of 70 mA was calculated from the plot.

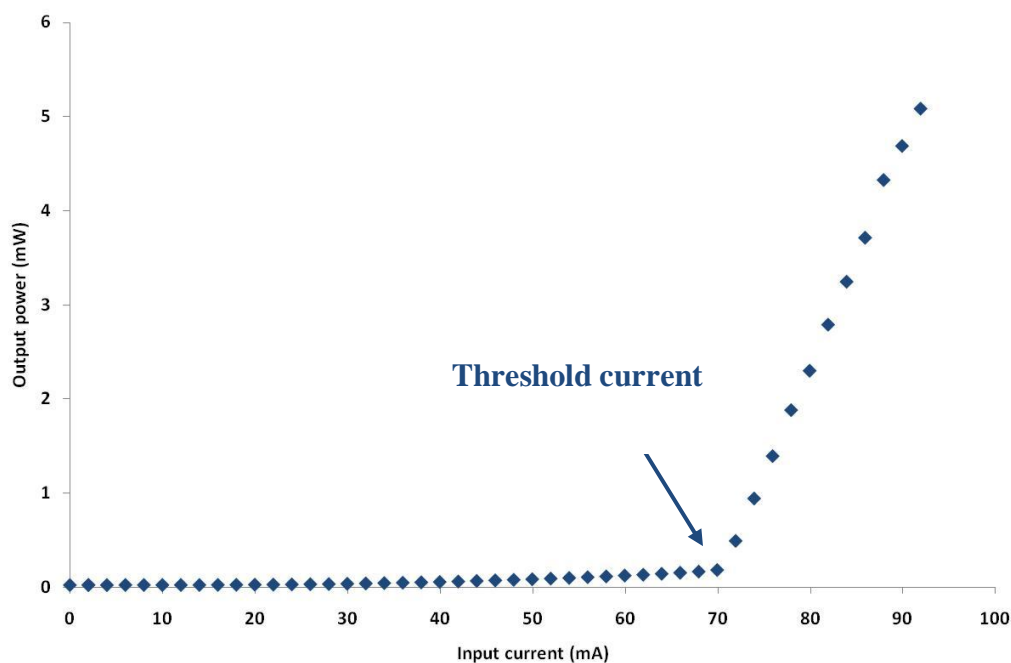


Figure 74 – Threshold current plot for the ICLAS system, acquired using pure ethanol

For comparison, a set of IR-140 standards in the concentration range 2.5-20 mg L<sup>-1</sup> were analysed using singlepass spectrometry. Due to the concentration limits of both systems, the concentration of the standards used for each were different. Table 28 and Table 29 show the recorded absorbances of a series of IR-140 standards by ICLAS and UV-visible spectrometry, respectively (each value is an average of three measurements). The data in Table 28 illustrates that the input current of the ICLAS system has a significant effect on the resulting absorbance data.

**Table 28 –ICLAS absorbance values of IR-140 standards in the range 0 -2.92 mg L<sup>-1</sup> acquired using different input currents; n=3**

| <b>Standard concentration (mg/L)</b> | <b>Absorbance at 73.5 mA (1.05 x threshold current)</b> | <b>Absorbance at 87.5 mA (1.25 x threshold current)</b> | <b>Absorbance at 105 mA (1.5 x threshold current)</b> |
|--------------------------------------|---|---|---|
| 0                                    | 0   | 0   | 0   |
| 0.73                                 | 0.053   | 0.332   | 0.163   |
| 1.46                                 | 0.097   | 0.646   | 0.391   |
| 2.19                                 | 0.132   | 0.804   | 0.503   |
| 2.92                                 | 0.164   | 0.848   | 0.929   |

**Table 29 – Absorbances recorded for standard solutions of IR-140 in the range 0-20 mg L<sup>-1</sup> by singlepass UV-visible spectrometry; n=3**

| <b>Standard concentration (mg/L)</b> | <b>Absorbance</b> |
|--------------------------------------|-------------------|
| 0                                    | 0                 |
| 2.5                                  | 0.005             |
| 5                                    | 0.038             |
| 10                                   | 0.015             |
| 15                                   | 0.273             |
| 20                                   | 0.389             |

Figure 75 shows the effect of altering the ICLAS input current on the measured absorbance of IR-140 and compares the absorbances obtained when using a conventional UV-visible spectrometry.

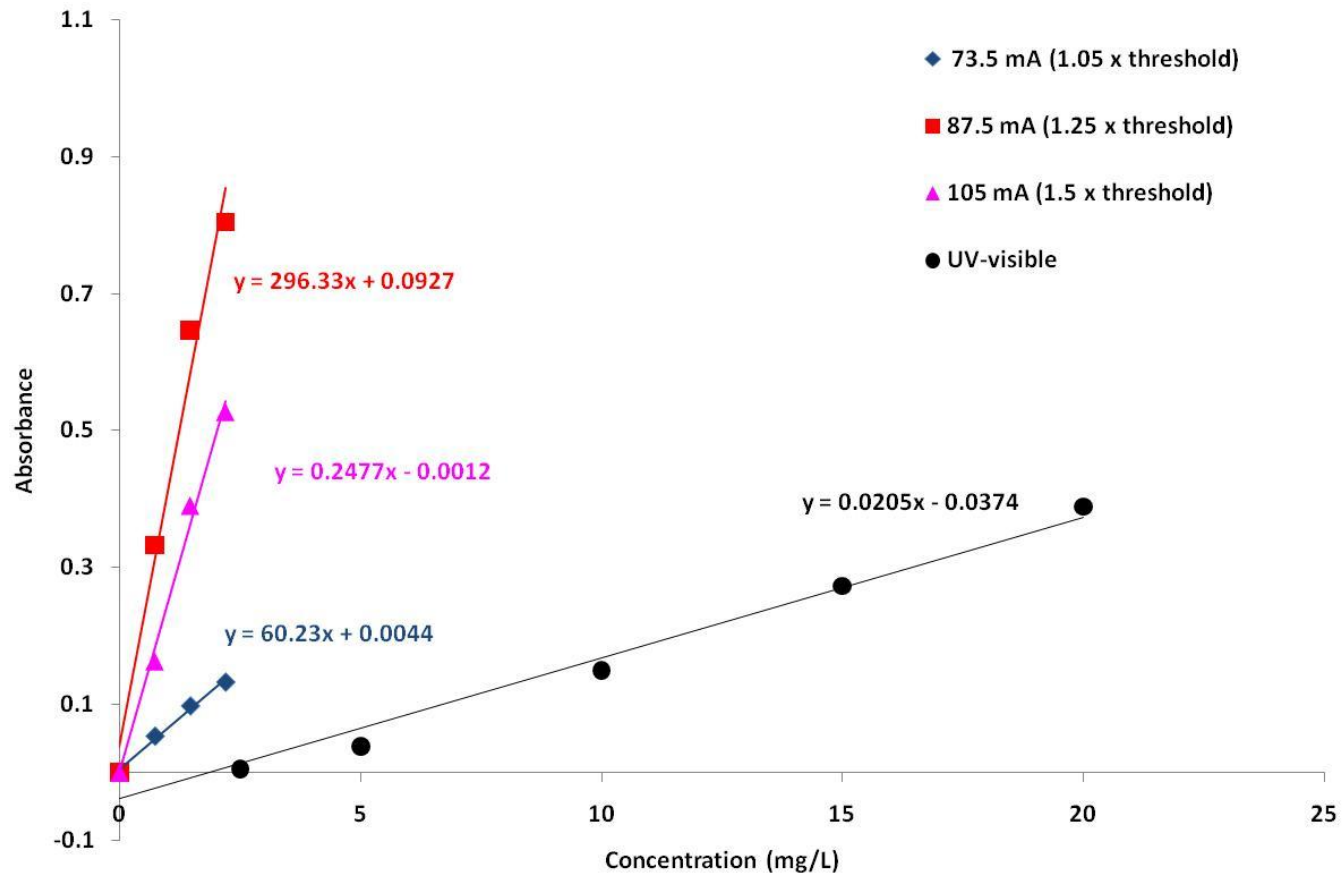


Figure 75 – Comparison of the change in absorbance with the increasing concentration of IR-140 for UV-visible spectrometry and ICLAS operated at different input currents

Figure 75 shows by the different slopes obtained, that the measured IR-140 absorbances are affected by the input current used. The sensitivity of a set of measurements is defined as the slope of the calibration graph and provided the data is linear in its response, the sensitivity can be measured as any point on the slope. By comparing the slopes in Figure 75 it can be seen that changing the input current of the system affects the sensitivity of the measurements recorded; it is apparent that the greatest sensitivity is achieved when using input currents 1.25 times that of the threshold current and the lowest sensitivity (by a factor of 5) is seen with input currents 1.05 times the threshold current. Such significant differences illustrate the importance of tailoring the ICLAS system to suit the type of analysis being carried out.

Furthermore, it is shown that regardless of the input current used the data obtained by the multipass ICLAS method is significantly more sensitive than that from the UV-visible data. Table 30 illustrates that an enhancement in the sensitivity is seen with each multiple of the threshold current used. It would be expected to see large enhancement factors when the optimum acquisition parameters are used for the concentration range being analysed. Consequently, it is apparent that the optimum conditions are not provided by the lowest input current as very little intracavity enhancement is observed. At this input current, there is a delicate balance between the intracavity losses and the gain of the system and consequently the relatively large changes in concentration of the standards introduce extra intracavity loss, quenching the laser action and resulting in the system essentially acting as an LED. The small level of enhancement calculated is a consequence of the reflection of light back from the grating, increasing the effective path length but only by a few times and thus achieving only a small enhancement.

The largest intracavity enhancement is observed when an input current of 1.25 times the threshold current is used which suggests that for the concentration range analysed this was the optimum setting. It is apparent, however, that an input current of 1.5 times the threshold current achieves a similar intracavity enhancement.



Nevertheless, at such a large multiple from the threshold current, the gain of the system is in such an excess compared to the losses that the optimal effect of intracavity enhancement would only be produced with greater step changes in the standard concentrations; this is confirmed by the similarity of the enhancement values calculated for the two input currents - the enhancement factor would be expected to be significantly larger at 1.5 times the threshold current if it was the optimum setting. This, therefore, highlights the importance of optimising the analysis parameters of the system as although in theory working at input currents close to the threshold current should provide better sensitivity, the minimum concentration selected in this study is too great for use at such low input currents and hence quenches the laser providing no intracavity enhancement – this finding was also reported by Elejalde and Girkin in 2007<sup>166</sup>. Data was not collected at input currents greater than 1.5 times the threshold current owing to the minimal sensitivity gains that would be seen. Despite identifying the optimum input current, the sensitivity gain achieved (x 14) is still relatively small; enhancements as low as ten have previously been reported in gas phase ICLAS systems<sup>170</sup> as well as gains as high as several million<sup>171</sup> with no obvious reason for the wide range of values seen. As discussed previously, it has been suggested that the intracavity enhancements observed with liquid samples will be less than for gaseous analytes.

**Table 30 – Comparison of the slopes of the multipass ICLAS absorbance data and singlepass UV-visible spectrometry**

| Input current            | ICLAS slope | UV-visible slope | Approximate enhancement factor |
|--------------------------|-------------|------------------|--------------------------------|
| 1.05 x threshold current | 60.24       | 20.7             | 3                              |
| 1.25 x threshold current | 296.3       | 20.7             | 14                             |
| 1.5 x threshold current  | 247.7       | 20.7             | 12                             |

#### **6.4.2 Testing of a prototype instrument**

In order to address the current demands for compact, portable instrumentation, a prototype compact instrument was designed by the Institute of Photonics, University of Strathclyde as can be seen in Figure 76. The configuration differs to that used in 6.4.1 with respect to the cavity length, width and the grade of optical components used: the cavity length and width were shortened to give dimensions of 18 cm and 10 cm, respectively, and the quartz cuvette was replaced by a 1 cm pathlength antireflection coated cuvette. The laser diode and grating (1200 lines per mm) were replaced by ‘Toptica high quality material’ versions (grating 1800 lines per mm) chosen to give the optimum reflectivity for the system.

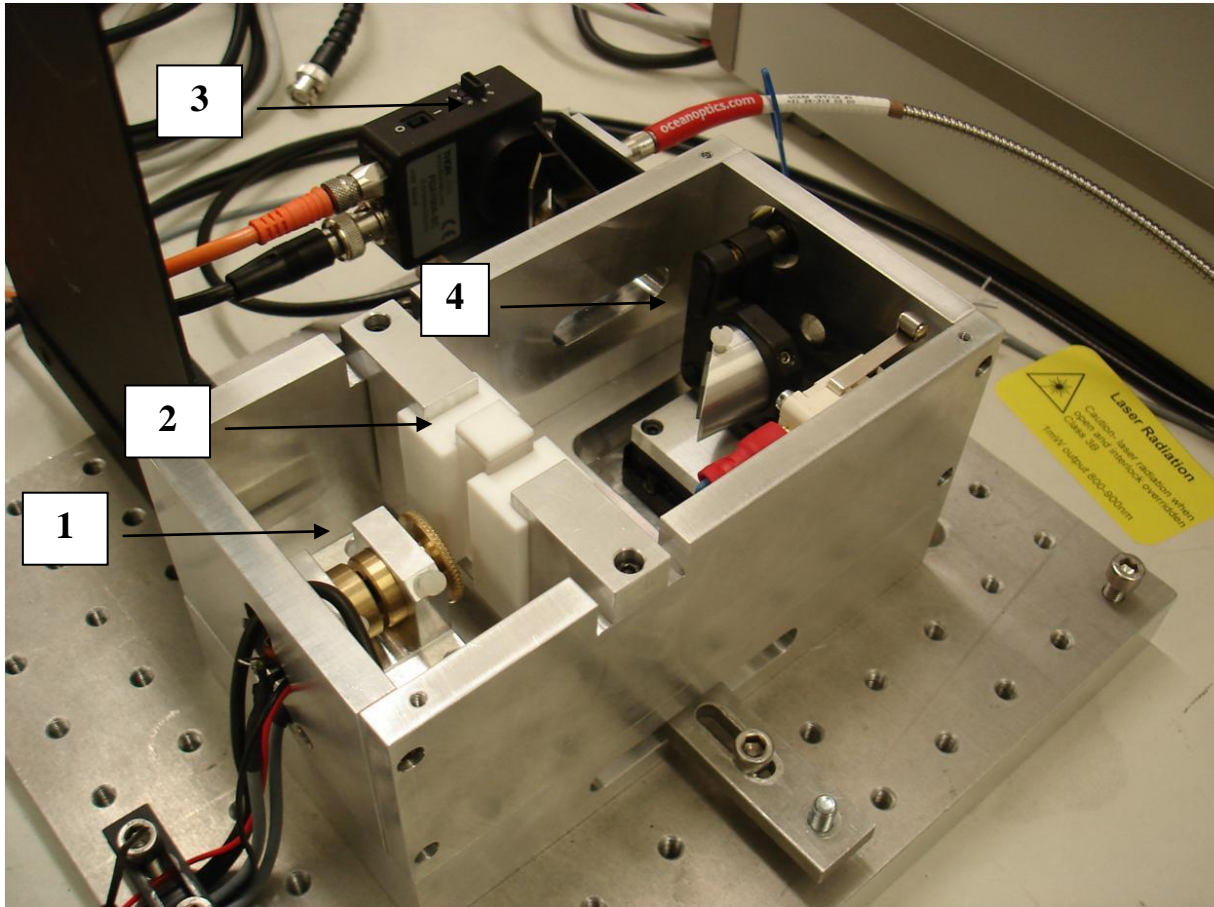


**Figure 76 – Photograph of a prototype compact ICLAS instrument with a cavity width and length of 10 cm and 18 cm, respectively. The set-up is comprised of an antireflection coated laser diode (1) and collimating lens, an antireflection coated 1 cm pathlength cuvette (2), a photodiode detector (3) and a 1800 lines per mm grating (4).**

The configuration shown in Figure 76 was used to analyse six standards of IR-140 covering the range 0-1 mg/L; Figure 77 illustrates three replicate data sets acquired at 1.25 x threshold current (90 mA) utilising the compact ICLAS configuration.

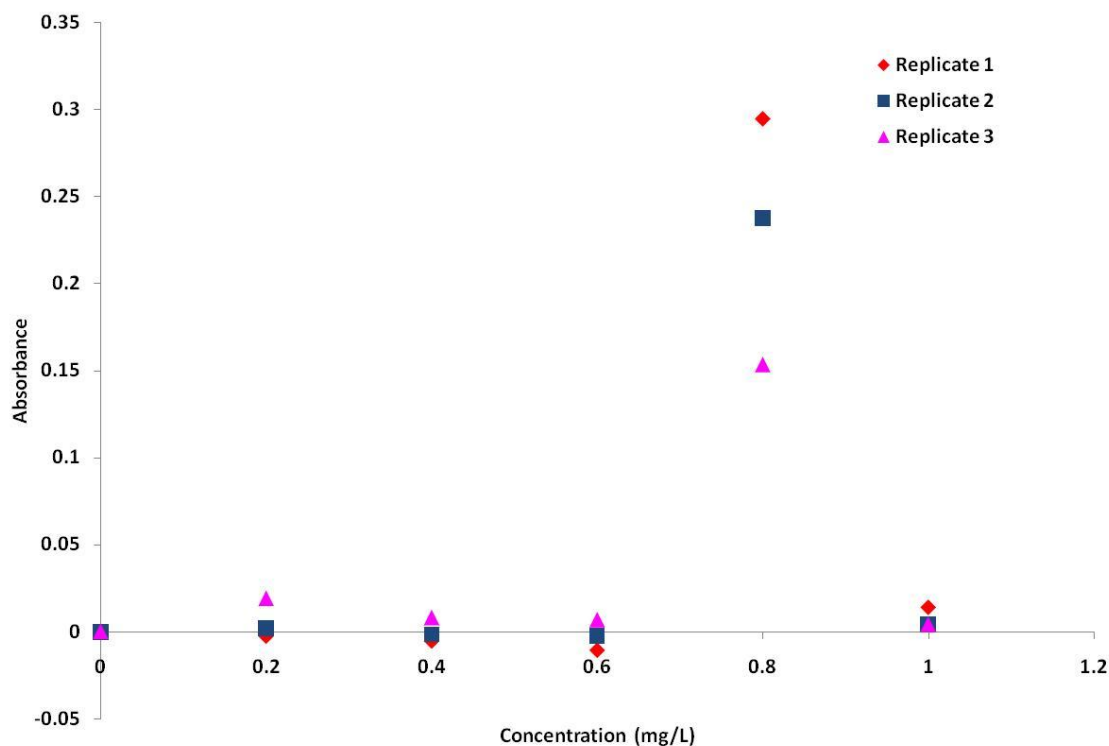


**Figure 77 – Three replicate ICLAS data sets acquired using the compact configuration at 1.25 x threshold current (90 mA), assessing the change in absorbance as the concentration of IR-140 is increased**

From Figure 77 it is clear that the data produced is not comparable to that acquired by the original ICLAS system; that is, there is no linear increase in the absorbance with the increasing concentration of the IR-140 dye. Moreover, it is apparent that in some cases at concentrations of 0.4 and 0.6 mg/L, the calculated absorbances are negative suggesting that more light has been transmitted through the standard than the blank. Furthermore, the only concentration that yields a significant response is that at 0.8 mg/L. Owing to the unsatisfactory nature of this data it was decided to prepare fresh standards and re-analyse the solutions using a range of input currents.

Figure 78 shows the change in absorbance measured as the concentration of the IR-140 dye is increased; data were acquired on the same day using the compact ICLAS configuration and varying the input current.

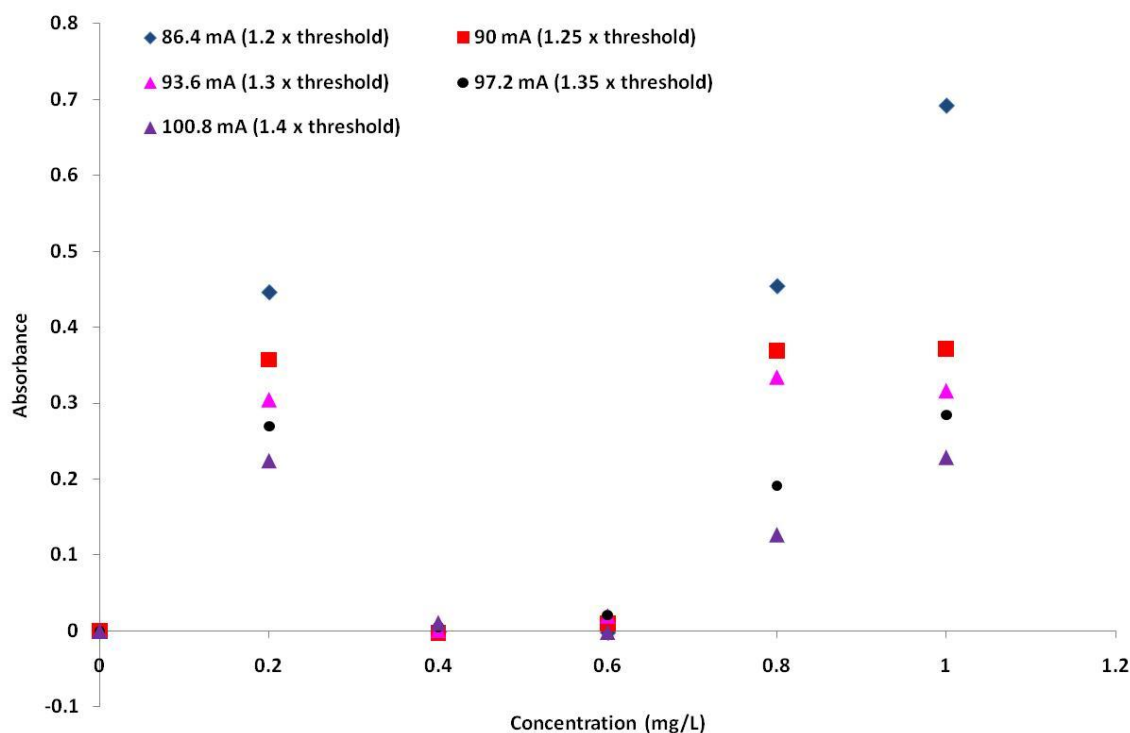


**Figure 78 – Comparison of the change in the absorbance with the increasing concentration of IR-140 dye standards, acquired using the compact ICLAS configuration at varying input currents as multiples of the threshold current**

From Figure 78 it is clear that whilst the data acquired at each input current demonstrates the same trend, it is not what would be expected from a correctly functioning system; there is no systematic change in the absorbance as the concentration is increased. Furthermore, the trends seen in Figure 77 and Figure 78 are significantly different even though the same standard concentrations were used in both studies. Nevertheless, it is interesting that the data in Figure 78 shows greater absorbances (for concentrations of 0.2, 0.8 and 1 mg/L IR140) when currents closer to the threshold current are used; however, there is no obvious reason why signals were not obtained for the 0.4 and 0.6 mg/L solutions.

As several variables were altered simultaneously (cavity length, width, optical components) in the construction of the compact ICLAS configuration, it was decided to dismantle the compact system and reposition the optical components to achieve the initial cavity length and width of 25 and 15 cm, respectively. Additional standards of IR-140 in ethanol were prepared to extend the concentration to 2 mg/L and the solutions were analysed using input currents between 1.05 and 1.3 times the threshold current.

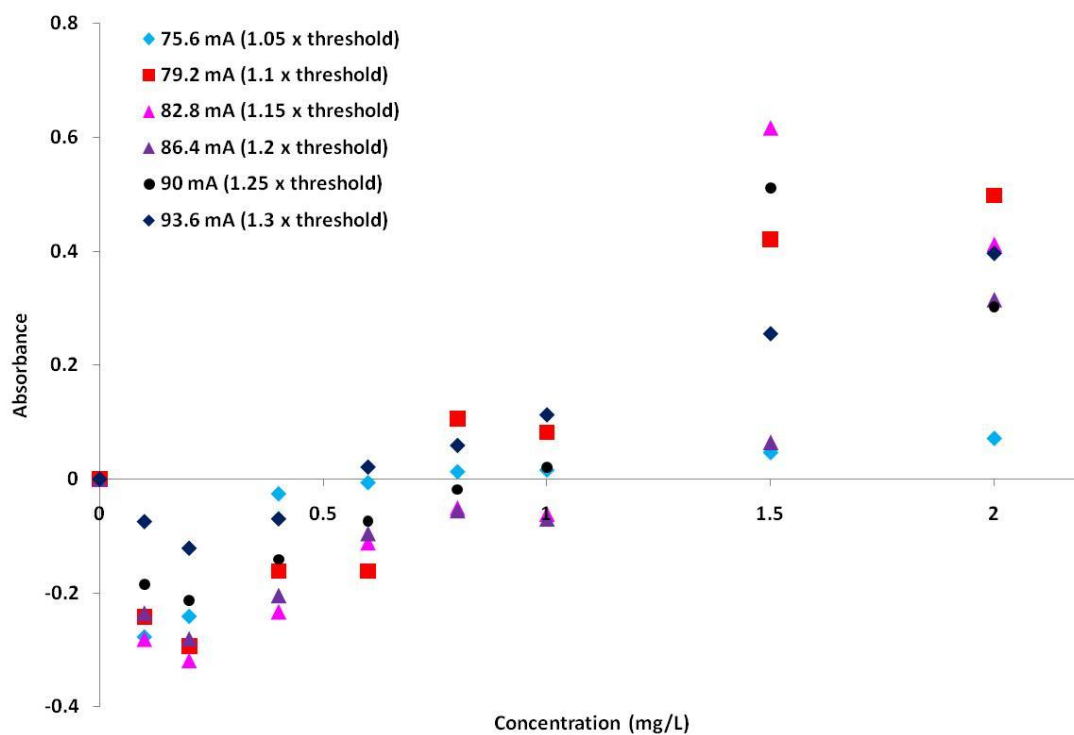
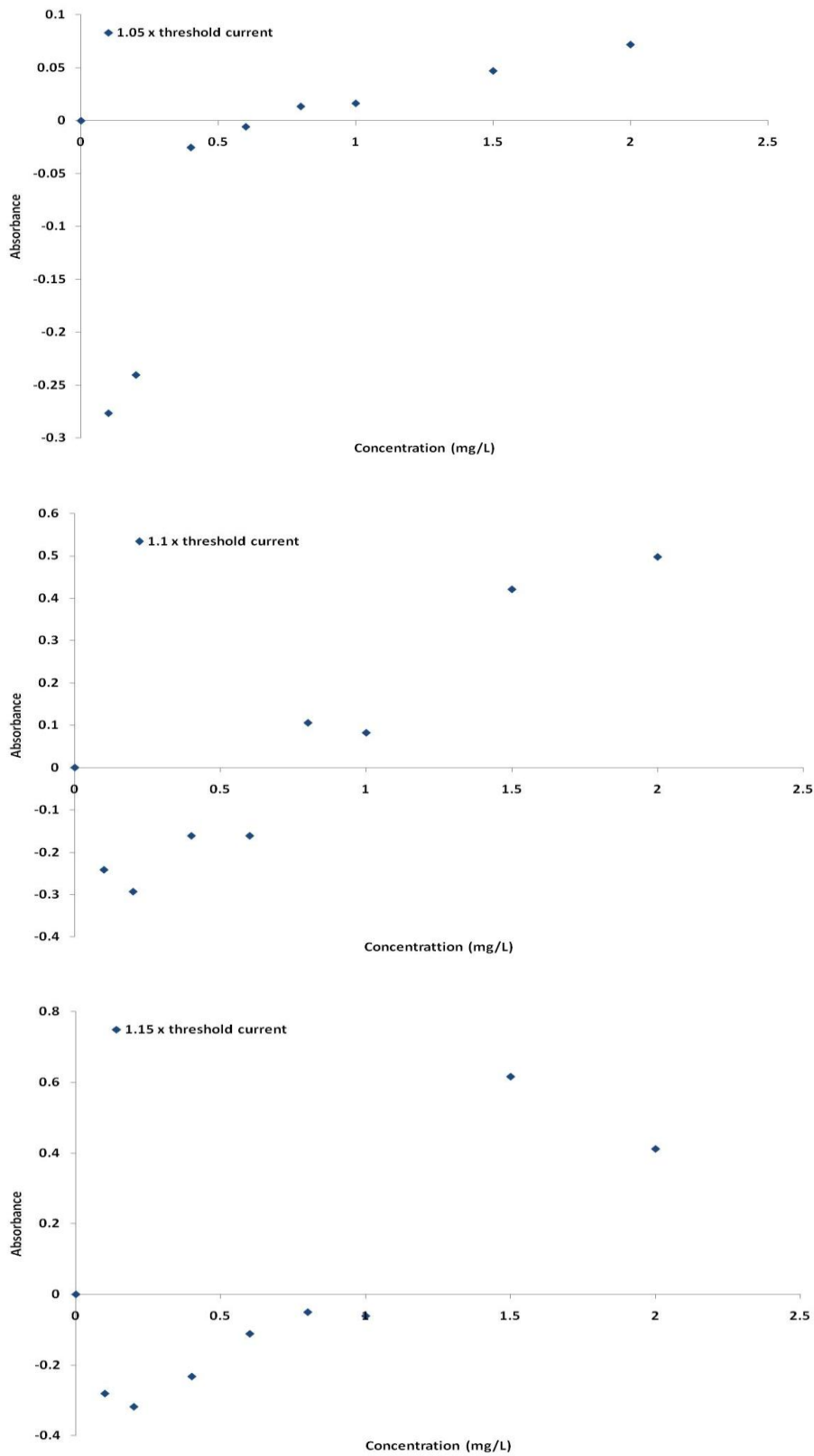
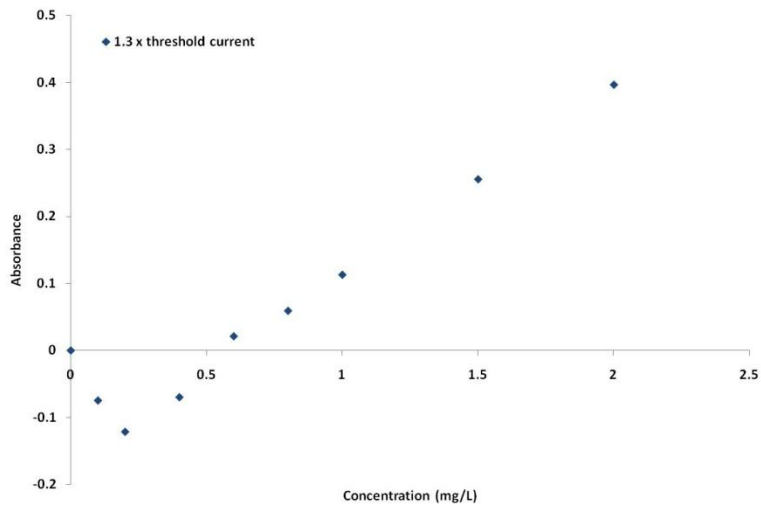
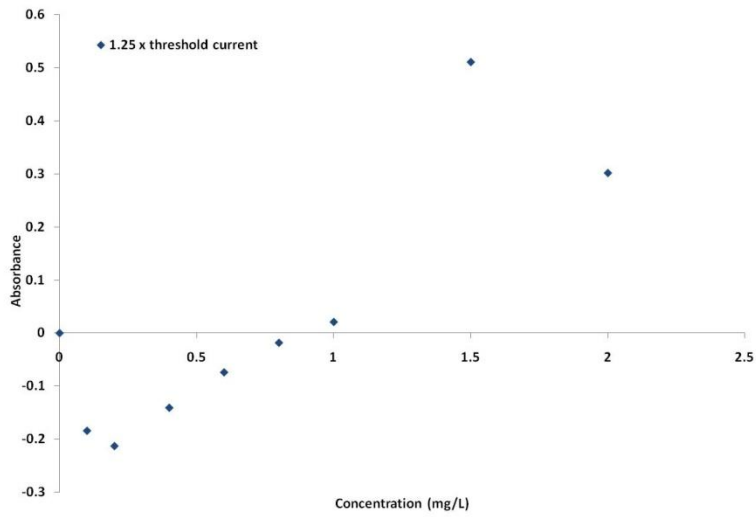
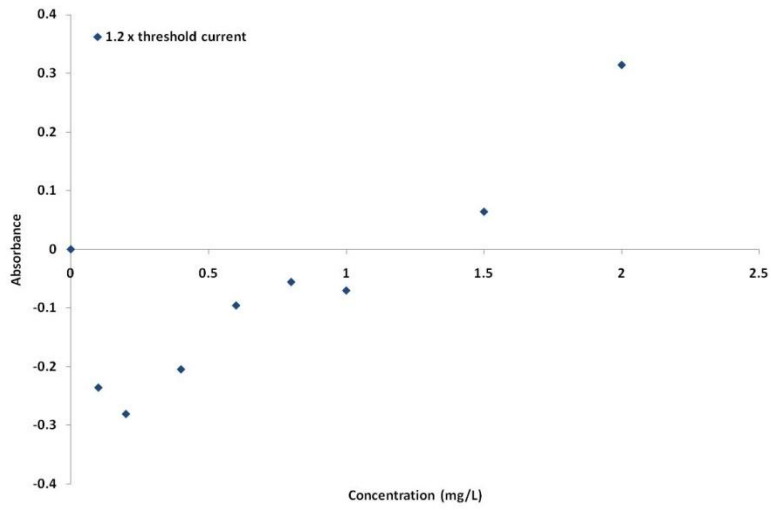


Figure 79 – Change in absorbance with the increasing concentration of IR-140 acquired at different input currents using the components of the compact ICLAS configuration, but with the cavity size of the initial configuration



**Figure 80 – Plots showing the change in absorbance with increasing concentration for 1.05, 1.1 and 1.15 times the threshold current**



**Figure 81 – Plots showing the change in absorbance with increasing concentration for 1.2, 1.25 and 1.3 times the threshold current**



From Figure 79 it is clear that increasing the width and length of the cavity has had no effect on the quality of the data acquired with the compact system. At all input currents, concentrations below 0.5 mg/L exhibit a negative absorbance suggesting a greater transmission of light through the standard solution containing the absorbing species than through the non absorbing diluents blank. Furthermore, as was seen in Figure 77 and Figure 78, the trends observed for the data acquired at all input currents within an analysis are consistent, however, between analyses the trends observed vary significantly. Although the data shown in Figure 79 is poor, it seems that there is a greater slope for the data points obtained at 1.05 times the threshold current but with a shorter linear range than the data points acquired at 1.3 times the threshold current which have a smaller slope (refer to Figure 80 and Figure 81). This is what would be expected as working close to the threshold current of the system allows for very sensitive detection over a narrow range of concentrations whereas operation at more stable currents further from the threshold current sacrifices sensitivity to small changes in concentration but allows analysis over a wider dynamic range. Despite the poor results, the threshold current experiments carried out before each set of absorbance measurements were consistent with the curves acquired using the initial ICLAS configuration. It was therefore apparent that random, unexplainable results were only observed in the presence of the absorbing species.

## **6.5 Conclusions**

It has been demonstrated that intracavity laser absorption spectrometry is capable of enhancing the absorption of liquid analytes by utilising a multipass effect of radiation through the sample. ICLAS measurements acquired using a wavelength selective cavity constructed on an optical bench and operated at an input current of 1.25 times the threshold current provided an enhancement factor of 14 times in comparison to measurements made using single pass spectrometry. It was apparent that the magnitude of the enhancement observed was dependent upon the input current utilised and how suited this was to the concentration range being analysed.

Data acquired using the compact ICLAS system highlighted the importance of understanding the effect of each instrumental component and parameter on the behavior of the system. Data obtained were not comparable to that acquired using the initial configuration and furthermore, whilst the trends observed were consistent within experiments, there was significant day to day variation owing to fluctuations within the ICLAS system; this required a regular time consuming process of altering the optical configuration of the system, a problem also reported by Unger and Patonay<sup>178</sup>. Despite varying different operational parameters, no data resembled that acquired with the initial set-up and furthermore, unpredictable data was only acquired when the absorbing species was present; in contrast threshold current experiments carried out using the non absorbing diluent blank were in good agreement with those acquired using the initial set-up.

The problems encountered with the ICLAS technique reinforces the reasons for its demise in earlier years<sup>170, 172, 173</sup>. Whilst the theory behind the technique suggests it has great potential as a flexible method for trace liquid analysis in process environments, it is important that not only the fundamental theory is understood but also the fundamental aspects of data acquisition. With increased research into the topic and further basic investigations into the effect of the instrumental components on the intracavity effect, hopefully the understanding of the technique will be boosted, aiding the technique's development and integration into mainstream analysis of liquids.

## **7. Conclusions and suggestions for future work**

### **7.1 Conclusions**

The goals outlined at the start of this investigation were:

- To characterise the propagation of light through solid pharmaceutical samples in both reflectance and transmission Raman modes and assess the effect of particle size and shape on Raman measurements. A rigorous experimental study will provide complementary data to the theoretically modeled studies reported in the literature.
- To investigate the variation in the API mass in a large sample set of low concentration OTC pharmaceutical tablets using HPLC.
- Assess the feasibility of transmission and reflectance Raman spectroscopy for the determination of the API in low concentration pharmaceutical tablets.
- To investigate the use of large spot size Raman mapping for assessing the content uniformity of pharmaceutical tablets.
- Construct an ICLAS system and assess its potential for the analysis of liquid samples

#### ***7.1.1 Study of tablet – to – tablet variation with respect to the mass of a low concentration API***

An HPLC method was successfully developed and utilised for the determination of a low concentration API in Chlortrimeton allergy tablets. Despite utilising a multi-stage sample preparation, the average API mass was calculated to be 3.98 mg and was found to be in good agreement with the stated API mass of 4 mg per tablet. Nevertheless, outlier tablets displaying an API mass significantly removed from the mean value (3.6 – 4.4 mg) were apparent and furthermore, samples of significantly varied whole tablet mass were identified (118.5 – 250.66 mg) ; this highlighted two sources of variation within the study.

Five outlier tablets showing no correlation between the fluctuating whole tablet mass and the API mass were identified. As tablets prepared from a homogeneous blend of constituents would result in a proportional increase or decrease of the API with a fluctuation in the whole tablet mass, the results reported suggested inhomogeneities were present.

As the tablets used in the study were '4 hour tablets' and hence were designed to be taken up to four times in one day, for a prolonged period of time, the potential problem of variations in the amount of active ingredient delivered to the patient is mitigated. The outlier samples discussed illustrate the difficulties associated with the preparation of powder mixtures. Furthermore, this highlights the advantages of the real-time monitoring of the preparation stages of powder mixtures, in order to detect quickly and correct any manufacturing problems so that the end product delivered meets the desired specifications.

### ***7.1.2 Investigation of the effect of powders on the propagation of photons through diffusely scattering media***

The results discussed in chapter 3 highlighted the need for a non-invasive method of analysis such as Raman spectrometry, for the determination of the API content of pharmaceutical tablets. Prior to the development of a non-invasive method of analysis, an in depth study of the factors affecting the propagation of photons in powders was undertaken in order to attain a fundamental understanding of the technique that could be applied to direct tablet analysis.

An experimental assessment of the effect of a moving Raman active layer through a 4 mm depth of different loose powders on the recorded transmission Raman measurements was undertaken; a similar study had been carried out by Matousek and Parker<sup>59</sup>, where Monte Carlo simulations were used to model the effect of a moving Raman active inter-layer.

Experimental results showed little difference in the measured transmission Raman intensity when a compressed Raman active layer was placed on top or below a 4 mm depth of loose powder (Avicel 0-38, 53-106, 150-212  $\mu\text{m}$  and aspirin 150-212  $\mu\text{m}$ ). Matousek and Parker also found that similar transmission Raman intensities were achieved when Monte Carlo simulations were used to model the transmission Raman signal when a Raman active material was placed on the top or bottom of a bulk material. Nevertheless, when the inter-layer was embedded in the loose powder, the transmission Raman signal was always found to be greater than when the inter-layer was on the top or bottom of the bulk powder.

The size and shape of the particles of the loose powder were also shown to influence the magnitude of the transmission Raman signal for all positions of the Raman active layer, within or on the surface of the loose powder, this was attributed to the different particle packing efficiencies that would be seen with materials of differing particle sizes. For all particle size ranges of Avicel, a greater transmission Raman intensity was recorded when 1 mm of powder was placed before the Raman active layer compared to when 1 mm of powder was present after the Raman active layer. Conversely, for the single size range of aspirin studied, the reverse was found to be true. The experimental results obtained from this study showed the transmission Raman measurements to be sensitive to the location of the Raman active layer and furthermore the physical properties of the bulk material of the sample; the opposite conclusion to that drawn by Matousek and Parker when similar data was modeled by Monte Carlo simulations.

### ***7.1.3 Non-invasive analysis of Chlortrimeton tablets by Raman spectrometry***

A rigorous assessment of the capabilities of both reflectance and transmission mode wide area illumination Raman measurements for the quantitative determination of a large sample set of over-the-counter, low concentration pharmaceutical tablets was carried out. External calibration tablets were prepared and were used to predict the API mass in the sample tablets. The data acquired in chapter 4 suggested particle size

effects for loose materials; this work investigated the effect of material particle size on the Raman measurements of compacted materials. Furthermore, Raman mapping was used to assess the degree of homogeneity of calibration samples.

Univariate prediction models based on external synthetic calibration sets covering the range 0- 8 mg API predicted the average API mass of the sample set to be 4.3 and 3.9 mg when using peak areas and peak intensities, respectively. It was found that reducing the calibration range improved the peak intensity calibration model slightly, providing an average predicted API mass of 4 mg and reducing the % CV of the measurements from 3.3 to 1.9 %; this was in good agreement with the average predicted mass of 3.98 mg reported from HPLC data (chapter 3) and furthermore, showed significantly lower CV values (6.3 % from HPLC data). This improvement however, was not reflected in the peak area data owing to the different spectral features of the analyte peak in the calibration and sample tablets. Consequently, it can be concluded that peak areas, in this case, are not suitable for use when predicting the sample tablet API mass.

The current study has shown the potential of wide area illumination reflectance Raman spectrometry for the quantitative determination of samples containing approximately 2% w/w API and furthermore, has been demonstrated using a sample size of > 380 tablets.

Transmission mode models based on calibration tablets covering the range 0-8 mg API, predicted the average API mass in the sample tablets to be approximately twice that of the stated mass. Calibration tablets comprised of varying Avicel particle sizes were prepared and a clear particle size effect on the predicted API mass values in the transmission Raman mode. When the average particle size of the Avicel used in the calibration tablets was increased to 180  $\mu\text{m}$ , the average predicted API mass was found to be in good agreement with the stated API mass (4 mg). This suggests that the calibration tablets made using Avicel PH-200 are most similar to the Chlortrimeton tablets, with respect to the material properties, in particular the

material particle size. However, it is possible that the absorption characteristics of Avicel and the Chlortrimeton tablets are significantly different such that by using Avicel PH200, the differences are compensated for; consequently it should not necessarily be assumed that the average particle of the material in the sample tablet is 180  $\mu\text{m}$ . This does however highlight that either matrix matched calibration tablets or a previously analysed set of samples (as standards) are required for accurate analysis in transmission mode.

Reflectance Raman spectra of a calibration tablet illustrated differences in the amount of API on both sides however this was not evident in the transmission Raman spectra which was thought to be a consequence of the different sampling methods of the two measurement types; surface biased reflectance measurements compared to ‘averaged’ transmission mode measurements. The differences identified by the reflectance mode measurements were confirmed by Raman micro-maps and reflectance Raman mapping with the PhAT probe proved useful to examine inhomogeneities in the distribution of chlorpheniramine maleate in calibration tablets prepared from Avicel. It can be concluded that PhAT Raman mapping is potentially suited for the rapid homogeneity screening of pharmaceutical tablets.

#### ***7.1.4 The development of intracavity laser absorption spectrometry for trace liquid analysis***

High performance liquid chromatography (HPLC) is widely used for chemical analysis in many industries, including the pharmaceutical industry. The technique relies on having a sensitive detection method that is capable of quantifying the small amounts of separated compounds in sample components that elute from the chromatographic column. Despite being widely used in many analytical applications, time consuming, chemical derivatisation of the sample is often required to increase the absorptivity of the analyte and in turn improve the sensitivity. An alternative way to increase the sensitivity is to increase the pathlength however, a

significant physical increase in the pathlength of a conventional flow cell is not possible. Nevertheless, it has been reported that a significant increases in the effective pathlength can be achieved by using intracavity laser absorption spectrometry (ICLAS).

The potential of ICLAS as an analytical technique for the determination of trace liquid analytes has been evaluated and it has been demonstrated that ICLAS is capable of enhancing the absorption of liquid analytes by utilising a multipass effect of radiation through the sample. ICLAS measurements acquired using a wavelength selective cavity constructed on an optical bench and operated at an input current of 1.25 times the threshold current provided an enhancement factor of 14 times in comparison to measurements made using single pass spectrometry.

Nevertheless, this enhancement could not be replicated using a compact, portable ICLAS system devised by the Institute of Photonic, University of Strathclyde. Moreover, whilst the trends observed were consistent within experiments, there was significant day to day variation owing to fluctuations within the ICLAS system; this required a regular time consuming process of altering the optical configuration of the system, a problem also reported by Unger and Patonay<sup>178</sup>. Despite varying different operational parameters, no data resembled that acquired with the initial set-up. This however, was only observed when the analyte was present; threshold current experiments using the non absorbing diluents blank, provided good quality data, in good agreement with that acquired using the initial set-up. The significantly different data produced using both systems highlights the unpredictable nature of the technique and suggests difficulties with regards to the reproducibility of data when using different instruments.

## **7.2 Suggestions for future work**

- Vary the Raman active layer and the loose material used in the photon propagation study to investigate the different trends seen with materials of similar or different physical properties.



- Carry out a more rigorous investigation of micro and PhAT Raman mapping using samples with a known inhomogeneity or a bi-layer sample to assess the capabilities of both methods.
- Investigate further the potential of ICLAS for liquid analysis starting with a fundamental study encompassing the effect of cavity length, width and the position of the optical components within the overall set up. Furthermore, an assessment of the repeatability of data acquired using different instruments that are comprised of the same optical components in identical configurations should be carried out.

## 8. References

1. J.B.Callis, D. L. Illman and B. R. Kowalski, *Analytical Chemistry*, 1987, **9**, 634A-637A.
2. C.Coffey, B. E. Codey Jr and D. S. Walker, *Analytica Chimica Acta*, 1999, **395**, 335-341.
3. J.A.Westerhuis, J. P. Gurden and A. K. Smilde, *Analytical Chemistry*, 2000, **72**, 5322-5330.
4. E.D.Lipp and R. L. Grosse, *Applied Spectroscopy*, 1995, **52**, 42-46.
5. J.B.Callis, D. L. Illman and B. R. Kowalski, *Analytical Chemistry*, 1987, **62**, 624A.
6. J.Workman, D. J. Veltkamp, S. Doherty, B. B. Anderson, E. Creasy, M. Koch, J. F. Tatera, A. L. Robinson, L. Bond, L. W. Burgess, G. N. Bokerman, A. H. Ullman, G. P. Darsey, F. Mozayeni, J. A. Bamberger and M. S. Greenwood, *Analytical Chemistry*, 1999, **71**, 121R.
7. *FDA PAT Initiative* [www.fda.gov](http://www.fda.gov), 2009.
8. F.McLennan and B. R. Kowalski, *Process Analytical Chemistry, Blackie Academic & Professional, London*, 1995.
9. N.S.Sahni, T. Isaksson and T. Naes, *Chemometrics and Intelligent Laboratory Systems*, 2001, **56**, 105.
10. K.A.Bakeev, *Process Analytical Technology, Blackwell Science Publishing Inc*, 1999.
11. *Orange book (electronic copy)*, [www.fda.gov/cder](http://www.fda.gov/cder), 2009.
12. P.K.Aldridge, *European Patent Application, 0 631 810 A1*, 1994.
13. P.A.Hailey, P. Doherty, P. Tapsell, T. Oliver and P. K. Aldridge, *Journal of Pharmaceutical and Biomedical Analysis*, 1996, **14**, 551.
14. J.B.Gray, *Chemical Engineering Progress*, 1957, **21**, 843.
15. M.D.Aston, C. Schofield and F. H. Valentin, *Chemical Engineering Science*, 1966, **21**, 843.
16. R.W.Miller, *Biennial Conference*, 1999, **26**, 17.
17. S.M.Han and P. G. Faulkner, *Journal of Pharmaceutical and Biomedical Analysis*, 1996, **14**, 1681.

18. C.Gustafsson, C. Nystrom and H. Lennholm, *Journal of Pharmaceutical Science*, 2003, **92**, 460.
19. J.G.Bouchard, P. A. Payne and S. Szyszko, *Trans IchemE*, 1994, **72**, 20.
20. M.Whitaker, G. R. Baker, J. Westrup, P. A. Goulding, D. R. Rudd, R. M. Belchamber and M. P. Collins, *International Journal of Pharmaceutics*, 2000, **205**, 79.
21. N.Townshend, *Monitoring of Particulate Processes Using Acoustic Emission*, Department of Pure and Applied Chemistry, University of Strathclyde 2006.
22. W.D.Hegreth, C. Jaeckle and M. Krell, *Polymer Reaction Engineering*, 2003, **11**, 663.
23. E.N.Mills, M. L. Parker, N. Wellner, G. Toole, K. Feeney and P. R. Shewry, *Journal of Cereal Science*, 2005, **41**, 193.
24. U. V. Stockar, S. Valentinotti, I. Marison, C. Cannizzaro and C. Herwig, *Biotechnology Advances*, 2003, **21**, 417.
25. C.J.Strachan, T. Rades, K. C. Gordon and J. Rantanen, *Journal of Pharmacy and Pharmacology*, 2007, **59**, 179.
26. G.Finni, *Journal of Raman Spectroscopy*, 2004, **35**, 335.
27. T.R.M.DeBeer, W. R. G. Baeyens, Y. Vander Hayden, P. Remon, C. Vervaeet and F. Verpoort, *European Journal of Pharmaceutical Sciences*, 2007, **30**, 229.
28. W.H.Doub, P. Adams, J. A. Spencer, L. F. Buhse, M. P. Nelson and P. J. Treado, *Pharmaceutical Research*, 2007, **24**, 934.
29. L. L. Augsburger, S. W. Hoag, J. Geoffroy and D. Rivkees, *Pharmaceutical Dosage Forms:Tablets, 3rd edition*, Informa Healthcare, USA, Inc., 2008, 85-113.
30. O.Svensson, M. Josefson and F. W. Langkilde, *Chemometrics and Intelligent Laboratory Systems*, 1999, **49**, 49.
31. J. F. V. Staden, M. A. Makhafola and D. De Waal, *Applied Spectroscopy*, 1996, **50**, 991.
32. B. D. Larsen, D. H. Christensen, A. Holm, R. Zillmer, O. Fauskov and J. Nielsen, *American Chemical Society*, 1996, **115**, 6247.

33. J.W.Schopperelrei, M. L. Keike and T. B. Brill, *Journal of Physical Chemistry*, 1996, **100**, 7463.
34. A.Schwartz and K. Berglund, *Journal of Crystal Growth*, 1999, **203**, 599.
35. F.Wang, J. Wachter, F. Antosz and K. Berglund, *Organic Process Reasearch and Development*, 2000, **4**, 391.
36. J.Falcon and K. Berglund, *Journal of Crystal Growth*, 2004, **4**, 457.
37. Y.Hu, J. Liang, A. Myerson and L. S. Taylor, *Industrial and Engineering Chemical Research*, 2005, **44**, 1233.
38. J.Scholl, D. Bonalumi, L. Vicum and M. Mazzotti, *Crystal Growth and Design*, 2006, **6**, 881.
39. L.Fan, T. Chen, Yi-Ming and F. S. Lai, *Powder Technology*, 1990, **61**, 255.
40. J.C.Williams, *Powder Technology*, 1976, **15**, 245.
41. G.Vergote, T. De Beer, C. Vervaet, J. P. Remon, W. Baeyens, N. Dierieux and F. Verpoort, *European Journal of Pharmaceutical Sciences*, 2004, **21**, 479.
42. F.Clarke, M. Jamieson, D. Clark, S. Hammond, R. Jee and A. Moffat, *Analytical Chemistry*, 2001, **73**, 2213.
43. H.Wikstrom, I. R. Lewis and L. S. Taylor, *Applied Spectroscopy*, 2005, **59**, 934.
44. J.Rantanen, S. Lehtola, P. Ramet, J. P. Mannermaa and J. Yliruusi, *Powder Technology*, 1998, **99**, 163.
45. H. Wikstrom, P.J. Marsac and L. S. Taylor, *J. Pharm. Sci*, 2005, **94**, 209.
46. J. Rantanen, S. Lehtola, P. Ramet, J. P. Mannermaa and J. Yliruusi, *Powder Technology*, 1998, **99**, 163.
47. J. Rantanen, H. Wikstrom, R. Turner and L. S. Taylor, *Anal. Chem*, 2005, **77**, 556.
48. C. Kontoyannis, *J. Pharm. Biomed. Anal*, 1995, **13**, 73.
49. C. Wang, T. Vickers and C. Mann, *J. Pharm. Biomed. Anal*, 1997, **16**, 87.
50. T. Niemezyk, M. Delagado-Lopez and F. Allen, *Anal. Chem*, 1998, **70**, 2762.
51. J. Johanson, S. Folestad, *Eur. Pharm. Rev*, 2003, **8**, 36.
52. J. Johanson, S. Pettersson and S. Folestad, *J. Pharm. Biomed. Anal*, 2005, **39**, 516.

53. F.W.Langkilde, J. Sjoblom, L. Tekenbergs-Hjelte and J. Mrak, *Journal of Pharmaceutical and Biomedical Analysis*, 1997, **15**, 687.
54. A.T.G.DePaepe, J. M. Dyke, P. J. Hendra and F. W. Langkilde, *Spectrochimica Acta Part A*, 1997, **53**, 2261.
55. J. J. O'Brien and H. Cao, *Journal of Quantitative Spectroscopy and Radiative Transfer*, 2002, **75**, 323.
56. H. Owen, D. J. Strachan, J. B. Slater and J. M. Tedesco, *USA Patent US2005140973*, 2005.
57. C.Eliasson, N. A. MacLeod, L. C. Jayes, F. C. Clarke, S. V. Hammond, M. R. Smith and P. Matousek, *Journal of Pharmaceutical and Biomedical Analysis*, 2008, **47**, 221.
58. J.Kim, J. Noh, H. Chung, Y. Woo, M. S. Kemper and Y. Lee, *Analytica Chimica Acta*, 2007, **598**, 280.
59. P.Matousek and A. W. Parker, *Applied Spectroscopy*, 2006, **60**, 1353.
60. J.Johanson, A. Sparen, O. Svensson, S. Folestad and M. Claybourn, *Applied Spectroscopy*, 2007, **61**, 1211.
61. M.J.Pelletier, *Analytical Applications of Raman Spectroscopy*, Blackwell Science Publishing Inc, 1999.
62. I.R.Lewis, G. Howell and M. Edwards, *Handbook of Raman Spectroscopy*, Marcel Dekker, 2001.
63. R.S.Krishnan and R. K. Shankar, *Journal of Raman Spectroscopy*, 1981, **10**.
64. E.Smith and G. Dent, *Modern Raman Spectroscopy A Practical Approach*, John Wiley & Sons, 2005.
65. M.Kerker, *The scattering of light and other electromagnetic radiation*, Academic Press, New York, 1969.
66. P.Matousek, *Chemical Society Reviews*, 2007, **36**, 1292.
67. P.Matousek and A. W. Parker, *Journal of Raman Spectroscopy*, 2007, **38**, 563.
68. G.Kortum, *Reflectance Spectroscopy:Principles, Methods, Applications*, Springer-Verlag, Berlin, 1969, 26.
69. B. G. Osborne, T. Fearn and P. H. Hindle, *Longman Scientific and Technical, UK*, 1993, 1-47.

70. D.L.Wetzel, *Analytical Chemistry*, 1983, **55**, 1165.
71. D.A.Burns and E. W. Ciurczak, *Practical Spectroscopy Series Vol. 13. Marce Dekker Inc.*, 1992, 13-35.
72. P.Kubelka and F. Munk, *Zeitschrift fur Technische Physik*, 1931, **12**, 593-601.
73. *Kaiser Optical Systems Inc Website. [www.kosi.com](http://www.kosi.com)*, 2009.
74. M.M.Carrabba and R. D. Rauh, *US Patent 5112127*, 1992.
75. J.B.Slater, *US Patent 2003/0147593*, 2003.
76. <http://www.kosi.com.raman/probes/mkii.html>.
77. H. Owen, D. J. Strachan, J. B. Slater and J. M. Tedesco, *USA Patent US2005140973*, 2005.
78. <http://www.kosi.com.raman/analyzers/phat.html>.
79. N.Everall, H. Owen and J. Slater, *Applied Spectroscopy*, 1995, **49**, 610.
80. G.J.Gervasio and M. J. Pelletier, *Journal of Process Analytical Chemistry*, 1997, **3**.
81. *Kaiser Raman Products Technical Note, [www.kosi.com](http://www.kosi.com)*.
82. *Kaiser Optical Systems Inc.,2008487 V2.0*.
83. *Kaiser Optical Systems Inc.,2011120 R1*.
84. Ch.LakshmiNarayana, T. Suresh, S. Mahender Rao, P. K. Dubey and J. Moses Babu, *Journal of Pharmaceutical and Biomedical Analysis*, 2003, **32**, 21.
85. A.Halabi, C. Ferrayoli, M. Palacio, V. Dabbene and S. Palacios, *Journal of Pharmaceutical and Biomedical Analysis*, 2004, **34**, 45.
86. D.B.Pathare, A. S. Jadhav and M. S. Shingare, *Journal of Pharmaceutical and Biomedical Analysis*, 2006, **41**, 1152.
87. J.Lambropoulos and A. B. Bergholdt, *Journal of Pharmaceutical and Biomedical Analysis*, 2000, **24**, 251.
88. J. C. Spell and J. T. Stewart, *Journal of Pharmaceutical and Biomedical Analysis*, 1998, **18**, 453.
89. J.T.Franeta, D. Agbaba, S. Eric, S. Pavkov, M. Aleksic and S. Vladimirov, *Il Farmaco*, 2002, **57**, 709.

90. R.Lui, J. Zhang, M. Liang, W. Zhang, S. Yan and M. Lan, *Journal of Pharmaceutical and Biomedical Analysis*, 2007, **43**, 1007.
91. G.Santoni, L. Fabbris, P. Gratteri, G. Renzi and S. Pinzauti, *International Journal of Pharmaceutics*, 2007, **328**, 105.
92. N.Daraghmeh, M. Al-Omari, A. A. Badwan and A. M. Jaber, *Journal of Pharmaceutical and Biomedical Analysis*, 2001, **25**, 483.
93. A.Mohammadi, N. Rezanour, M. Ansari Dogaheh, F. Ghorbani Bidkorbeh, M. Hashem and R. B. Walker, *Journal of Chromatography B*, 2007, **846**, 215.
94. S. H. Tabasi, R. Fahmy, D. Bensley, C. O'Brien and S. W. Hoag, *Journal of Pharmaceutical Sciences*, 2008, **97**, 4040.
95. W. Y. Li, L. Bagnol, M. Berman, R. A. Chiarella and M. Gerber, *International Journal of Pharmaceutics*, 2009, **380**, 49-54.
96. M. Alcala, J. Leon, J. Roperro, M. Blanco and R. J. Romanach, *Journal of Pharmaceutical Sciences*, 2008, **97**, 5318-5327.
97. R.L.Green, M. D. Mowery, J. A. Good, J. P. Higgins, S. M. Arrivo, K. McColough, A. Mateos and R. A. Reed, *Applied Spectroscopy*, 2005, **59**, 340.
98. *USFDA Draft Guidance for Industry: PAT - a framework for innovative pharmaceutical manufacturing and quality assurance*, 2003.
99. *2008 USPC Official Guide, USP monograph on Chlorpheniramine maleate, valid from 01/08/08 - 30/11/08*.
100. M.Dyrby, S. B. Engelsen, L. Norgaard, M. Bruhn and L. Ludensberg-Nielsen, *Applied Spectroscopy*, 2002, **56**, 579.
101. J.Breitenbach, W. Schrof and J. Neumann, *Journal of Pharmaceutical Research*, 1999, **16**, 1109.
102. J.Johanson, S. Pettersson and S. Folestad, *Journal of Pharmaceutical and Biomedical Analysis*, 2005, **39**, 510.
103. D.S.Moore and R. J. Scharff, *Anal. Bioanal. Chem.*, 2009, **393**, 1571.
104. C.Dunsby and P. M. W. French, *Journal of Physics D:Applied Physics*, 2003, **36**, R207.

105. P. Matousek, I. P. Clark, E. R. C. Draper, M. D. Morris, A. E. Goodship, N. Everall, M. Towrie, W. F. Finney and A. W. Parker, *Applied Spectroscopy*, 2005, **59**, 393.
106. N. Everall, T. Hahn, P. Matousek, A. W. Parker and M. Towrie, *Applied Spectroscopy*, 2001, **55**, 1701.
107. N. Everall, T. Hahn, P. Matousek, A. W. Parker and M. Towrie, *Applied Spectroscopy*, 2004, **58**, 591.
108. N. A. MacLeod and P. Matousek, *Applied Spectroscopy*, 2008, **11**, 291A.
109. J. Wu, Y. Wang, L. Perelman, I. Itzkan, R. Dasari and M. S. Feld, *Applied Optics*, 1995, **34**, 3425.
110. P. Matousek, N. Everall, M. Towrie and A. W. Parker, *Appl. Spectrosc.*, 2005, **59**, 200.
111. B. Schrader and G. Bergmann, *Zeitschrift für Analytische Chemie Fresenius*, 1967, **225**, 230.
112. A. Carden and M. D. Morris, *Journal of Biomedical Optics*, 2000, **5**.
113. N. Stone, C. Kendall, N. Shepherd, P. Crow and H. Barr, *Journal of Raman Spectroscopy*, 2002, **33**, 564.
114. L. J. Bellamy, *University of Strathclyde PhD Thesis: Application of Non-invasive Process Analytical Technologies to Characterise the Factors Influencing Mixing and Measurement of Powders*, 2005.
115. *Sigma Aldrich*, [www.sigmaaldrich.com](http://www.sigmaaldrich.com).
116. L. J. Bellamy, D. Littlejohn and A. Nordon, *Analyst*, 2008, **133**, 58.
117. S. R. Byrn, R. R. Pfeiffer, G. Stephenson, D. J. W. Grant and W. B. Gleason, *Chemistry of Materials*, 1994, **6**, 1148.
118. J. Workman, M. Koch and D. J. Veltkamp, *Analytical Chemistry*, 2003, **75**, 2859.
119. D. E. Bugay, *Advanced Drug Delivery Reviews*, 2001, **48**, 43.
120. C. J. Strachan, P. F. Taday, D. A. Newnham, K. C. Gordon and J. A. Zeitler, *Journal of pharmaceutical Sciences*, 2005, **94**, 837.
121. U. Grummisch, *Pharmaceutical Industry*, 1998, **60**, 1002.
122. J. Workman, *Journal of Near Infrared spectroscopy*, 1993, **1**, 221.
123. J. D. Kirsch and J. K. Drennen, *Applied Spectroscopy*, 1995, **30**, 139.



124. J.Gottfries, H. Depui, M. Fransson, M. Jongeneelen, M. Josefson, F. W. Langkilde and D. T. Witte, *Journal of Pharmaceutical and Biomedical Analysis*, 1996, **14**, 1495.
125. P.Corti, G. Ceramelli, E. Dreassi and S. Mattii, *Analyst*, 1999, **124**, 755.
126. P.Merckle and K. A. Kovar, *Journal of Pharmaceutical and Biomedical Analysis*, 1998, **17**, 365.
127. Q.Wang and S. DeJesus, *Journal of Near Infrared spectroscopy*, 1998, **6**, A223.
128. J.Johansson, S. Folestad, M. Josefson, A. Sparen, C. Abrahamsson, S. Andersson-Engels and S. Svanberg, *Applied Spectroscopy*, 2002, **56**, 725.
129. A.C.Williams, V. B. Cooper, L. Thomas, L. J. Griffith, C. R. Petts and S. W. Booth, *International Journal of Pharmaceutics*, 2004, **275**, 29.
130. C.Wang, T. Vickers and C. Mann, *Journal of Pharmaceutical and Biomedical Analysis*, 1997, **16**, 87.
131. J.Johansson, S. Pettersson and S. Folestad, *Journal of Pharmaceutical and Biomedical Analysis*, 2005, **39**, 510.
132. S.E.J.Bell, D. T. Burns, A. C. Dennis, L. J. Matchett and J. S. Speers, *Analyst*, 2000, **125**, 1811.
133. D.S.Hausman, R. T. Cambron and A. Sakr, *International Journal of Pharmaceutics*, 2005, **299**, 19.
134. R.Szostak and S. Mazurek, *Analyst*, 2002, **127**, 144.
135. T. M. Niemczyk, M. M. Delagdo-Lopez and F. S. Allen, *Analytical Chemistry*, 1998, **70**, 2762.
136. M. Kim, H. Chung, Y. Woo and M. Kemper, *Analytica Chimica Acta*, 2006, **579**, 209.
137. M. Kim, H. Chung, Y. Woo and M. Kemper, *Analytica Chimica Acta*, 2007, **587**, 200.
138. J. Kim, J. JNoh, H. Chung, Y. Woo, M. Kemper and Y. Lee, *Analytica Chimica Acta*, 2007, **598**, 280.
139. P. Matousek and A. W. Parker, *Journal of Raman Spectroscopy*, 2007, **38**, 563.

140. *International Conference on Harmonization of Technical Requirements for Registration of Pharmaceuticals for Human Use (ICH), Section Q3A: Guidelines on Impurities in New Drug Products.*
141. L. Q. Chu, H. Q. Mao and W. Knoll, *Polymer*, 2006, **47**, 7406.
142. L. Q. Chu, W. J. Tan, H. Q. Mao and W. Knoll, *Macromolecules*, 2006, **39**, 8742.
143. H. Takahashi, K. Fujita and H. Ohno, *Chemistry Letters*, 2007, **36**, 116.
144. P. Zuo, A. Sutresno, C. Li, Y. Koyama and H. Nagae, *Chemical Physics Letters*, 2007, **440**, 360.
145. Y. Tamaki, A. Furube, M. Murai, K. Hara, R. Katoh and M. Tachiya, *Physical Chemistry Chemical Physics*, 2007, **9**, 1453.
146. A. Saeki, S. Seki, Y. Koizumi and S. Tagawa, *Journal of Photochemistry and Photobiology A - Chemistry*, 2007, **186**, 158.
147. D. Romanini and K. K. Lehmann, *Journal of Chemical Physics*, 1993, **99**, 6287.
148. G. P. Miller and C. B. Winstead, *Journal of Analytical Atomic Spectrometry*, 1997, **12**, 907.
149. Z. Qi, N. Matsuda, T. Yoshida, H. Asano, A. Takatsu and K. Kato, *Optics Letters*, 2002, **27**, 2001.
150. R. Katoh, A. Furube, K. Hara, S. Murata, H. Sugihara, H. Arakawa and M. Tachiya, *Journal of Physical Chemistry, B*, 2002, **106**, 12957.
151. T. Yoshihara, M. Murai, Y. Tamaki, A. Furube and R. Katoh, *Chemical Physics Letters*, 2004, **394**, 161.
152. A. O'Keefe and D. A. G. Deacon, *Review of Scientific Instruments*, 1988, **59**, 2544.
153. T. G. Slinger, D. L. Huestis, P. C. Cosby, H. Naus and G. Meijer, *Journal of Chemical Physics*, 1996, **105**, 9393.
154. R. Engeln, G. Helden, G. Berden and G. Meijer, *Chemical Physics Letters*, 1996, **262**, 105.
155. E. Quandt, I. Kraemer and H. F. Dobele, *Europhysics Letters*, 1998, **45**, 32.
156. J. B. Paul, C. P. Collier, R. J. Saykally, J. J. Scherer and A. O'Keefe, *Journal of Physical Chemistry*, 1997, **101**, 5211.

157. A. O'Keefe, J. J. Scherer, A. L. Cooksey, R. Sheeks, J. Heath and R. J. Saykally, *Chemical Physics Letters*, 1990, **172**, 214.
158. T. Yu and M. C. Lin, *Journal of American Chemical Society*, 1994, **115**, 4371.
159. T. Yu and M. C. Lin, *Journal of Physical Chemistry*, 1994, **98**, 9697.
160. R. T. Jongma, M. G. H. Boogarts, I. Holleman and G. Meijer, *Review of Scientific Instruments*, 1995, **66**, 2821.
161. P. Zalicki, Y. Ma, R. N. Zare, E. H. Wahl, J. R. Dadamino, T. G. Owano and C. H. Kruger, *Chemical Physics Letters*, 1995, **234**, 269.
162. G. Berden, R. Peeters and G. Meijer, *International Reviews in Physical Chemistry*, 2000, **19**, 565.
163. S. Xu, G. SHa and J. Xie, *International Reviews in Physical Chemistry*, 2002, **19**, 565.
164. A. J. Alexander, *Analytical Chemistry*, 2006, **78**, 5597.
165. L. VanDerSneppen, A. Wiskerke, F. Ariese, C. Gooijer and W. Ubachs, *Analytica Chimica Acta*, 2006, **558**, 2.
166. U. Elejalde and J. M. Girkin, *Applied Optics*, 2007, **46**, 3995.
167. V. M. Baev, T. Latz and P. E. Toschek, *Applied Physics B*, 1999, **69**, 171.
168. A. A. Kachanov, F. Stoeckel, A. Charvat and J. J. O'Brien, *Applied Optics*, 1997, **36**, 4062.
169. J. Ye, L. S. Ma and J. L. Hall, *Journal of the Optical Society of America B*, 1998, **15**, 6.
170. N. Dutta, R. T. Warner and G. J. Wolga, *Optics Letters*, 1977, **1**, 155.
171. V. M. Baev, T. P. Belikova, E. A. Sviridenkov and A. F. Suchkov, *Soviet Journal of Experimental and Theoretical Physics*, 1978, **47**, 21.
172. G. O. Brink, *Optics Communications*, 1980, **32**, 123.
173. R. A. Keller, E. F. Zalewski and N. C. Peterson, *Journal of the Optical Society of America* 1972, **62**, 319.
174. W. Brunner and H. Paul, *Optics Communications*, 1974, **12**, 252.
175. S. J. Harris, *Applied Optics*, 1984, **23**, 1311.
176. H. Naus, I. H. M. van Stokkum, W. Hogervorst and W. Ubachs, *Applied Optics*, 2001, **40**, 4416.

177. E. Kleist and H. Bettermann, *Optics Letters*, 1988, **13**, 449.
178. E. Unger and G. Patonay, *Analytical Chemistry*, 1989, **61**, 1425.
179. A. J. G. Mank, O. Larsen, H. Lingeman, C. Gooijer, U. Brinkman and N. Velthorst, *Analytica Chimica Acta*, 1996, **323**, 1.
180. W. J. Childs, M. S. Fred and L. S. Goodman, *Applied Optics*, 1974, **13**, 2297.
181. A. Campargue, S. Mikhailenko and A. W. Liu, *Journal of Quantitative Spectroscopy and Radiative Transfer*, 2008, **2008**, 2832.
182. J. S. Shirk, T. D. Harris and J. W. Mitchell, *Analytical Chemistry*, 1980, **52**, 1701.
183. E. N. Antonov, *Optics Communications*, 1975, **15**, 99.